

OPTIMIZATION OF COMPOSITE BOX-BEAM STRUCTURES INCLUDING EFFECTS OF SUBCOMPONENT INTERACTION

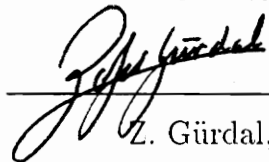
by

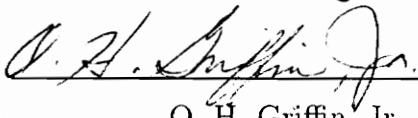
Scott Alan Ragon

Thesis submitted to the faculty of the
Virginia Polytechnic Institute and State University
in partial fulfillment of the requirements for the degree of

Master of Science
in
Engineering Mechanics

APPROVED:



Z. Gürdal, Chairman

O. H. Griffin, Jr.

R. T. Haftka

July, 1994
Blacksburg, Virginia

C.2

LD
5655
V855
1994
R346
C.2

OPTIMIZATION OF COMPOSITE BOX-BEAM STRUCTURES INCLUDING EFFECTS OF SUBCOMPONENT INTERACTION

by

Scott Alan Ragon

Zafer Gürdal, Chairman

Engineering Science and Mechanics

(ABSTRACT)

Minimum mass designs are obtained for a simple box beam structure subject to bending, torque and combined bending/torque load cases. These designs are obtained subject to point strain and linear buckling constraints. The present work differs from previous efforts in that special attention is paid to including the effects of subcomponent panel interaction in the optimal design process. Two different approaches are used to impose the buckling constraints. When the global approach is used, buckling constraints are imposed on the global structure via a linear eigenvalue analysis. This approach allows the subcomponent panels to interact in a realistic manner. The results obtained using this approach are compared to results obtained using a traditional, less expensive approach, called the local approach. When the local approach is used, in-plane loads are extracted from the global model and used to impose buckling constraints on each subcomponent panel individually. In the global cases, it is found that there can be significant interaction between skin, spar, and rib design variables. This coupling is weak or nonexistent in the local designs. It is determined that weight savings of up to 7% may be obtained by using the global approach instead of the local approach to design these structures.

Several of the designs obtained using the linear buckling analysis are subjected to a geometrically nonlinear analysis. For the designs which were subjected to bending loads, the innermost rib panel begins to collapse at less than half the intended design load and in a mode different from that predicted by linear analysis. The discrepancy between the predicted linear and nonlinear responses is attributed to the effects of the nonlinear rib crushing load, and the parameter which controls this rib collapse failure mode is shown to be the rib thickness. The rib collapse failure mode may be avoided

by increasing the rib thickness above the value obtained from the (linear analysis based) optimizer. It is concluded that it would be necessary to include geometric nonlinearities in the design optimization process if the true optimum in this case were to be found.

DEDICATION

This work is dedicated to my mother, Karen Burnett, and to the memory of my father, Hugh Ragon.

ACKNOWLEDGMENTS

This study was supported by the NASA-Virginia Tech Composites Program under NASA Grant NAG 1-343. The author would like to thank Dr. Zafer Gürdal and Dr. James H. Starnes, Jr. for their guidance and advice during the course of this research. Thanks are also due to Dr. O. Hayden Griffin, Jr. and Dr. Raphael T. Haftka for their helpful advice.

TABLE OF CONTENTS

List of Figures	viii
List of Tables	xiii
Chapter 1 Introduction and Literature Review	1
1.1 Introduction	1
1.2 Literature Review	5
1.3 Scope of the present work	10
Chapter 2 Analysis and Optimization Tools	11
2.1 Computational Mechanics Testbed	11
2.2 Linear Buckling Analysis	12
2.3 Geometrically Nonlinear Analysis	13
2.4 Optimization Terminology	14
2.5 Optimization Algorithms	16
2.5.1 Sequential Convex Programming	16
2.5.2 Method of Feasible Directions	17
2.6 Testbed Optimization (TBOP)	18
2.6.1 Overview	19
2.6.2 Baseline Capabilities	21
2.6.3 Modifications and Enhancements	24
Chapter 3 Model Description	37
3.1 Physical Model	37
3.2 Finite Element Model	37
3.3 Panel Modelling	39
3.4 Material Properties	41
3.5 Mesh Convergence	43
3.6 D_{16} and D_{26} terms	44
<i>Table of Contents</i>	vi

Chapter 4	Results of Linear Design Study	47
4.1	Upward Bending	51
4.1.1	Design B3G: Global Approach	51
4.1.2	Design B9G: Global Approach	60
4.1.3	Design B9GP: Global Approach	67
4.1.4	Summary of Interaction Effects: Designs B3G-B9GP	71
4.1.5	Designs B3L-B9LP: Local Approach	72
4.2	Torque	83
4.2.1	Design T3G: Global Approach	84
4.2.2	Design T9G: Global Approach	92
4.2.3	Summary of Interaction Effects: Designs T3G and T9G	93
4.2.4	Designs T3L and T9L: Local Approach	96
4.3	Combined Bending and Torque Loads	102
4.3.1	Designs C3G and C9GP: Global Approach	103
4.3.2	Summary of Interaction Effects: Designs C3G and C9GP	113
4.3.3	Designs C3L and C9LP: Local Approach	113
4.3.4	Designs C3G-1 and C3G-2: Global Approach	119
4.4	Smeared Stiffener Approach	121
4.5	Effect of Rib Spacing	133
4.6	Effect of Box Beam Width	145
Chapter 5	Nonlinear Analysis	158
5.1	Bending Designs	158
5.2	Torque Designs	172
5.3	Combined Bending/Torque Designs	173
Chapter 6	Conclusions and Recommendations for Future Work	180
6.1	Conclusions	180
6.2	Recommendations for Future Work	182
References		184
Appendix A	Derivation of the Buckling Load of a Simply Supported Plate Subject to a Linearly Varying Edge Load	189

LIST OF FIGURES

1.1	Lockheed Technology Integration Box Beam (TIBB)	2
1.2	ICAPS Wingbox	3
2.1	TBOP Flowchart	20
2.2	Typical Blade Stiffener	29
2.3	Location of Finite Element Centroid on Stiffener Cross Sect: Method 1	30
2.4	Location of Finite Element Centroid on Stiffener Cross Sect: Method 2	31
2.5	Comparison of PASCO and TBOP smeared stiffener results for a blade stiffened panel	33
3.1	C-130 Box Beam	38
3.2	Undeformed Mesh	39
3.3	Bending Load Case	40
3.4	Torque Load Case	40
3.5	Three Design Variable Case	41
3.6	Nine Design Variable Case	42
4.1	Design B3G – Active buckling mode 1 ($\lambda=.9997$)	52
4.2	Design B3G – Active buckling mode 2 ($\lambda=1.005$)	53
4.3	Design B3G – Linear Approximation to Design Space	54
4.4	Design B3G – Upper Skin Nx Load	55
4.5	Design B3G – Upper Skin Ny Load	56
4.6	Design B3G – Upper Skin Nxy Load	56
4.7	Design B3G – Spar Nx Load	57
4.8	Design B3G – Spar Nz Load	57
4.9	Design B3G – Spar Nxz Load	58
4.10	Design B3G – Second Rib Ny Load	59
4.11	Design B3G – Second Rib Nz Load	59
4.12	Design B3G – Second Rib Nyz Load	60
4.13	Design B9G – Active Buckling Mode 1 ($\lambda = .9976$)	62
4.14	Design B9G – Active Buckling Mode 2 ($\lambda = 1.003$)	62

4.15 Comparison of Designs B3G-B9GP	64
4.16 Design B9G – Upper Skin Nx Load	65
4.17 Design B9G – Upper Skin Ny Load	65
4.18 Design B9G – Second Rib Ny Load	66
4.19 Design B9G – Second Rib Nz Load	66
4.20 Design B9GP – Upper Skin Nx Load	69
4.21 Design B9GP – Upper Skin Ny Load	69
4.22 Design B9GP – Second Rib Ny Load	70
4.23 Design B9GP – Second Rib Nz Load	70
4.24 Comparison of designs B3G and B3L	74
4.25 Design B3L – Linear Approximation to Design Space	77
4.26 Design B3L – Upper Skin Nx Load	77
4.27 Design B3L – Upper Skin Ny Load	78
4.28 Design B3L – Upper Skin Nxy Load	78
4.29 Comparison of designs B9G and B9L	80
4.30 Comparison of designs B9GP and B9LP	82
4.31 Design T3G – Active buckling mode 1 ($\lambda=.9983$)	86
4.32 Design T3G – Active buckling mode 2 ($\lambda=1.007$)	87
4.33 Design T3G – Linear Approximation to Design Space	88
4.34 Design T3G – Upper Skin Nx Load	88
4.35 Design T3G – Upper Skin Ny Load	88
4.36 Design T3G – Upper Skin Nxy Load	89
4.37 Design T3G – Spar Nx Load	90
4.38 Design T3G – Spar Nz Load	90
4.39 Design T3G – Spar Nxz Load	90
4.40 Design T3G – Second Rib Ny Load	91
4.41 Design T3G – Second Rib Nz Load	91
4.42 Design T3G – Second Rib Nyz Load	92
4.43 Design T9G – Active Buckling Mode 1 ($\lambda = .9981$)	94
4.44 Design T9G – Active Buckling Mode 2 ($\lambda = 1.008$)	94
4.45 Comparison of designs T3G and T9G	95
4.46 Comparison of designs T3G and T3L	97
4.47 Design T3L – Linear Approximation to Design Space	99
4.48 Design T3L – Upper Skin Chordwise (Nx) Load	99

4.49 Design T3L – Upper Skin Spanwise (N_y) Load	100
4.50 Design T3L – Upper Skin Shear (N_{xy}) Load	100
4.51 Comparison of designs T9G and T9L	102
4.52 Design C3G – Active buckling mode 1 ($\lambda=.9984$)	104
4.53 Design C3G – Active buckling mode 2 ($\lambda=1.008$)	105
4.54 Design C3G – Linear Approximation to Design Space	106
4.55 Comparison of designs B3G – C3G	107
4.56 Design C3G – Upper Skin N_x Load	107
4.57 Design C3G – Upper Skin N_y Load	108
4.58 Design C3G – Upper Skin N_{xy} Load	108
4.59 Design C3G – Left Spar N_x Load	109
4.60 Design C3G – Left Spar N_z Load	109
4.61 Design C3G – Left Spar N_{xz} Load	110
4.62 Design C3G – Right Spar N_x Load	110
4.63 Design C3G – Right Spar N_z Load	110
4.64 Design C3G – Right Spar N_{xz} Load	111
4.65 Design C3G – Second Rib N_y Load	111
4.66 Design C3G – Second Rib N_z Load	111
4.67 Design C3G – Second Rib N_{yz} Load	112
4.68 Design C9GP – Active Buckling Mode 1 ($\lambda = 1.003$)	114
4.69 Design C9GP – Active Buckling Mode 2 ($\lambda = 1.008$)	114
4.70 Comparison of designs C3G and C9GP	115
4.71 Comparison of designs C3G and C3L	117
4.72 Comparison of designs C9GP and C9LP	118
4.73 Comparison of designs C3G, C3G-1, and C3G-2	121
4.74 Design B5GS – Active Buckling Mode 1 ($\lambda = 1.001$)	124
4.75 Design B5GS – Active Buckling Mode 2 ($\lambda = 1.005$)	126
4.76 Design B5GS – Active Buckling Mode 3 ($\lambda = 1.008$)	126
4.77 Design B5GS – Active Buckling Mode 4 ($\lambda = 1.010$)	127
4.78 Design B5GS – Active Buckling Mode 5 ($\lambda = 1.010$)	127
4.79 Design T5GS – Active Buckling Mode 1 ($\lambda = 1.005$)	129
4.80 Design T5GS – Active Buckling Mode 2 ($\lambda = 1.006$)	129
4.81 Design T5GS – Active Buckling Mode 3 ($\lambda = 1.009$)	130
4.82 Design T5GS – Active Buckling Mode 4 ($\lambda = 1.009$)	130

4.83	Design T5GS – Active Buckling Mode 5 ($\lambda = 1.012$)	131
4.84	Design C5GS – Active Buckling Mode 1 ($\lambda = 1.000$)	131
4.85	Design C5GS – Active Buckling Mode 2 ($\lambda = 1.005$)	133
4.86	Comparison of designs B3G - B3G-R2	136
4.87	Comparison of designs B9GP - B9GP-R2	137
4.88	Comparison of designs T3G - T3G-R2	141
4.89	Comparison of designs T9G - T9G-R2	142
4.90	Design B3GW – Active buckling mode 1 ($\lambda=1.001$)	151
4.91	Design B3GW – Active buckling mode 2 ($\lambda=1.005$)	151
4.92	Design B3GW – Active buckling mode 3 ($\lambda=1.010$)	152
4.93	Comparison of designs B3G and B3GW	152
4.94	Comparison of designs B9GP and B9GPW	153
4.95	Design B9GPW – Active buckling mode 1 ($\lambda=.9976$)	154
5.1	Design B3G – Nonlinear Deformed Mesh ($\lambda=.48$ Scale=30X)	159
5.2	Design B3G – Nonlinear Deformed Mesh ($\lambda=.51$ Scale=30X)	159
5.3	Design B3G – Nonlinear Deformed Mesh ($\lambda=.89$ Scale=30X)	160
5.4	Design B3G Nonlinear Deformation History	161
5.5	Nonlinear Crushing Loads	162
5.6	Design B3G – Nonlinear Deformed Mesh ($\lambda=.48$ Scale=30X)	162
5.7	Design B3G – Nonlinear Deformed Mesh ($\lambda=.51$ Scale=30X)	163
5.8	Design B3G – Nonlinear Deformed Mesh ($\lambda=.72$ Scale=30X)	163
5.9	Design B3G – Critical Rib Crushing Loads (N_z)	164
5.10	Design B3G – Critical Rib Bending Moment (M_z)	164
5.11	Design B9G – Nonlinear Deformed Mesh ($\lambda=.30$ Scale=30X)	165
5.12	Design B9G – Nonlinear Deformation History	166
5.13	Design B9GP – Nonlinear Deformed Mesh ($\lambda=.45$ Scale=30X)	166
5.14	Design B9GP – Nonlinear Deformation History	167
5.15	Design B9GP – Nonlinear Deformed Mesh ($\lambda=.83$ Scale=30X)	167
5.16	Design B5GS – Nonlinear Deformation History	168
5.17	Design B3G (increased rib thk) – Critical Buckling Mode ($\lambda = 1.00$) .	169
5.18	Design B3G (increased rib thk) – Nonlinear Deformed Mesh ($\lambda=1.01$ Scale=30X)	170
5.19	Design B3G (increased rib thk) – Nonlinear Deformation History . . .	170

5.20	Design T3G – Nonlinear Deformed Mesh ($\lambda=1.02$ Scale=10X)	172
5.21	Design T3G – Nonlinear Deformation History	173
5.22	Design T9G – Nonlinear Deformed Mesh ($\lambda=1.01$ Scale=10X)	174
5.23	Design T9G – Nonlinear Deformation History	174
5.24	Design T9G – Nonlinear Deformed Mesh ($\lambda=1.00$ Scale=10X)	175
5.25	Design T5GS – Nonlinear Deformation History	175
5.26	Design C3G – Nonlinear Deformed Mesh ($\lambda=0.97$ Scale=10X)	176
5.27	Design C9GP – Nonlinear Deformed Mesh ($\lambda=0.97$ Scale=10X) . . .	177
5.28	Design C3G – Nonlinear Deformation History	177
5.29	Design C9GP – Nonlinear Deformation History	178
5.30	Design C5GS – Nonlinear Deformed Mesh ($\lambda=1.02$ Scale=10X) . . .	178
5.31	Design C5GS – Nonlinear Deformation History	179
A.1	Variation of the Critical Buckling Load with α	193

LIST OF TABLES

3.1	Assumed Material Properties (Graphite-Epoxy)	42
3.2	Assumed Material Strain Allowables (Graphite-Epoxy)	43
3.3	Mesh Convergence Study: Bending Design B3G	45
3.4	Mesh Convergence Study: Torque Design T3G	45
3.5	Mesh Convergence Study: Bending Design B9GP	45
3.6	Mesh Convergence Study: Torque Design T9G	45
4.1	Summary Description of Each Design Case: Part 1	49
4.1	Summary Description of Each Design Case: Part 2	50
4.2	Results – Design Case B3G	52
4.3	Design B3G – Active buckling constraint gradients	53
4.4	Results – Design Case B9G	61
4.5	Design B9G – Active buckling constraint gradients	63
4.6	Results – Design Case B9GP	68
4.7	Design B9GP – Active buckling constraint gradients	68
4.8	Results – Design Case B3L	74
4.9	Design B3L – Active buckling constraint gradients	77
4.10	Results — Design Case B9L	79
4.11	Results — Design Case B9L-A	81
4.12	Results — Design Case B9LP	82
4.13	Design B9L – Active buckling constraint gradients	83
4.14	Design B9LP – Active buckling constraint gradients	84
4.15	Results – Design Case T3G	86
4.16	Design T3G – Active buckling constraint gradients	87
4.17	Results – Design Case T9G	93
4.18	Design T9G – Active buckling constraint gradients	95
4.19	Results – Design Case T3L	97
4.20	Design T3L – Active buckling constraint gradients	98
4.21	Results — Design Case T9L	101
4.22	Design T9L – Active buckling constraint gradients	103

4.23 Results – Design Case C3G	104
4.24 Design C3G – Active buckling constraint gradients	105
4.25 Results – Design Case C9GP	113
4.26 Design C9GP – Active buckling constraint gradients	115
4.27 Results — Design Case C3L	116
4.28 Results — Design Case C9LP	117
4.29 Design C3L – Active buckling constraint gradients	118
4.30 Design C9L – Active buckling constraint gradients	119
4.31 Results – Design Case C3G-1	120
4.32 Results – Design Case C3G-2	120
4.33 Results — Design Case B5GS	125
4.34 Design B5GS – Active buckling constraint gradients	125
4.35 Results — Design Case T5GS	128
4.36 Design T5GS - Active Buckling constraint gradients	128
4.37 Results — Design Case C5GS	132
4.38 Design C5GS – Active buckling constraint gradients	132
4.39 Results — Design Case B3G-R1	135
4.40 Results — Design Case B3G-R2	136
4.41 Results — Design Case B9GP-R1	137
4.42 Results — Design Case B9GP-R2	138
4.43 Results — Design Case B3L-R2	138
4.44 Results — Design Case B9LP-R2	139
4.45 Results — Design Case T3G-R1	140
4.46 Results — Design Case T3G-R2	140
4.47 Results — Design Case T9G-R1	141
4.48 Results — Design Case T9G-R2	142
4.49 Results — Design Case T3L-R2	143
4.50 Results — Design Case T9L-R2	143
4.51 Results — Design Case B5GS-R1	145
4.52 Results — Design Case B5GS-R2	146
4.53 Results — Design Case T5GS-R1	147
4.54 Results — Design Case T5GS-R2	148
4.55 Results — Design Case B3GW	150
4.56 Design B3GW – Active buckling constraint gradients	150

4.57 Results — Design Case B9GPW	153
4.58 Design B9GPW – Active buckling constraint gradients	154
4.59 Results – Design Case B3LW	155
4.60 Results — Design Case B9LPW	156
4.61 Design B3LW – Active buckling constraint gradients	156
4.62 Design B9LPW – Active buckling constraint gradients	157
5.1 Results – Design Case B2G	171

Chapter 1

INTRODUCTION AND LITERATURE REVIEW

1.1 Introduction

In recent years, there has been a concerted effort in the commercial aerospace industry to utilize advanced composite materials in the design of primary load carrying structures such as wings and fuselages. Production aircraft have used composite materials in less critical secondary and control surface structures for several years now, and significant weight savings have been obtained as a result. The full weight savings potential of composite materials cannot be realized, however, until composites are used as part of wing and fuselage structures, which make up around 75 percent of the total structural weight of a large transport type aircraft [1].

The effort to build large commercial wingbox structures out of composite materials began in the late 1970's with NASA funded studies by Lockheed-California and the Douglas Aircraft Company [2, 3]. The Lockheed team produced a detailed development plan for an L-1011 wingbox, and the Douglas team did likewise for a DC-9 wingbox. In each case, the plans included consideration of design, manufacturing and testing issues.

More recently, NASA's Advanced Composites Technology (ACT) Program was initiated to develop design concepts, analysis methods, manufacturing techniques, and materials applicable to composite aircraft structures. The stated goal of this program is to develop composite structures that are 30–50 percent lighter and 20–30 percent less costly than presently existing metallic structures.

As part of the ACT program, the Lockheed Aeronautical Systems Company designed, fabricated, and tested a composite box beam similar to that present in the C-130 inner wing (see Figure 1.1) [4, 5, 6]. The resulting design was 25 percent lighter and was predicted to be 5 percent less costly than the metallic baseline design. Although the composite design failed prematurely in the testing phase of the program as a result of local stress concentrations [6, 7], it demonstrated the feasibility of producing cost competitive, lightweight composite wingbox structures. Experience gained in this program provided valuable data for the growing technology base on

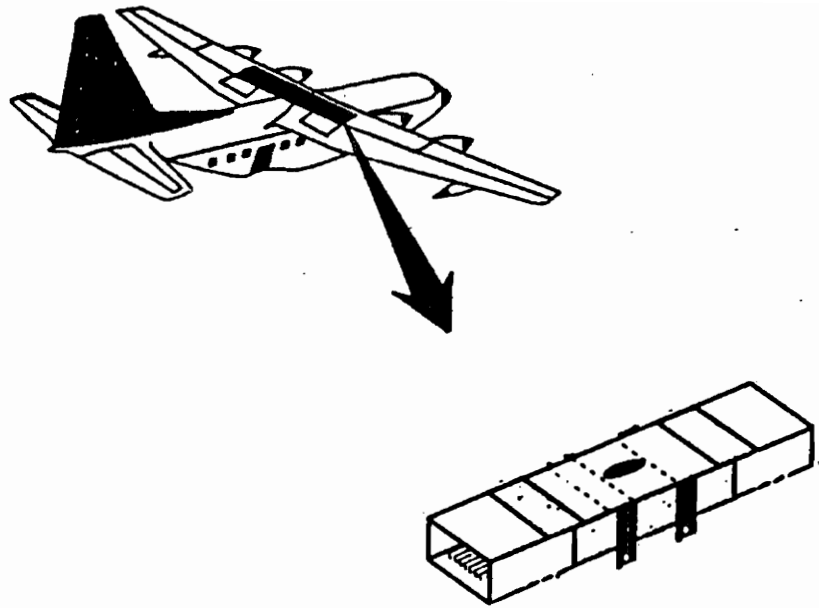


Figure 1.1: Lockheed Technology Integration Box Beam (TIBB)

large composite structures.

Also as part of the ACT program, Douglas Aircraft Company has initiated a program for the design of Innovative Composite Aircraft Primary Structure (ICAPS). The stated goal of this program is to develop a composite wing box for a short-haul transport that is 30 percent lighter and 40 percent less costly than a comparable metallic structure (see Figure 1.2) [8]. The structures developed as part of this program are scheduled to be incorporated in the planned MD-XX vehicle.

In preparation for and in addition to these efforts to fabricate a complete wing box structure, a number studies and tests have been performed on individual wing box components such as skin and spar panels. Numerous design studies and testing programs have been completed. In addition to the references cited above, references [1, 9, 10] typify these activities.

Designing structures out of fiber reinforced composite materials is a much more challenging task as compared to designing the same structures with metals. There are many more variables, such as individual ply thicknesses and ply orientations, that must be considered in the design process. The resulting complexity gives the designer considerable freedom to tailor the structure to specific loading conditions,

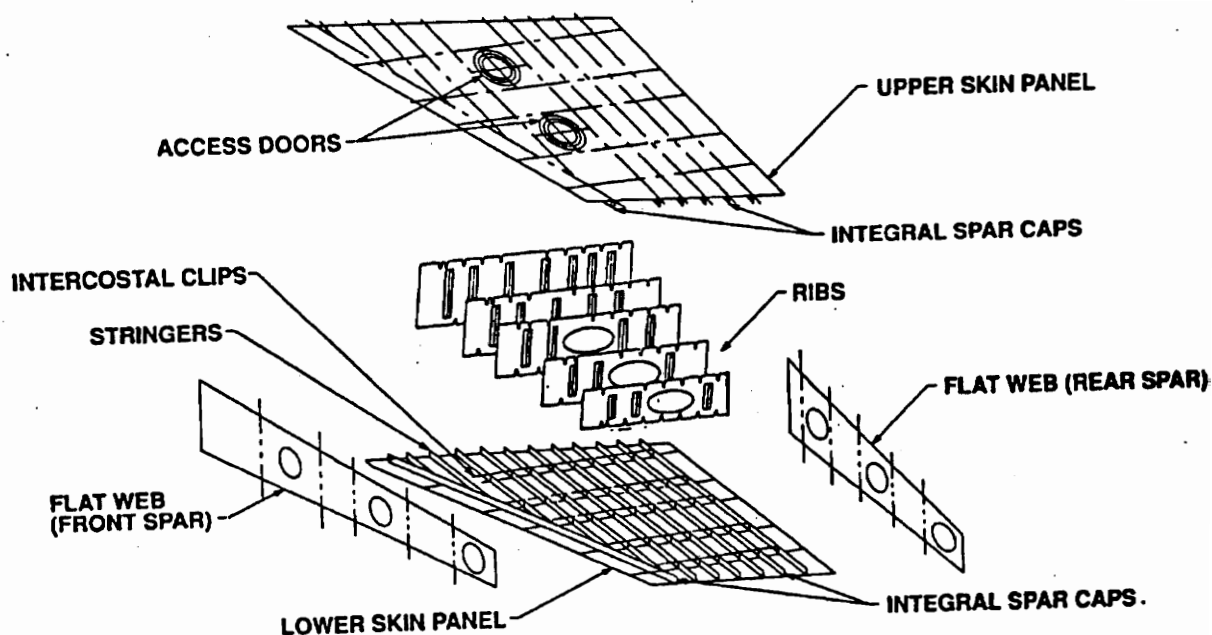


Figure 1.2: ICAPS Wingbox

but it also makes his or her job much more difficult. Rules of thumb and past experience with metals often do not apply to composite structures, as their response is frequently non-intuitive. Traditional design methods, such as the fully stressed design (FSD) procedure [11], often do not give satisfactory results when applied to composite materials.

As a result, there is a growing interest in using formal mathematical optimization techniques to design composite aircraft structures. A number of design studies have focused on obtaining optimal designs for individual wing box components such as skin and rib panels, and optimized panel designs have been obtained subject to both strength and buckling constraints and under a variety of loading conditions. Other researchers have obtained optimal designs for complete wing box structures of varying complexity. These designs have been obtained subject to various combinations of aeroelastic, strength, stability, and displacement constraints.

In the present work, this line of research is continued and optimal designs for a simple rectangular wing box are presented. This work differs from previous efforts in that special attention is paid to including the effects of subcomponent panel interaction in the optimal design process. In a physical wing box structure, the actual

boundary conditions of an embedded structural panel are not well known; complex loads and deformations are induced in each panel by attached panels and by the structure as a whole. Actual buckling modes and deformation patterns may include the compatible interaction of two or more connected panels. As a result it may be necessary to design each subcomponent panel, not in isolation, but as an integral part of the whole structure. This may be accomplished by utilizing analysis models wherein the component panels are allowed to interact with one another through their attached edges. The result will be more realistic inter-panel boundary conditions and loads for each panel of interest.

Panel interaction effects are potentially important to the design of complex built up structures such as wingboxes. Including panel interaction effects in the design optimization process may lead to lighter designs than would have been obtained otherwise. For example, in a skin-panel/rib-panel interaction, it may be found that increasing the rib thickness provides increased restraint against skin buckling, thereby allowing the skin thickness to be reduced. Panels may also interact in unfavorable ways, leading to unexpected failure modes. In the latter case, it would be important to include the interaction effects in the design process so that these failure modes can be avoided. Because some of the panel interactions may be nonlinear, it may also be important to consider the geometrically nonlinear response of the structure in some cases.

The overall goal of the present work is to include the effects of panel interaction in the design optimization process for a representative wing box structure. The specific goals are as follows:

- Obtain optimal wing box designs based on linear analysis for several different geometries and loading conditions.
- Compare the results obtained using the present approach to those obtained using traditional methods.
- Draw conclusions about the nature of significant panel interaction effects and their importance to the optimal designs obtained.
- Assess the importance of geometric nonlinearities on the response of these optimal designs and determine if there are nonlinear interaction effects that are important to the structural response.

The remainder of this thesis is organized as follows: The rest of this chapter is devoted to a literature review and description of the scope of the present study. Chapter 2 describes the analysis and design tools that were utilized and/or developed in the course of this study. The finite element models that were used are described in Chapter 3, along with a discussion of mesh convergence. In Chapter 4, optimal wingbox designs are presented for different geometries and different combinations of design variables. The effects of panel interaction on these designs is discussed and a comparison is made to several designs obtained using traditional methods. Finally, in Chapter 5, there is a discussion concerning the effects of geometric nonlinearities on several of the designs presented in Chapter 4.

1.2 Literature Review

A number of design studies have focused on the optimal design of individual wing box structural panels such as skin panels, spar panels, and rib panels. Optimal panel designs have been obtained subject to strength and buckling constraints and under a variety of different loading conditions. These studies were commonly performed using analysis models that ignored the connectivity between attached panels and used idealized boundary conditions and loads for each panel.

An early example of this type of work may be found in a study performed by Stroud and Agranoff [12], where hat stiffened and corrugated panels subject to longitudinal compression and shear loads were considered. Each panel was modelled as an assembly of rectangular plate elements connected along their longitudinal edges. Minimum mass designs were obtained subject to constraints on overall and local buckling, strength, stiffness, and minimum gage size. The design variables were taken to be the thicknesses and lengths of the elements that define the panel cross sections. Overall buckling modes were taken into account using the smeared stiffness approach, and local buckling modes were taken into account through a simplified analysis in which each plate element was considered individually assuming that it had simply supported boundary conditions.

A more recent study by Swanson and Gürdal [13] considered the minimum mass design of aircraft rib panels subject to axial compression, shear, and normal pressure loads. Like reference [12], each panel was modelled as an assemblage of longitudinally connected plate elements. A wide variety of cross sections and stiffener arrangements

were compared. Design variables were the thicknesses and lengths of cross sectional elements, and constraints included global and local buckling, strength, and geometric constraints. The design optimization and panel analysis was performed using the PASCO code [14], which, unlike [12], accounts for the continuity of local buckled mode shapes across neighboring plate elements.

While this individual panel approach has generated much useful data, the results may not directly apply to panels that are an integral part of a larger wingbox structure. There are two drawbacks associated with the individual panel approach. First, it is well known that in the case of the optimization of a redundant structure made up of several components, minimization of each of the component masses does not guarantee minimization of the total mass [15]. In a real structure, increasing the thickness of one component will draw more load to that component, thus reducing the loads that must be resisted by the other components. Likewise, reducing the stiffness of a given component will increase the load that must be carried by neighboring components. Changing the thickness of a given component, then, not only changes the stress state in that component, but affects the load path in the structure as a whole. These effects cannot be taken into account when optimizing an isolated component.

Second, in the actual structure, the boundary conditions at the edge of each of the panels may be considerably more complex than those commonly assumed. This is because the edge conditions on each panel can be affected by the other panels to which it is attached as well as by the deformations of the structure as a whole (panel interaction). Different edge conditions may have a considerable effect on a panel's behavior, and its response may differ substantially from the response obtained when considering the isolated panel. Buckling eigenmodes of the global structure may involve compatible deformations of one or more of the subcomponent panels. In order to obtain more realistic optimal designs, then, it may be necessary to take into account panel interaction effects by analyzing and optimizing wing box panels not in isolation, but as part of a larger built-up structure.

Several researchers have focused on obtaining optimal designs for complete wing box structures. In addition to having the potential to address the shortcomings associated with individual panel design, this approach allows constraints to be imposed on the wingbox global structural response as well as on the response of the individual subcomponent panels. Global constraints may include aeroelastic constraints, over-

all buckling or vibrational constraints, and overall displacement or twist constraints. The disadvantage of the global approach is the complexity and potential expense of the resulting design problem. In order to hold the problem to a manageable size, details of individual panel design and response must often be neglected.

A study involving the optimization of complete composite wing box structures was described by Sobieszczanski-Sobieski in 1979 [15]. Here, a series of optimal designs pertaining to the low aspect ratio wing of a large transport aircraft were generated in order to compare a number of different design alternatives. Loads were generated by an aerodynamic model and the effects of aeroelasticity were included in the analysis. The design variables described the construction of each of the sandwich skin panels: the thicknesses and orientations of the plies in the composite face sheets and the total sandwich thickness. Constraints included panel buckling, strain, stress, and minimum gage constraints.

The optimization of each of the wing cover panels was performed separately and in isolation from the structure as a whole. For each panel, the corresponding membrane forces N_x , N_y , and N_{xy} were extracted from the global model and held constant while the mass of the isolated panel was optimized. After each individual panel was minimized, the global model was updated and new loads were generated. This procedure was continued until the process converged.

Breaking the larger optimization problem down into a series of smaller optimization problems in this way drastically reduces the complexity and expense of the design problem, but, as noted by Sobieski, does not guarantee optimization of the structure as a whole. This is because this approach is still essentially the same as the individual panel approach described previously. During each individual optimization problem, the loads are held constant and a change in the panel stiffness is not allowed to affect the load path in the structure as a whole.

The first time this problem was corrected and panel buckling constraints were handled directly at the global level was in a study by Starnes and Haftka [16]. Here, the WIDOWAC [17] program was used to obtain minimum mass designs for a multi-spar high aspect ratio wing. An unstiffened panel buckling constraint was combined with strength, minimum gage, displacement, and twist constraints to obtain results for both isotropic and laminated composite structures.

All constraints were imposed on the global wingbox level, and a single optimization problem was formulated for the entire structure. The unstiffened panel buckling

constraints were based on an a semi-empirical buckling analysis for simply supported plates subject to in-plane forces. A global finite element model composed of rod elements for the rib and spar caps, constant strain membrane elements for the skin panels, and shear elements for the rib and spar panels was used. Design variables were the thicknesses or areas of these structural elements.

In order to demonstrate the advantages of including all the constraints at the global level, the results of this study were compared to the results obtained using the individual panel approach. One of the skin panels was removed from the global model (along with the applicable edge loads) and optimized separately. The optimal thickness for this individual panel was about 7% less than the corresponding panel that was optimized as part of the global structure. As a check, the thicker panel was replaced by the thinner panel in the global structure, and the global structure was re-analyzed. As a consequence of significant internal load redistribution away from the thinner panel, a number of the other panels violated their buckling constraints. This demonstrated the importance of including constraints on the global level, and clearly illustrated the pitfalls associated with the individual panel approach.

Although the global approach used in this work corrected a major problem with the individual panel approach and resulted in better a better global design, the complexity of the design problem was greatly increased. Instead of solving many simple optimization problems, a single complex problem was solved. Because of the size, complexity, and potential cost of this problem, details of the individual panel designs were neglected. Instead of modelling the panel cross section in detail, each panel was instead modelled as an unstiffened panel.

Schmit and Mehrinfar [18] used a multilevel approach to address this problem. Here, a compromise was made between the individual panel approach and the global approach in the design of several simple wingbox structures. Strength, deflection, and overall panel buckling constraints were treated at the global level using equivalent thickness design variables while panel global and local buckling constraints were imposed at the component level using detailed panel dimensions as design variables. The key feature of this method was that instead of minimizing weight at the individual panel level, the objective was to minimize the change in the panel stiffness at this level. This procedure avoided a major drawback of the individual panel approach in that it allowed panel dimensions at the component level to change without significantly changing the load paths in the global structure. As a result, it became possible

to legitimately de-couple each of the detailed panel design problems from the global design problem, thus allowing the overall design to be obtained without neglecting details of local panel design.

The global finite element model used in Reference [18] was composed of rod elements for the spar and rib caps, shear panels for the ribs and spars, and membrane elements for the skin panels. The global buckling constraints were based on a semi-empirical buckling analysis valid for a panel with simply supported edges and subject to in-plane loads. If sandwich panels were considered, the component level buckling constraints are based either on the same semi-empirical buckling equations used at the global level or on a more refined eigenvalue analysis in which the panel was treated as an equivalent orthotropic plate subject to in-plane loads. If hat stiffened panels were used, the buckling analysis was the same as that used in [12].

Watkins [19] extended this multilevel approach to include ply orientation design variables at the component level and a new objective function at the component level. The objective function used at the component level was a multi-criteria objective function involving the minimization of a linear combination of the panel weight and change in the panel strain energy. The inclusion of weight in the objective function was an improvement over reference [18] in that there was an incentive at the component level to reduce the weight of a panel which satisfied the buckling constraints.

Most of the studies done on the optimization of global wing box structures have been performed using simplified models of the wing structure. A notable exception is a study performed by Walsh [20]. Here, a detailed finite element model of the wing and wing-fuselage interface of a large transport type wing was modelled using rod and membrane elements. The fuselage, empennage, engine, and landing gear were modelled with beam elements. Minimum weight designs subject to stress constraints were obtained and the results were compared to those obtained using the fully stressed design method.

One of the problems with the individual panel approach cited above is that it does not take into account panel interaction effects (the interaction between the design and response of one panel and the design and response of neighboring panels). Because of the way in which the buckling constraints were formulated and because of the way in which the individual panels were modelled, none of the global design studies cited here took these effects into account either. When panel buckling was

considered, the analysis was always based on a simply supported panel subject to a combination of in-plane forces. No buckling modes were considered which included the compatible deformations of more than one panel. Because many of the finite elements representing the component panels did not include bending stiffness (and because the spar and rib panels often did not include axial stiffness), none of the panels were able to interact with one another in a significant way. Bending moments could not be transferred from panel to panel along their connected edges and no complex deformation patterns involving more than one panel were possible.

1.3 Scope of the present work

Because the effects of panel interaction are potentially important, they are investigated in the present work. Minimum mass designs are obtained for several simple rectangular wing boxes subjected to bending and twisting loads. Buckling constraints and strain constraints are imposed on the design. In order to include panel interaction effects in the design process, each of the wingbox panels is modelled using finite elements which have both in-plane and out of plane bending stiffnesses as well as in-plane membrane stiffnesses. The buckling constraint is based on an eigenvalue analysis of the entire structure (which takes into account buckling modes involving the compatible interaction of several panels), and the strain constraint is based on the maximum strain criterion. All constraints are imposed on the global level.

Because of the size and complexity of the resulting design problem, it was necessary to limit this study to a small number (3-9) of design variables. Panels are modelled either as unstiffened plates (in which case the design variables represent the ply thicknesses) or using the smeared stiffness approach (in which case the design variables may represent the height, spacing and ply thicknesses of the stiffeners as well as the ply thicknesses of the base laminate).

In several tests of simple box beams in pure bending [21, 22], Antona, Gabrielli, and Romeo found that geometrically nonlinear effects, especially the rib crushing load [23], were important to the box beam's response and ultimate failure load. In order to investigate the possible effects of geometric nonlinearities on the optimum designs presented in the present work, several of these designs are subjected to a geometrically nonlinear analysis and the results are compared to the response predicted by a linear analysis.

Chapter 2

ANALYSIS AND OPTIMIZATION TOOLS

In this chapter the various analysis and optimization tools that were used in the course of the present study are discussed. The chapter begins with a brief discussion of the **CO**mputational **ME**chanics Testbed (**COMET**) and the specific algorithms and codes used to perform linear buckling and geometrically nonlinear analysis. The remainder of the chapter is devoted to the finite element based optimization system **TBOP**. The specific optimization algorithms that were used within the **TBOP** framework are discussed along with some basic optimization terminology. An overall description of the optimization system is presented followed by a discussion of several new capabilities and enhancements that were added to the basic optimization system during the course of this research.

2.1 Computational Mechanics Testbed

The finite element code used for the present work is the **CO**mputational **ME**chanics Testbed or **COMET** [24]. The **COMET** software system is a modular and flexible structural analysis system that was developed in order to serve as a testbed for studying computational methods and for exploring the uses of new multiprocessor and vector computers. The intention of the original **COMET** developers was to provide a shared computing environment for use by structural analysts, method developers, numerical analysts, and computer scientists [25].

COMET consists of a growing network of independently executable **FORTRAN** programs (or *processors*) that communicate with one another through a global database. In order to perform a particular task, the user coordinates the execution of the various processors by writing *procedures* in a high level procedural language known as the **Command Language for Applied Mechanics Processors** (or **CLAMP**). If new or special capabilities are desired, users have the option of writing their own processors which can then be compiled and linked for use in the **COMET** environment.

COMET was chosen for the present work because of its flexibility, accessibility, and because there was, at the time, unrestricted access to the source code. Another mo-

tivation for using COMET was the recent addition of several processors and procedures (collectively known as TBOP) that provide design optimization capabilities [26, 27]. These capabilities, including the modifications and enhancements that were added during the course of this research program, are described later in section 2.6.3.

2.2 Linear Buckling Analysis

Linear buckling analysis was performed using the processor EIG2 in COMET¹ [24]. EIG2 solves the linear generalized eigenproblem

$$\mathbf{A}\mathbf{x}_i - \lambda_i\mathbf{B}\mathbf{x}_i = 0, \quad (2.1)$$

where \mathbf{A} and \mathbf{B} are $n \times n$ matrices and \mathbf{x}_i is an $n \times 1$ vector. The solution is performed in two phases: In the first phase, the problem is reduced from order n to order m using a Rayleigh-Ritz approximation to the eigenvector \mathbf{x} . It is assumed that \mathbf{x} can be expressed as a linear combination of m trial vectors \mathbf{Y}_i :

$$\mathbf{x} = \mathbf{Y}_1 q_1 + \mathbf{Y}_2 q_2 + \cdots + \mathbf{Y}_m q_m = \mathbf{\Gamma} \mathbf{q}, \quad (2.2)$$

where $\mathbf{\Gamma}$ is a $n \times m$ matrix of the trial vectors and \mathbf{q} is a vector of unknowns. These trial vectors may be random vectors or approximations to the eigenvector obtained from a previous analysis. The reduced problem becomes:

$$\bar{\mathbf{A}} \mathbf{q} - \lambda \bar{\mathbf{B}} \mathbf{q} = 0, \quad (2.3)$$

where

$$\bar{\mathbf{A}} = \mathbf{\Gamma}^T \mathbf{A} \mathbf{\Gamma} \quad (2.4)$$

$$\bar{\mathbf{B}} = \mathbf{\Gamma}^T \mathbf{B} \mathbf{\Gamma}. \quad (2.5)$$

This reduced eigenproblem is then solved for all m eigenpairs $(\lambda_i, \mathbf{q}_i)$ using the Cholesky-Householder method.

¹ The processor used to perform linear buckling analysis during optimization was actually a modified version of EIG2 called MYEG. The only differences between EIG2 and MYEG are: (1) MYEG reads some of the user supplied input data from a different library than does EIG2, (2) MYEG exports the number of converged eigenvalues back to the calling procedure.

In the second phase of the solution, each of the reduced eigenvectors \mathbf{q}_i is normalized with respect to the $\bar{\mathbf{B}}$ matrix such that:

$$\bar{\mathbf{q}}_i^T \bar{\mathbf{B}} \bar{\mathbf{q}}_i = \mathbf{I} \quad (2.6)$$

and is then used, at the k_{th} iteration, to solve for the actual eigenvectors \mathbf{x}_i :

$$\mathbf{x}_i^{(k)} = \Gamma^{(k)} \bar{\mathbf{q}}_i^{(k)}. \quad (2.7)$$

A Stodola-type iteration is used to obtain improved trial vectors $\mathbf{Y}_i^{(k+1)}$ for the $(k+1)_{st}$ iteration:

$$\mathbf{A} \mathbf{Y}_i^{(k+1)} = \mathbf{B} \mathbf{x}_i^{(k)}. \quad (2.8)$$

Iterations continue until the required number of eigenvalues converge.

This algorithm is especially suited for use in the design optimization process because converged eigenvectors obtained for a given design may be used as trial vectors in the analysis of subsequent designs. If the change in the design variables from one design iteration to the next is small, convergence of the analysis procedure outlined here may be quite rapid (2-4 iterations in the present study).

2.3 Geometrically Nonlinear Analysis

Geometrically nonlinear static analysis was performed using the CLAMP procedure NL_STATIC_1 in COMET [28]. NL_STATIC_1 uses an arc-length controlled Newton-Raphson iterative/incremental technique to solve the nonlinear equilibrium equations

$$\mathbf{f}^{\text{int}}(\mathbf{d}) = \mathbf{f}^{\text{ext}}(\lambda), \quad (2.9)$$

where \mathbf{f}^{int} is the internal force vector, \mathbf{f}^{ext} is the external force vector, \mathbf{d} is the generalized displacement vector, and λ is a multiplier on the externally applied loads.

The load factor, λ , is increased from zero in a series of load steps or *increments*; at each increment, the equation is linearized and Newton-Raphson iterations are performed until the equation is satisfied. The arc-length method used here is a variant of Crisfield's algorithm [29]. Its use allows each load step to be selected automatically depending upon the shape of the load-displacement "path". The algorithm is capable of automatically traversing limit points.

NL_STATIC_1 utilizes a co-rotational algorithm for geometric nonlinearity at the element level that is built into the COMET ES elements [30]. This allows for arbitrarily large nodal rotations (although the use of simplified strain-displacement relations requires that the *strains* remain small).

2.4 Optimization Terminology

The objective of design optimization is to obtain the “best” design subject to a set of constraints or limitations on the design. Each candidate design is described and completely defined by a discrete set of parameters called *design variables*. The “best” design is defined to be the set (or sets) of design variables which maximize or minimize a merit or *objective function*. In structural optimization, the objective is often to minimize the weight of the structure, although there are many other possibilities (one may wish to maximize the buckling load, for example). The constraints are equality or inequality equations written in terms of the design variables or response quantities that limit the allowable combinations of the design variables to a *feasible domain*. These constraints may be simple functions of one design variable (specifying that a given design variable must not go below or above a certain threshold) or may be very complex explicit or implicit functions of all or most of the design variables (specifying, for example, that the overall displacement of a structure must be below a certain threshold).

Mathematically, the optimization problem is formulated as follows:

$$\begin{aligned}
 \text{Minimize :} & \quad f(\mathbf{x}) & (2.10) \\
 \text{subject to :} & \quad g_k(\mathbf{x}) \leq 0 & k = 1, \dots, l \\
 & \quad h_j(\mathbf{x}) = 0 & j = 1, \dots, m \\
 & \quad x_i^L \leq x_i \leq x_i^U & i = 1, \dots, n
 \end{aligned}$$

where f is the objective function, g_k is an inequality constraint, h_j is an equality constraint, \mathbf{x} is a vector of design variables, and x_i^L and x_i^U are lower and upper bounds, respectively, on the design variables.

All gradient based optimization algorithms (like the ones used in the present study) include the following two steps: First, starting at the initial design \mathbf{x}_1^0 , a “search direction” is calculated (if there are n design variables, this search direction

is an n -dimensional vector in the n -dimensional *design space*). Second, the objective function is minimized (or maximized) along this one-dimensional “search direction” and a new design point, \mathbf{x}_i^1 is obtained. From this new design point, a new search direction is calculated, and the procedure continues until a minimum (or maximum) point is found. The way in which the constraints are handled and the way in which the search direction is calculated varies from algorithm to algorithm, but the basic two steps are the same.

The typical optimization system consists of two or three distinct components: the optimizer itself, the analysis module, and optionally, the sensitivity module. As explained above, the optimization procedure is iterative; the objective function and constraints must be evaluated at each new design point and often during the one-dimensional searches. These function evaluations are carried out by the analysis module. The analysis module may consist of a simple FORTRAN code or may be a complex finite element analysis (as in the present study). In order to calculate the search direction at a given design point, the optimizer requires derivatives of the objective function and the constraint equations with respect to the design variables. These derivatives are either calculated analytically or semi-analytically by the sensitivity module or are obtained through the analysis module by overall finite differences.

The necessary condition for convergence of an optimization problem is the satisfaction of a set of equations known as the Kuhn-Tucker conditions [31]. A design point that satisfies the Kuhn-Tucker conditions may only be a local optimum, however. In general, there is no guarantee that there are not other design points somewhere in the design space which have an equal or better value of the objective function. In many practical design situations (especially in composite laminate design) several local minima may exist. In order to find the global optimum point (or points) using a gradient based optimization technique, the optimization algorithm must be re-started from several different initial points in the design space. The lowest (highest) optimum found from such a procedure would have a high probability of being the global optimum.

A new class of optimization algorithms (the genetic algorithm [31], for example) that do not utilize gradient information are much better at finding global optima, but require a very large number of function evaluations. These algorithms are not practical for use in the present work because of the high cost of performing a function evaluation (finite element analysis).

2.5 Optimization Algorithms

The optimizing program used for the present work was ADS (Automated Design Synthesis)[32] which allows the user to choose from several different optimization algorithms. ADS was selected because it was already integrated within the optimization system TBOP and because of the flexibility it offered in terms of available optimization algorithms. The algorithms used in the course of the present work are briefly described in this section. A discussion concerning the implementation of each algorithm may be found in section 2.6.3.

2.5.1 Sequential Convex Programming

Sequential approximate optimization techniques [31] are often used to solve a given design problem when the evaluation of some or all of the objective and/or constraint functions is overly expensive. In these cases, computationally expensive functions may be approximated in the neighborhood of the current design point by simpler functions. These “simple” functions (usually polynomials) are selected so that their values and the values of their derivatives may be calculated without recourse to an expensive analysis. They may also be selected in order make the resulting approximate sub-problem easier to solve. The simplified sub-problem is solved using a reliable optimization algorithm. After obtaining a solution to the sub-problem, the objective function, constraints, and required sensitivity derivatives corresponding to the original problem are calculated at the new design point. This data is used as a basis for constructing a new approximate sub-problem about this new point. The new problem is solved as before, and the iterations continue until the original design converges. This procedure is often more computationally efficient than solving the original problem directly, as considerably fewer expensive function evaluations are generally required.

It is often necessary to impose limits (move limits) on the amount by which the design variables are allowed to change during the solution of each approximate sub-problem. This is because the approximate problem is usually valid only near the current design point. The selection of these move limits may have a great effect on the convergence properties of the optimization problem as a whole (see section 2.6.3).

Sequential convex programming (SCP) [33] utilizes a sequential approximate optimization technique whereby each approximate sub-problem is a *convex programming*

problem [34]. A convex programming problem is an optimization problem wherein the constraint and objective functions are all convex functions. A convex set, S , is a set of points such that a line connecting any two points in S is entirely in S . A convex function $f(x)$ defined on a convex set is a function that always lies below the line connecting any two points on itself. [31, 34]. Convex programming problems have an advantage over other classes of optimization problems in that the Kuhn-Tucker conditions are sufficient conditions for convergence and any minimum (or maximum) found is guaranteed to be a global minimum (or maximum) [31, 34].

In the present work the modified method of feasible directions [35] was used to solve each approximate sub-problem generated by the sequential convex programming algorithm. The modified method of feasible directions is closely related to the method of feasible directions which is described in the next section.

2.5.2 Method of Feasible Directions

The Method of Feasible Directions (MFD) [31, 36, 37] is a gradient based optimization algorithm that directly incorporates constraint information in the solution procedure. This algorithm follows the general procedure described in section 2.4 on Optimization Terminology (calculation of a search direction followed by a one dimensional search, etc.).

This algorithm differs from other similar algorithms in the way in which the search direction is calculated. Starting with an initial design point that satisfies all the constraints, it looks for a search direction that is both “usable” and “feasible”. A “usable” direction, s , is a direction that improves the objective function. Mathematically, this may be stated as:

$$\nabla f(x) \cdot s \leq 0, \quad (2.11)$$

where $\nabla f(x)$ is the gradient of the objective function. A “feasible” direction is a direction along which the constraints are not immediately violated. Mathematically, this condition may be stated as:

$$\nabla A \cdot s \leq 0, \quad (2.12)$$

where A is a matrix that contains the transpose of the gradients of the active constraints. A direction that satisfies both of these requirements is found by solving the

following sub-problem:

$$\begin{aligned}
& \text{Maximize: } \beta & (2.13) \\
& \text{subject to: } \nabla f(x) \cdot \mathbf{s} + \beta \leq 0 \\
& \quad \mathbf{A} \mathbf{s} + \beta \boldsymbol{\theta} \leq 0 \\
& \quad \mathbf{s} \cdot \mathbf{s} \leq 1
\end{aligned}$$

The components of $\boldsymbol{\theta}$ are called *push-off factors* and control the amount by which the search direction will move away from the constraint boundaries. A small value of $\boldsymbol{\theta}$ results in a search direction that is nearly tangent to the constraint boundary and may be appropriate for constraints that linear or near linear. A large value of $\boldsymbol{\theta}$ results in a search direction that makes a large angle with the constraint boundary and is therefore appropriate for highly nonlinear constraints. The selection of the vector $\boldsymbol{\theta}$ was found to have important implications for the convergence properties of the designs studied in the present work (see section 2.6.3).

The direction finding sub-problem can be converted to a linear programming problem and may be efficiently solved [35]. Once the search direction is found, a one dimensional search is performed in this direction until the objective function is minimized (or maximized). The procedure continues until the design converges.

2.6 Testbed Optimization (TBOP)

The optimization system used in the present study is a general purpose finite element based system that was recently implemented within the COMET framework [26, 27]. This system links the optimization program ADS [32] with the analysis tools existing within COMET.

During the course of this research, several modifications and enhancements were made to the baseline TBOP system. These new capabilities are included in updated versions of the TBOP processors and procedures, which have the same names as the baseline versions with a “_c” or “_d” appended to the end of each. In addition, a modified version of the COMET processor LAU called LAUSS was added to the TBOP family.

An overview of TBOP is given in the next section, followed by two sections describing the design variables, constraints, and other options available within TBOP. The

first of the two sections gives a brief discussion of the capabilities built into the original TBOP and the second section consists of a detailed description of the modifications and enhancements made during the course of the present work.

2.6.1 Overview

TBOP consists of the processors BDLM, OPTI, and TB20 along with the controlling procedures `des_ana_iter`, `Branch_on_info`, `analysis`, and `derivative`. The manner in which the TBOP processors and procedures work together with ADS and other COMET analysis processors is illustrated in Figure 2.1.

The optimization system is arranged such that ADS is the “master” program and the other TBOP processors and procedures are the “slaves”, providing ADS with whatever information it requests. ADS controls the course of the optimization process through a parameter called `info`. If ADS requires the values of the objective or constraint functions, `info` is set equal to ‘1’, and if ADS requires objective function or constraint gradients, `info` is set equal to ‘2’. Depending on the value of `info` passed to it by ADS, TBOP makes the appropriate calculations and calls COMET procedures and processors as needed.

In the first step of the optimization process, the user defines a finite element model using the usual COMET processors [24]. After selecting the desired optimization algorithms via global macrosymbols [24] the user must call the TBOP processor OPTI (sub-processors DDVR and CONSTRAINT) to define the design variables and the constraints for the optimization run. This information is stored in the global database in the appropriate datasets. The user then calls OPTI (sub-processor OBJECTIVE) to calculate the objective function and TB20 (sub-processors INITIALIZE and MODIFY) to initialize ADS. It is at this point that the any of the default ADS optimization parameters may be modified [32].

The user then initiates the design optimization process by calling the procedure `des_ana_iter`. This procedure consists primarily of a “DO” loop that implements the optimization iterations. At the start of each iteration, `des_ana_iter` calls the procedure `Branch_on_info` which, depending on the current value of `info`, calls either the procedure `analysis` (`info=1`) or the procedure `derivative` (`info=2`).

If the procedure `analysis` is called, a finite element analysis is performed as a first step in obtaining the values of the objective function and the constraints. First, design variables describing details of laminate construction are converted to appropriate

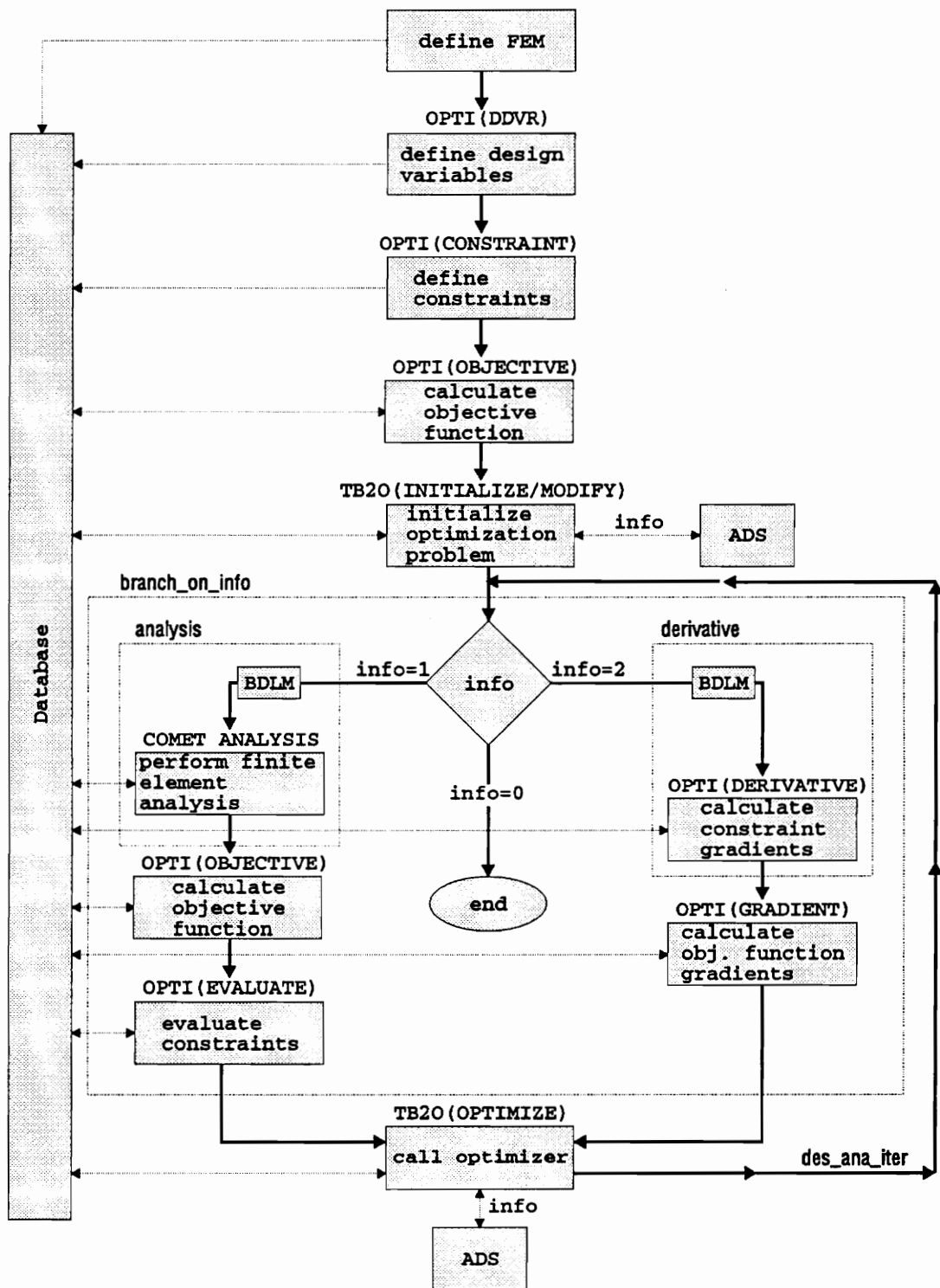


Figure 2.1: TBOP Flowchart

section property datasets by the processor BDLM. COMET analysis processors are then called to perform a linear static analysis and/or a linear buckling analysis. The results are written to the global database. After these analyses are performed, control is returned to the procedure `Branch_on_info` which calls the processor OPTI. OPTI uses the analysis results (along with the geometric and design information contained in the database) to calculate the current value of the objective function (sub-processor OBJECTIVE) and the current values of the constraints (sub-processor EVALUATE).

If the procedure `derivative` is called, calculations are performed in order to obtain information necessary for the gradient calculations. First, the values of the design variables are perturbed and the new section property data is written to the database with the help of BDLM. COMET processors are then called to reform the stiffness matrix. Depending on whether overall finite differences or the semi-analytical method (see section 2.6.2) are used to calculate the constraint gradients, a different set of calculations then follow. In either case, after the necessary data is generated, OPTI (sub-processor DERIVATIVE) is called and the values of the constraint gradients are calculated. Control then passes back to `Branch_on_info` and OPTI is called one last time (sub-processor GRADIENT) to calculate the gradient of the objective function.

After these calculations, `Branch_on_info` returns control to `des_ana_iter`. The processor TB20 is then called to gather, organize, and return the calculated data to ADS. After receiving this data, ADS continues with the optimization algorithm until it requires more information from TBOP. It then returns `info` to `des_ana_iter`, and the cycle begins again. These iterations continue until the design process converges or until the user specified maximum number of iterations is exceeded.

2.6.2 Baseline Capabilities

The original TBOP includes several types of design variables and constraints that are useful for designing general shell-like aircraft structures with laminated composite materials. Three different design variable types are supported: ply thickness, ply orientation, and stiffener height design variables. The first two variables may be used to describe some or all of the plies in a composite laminate. The third type of design variable was designed to specify the height of explicitly modelled stiffeners. It designates the size of certain groups of finite elements and thus allows for a limited amount of shape optimization.

Buckling, point strain, point displacement, and upper and lower bound constraints

may be imposed on the design. The buckling constraint is based upon linear buckling (eigenvalue) analysis. This type of constraint is used extensively in the present work and will be discussed in detail in the next section. The strain constraint uses a first ply failure analysis based upon the maximum strain failure theory to limit the allowed strains in the finite element model. Separate point strain constraints may be imposed at any or all of the element integration points in the model. The displacement constraint allows the user to impose limits on the displacement in any of the six degrees of freedom at any node in the finite element model.

TBOP always assumes that the objective function is the weight of the structure. As mentioned in [27], this allows many practical optimization problems to be solved, but poses a problem for the ply orientation design variables because the derivative of the structural weight with respect to these design variables is zero. In order to use these design variables, a different objective function (the buckling load, for example) would be more suitable. For this reason, ply orientation design variables are not used in this study.

Sensitivity derivatives (gradients of the objective function and constraints with respect to the design variables) may be calculated using overall finite differences or using the semi-analytical method. The semi-analytical method combines an analytical expression for the displacement derivatives with a finite difference approximation for the derivatives of the stiffness matrices [31]. For the case of applied nodal loads (only), the procedure is as follows: Starting with the equilibrium equations,

$$\mathbf{K}\mathbf{u} = \mathbf{f} \quad (2.14)$$

derivatives are taken with respect to each of the design variables, x_i :

$$\mathbf{K} \frac{d\mathbf{u}}{dx_i} + \frac{d\mathbf{K}}{dx_i} \mathbf{u} = \frac{d\mathbf{f}}{dx_i}, \quad (2.15)$$

where \mathbf{K} is the stiffness matrix, \mathbf{u} is the displacement vector, and \mathbf{f} is the loading vector. The derivative of the displacement vector \mathbf{u} with respect to the design variable x_i is then obtained by solving the above equation for $\frac{d\mathbf{u}}{dx_i}$. This quantity is the gradient of the displacement constraints and is also used to calculate gradients of the strain and buckling constraints. This method is computationally more efficient than the finite difference method, as the required matrix factorization has already been performed during the analysis phase and only forward and back substitution steps are required

to obtain the derivative information. For this reason, this method is often used when finite differences would be overly expensive (as in the present work).

TBOP was designed to work with all of the shell elements implemented within COMET (both the ES and SPAR elements). The structure may be loaded by applied nodal forces or by imposed non-zero displacements.

Buckling Constraints

The k th buckling constraint is formulated as follows:

$$g_k = v_k - \lambda_j \leq 0 \quad (2.16)$$

where λ_j is the j th eigenvalue obtained from a linear buckling analysis and v_k is the lowest allowable value of λ_j .

In order to assure structural stability for a given design, a constraint may be imposed on the lowest eigenvalue obtained from a linear buckling analysis. If there are several closely spaced modes near the lowest mode, however, it may be necessary to impose constraints on several eigenvalues near the lowest eigenvalue. Otherwise, two or more closely spaced modes may repeatedly switch places during the optimization process, each alternately becoming critical. In such a case, the optimization algorithm may get caught in a time consuming loop as, at a given iteration, it attempts to satisfy one constraint only to have it replaced by a different constraint at the next iteration. TBOP avoids this problem by implementing a strategy whereby eight to twelve modes near the critical mode are grouped according to their sensitivities to the design variables (those with similar sensitivities are grouped together). A constraint is then automatically imposed on the lowest eigenvalue within each group.

The derivative of each the eigenvalues with respect to the design variable x_i may be obtained by overall finite differences or by using values of $\frac{du}{dx_i}$ calculated using the semi-analytical method. In the latter case, the following equation is used for the eigenvalue derivatives:

$$\frac{d\lambda_j}{dx_i} = \frac{\mathbf{u}_j^T \left(\frac{d\mathbf{K}}{dx_i} + \lambda_j \frac{d\mathbf{K}_G}{dx_i} \right) \mathbf{u}_j}{\mathbf{u}_j^T \mathbf{K}_G \mathbf{u}_j} \quad (2.17)$$

where \mathbf{u}_j is the j th eigenvector and \mathbf{K}_G is the geometric stiffness matrix. In this equation, as in the semi-analytical method, $\frac{d\mathbf{K}}{dx_i}$ and $\frac{d\mathbf{K}_G}{dx_i}$ are calculated using a finite

difference formula. The perturbed value of \mathbf{K}_G is computed using the perturbed displacements, \mathbf{u}_i^P :

$$\mathbf{u}_i^P = \mathbf{u} + \frac{d\mathbf{u}}{dx_i} \Delta x \quad (2.18)$$

2.6.3 Modifications and Enhancements

The modifications and enhancements made to TBOP during the course of this research include the addition of two new constraint types, the addition of three new design variables, and enhancements to improve the convergence properties of the optimization system. The first new constraint, the “panel buckling” constraint, allows the user to isolate a subcomponent of the global model and impose a buckling constraint on it, treating it as though it were a simply-supported plate. This constraint forms the basis for the “local” approach used in Chapter 4 and allows the inter-stiffener constraints to be imposed as well (see below). The second new constraint type is a ply-percentage constraint, which limits the allowed thicknesses of specified laminate plies. The new design variables describe the height, spacing, and ply thickness of smeared blade stiffeners.

Panel Buckling Constraint

The panel buckling constraint type (keyword `panbuck`) allows the user to isolate a subcomponent panel from the global structure and treat it as a simply supported plate subjected to in-plane loads. A constraint may then be imposed on the buckling load of this isolated plate. This panel buckling constraint type was added to TBOP for two reasons. First, we wanted the capability to analyze and optimize the box-beam subcomponent panels using “traditional” methods wherein each subcomponent panel is analyzed and optimized separately from the other panels in the structure. The addition of this constraint type allows comparisons to be made between designs obtained using a global buckling analysis and designs obtained using more traditional methods. Second, this new constraint type provides a convenient method of imposing the inter-stiffener buckling constraints which are described below.

In order to use this constraint, the user first specifies the overall dimensions of the panel using the keywords `pbwid` and `pblen`. The panel loads are then defined by referring to the global model. Using the appropriate keywords (`pbnod` and `pbelem`),

the user specifies which finite elements and nodes are to be used to obtain the panel loads. A different element and node may be chosen for the local N_x loads, the local N_y loads, and the local shear (N_{xy}) loads. In order to provide some flexibility, the user may also indicate whether the N_x and N_y loads are constant, or whether they are to vary linearly over the panel edges. The user does this by specifying a value of α_x (keyword `palpx`) and α_y (keyword `palpy`). The magnitude of the N_x and N_y loads are then defined using the following equations:

$$N_x = n_x(1 - \alpha_x \frac{y}{b}) \quad (2.19)$$

$$N_y = n_y(1 - \alpha_y \frac{x}{a}) \quad (2.20)$$

where n_x and n_y are the baseline values of the panel loads, a is the panel length in the local x direction, b is the panel length in the local y direction, and α_x and α_y are parameters which specify how the panel loads are to vary. A value of $\alpha = 0.0$ corresponds to a constant load, a value of $\alpha = 2.0$ corresponds to a load which varies linearly from $+n$ to $-n$, and a value of $\alpha = 1.0$ corresponds to a load which varies linearly from $+n$ to zero. Any value of α_x and α_y between 0.0 and 2.0 may be chosen.

The buckling analysis itself is performed using well known equations for simply supported plates subjected to constant in-plane loads [38] and using the buckling equations for plates subjected to linearly varying loads derived in Appendix A. Buckling loads for an applied N_x load, an applied N_y load, and an applied N_{xy} load are each calculated separately. The overall buckling constraint is then formulated using the following interaction equation [39]:

$$g_l = (\frac{N_x}{N_{x_{cr}}}) + (\frac{N_y}{N_{y_{cr}}}) + (\frac{N_{xy}}{N_{xy_{cr}}})^2 - 1.0 \leq 0 \quad (2.21)$$

After each change in the design variables during the optimization process, the global model is updated and the panel loads are re-computed. In this way, the internal loads are allowed to redistribute throughout the structure as the design changes.

In order to implement this constraint in TBOP new datasets were created to contain the values and gradients of the constraint. OPTI was modified in order to calculate the constraint values and derivatives. In addition to the keywords already mentioned, the keywords `pbgrou`, `pctype`, and `pbsect` are also recognized by OPTI/CONSTRAINT and are used to describe each panel buckling constraint.

Ply Percentage Constraints

The ply percentage constraint was added to TBOP to limit the allowable laminate designs. This constraint limits the allowable thickness of a specified ply to a given percentage of the total laminate thickness. For example, if $(x_1, x_2, x_3 \dots, x_n)$ are the ply thickness design variables corresponding to an n ply laminate, the ply percentage constraint limiting the value of x_k ($k \leq n$) to $p_{max}\%$ of the total laminate thickness would be formulated as:

$$g = 1.0 - \frac{x_k}{x_1 + x_2 + x_3 + \dots + x_n} \leq p_{max}/100 \quad (2.22)$$

In general, scale factors $(c_0, c_1, c_2, \dots, c_n)$ may be specified for each design variable, in which case the constraint is formulated as:

$$g = 1.0 - \frac{c_0 x_k}{c_1 x_1 + c_2 x_2 + c_3 x_3 + \dots + c_n x_n} \leq p_{max}/100 \quad (2.23)$$

In order to implement the ply percentage constraint in TBOP, a new dataset was created to contain the values and gradients of the new constraint. Additional code was added to OPTI in order to calculate the constraint value and derivatives and to read and write this data to the appropriate datasets. The keywords `plypercent`, `plydv`, `assocdv`, `scale`, and `limit` are now recognized by OPTI/CONSTRAINT and are used to describe each ply percentage constraint.

Examples of the use and application of this constraint may be found in Chapter 4.

Smeared Stiffness Design Variables

When designing aircraft structures for global response, it is sometimes useful to make use of “smeared stiffeners”. In this approach, stiffened panels are modelled as flat plates which have the effects of the stiffeners mathematically “smeared” into them. In the case of a laminated composite panel, this entails modifying the ABD matrix of the base laminate to take into account the increased axial and bending stiffness provided by the stiffeners. The modified laminate then behaves *globally* as if the stiffeners were still present. This method can not, of course, take into account any details about the stiffener response or localized failure mechanisms involving the stiffeners, but can still be useful for predicting the overall response of the stiffened panel.

The smeared stiffener approach is attractive when the cost of explicitly modelling each stiffener in a structure becomes prohibitively large. This may happen when a

large structure (involving several different subcomponents) is modelled, and when design optimization (which may require a large number of analyses) is to be performed.

In order to utilize the smeared stiffener approach in the present work, three smeared stiffness design variable types were added to TBOP. These design variables allow the user to specify the height (keyword `sheight`), spacing (keyword `spacing`), and ply thicknesses (keyword `sthickness`) of smeared blade stiffeners which may then be added to any or all of the laminates defined in the design model. The new design variables may be used in any combination to describe any given stiffener.

In order to implement the smeared stiffener concept within COMET, the processor LAU (Laminate Analysis Utility) was modified. The modified version, called LAUSS, retains all the capabilities of LAU, but also automatically searches the current database for a new dataset (`SMR.DAT.1.1`) describing the smeared stiffeners. If this dataset is found, the stiffeners are smeared into the appropriate base laminates and the resulting smeared ABD matrices are created. If the dataset is not found, no changes are made to the ABD matrices. The existence of LAUSS means that the smeared stiffness concept may be used independently of TBOP; if the analyst wishes to use smeared stiffeners when performing an analysis, he or she needs only to replace LAU with LAUSS and provide the appropriate datasets describing the stiffeners.

The smeared stiffness dataset includes entries for the three design variables as well as entries for the direction of the stiffeners and for the length and width of the base laminate. The stiffener lamina thicknesses are described in separate datasets (`STF.LAM.*.1`) similar to the `SUB.LAM.*.1` datasets used by the baseline TBOP[27].

The base laminate dimensions are used by OPTI to calculate the objective function. The base laminate width is divided by the stiffener spacing to obtain the number of stiffeners. This is then multiplied by the base laminate length, the stiffener height, and the total stiffener laminate thickness to obtain the total stiffener volume. The weight is then obtained by multiplication with the material density. It is noted that, if a portion of any smeared stiffener is described by a design variable, the weight of the entire stiffener is included in the objective function. This differs from the usual case where only the portion of the structure described by the design variables is included in the objective function.

One additional difference between LAUSS and LAU is the addition of a parameter allowing the user to control the existence of the anisotropic bending-twisting terms D_{16} and D_{26} . If, when executing LAUSS, the user wishes to zero out the D_{16} and D_{26}

terms from the ABD matrices that are generated, the reset parameter `ISP0` should be set to '1'. The default for `ISP0` is '0', in which case the D_{16} and D_{26} terms are not affected. A new argument called `ispo` corresponding to `ISP0` was also added to `des_ana_iter`. If `ispo=0`, `TBOP` will use `ISP0=0` when calling `LAUSS`, and similarly for `ispo=1`. The default is `ispo=0`.

The smearing scheme implemented for use in the present work is based on the scheme used by the panel analysis/optimization code `PASCO` [14]. In this method, only the A_{11} , D_{11} , D_{12} , and D_{66} terms in the base laminate are affected by the stiffeners. Both the base laminate and stiffener laminate are assumed to be symmetric (no B matrix). The formulas for the smeared ABD terms (simplified for a blade stiffener) as a function of the base (b) and stiffener (s) ABD terms are as follows:

$$A_{11}^{smeared} = A_{11}^b - \frac{(A_{12}^b)^2}{A_{22}^b} + \frac{b_s}{b_b} \left(A_{11}^s - \frac{(A_{12}^s)^2}{A_{22}^s} \right) \quad (2.24)$$

$$D_{11}^{smeared} = D_{11}^b + \left(A_{11}^b - \frac{(A_{12}^b)^2}{A_{22}^b} \right) z_b^2 + \frac{1}{b_b} \left[\left(A_{11}^s - \frac{(A_{12}^s)^2}{A_{22}^s} \right) (b_s z_s^2 + \frac{b_s^3}{12}) \right] \quad (2.25)$$

$$D_{12}^{smeared} = D_{12}^b + \frac{b_s}{b_b} D_{12}^s \quad (2.26)$$

$$D_{66}^{smeared} = D_{66}^b + \frac{b_s}{b_b} D_{66}^s \quad (2.27)$$

where b_b is the width of the base laminate (the distance between adjacent stiffeners), b_s is the height of the stiffeners, and z_b and z_s are the distances from the centroid of the cross section to the centroid of the base laminate and to the centroid of the stiffener, respectively (see Figure 2.2).

Two different methods may be used to link the resulting ABD matrixes to the finite element model, both of which have advantages and disadvantages as applied to the present work. In the first method, the finite elements representing the stiffened panel are assumed to be at a local z location that is coincident with the panel centroid (see Figure 2.3). It should be noted that if the stiffener height varies (as it does if it is a design variable), the distance between the panel centroid (finite element nodes) and the base laminate varies as well. In the present work this causes some difficulty because the outer dimensions of the wing box are defined by the location of the

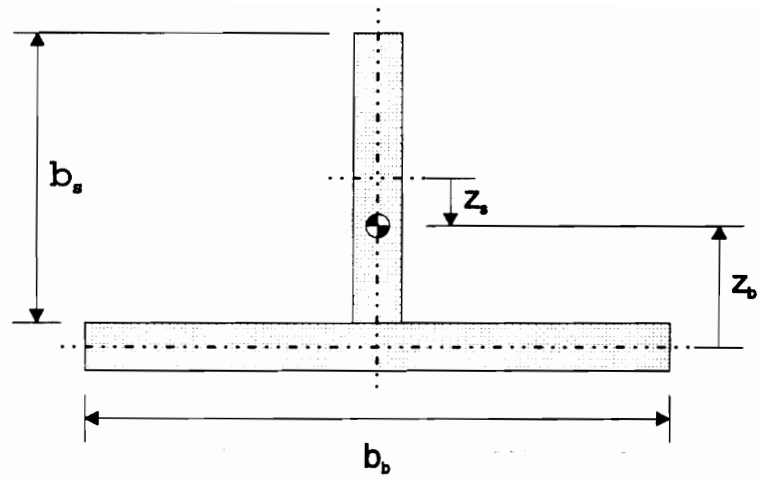


Figure 2.2: Typical Blade Stiffener

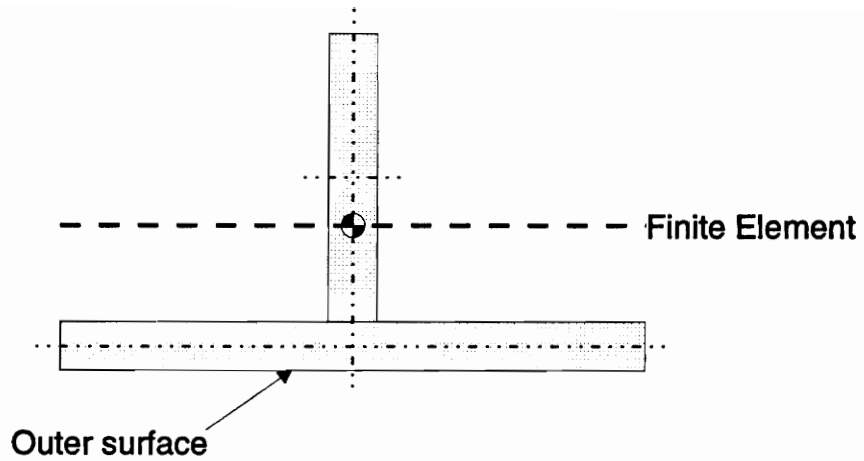


Figure 2.3: Location of Finite Element Centroid on Stiffener Cross Sect: Method 1

base laminate (see Chapter 3 for a description of the models used). This means that changing the stiffener height also changes the effective outer dimensions of the wing box by an amount equal to the change in the location of the centroid. The advantage of this method is that loads and boundary conditions applied to the finite element nodes are applied directly to the centroid of the panel (there is no offset between the finite element nodes and the panel centroid).

In the second method, the finite elements representing the stiffened panel are assumed to be coincident with the base laminate. This resolves the problem with the first method because the location of the base laminate now remains constant when the stiffener height is varied (see Figure 2.4). A new problem arises, however. Because the smeared ABD matrices calculated above apply to the centroid of the cross section, they must be modified so that they correspond to the base laminate.

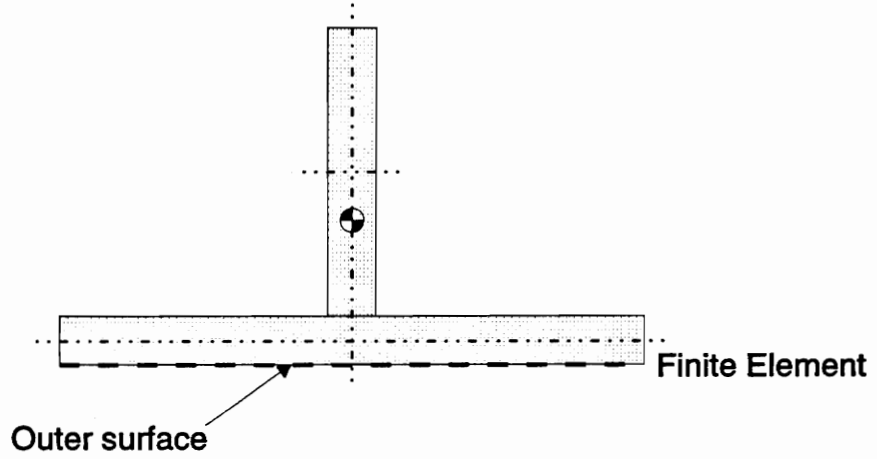


Figure 2.4: Location of Finite Element Centroid on Stiffener Cross Sect: Method 2

This entails offsetting the B and D matrices as follows:

$$\bar{B}_{ij}^{smeared} = A_{ij}^{smeared} z_b \quad (2.28)$$

$$\bar{D}_{ij}^{smeared} = D_{ij}^{smeared} + A_{ij}^{smeared} z_b^2 \quad (2.29)$$

where i and j independently take on the values 1, 2, and 6.

Note that the resulting B matrix now contains non-zero terms. This reflects the fact that loads and boundary conditions applied to the finite element nodes are now offset from the panel centroid. An axial load applied to the finite element nodes will now induce bending in the element.

In the present work, loads and boundary conditions must be applied to the finite

element nodes. (COMET does not allow loads and boundary conditions to be offset from the finite element nodes, nor are there “rigid link” elements available.) This means that, when this second method is used, the loads and boundary conditions are not applied to the panel centroids, but are offset by the distance from the centroid to the base laminate.

Because both methods present some difficulties for the present work, neither appears to be superior to the other. Because method 1 is easier to implement, it was used for the present work and results are presented in Chapter 4. Future investigations can focus on the effectiveness of these and other smearing schemes.

In order to partially test the accuracy and capabilities of the smeared stiffener design variables, a test problem was devised. The test problem is a 30 *in* by 30 *in* blade stiffened panel loaded by a constant compressive load in the stiffener direction. The base laminate has a layup of $(45/-45/-45/45/0/90)_s$, and the stiffener has a layup of $(45/-45/-45/45/0)_s$. This panel is the same as the panel in used in Example 1 from Reference [40].

The structural weight was minimized subject to a compressive load of 1000 *lb/in* and a constraint on panel buckling. Design variables were the ply thicknesses and the stiffener height. A lower bound of 0.0055 *in* was placed on the ply thickness design variables.

Two programs were used to perform the optimization. First, results were obtained using PASC0, which models the stiffener explicitly. Results were then obtained using the smeared stiffness capabilities of TBOP. At first, the comparison was not encouraging because the results obtained using the two methods were quite different. TBOP arrived at designs which had tall, thin stiffeners and a thin base laminate. The PASC0 designs had smaller, thicker stiffeners, and a thicker base laminate. This discrepancy was corrected by including in TBOP a local buckling constraint on the base laminate segments between the stiffeners. This local constraint was added using the panel buckling constraint discussed in Section 2.6.3.

The resulting TBOP results for a stiffener spacing of 5.00 *in* are compared to the corresponding PASC0 results in Figure 2.5. The first five design variables (which describe ply thicknesses) are read off the left scale, and the last design variable (which describes the stiffener height) is read off the right scale. Several different designs were obtained using TBOP, and are designated as TBOP 1 through TBOP 4. Each of these designs was obtained by starting the optimizer at a different point in the design space,

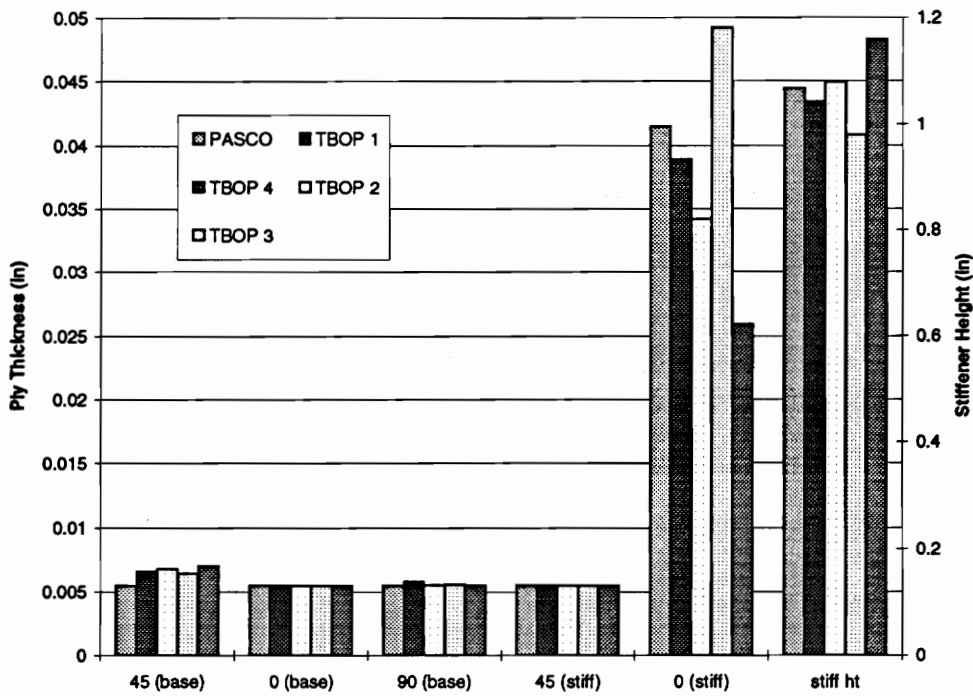


Figure 2.5: Comparison of PASCO and TBOP smeared stiffener results for a blade stiffened panel

and all have objective functions that were within 1-2% of one another. The design which is in best agreement with the PASCO results is the one designated TBOP 1. The other designs differ from the PASCO design in the relative magnitudes of the stiffener height and the thickness of the 0° stiffener plies. Some of these designs have a higher 0° stiffener thickness and a lower stiffener height, while others have a lower 0° stiffener thickness and a higher stiffener height.

When designing structures of this type, it is common to obtain several optimal or near-optimal designs in this manner. Multiple optima for blade stiffened panels were also found in Reference [41]. In this study, the different “optimal” designs differed from one another in a similar fashion to the designs TBOP 1 through TBOP 4.

Results obtained using other values for the stiffener spacing yielded similar results. In order to completely assess the merits of the TBOP smeared stiffness scheme, it would, of course, be necessary to perform a much more through investigation. The results obtained here merely indicate that this scheme yields realistic results for the structures and loads considered here.

It should be noted that PASCO measures the stiffener height from the middle surface

of the base laminate. This is different from the TBOP procedure whereby the stiffener height is measured from the upper surface of the base laminate. The results shown in Figure 2.5 have been adjusted to take into account this discrepancy.

Implementation Issues

During the course of the present research, a considerable amount of time was spent obtaining converged optimal designs for the various cases that are presented here. As mentioned previously, the criteria for deciding whether or not a given design point is optimal or not are the Kuhn-Tucker conditions. Satisfaction of the Kuhn-Tucker conditions within a given error tolerance constitutes convergence of the design process.

In the process of obtaining converged designs for the present work, various lessons and procedures that either allowed or hastened convergence were learned. As this knowledge was obtained, it was implemented into the design optimization process. This sometimes took the form of enhancements to TBOP, but more often the knowledge allowed for a more judicious choice of optimization algorithms or of the parameters that control the algorithms. In this section, some of this knowledge concerning convergence is presented along with a description of the enhancements made to TBOP in order to improve its convergence properties for the present work.

Each design problem was begun using the sequential convex programming (SCP) algorithm [33]. A sequential approximate algorithm was selected because the constraint evaluations were expensive; each involved a finite element based linear buckling analysis. Experience of a previous researcher indicated that the modified method of feasible directions would work well in solving the sub-problem generated by SCP, and this algorithm was used for that purpose.

The selection of appropriate move limits proved to be very important when using the SCP algorithm. This was primarily due to the buckling constraints. In a thin walled built-up structure (like the one used in the present work) the buckling eigenvalues are often closely spaced. This is especially true near the optimal design point. As mentioned in the section dealing with the buckling constraints, TBOP keeps track of eight to twelve of the buckling eigenvalues near the critical eigenvalue to guard against the phenomena of mode-switching. If the move limits are too large, however, an eigenvalue that is not included in the lower eight to twelve modes at one design point may suddenly be violated at the next design point. If the move limits were too large, it was not uncommon to have $\lambda_{cr} = 1.0$ at one design point and $\lambda_{cr} = 0.4$ at

the next design point. Care must be taken in reducing the move limits, however, or the convergence process may become unacceptably slow.

A move limit strategy based upon the value of the Lagrangian function [31] was added to TBOP/ADS to improve the move limit selection. Instead of basing the move limit size on the value of the most critical constraint (as is done in ADS), the move limit size was based upon the value of the Lagrangian function. If the Lagrangian function increased more than 5% from one iteration to the next, the move limits were decreased by 20%. This strategy appeared to work well for the present designs when the initial move limits were selected to be 20-30% of the design variables.

The Lagrangian function, \mathcal{L} , potentially includes contributions from all the constraints as well as the objective function. For inequality constraints, it may be expressed as follows:

$$\mathcal{L} = f - \sum_{j=1}^{n_g} \lambda_j g_j, \quad (2.30)$$

where f is the objective function, n_g is the number of inequality constraints, g_j is the j_{th} inequality constraint and λ_j is the lagrange multiplier [31] associated with g_j . The lagrange multipliers were computed by finding the least squares solution to the following set of equations [31]:

$$\nabla f - \mathbf{N} \lambda = 0, \quad (2.31)$$

where ∇f is the gradient of the objective function, and \mathbf{N} is a matrix whose columns are the gradients of the inequality constraints.

The SCP algorithm did an acceptable job in obtaining a design in the neighborhood of the optimal point, but convergence often became very slow or non-existent thereafter. To combat this, a strategy was developed whereby another algorithm was programmed to take over when the changes in the objective function from one SCP iteration to the next became small. Both the modified method of feasible directions (MMFD) [35] and the method of feasible directions (MFD) [36, 37] were considered as choices for this second algorithm. For the limited number of test cases examined, the method of feasible directions converged to the optimal point more quickly, and as a result, was selected to be the “second” algorithm.

While potentially more expensive than the SCP algorithm, the MFD algorithm was able to accomplish what the SCP algorithm often could not: make the final

adjustments to the design variables and satisfy the Kuhn-Tucker conditions. It is noted that often the key to success with this algorithm was the selection of the push-off factors. Because of the nonlinear nature of the constraints, the push-off factors generally need to be high (in the range 3.0-10.0). Often, when this algorithm appeared to be having trouble converging, an increase in the push-off factors solved the problem.

It is noted that the original version of TBOP did not always work correctly in association with the MFD and MMFD algorithms when implemented in isolation from the SCP algorithm. This had to do with a problem with the way in which the buckling constraints were handled. This problem has been corrected in the latest version of TBOP.

Chapter 3

MODEL DESCRIPTION

In this chapter, the box beam model(s) used in the current study are described. The chapter begins with a description of the physical structure that is being modelled and then presents the finite element idealization of this structure. This discussion includes a consideration of the boundary conditions and load cases used. The following section describes the various design variables used in the linear design study and discusses the manner in which the individual panels making up the structure were modelled. The chapter ends by discussing mesh convergence issues and with a brief discussion of the D_{16} and D_{26} coupling terms that arise in Classical Lamination Theory.

3.1 Physical Model

The structure that was investigated is a rectangular two spar box beam with overall dimensions similar to those found in the inboard section of a large transport aircraft wing. This structure is similar in overall dimensions to the C-130 box beam (see Figure 3.1) that has been examined by previous researchers [5, 6, 7]. The baseline structure considered here is 150 *in* long, 48 *in* wide, and 24 *in* high. Structures with rib spacings of 30.0 *in*, 22.5 *in*, and 15.0 *in* are each considered along with an alternate structure which is 96.0 *in* wide.

3.2 Finite Element Model

Analysis and design optimization was performed using a global finite element model of the structure. The structure was modelled using the EX97 shell element available through the Computational Mechanics Testbed (COMET) [24, 25]. EX97 is a bi-quadratic 9-noded assumed natural-coordinate strain (ANS) transverse shear deformable (C^0) quadrilateral shell element [42]. These elements are capable of modelling arbitrarily large rotations (but only small strains) when the co-rotational utility available in COMET is used (as it was here).

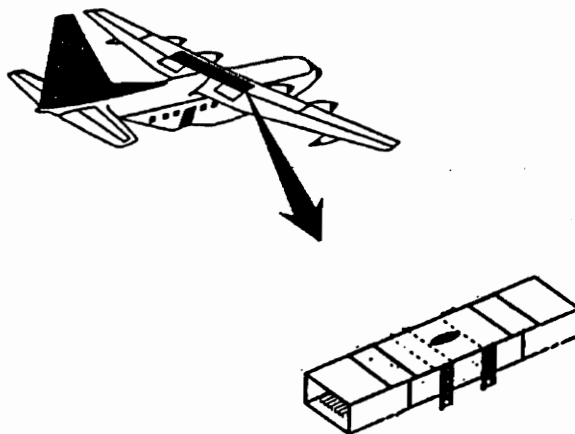


Figure 3.1: C-130 Box Beam

A typical finite element mesh is shown in Figure 3.2 along with the global coordinate system. For purposes of illustration, the structure has been cut along the mid-chord line and “opened up”. The top portion of the figure shows the “inside” of the structure, and the bottom portion of the figure shows the “outside” of the structure. An extra rib near the outboard end of the beam was added in order to prevent excessive local deformation near the load introduction points (this was necessary when geometrically nonlinear analyses were performed).

Boundary conditions at the root were chosen to represent a wing-fuselage connection. Skin nodes were restrained from translating in the spanwise (x) or chordwise (y) directions, but were not restrained otherwise. Spar nodes were restrained from translating in either the spanwise (x), chordwise (y), or vertical (z) directions, and were also restrained from rotating about the chordwise (y) axis.

The two primary load cases, the bending and torque load cases, are illustrated in Figures 3.3 and 3.4. In the bending load case, a 100,000 lb upward load was applied to each of the outboard spars, resulting in a $30.0E6$ lb/in bending moment at the root of the structure. In the torque load case, a 200,000 lb upward load was applied to the left spar, and a 200,000 lb downward load was applied to the right spar, resulting in a $9.6E6$ lb/in moment along the length of the structure. These load cases were chosen because they result in bending and torque moments at the root of the structure which are similar to those found in actual structures of this type. Additional load cases consisting of linear combinations of the torque and bending load cases were also

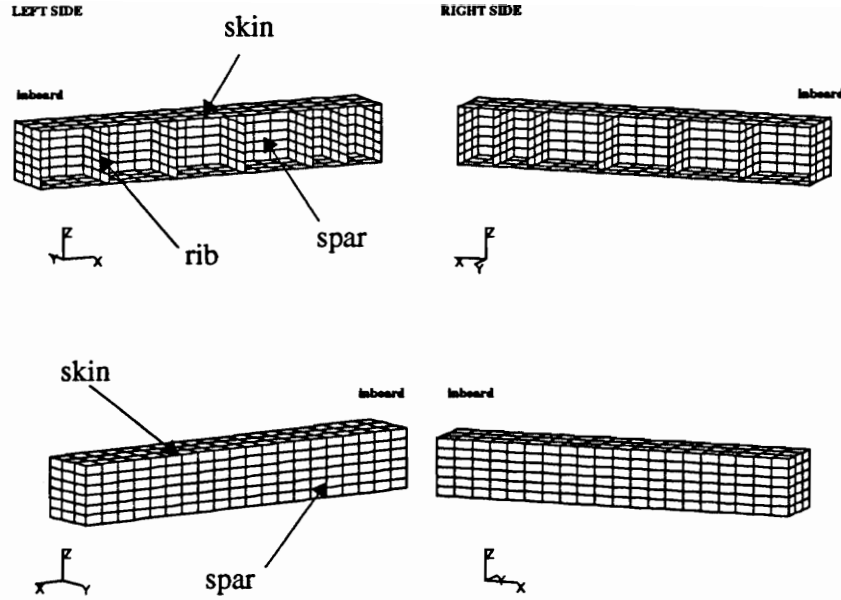


Figure 3.2: Undeformed Mesh

imposed on the structure.

3.3 Panel Modelling

Within the global model, the individual skin, spar, and rib panels were modelled in one of two ways. For the majority of the analyses, the panels were modelled as unstiffened plates made up of $\mp 45^\circ$, 0° , and 90° plies. For several of the analyses, however, the skin panels were assumed to be stiffened longitudinally by blade stiffeners. In this case, these blade stiffeners were mathematically “smeared” into the base laminate so that the panel behaved *globally* like a stiffened panel (See Chapter 2).

In the first case (unstiffened plates), both a three design variable and nine design variable set were used. The three design variable set consisted of variables which defined the thickness of each skin ply, the thickness of each spar ply, and the thickness of each rib ply (Figure 3.5). In this case, a $(\mp 45/90/0)_s$ quasi-isotropic stacking sequence was maintained for each panel. In the nine design variable case, the thickness of each of the $\mp 45^\circ$ plies, 90° plies, and 0° plies were allowed to vary independently in each of the three panel types. This arrangement is illustrated in Figure 3.6. When smeared stiffeners were utilized, a design variable defining the smeared stiffener height

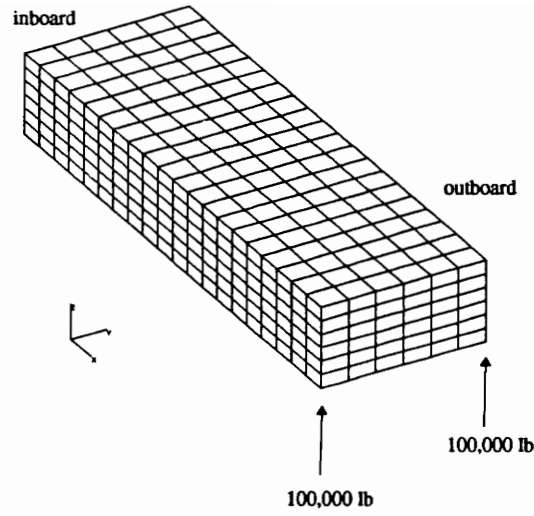


Figure 3.3: Bending Load Case

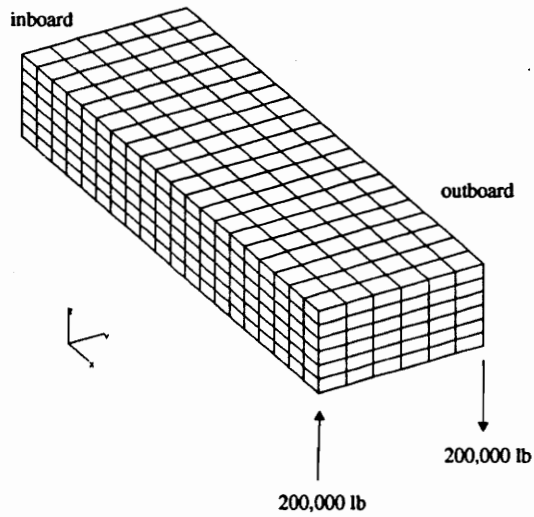


Figure 3.4: Torque Load Case

Design Variable	Description
x_1	Skin ply thickness (in)
x_2	Spar ply thickness (in)
x_3	Rib ply thickness (in)
f	Weight (lb)

For example:
Skin Panel

x_1	-45
x_1	+45
x_1	90
x_1	0
x_1	0
x_1	90
x_1	+45
x_1	-45

total thickness= $8 \cdot x_1$

Figure 3.5: Three Design Variable Case

and a design variable describing the smeared stiffener ply thickness were used as well. The design variables describing ply thicknesses had lower bounds of .006 *in*, and the design variable describing the smeared stiffener height had an upper bound of 3.00 *in*. The thicknesses of the outermost two rib panels were held constant during the design process. These rib plies were fixed at .025 *in* for the bending load case, and at .045 *in* for the torque and combined bending/torque load cases.

These choices of design variables mean that the upper and lower skin panels have the same designs. In a “real” wing box structure, the upper skin panel would have a different design from the lower skin panel. In this case, the upper skin panel is typically designed for buckling, and the lower skin panel is designed from strength considerations. A possible direction for future work would be to include more and different design variable sets in this study.

The inter-panel joints were not explicitly modelled. The individual panels were connected rigidly to one another so that undeformed right angles remained right angles as the structure deformed.

3.4 Material Properties

The material properties and maximum strain values used in this work are presented in Tables 3.1 and 3.2. These properties are typical values for a graphite-epoxy material system.

Design Variable	Description
x_1	$\mp 45^\circ$ Skin ply thickness (in)
x_2	90° Skin ply thickness (in)
x_3	0° Skin ply thickness (in)
x_4	$\mp 45^\circ$ Spar ply thickness (in)
x_5	90° Spar ply thickness (in)
x_6	0° Spar ply thickness (in)
x_7	$\mp 45^\circ$ Rib ply thickness (in)
x_8	90° Rib ply thickness (in)
x_9	0° Rib ply thickness (in)
f	Weight (lb)

For example:
Skin Panel

x_1	-45
x_1	+45
x_2	90
x_3	0
x_3	0
x_2	90
x_1	+45
x_1	-45

$$\text{total thickness} = 4 * x_1 + 2 * x_2 + 2 * x_3$$

Figure 3.6: Nine Design Variable Case

Table 3.1: Assumed Material Properties (Graphite-Epoxy)

Property	Value
E_1	20.0E6 lb/in ²
E_2	1.30E6 lb/in ²
G_{12}	1.03E6 lb/in ²
ν_{12}	.30
ρ	.057 lb/in ³

Table 3.2: Assumed Material Strain Allowables (Graphite-Epoxy)

Property	Value
ϵ_1^T	.009
ϵ_1^C	.008
ϵ_2^T	.0055
ϵ_2^C	.029
γ_{12}	.025

3.5 Mesh Convergence

In design optimization, the structure is analyzed repeatedly during the course of the optimization process. For this reason, it is important to keep the cost of each analysis as low as possible. When the analysis model is a finite element model (as it is here), it is important to choose the mesh size appropriately. The best mesh will be the one that is as coarse (computationally inexpensive) as possible while still retaining the desired accuracy.

Several mesh sizes were investigated for the present study. Each of these meshes is identified by a code $n_l \times n_w \times n_h$ which specifies the number of elements in the length direction, n_l , the number of elements in the width direction, n_w , and the number of elements in the height direction, n_h . Each of the elements so specified is a nine-noded bi-quadratic element.

The finest mesh investigated was 30x12x9 and was used as the baseline mesh to which the results of the other meshes were compared. Comparisons were made for both the bending and torque load cases. The results of the convergence study are summarized in Tables 3.3 and 3.4; in Table 3.3, the results for the optimal design B3G are presented, and in Table 3.4, the results for the optimal design T3G are presented (see Chapter 4 for a description of these designs). The first three eigenvalues obtained for each mesh are presented in each case.

The eigenvalues for the 20x9x6 case are all within 1.0% of those obtained for the 30x12x9 case for both load cases. The mode shapes corresponding to the first three modes are likewise the same. Based on this data, it was determined that the 20x9x6 mesh was adequate for the present design study.

In examining the buckled mode shapes for the 20x9x6 mesh, it appeared that both n_w and n_h could be further reduced. This resulted in the 20x6x4 mesh. The results obtained with this mesh were not encouraging, however. The eigenvalues for this case began to deviate from the 30x12x9 case, and more importantly, the lowest eigenmodes no longer matched the 30x12x9 modes.

This problem was solved by increasing n_h back to 6 and obtaining the 20x6x6 mesh. This mesh is nearly as accurate as the 20x9x6 mesh (all three eigenvalues are within 1.5% of the 30x12x9 mesh), and predicts the same eigenmodes as the 30x12x9 mesh. This mesh was therefore chosen to be the best compromise between accuracy and computational expense and is the mesh used throughout this design study.

As an additional precaution, the 20x6x6 mesh was compared to the 30x12x9 mesh for two of the nine design variable optimal designs. Unlike the three design variable designs, the nine design variable panels were not constrained to be quasi-isotropic, and therefore the resulting design may have a more complex structural response. Table 3.5 presents the results for design B9GP, and Table 3.6 presents the results for design T9G (see Chapter 4 for a description of these designs). As before, the first three eigenvalues are shown in each case.

In the bending case, the third 20x6x6 eigenmode corresponds to the first 30x12x9 eigenmode. The difference between the eigenvalues is 2.9% in this case. Although this deviation may be a little high, this mode is a rib buckling mode, and like many such modes presented in Chapter 4, is controlled almost exclusively by the rib design variable. As a result (the rib panels make up a small percentage of the overall structural weight), the effect of this mode on the objective function would be small, and therefore its accuracy is less important than those modes (like mode 1) which involve the buckling of the skin and spar panels as well. The 20x6x6 eigenmodes 1 and 2 have eigenvalues which are within 1.5% of the corresponding 30x12x9 eigenvalues (modes 2 and 3). In the torque case, all three eigenvalues are within 1.6% of the 30x12x9 eigenvalues, and all three eigenmodes match the 30x12x9 eigenmodes.

3.6 D_{16} and D_{26} terms

It is well known that the bending-twisting coupling terms D_{16} and D_{26} (which appear as part of Classical Lamination Theory) may affect both the buckling loads and modes of laminated composite plates [38]. For the present work, a few optimization runs

Table 3.3: Mesh Convergence Study: Bending Design B3G

	Mesh			
Eigenvalue	20x6x4	20x6x6	20x9x6	30x12x9
1	1.001	.9997	.9963	.9889
2	1.030	1.005	1.004	.9979
3	1.039	1.022	1.017	1.007

Table 3.4: Mesh Convergence Study: Torque Design T3G

	Mesh			
Eigenvalue	20x6x4	20x6x6	20x9x6	30x12x9
1	1.004	.9983	.9961	.9858
2	1.018	1.007	1.003	.9963
3	1.020	1.016	1.014	1.003

Table 3.5: Mesh Convergence Study: Bending Design B9GP

	Mesh	
Eigenvalue	20x6x4	30x12x9
1	1.002	.9902
2	1.006	.9915
3	1.019	.9938

Table 3.6: Mesh Convergence Study: Torque Design T9G

	Mesh	
Eigenvalue	20x6x4	30x12x9
1	.9981	.9843
2	1.008	.9919
3	1.020	1.006

were made in order to determine the sensitivity of the results to the presence or absence of these terms. For the three design variable bending case (see design B3G in Chapter 4) it was found that these coupling terms do affect the results of the optimization run, but only slightly. The skin and spar design variables changed by 1% and the spar design variable changed by 5%. The difference in the value of the optimal objective function was only 0.1%. For the three design variable torque case, the results of the optimization run were not affected by the D_{16} and D_{26} terms at all.

The effects of the coupling terms are exaggerated in this study as compared to “real” structures because of the stacking sequences that were assumed for each panel. In a “real” structure, the $\mp 45^\circ$ plies, the 90° plies, and the 0° plies would be dispersed through the thickness of the laminates. This dispersal has the effect of minimizing the effects of the D_{16} and D_{26} terms on the structural response [38]. In the present models, however, each ply orientation is grouped together in the laminate with other plies of the same orientation. This arrangement has the effect of maximizing the effects of the coupling terms.

Because the coupling terms do not appear to have a significant effect on the optimization results, and because including these terms would unrealistically magnify their effect on the structural response, these terms were neglected (zeroed out) for the purposes of the present study.

Chapter 4

RESULTS OF LINEAR DESIGN STUDY

In this chapter, the results of the linear design study are presented. For each of several load cases, geometries, and choices of design variables, minimum mass box beam designs are presented and compared to one another. The effects of subcomponent interaction on each of these designs are discussed and design trends are deduced.

Each design presented here was obtained by imposing both panel buckling constraints and material failure (strain) constraints on the structure while minimizing the total structural weight. Two different approaches were used to impose the panel buckling constraints. In the first approach (the *global* approach), the buckling constraints are based upon a linear eigenvalue analysis of the entire structure. This approach allows the subcomponent panels to interact with one another in a realistic manner, and should yield results that are more accurate than those obtained by optimizing each panel separately. The drawback to the global approach is its high computational expense. In order to assess the advantages of the global approach, many of the global results are compared to results obtained using a simpler, less expensive approach, called here the *local* approach. In the local approach, the panel buckling constraints are evaluated separately for each subcomponent panel. The individual panel loads are still obtained from the global structural model, but each buckling constraint is based on formulas for simply supported plates subject to in-plane edge loads. Strain constraints in all cases were based upon the maximum strain failure criterion. It is noted that each of the designs presented here was buckling critical; none of these strain constraints were active at any of the optimum design points.

In addition to the panel buckling and strain constraints, several of the designs were also subject to ply-percentage constraints. These constraints apply to panel laminate design; they impose an upper limit on the percentage of the total laminate thickness that any given ply orientation may attain.

For many of the designs presented in this chapter, an attempt was made to determine whether the design obtained was a true global optimum or whether it was only a local optimum. As mentioned in Chapter 2, this may be accomplished by starting

the optimizer at different initial points in the design space and then comparing the final results of the optimization process to one another. If the optimizer repeatedly returns to the same final design point, there is an increased probability that this final point is a global optimum. Because the global approach is computationally expensive, it was only possible to make a limited number of these “extra” design runs in the course of this design study.

In the discussion which follows, the designs are grouped according to the load case for which they were designed. Within each group, different box beam designs are compared and discussed. These designs differ from one another in the number and types of design variables used and also in the method (global or local) used to impose the buckling constraints. The chapter begins by considering those designs obtained subject to an upward bending load only. Designs obtained subject to an applied torque load are considered second, and designs which were obtained subject to combinations of both bending and torque loads are considered third. The last several sections consider the effects of rib spacing, box beam width, and smeared skin stiffeners on these results.

A summary description of each design case included in the present design study is presented in Table 4.1. In order to make identification easier, each design case is designated according to a code such as “B9G”, “T3L”, or “C3G”. The first letter of this code designates the load case: “B” for bending, “T” for torque, and “C” for a combination of bending and torque loads. The second number designates the number of design variables used, and the third letter indicates whether the global (“G”) or local (“L”) approach was used to impose the panel buckling constraints. Additional letters may be appended onto this base code to further identify the design case: “P” to indicate that ply percentage constraints were imposed, “S” to indicate that smeared stiffener design variables were included, and “W” to indicate that the box beam width was different from the baseline. A detailed description of each load case and design variable set may be found in Chapter 3.

The global coordinate system used in the following sections is as follows: The x-axis is in the spanwise direction, the y-axis is in the chordwise direction, and the z-axis is in the wing thickness (vertical) direction. In the skin and spar panels, the 0° plies run in the spanwise direction, and in the rib panel, the 0° plies run in the vertical direction.

Table 4.1: Summary Description of Each Design Case: Part 1

ID	Box Geometry				Load Case	No. Design Variables
	L	W	H	Rib Sp.		
B3G	150"	48"	24"	30.0"	B	3
B9G	150"	48"	24"	30.0"	B	9
B9GP	150"	48"	24"	30.0"	B	9*
B3L [†]	150"	48"	24"	30.0"	B	3
B9L [†]	150"	48"	24"	30.0"	B	9
B9LP [†]	150"	48"	24"	30.0"	B	9*
T3G	150"	48"	24"	30.0"	T	3
T9G	150"	48"	24"	30.0"	T	9
T3L [†]	150"	48"	24"	30.0"	T	3
T9L [†]	150"	48"	24"	30.0"	T	9
C3G	150"	48"	24"	30.0"	C	3
C9GP	150"	48"	24"	30.0"	C	9*
C3G-1	150"	48"	24"	30.0"	C	3
C3G-2	150"	48"	24"	30.0"	C	3
B5GS [‡]	150"	48"	24"	30.0"	B	5
T5GS [‡]	150"	48"	24"	30.0"	T	5
C5GS [‡]	150"	48"	24"	30.0"	C	5
B3G-R1	150"	48"	24"	22.5"	B	3
B3G-R2	150"	48"	24"	15.0"	B	3
B9GP-R1	150"	48"	24"	22.5"	B	9*
B9GP-R2	150"	48"	24"	15.0"	B	9*
B3L-R2 [†]	150"	48"	24"	15.0"	B	3
B9LP-R2 [†]	150"	48"	24"	15.0"	B	9*

* Ply-percentage constraints imposed

[†] Simplified buckling analysis used[‡] Smeared Skin Stiffeners Used

Table 4.1: Summary Description of Each Design Case: Part 2

ID	Box Geometry				Load	No. Design
	L	W	H	Rib Sp.	Case	Variables
T3G-R1	150"	48"	24"	22.5"	T	3
T3G-R2	150"	48"	24"	15.0"	T	3
T9G-R1	150"	48"	24"	22.5"	T	9
T9G-R2	150"	48"	24"	15.0"	T	9
T3L-R2 [†]	150"	48"	24"	15.0"	T	3
T9L-R2 [†]	150"	48"	24"	15.0"	T	9
B5GS-R1 [‡]	150"	48"	24"	22.5"	B	5
B5GS-R2 [‡]	150"	48"	24"	15.0"	B	5
T5GS-R1 [‡]	150"	48"	24"	22.5"	T	5
T5GS-R2 [‡]	150"	48"	24"	15.0"	T	5
B3GW	150"	96"	24"	30.0"	B	3
B9GPW	150"	96"	24"	30.0"	B	9*
B3LW [†]	150"	96"	24"	30.0"	B	3
B9LPW [†]	150"	96"	24"	30.0"	B	9*

* Ply-percentage constraints imposed

[†] Simplified buckling analysis used

[‡] Smeared Skin Stiffeners Used

4.1 Upward Bending

In this first section, minimum mass designs are presented for box beams which were subjected to symmetric bending and shearing loads only (no torque loads). In each case, both spars were loaded by a 100,000 *lb* upward load at their outboard ends.

The first three designs (B3G, B9G and B9GP) were obtained using the global approach. These designs will be examined in detail and will serve as the baseline designs to which the local designs will be compared. Each of these designs is for a beam which is 150" long, 48" wide, and 24" high with 30" rib spacing. Each of the skin, spar, and rib panels were modelled as flat plates using $\mp 45^\circ$, 0° , and 90° ply orientations. Design B3G is described by three design variables, and designs B9G and B9GP are described by nine design variables.

4.1.1 Design B3G: Global Approach

Design B3G is described by the design variables t_{sk} , t_{sp} , and t_{rb} , which define the thickness of each of the skin plies, the thickness of each of the spar plies, and the thickness of each of the rib plies, respectively. These design variables constrain each of the 0° , $\mp 45^\circ$, and 90° plies in a given panel to be the same thickness, thereby constraining each of the panels to be $(\mp 45/90/0)_s$ quasi-isotropic laminates.

The results of this design case are summarized in Table 4.2. Two buckling constraints were active at the optimal point. The mode shapes corresponding to the two active buckling constraints are given in Figures 4.1 and 4.2. The first mode is an interactive mode characterized by the compatible and simultaneous buckling of the upper skin panel, the inboard spar panels, and the two inboard rib panels. This buckling mode does not correspond to the buckling of a single isolated panel, but is instead characterized by the compatible buckling of several of the subcomponent panels comprising the structure. In the second active buckling mode, the second rib panel buckles independently of the other panels in the structure.

The extent to which the value of each design variable influences the values of the active constraints can be determined by examining the gradients of the active constraints (the derivatives of each of the active constraints with respect to each of the design variables). The active constraint gradients for design B3G are presented in Table 4.3. Each constraint is normalized so that it indicates the percentage change in the constraint with respect to a single ply thickness (.006 *in*). The numbers

Table 4.2: Results – Design Case B3G

Design Case: B3G			
Geometry: 150"x48"x24"			
Rib Spacing: 30.0"			
Loading: Upward Bending			
Active Constraints:			
<i>Buckling Mode</i>	1	2	
Eigenvalue	.9997	1.005	
Description	Ply thickness (<i>in</i>)		
Skin	.137		
Spar	.0395		
Rib	.0118		
Weight (<i>lb</i>)	1088.2		

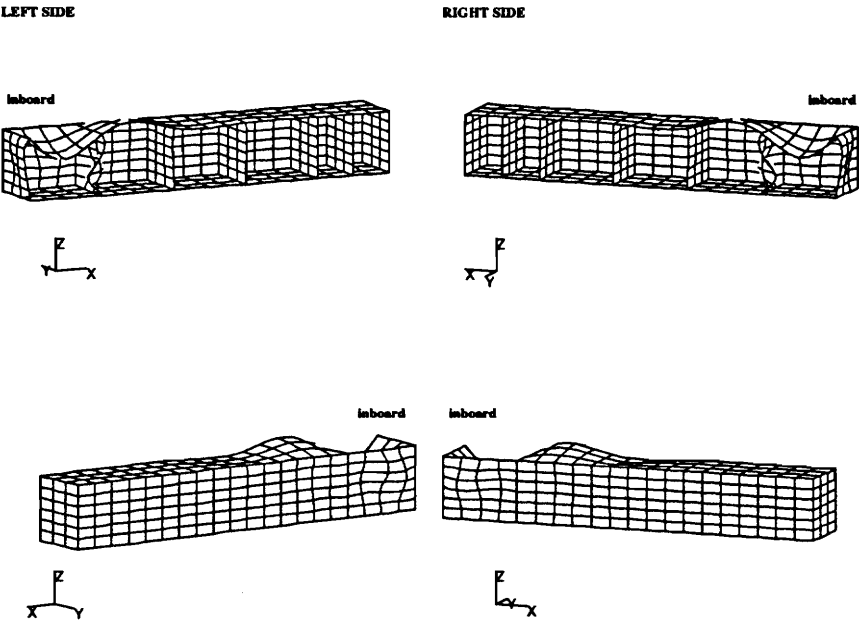


Figure 4.1: Design B3G – Active buckling mode 1 ($\lambda=.9997$)

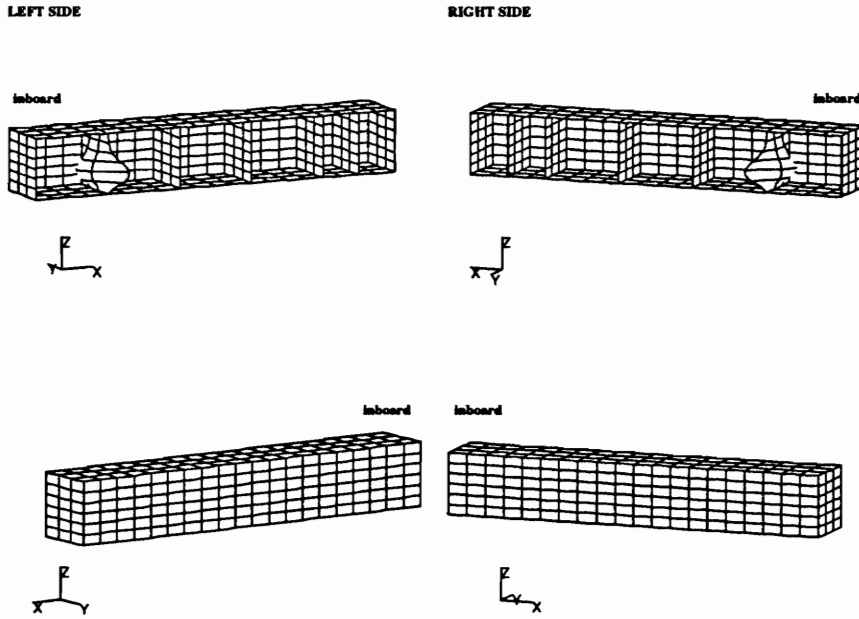


Figure 4.2: Design B3G – Active buckling mode 2 ($\lambda=1.005$)

in parentheses are normalized by dividing the derivatives of each constraint by the magnitude of the largest derivative for that constraint. It is noted that the skin and spar design variables are coupled in mode 1, while mode 2 is dominated by the rib design variable.

The constraint gradients can be used to construct a linear approximation to each of the constraint surfaces near the optimal point. For the current design (three design variables), a graphical representation of the design space *in the immediate neighborhood of the optimal point* can then be plotted. Such a plot allows the relationships between the various design variables and constraint surfaces to be easily visualized.

Table 4.3: Design B3G – Active buckling constraint gradients

DV		Mode 1		Mode 2	
1	t_{sk}	-11.2	(-1.00)	-3.8	(-.037)
2	t_{sp}	-5.1	(-.452)	-0.0	(-.005)
3	t_{rb}	-0.5	(-.041)	-104.1	(-1.00)

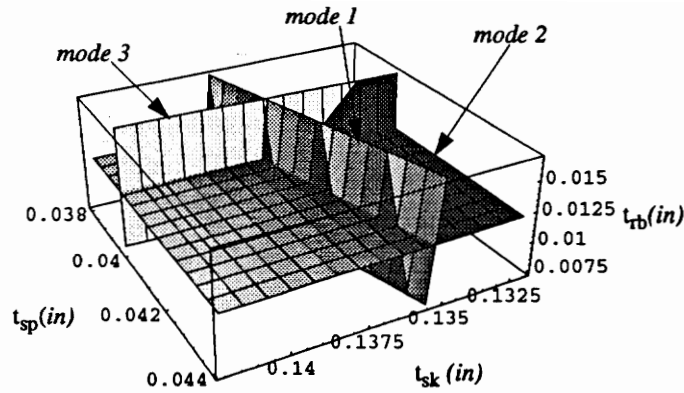


Figure 4.3: Design B3G – Linear Approximation to Design Space

A plot of the design space corresponding to the current design is given in Figure 4.3. The skin, spar, and rib ply thickness are each plotted along one of the axes, and the linear approximations to each constraint surface are plotted as planes. Both active constraints are included in the plot along with a third constraint which has a small constraint margin ($\lambda = 1.022$). The shading of each surface represents the value of the objective function; the darker the surface, the lower the objective function.

In mode 2, the rib does not interact significantly with either the skin or spar panels (neither the skin nor the spar design variables have a significant effect on this constraint). The first mode, on the other hand, shows interaction between all three design variables, most noticeably between the spar and the skin design variables. The plot indicates that certain trade-offs between these design variables could be made if desired. For example, if one wished to reduce the skin ply thickness by some (small) amount without violating the first constraint, it appears that this could be accomplished by increasing the spar ply thickness and/or the rib ply thickness by an amount indicated by the plot.

In practice, however, the situation is not as simple as this. Because there are many closely spaced buckling modes near the optimal design point, any significant move in design space is likely to change the active constraint set, thus invalidating the approximation used to construct the plot. The plot can be used to visualize the design space *at the optimal point* and to illustrate design variable coupling there, but cannot be reliably used to predict the effects of changes in the design variables unless

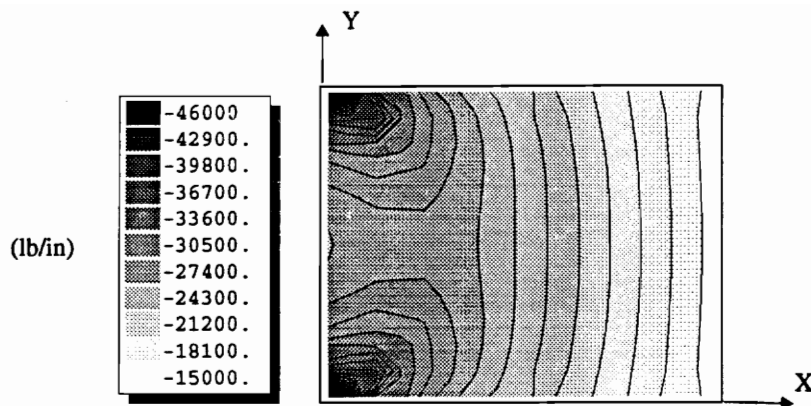


Figure 4.4: Design B3G – Upper Skin Nx Load

many more constraints (in this case, 10-20) are included in the plot.

It should be noted that the presence of the interactive buckling mode (mode 1) is not specific to an optimized design. In the course of this design study, several non-optimal designs were analyzed using a linear eigenvalue analysis. In the majority of these cases, one or more of the lowest buckling modes were interactive modes in which one or more of the skin, spar, and rib panels buckled in unison.

In order to better understand the behavior of this structure, it is necessary to look at the internal loads induced in each critical panel. For this design case (B3G), the major loads in each panel will be examined in some detail. For designs B3G and B9G, loads will be examined and comparisons will be made only as needed.

The loads induced in the upper skin are shown in Figures 4.4–4.6. Loads are designated according to the global coordinate system (see Chapter 3). In Figures 4.4 through 4.6 the loads in the box beam spanwise direction (N_x), the loads in the chordwise direction (N_y), and the in-plane shear loads (N_{xy}) are illustrated, respectively. Each of these figures includes that portion of the upper skin extending 60" in the spanwise direction from the inboard edge of the beam (that portion of the skin which covers the first two rib bays and constitutes the first two skin panels).

The primary load on the upper skin is a compressive (N_x) load which, at the root, reaches 27,000 *in-lb* at the mid-chord and 46,000 *in-lb* at the panel edges. Away from the root, the load is distributed more uniformly in the chordwise direction. This N_x load, along with a corresponding tensile load in the lower skin, couples out most of the overall bending load applied to the box beam. This load is accompanied by a

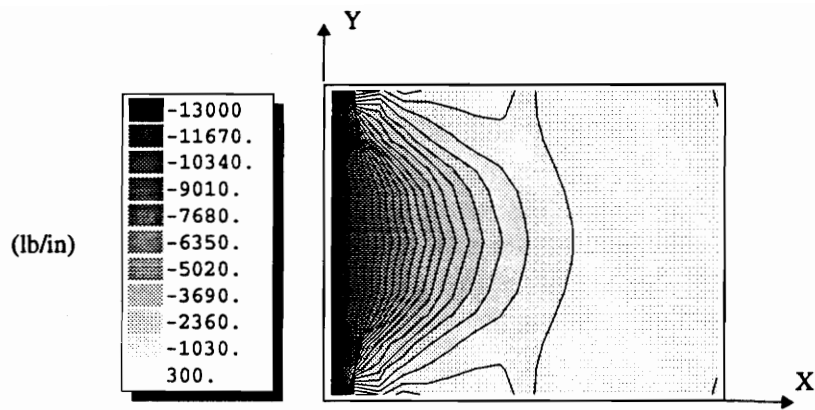


Figure 4.5: Design B3G – Upper Skin Ny Load

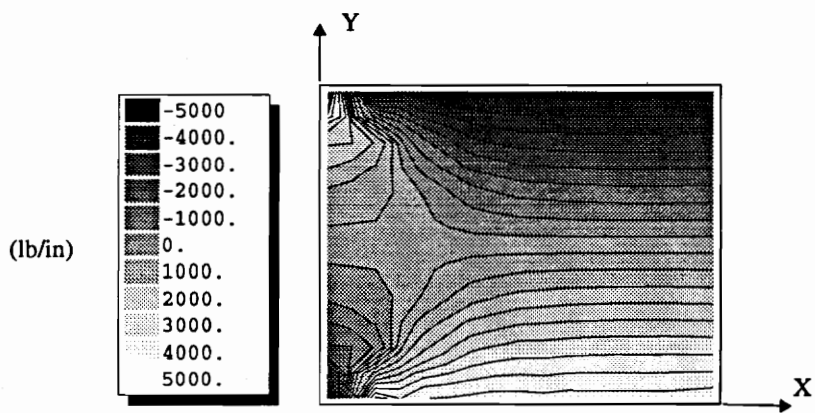


Figure 4.6: Design B3G – Upper Skin Nxy Load

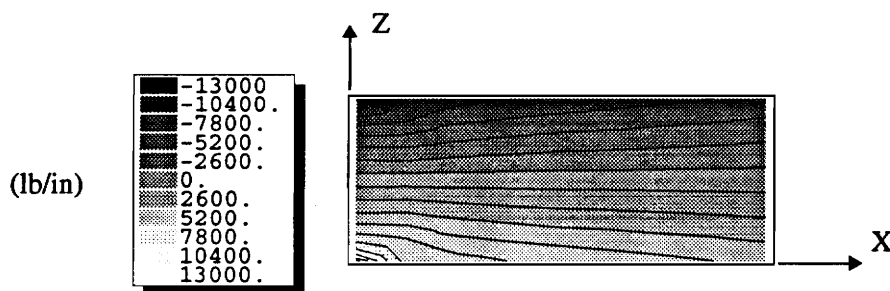


Figure 4.7: Design B3G – Spar Nx Load

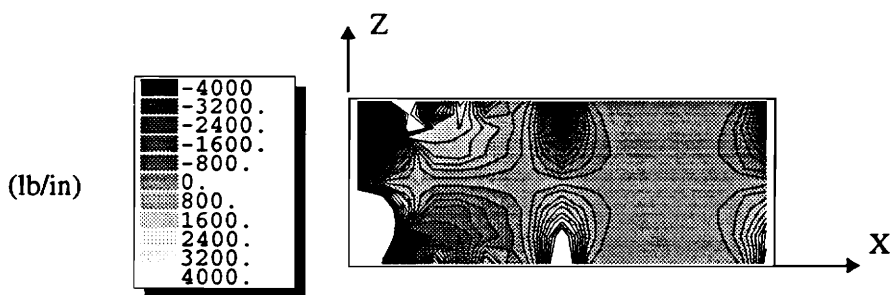


Figure 4.8: Design B3G – Spar Nz Load

5,000 *in-lb* shear load (N_{xy}) induced by the spar panels along both of the longitudinal edges of the skin. Because of the transverse restraint imposed by the root boundary conditions, there is also a transverse compressive load (N_y) induced in the skin panel at the root which extends over most of the first rib bay. This load peaks at 13,000 *in-lb*. The loads induced in the lower skin are the same, except that the signs of the loads are reversed.

The loads induced in the spar panels are illustrated in Figures 4.7–4.9. The spanwise loads (N_x) are shown in Figure 4.7, the vertical loads (N_z) are shown in Figure 4.8, and the shear loads (N_{xz}) are shown in Figure 4.9. As with the skin panel, the portion of the spar which is shown extends 60" in the spanwise direction from the inboard end of the box beam.

The primary load carried by the spar is a 4,200 *in-lb* shear load (N_{xz}). Most of the vertical load that was applied at the outboard end of the box beam is carried in

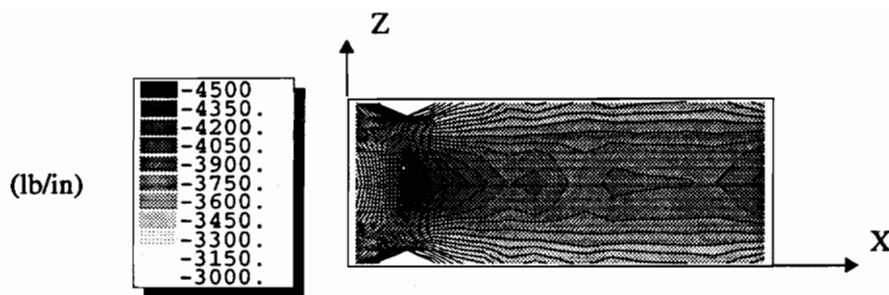


Figure 4.9: Design B3G – Spar N_{xz} Load

this manner by the spar panels. The spar is also loaded by an in-plane bending load in the longitudinal direction. This load, at the root, peaks at $\mp 13,000$ *lb-in* at the upper and lower panel edges, respectively. This load represents that portion of the overall bending moment that is carried by the spars (the rest of the overall bending load is reacted by the compressive load in the upper skin panel and the tensile load in the lower skin panel).

In addition to these loads, there are more localized transverse loads (N_z) induced in the spar at the spar-rib attachment lines. These loads result from the Poisson effect: the upper portion of the spar is in compression (because of the longitudinal bending load) and likewise, the lower portion of the spar is in tension. Because of the Poisson effect, the upper portion of the spar wants to expand in the vertical direction and the lower portion of the spar wants to contract in the vertical direction. This expansion/contraction is resisted to some extent by the attached rib panel. The result is a vertical tensile load at the bottom portion of the spar and a vertical compressive load at the top portion of the spar. While these localized loads are less important for the spar panel, they can be important to the response of the rib panel.

The loads in the critical rib panel are illustrated in Figures 4.10–4.12. The loads shown are those induced in the second rib as counted from the inboard end of the box beam. This rib carries higher loads than the first rib (the boundary conditions at the root reduce the loads carried by the first rib) and is the rib which buckles in both mode 1 and mode 2 in the present design case (B3G). The rib loads in the box beam chordwise direction (N_y) are illustrated in Figure 4.10, the rib loads in the box beam vertical direction (N_z) are illustrated in Figure 4.11, and the rib shear loads (N_{yz})

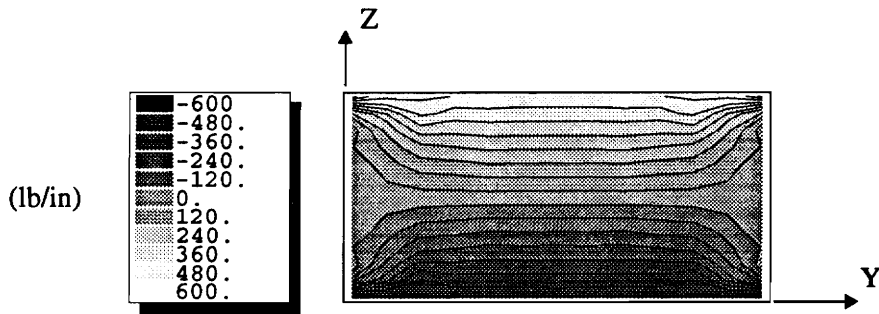


Figure 4.10: Design B3G – Second Rib Ny Load

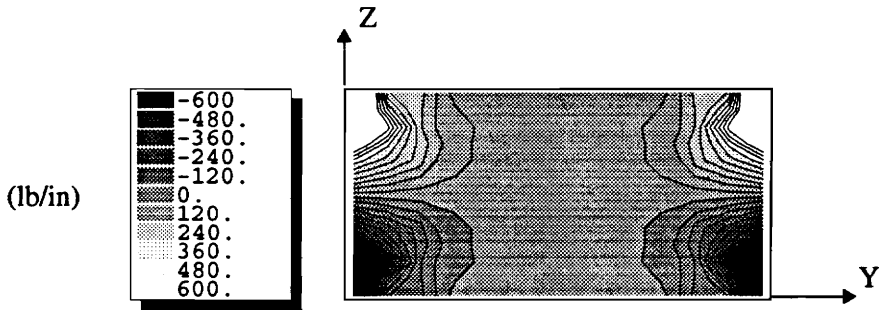


Figure 4.11: Design B3G – Second Rib Nz Load

are illustrated in Figure 4.12.

For this load case (no torque loads), there are no large loads acting on the rib panel, and the rib's main function is to provide support for the upper skin panel (which is in compression) and the spar panels. There are several loads that are induced in the rib panel, however, that can determine its design in this case. The first such load, already discussed in conjunction with the spar panel, is the Nz load induced in the box beam vertical direction at the rib-spar interface. As discussed above, this load is caused by the Poisson effect in the spar panel. The effect on the rib panel is to induce a vertical tensile load at the upper corners of the panel and a vertical compressive load at the lower corners of the panel. Vertical shear loads are induced in the transverse edges of the rib panel to counteract these loads. The second load that can be induced in the rib panel is also caused by the Poisson effect. For the current load case, the upper skin panel is in compression in the x -direction and wants to expand in the chordwise

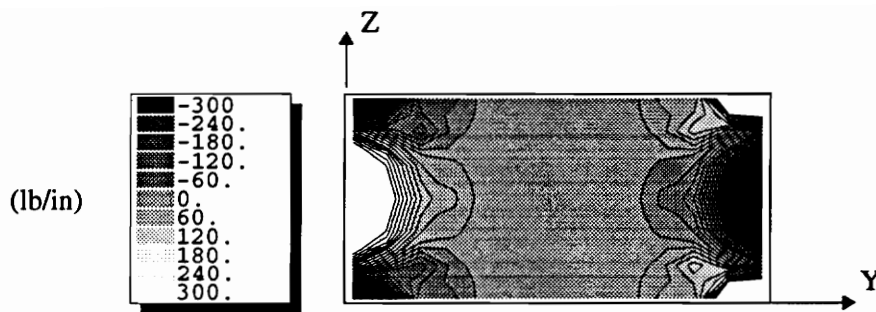


Figure 4.12: Design B3G – Second Rib Nyz Load

direction; likewise, the lower skin panel is in tension in the x -direction and wants to contract in the chordwise direction. This expansion/contraction is resisted by the rib panel at the skin-rib interface. As a result, the upper edge of the rib panel is put into chordwise tension (N_y), and the lower edge is put into chordwise compression. It is this latter compression load that is the main contributor to the second buckling mode for design B3G.

In summary, then, we have the usual distribution of the shear and bending loads in a box beam: the vertical shearing load is carried mostly by the spar panels (there is no other significant load path), and the overall bending load is shared between the skin and spar panels. Most of this overall bending load is carried by the skin panels, but, as noted, some is shared with the spar panels. (The distribution of the bending load between the skin and spar panels is determined by the skin and spar designs.) The rib loads (for this bending case) are determined by the interaction of the rib panel with the spar and skin panels. Both the skin and spar panels induce local loads in the rib panel. In this case (design B3G), the loads induced by the skin panel appear to drive the rib design.

4.1.2 Design B9G: Global Approach

In this section, a design is presented for the same structure as for design B3G, but more design variables are used. Instead of constraining each of the panels to a quasi-isotropic configuration, the $\mp 45^\circ$ plies, the 90° plies, and the 0° plies in each panel are allowed to vary independently from one another, resulting in a total of nine design variables (three for each panel).

Table 4.4: Results – Design Case B9G

Design Case: B9G			
Geometry: 150"x48"x24"			
Rib Spacing: 30.0"			
Loading: Upward Bending			
Active Constraints:			
<i>Buckling Mode</i>	1	2	3
Eigenvalue	.9976	1.003	1.006
Description	$\mp 45^\circ$	90°	0°
Skin ply thk (<i>in</i>)	.006*	.006*	.460
Spar ply thk (<i>in</i>)	.0210	.0267	.0945
Rib ply thk (<i>in</i>)	.006*	.006*	.00659
Weight (<i>lb</i>)	961.2		

* lower bound

The results for design B9G are presented in Table 4.4. Three buckling constraints were active at the optimal point; the buckling modes corresponding to the first two constraints are illustrated in Figures 4.13 and 4.14. Mode 1 is similar to the first mode from design case B3G in that it is an interactive mode involving the simultaneous and compatible buckling of the upper skin, inboard spar, and inner rib panels. The second and third modes are local rib buckling modes (only mode 2 is shown because mode 3 is the same as mode 2, except that it is anti-symmetric with respect to the mid-chord line). The two local rib buckling modes are different from the local rib buckling mode obtained for design case B3G. In design case B3G, the rib buckled along its entire width; here, the rib buckles locally near the spar-rib attachment lines.

An examination of the active constraint gradients (Table 4.5) reveals there is significant coupling between all nine design variables in mode 1. This coupling is stronger and more significant than that obtained for design B3G. For modes 2 and 3, there is negative coupling between the skin and rib panels; increasing the $\mp 45^\circ$ and 90° plies in the skin has an adverse effect on the rib constraints (this will be explained below).

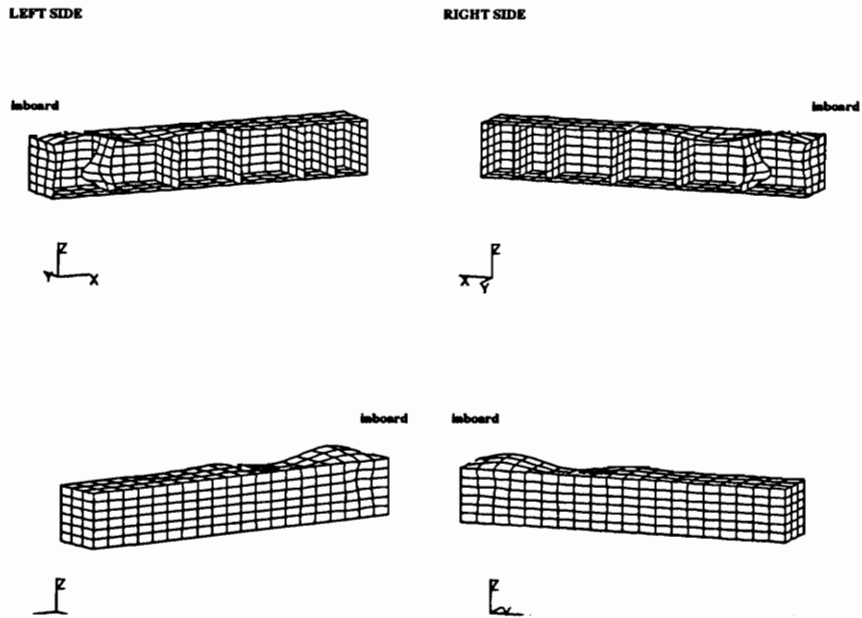


Figure 4.13: Design B9G – Active Buckling Mode 1 ($\lambda = .9976$)

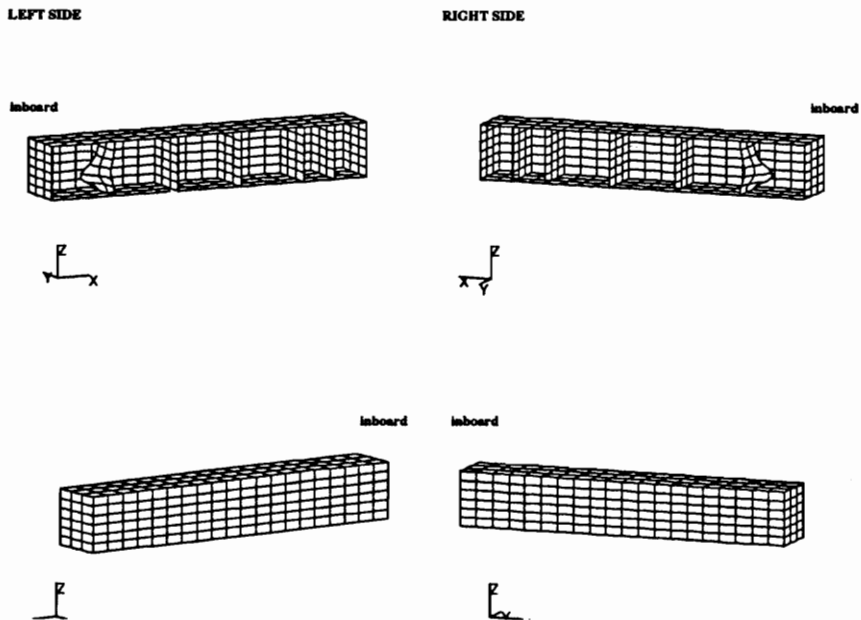


Figure 4.14: Design B9G – Active Buckling Mode 2 ($\lambda = 1.003$)

Table 4.5: Design B9G – Active buckling constraint gradients

DV		Mode 1		Mode 2		Mode 3	
1	t_{sk}^{45}	-4.3	(-1.00)	+16.9	(+.166)	+17.8	(.174)
2	t_{sk}^{90}	-1.1	(-.247)	-5.2	(-.051)	-5.3	(-.052)
3	t_{sk}^0	-3.2	(-.741)	+0.1	(+.001)	+0.0	(+.000)
4	t_{sp}^{45}	-3.0	(-.702)	+3.3	(+.033)	+3.5	(+.035)
5	t_{sp}^{90}	-1.5	(-.358)	-2.5	(-.024)	-2.6	(-.025)
6	t_{sp}^0	-1.4	(-.336)	-0.2	(-.002)	-0.2	(-.002)
7	t_{rb}^{45}	-1.4	(-.317)	-101.8	(-1.00)	-101.9	(-1.00)
8	t_{rb}^{90}	-0.5	(-.107)	-57.7	(-.567)	-57.9	(-.568)
9	t_{rb}^0	-0.7	(-.172)	-74.3	(-.730)	-74.6	(-.733)

The values of the design variables for designs B3G and B9G are compared in Figure 4.15. Several significant differences are noted. First, now that the skin panel is no longer constrained to be quasi-isotropic, the optimizer has chosen to reduce the thickness of both the $\mp 45^\circ$ and 90° plies to their lower bounds while increasing the 0° plies to 96% of the total laminate thickness. While the total skin thickness is 13% less than it was for case B3G, it is now almost entirely 0° plies. (These results indicate that it would be beneficial to add stiffeners to the skin in the longitudinal direction). This results in a skin laminate that is very stiff in the spanwise direction and soft in the chordwise direction.

The effect of this stiffness disparity on the load distribution in the upper skin is illustrated in Figures 4.16 and 4.17 (the load distribution in the lower skin is the same, except that the signs of the loads are reversed). In the longitudinal direction, the load distribution is no longer uniform in the chordwise direction anywhere along the first several skin panels; more load is carried near the edges of the panels (near the spars) than in the center of the panel (compare to Figure 4.4). At the root, the load ranges from 22,000 *in-lb* at the mid-chord to a maximum of 55,000 *in-lb* at the edges of the panel (in the previous case, the maximum load was 46,000 *lb/in*). In the chordwise direction, the contrast with the previous design case is even greater. Because the skin is now much softer in this direction, the magnitude of the induced compressive load is now much smaller (1,400 *in-lb* compared to 13,000 *in-lb*). Although the magnitude

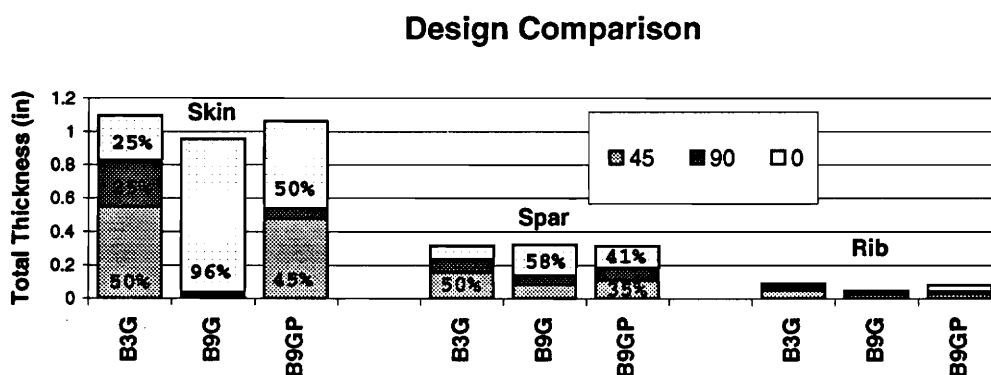


Figure 4.15: Comparison of Designs B3G-B9GP

of this Ny load is smaller, the skin area affected by this compressive load extends much further along the length of the box beam, completely covering the first two skin panels.

Each of the design variables describing the rib panels are either at their lower bounds or are very near their lower bounds, resulting in a rib panel which is only 0.049" thick. This is in contrast to the previous design (B3G), where the rib panel was nearly twice as thick (0.095"). The controlling factor for the previous rib design (design B3G) was the compressive (Ny) load induced on the lower edge of the second *rib* panel by the transverse contraction of the lower *skin* panel (Figure 4.10). Because the *skin* panel in the current design case is softer in the chordwise direction, this induced load is smaller. In fact, because the induced chordwise (Ny) load in the *skin* panel (Figure 4.17) extends past the first rib bay, the lower skin panel does not contract at the mid-chord of the second rib, but expands instead. The resulting Ny loading in the second rib panel is illustrated in Figure 4.18. The sign of the Ny loads induced at the panel mid-chord are reversed from those obtained for design B3G (compare to Figure 4.10). The magnitude of this induced load is also smaller than it was previously (200 lb/in vs. 600 lb/in). As a result, the load that actually controls

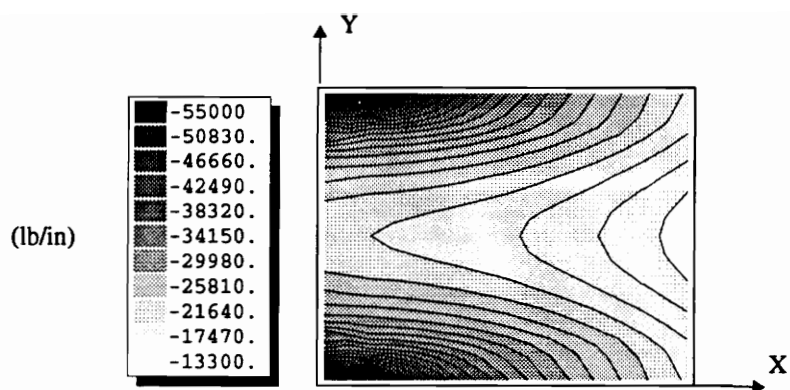


Figure 4.16: Design B9G – Upper Skin Nx Load

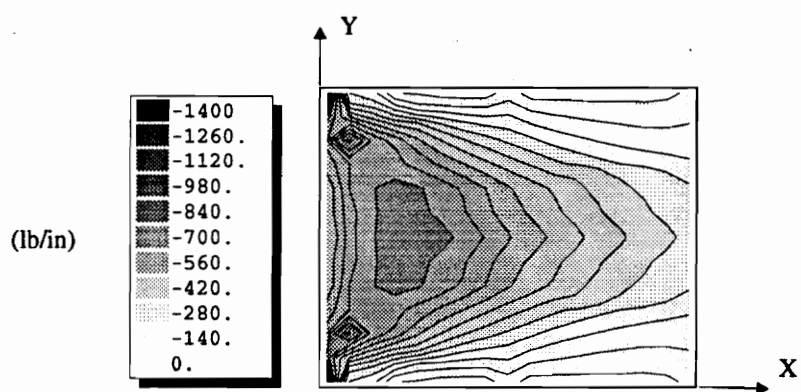


Figure 4.17: Design B9G – Upper Skin Ny Load

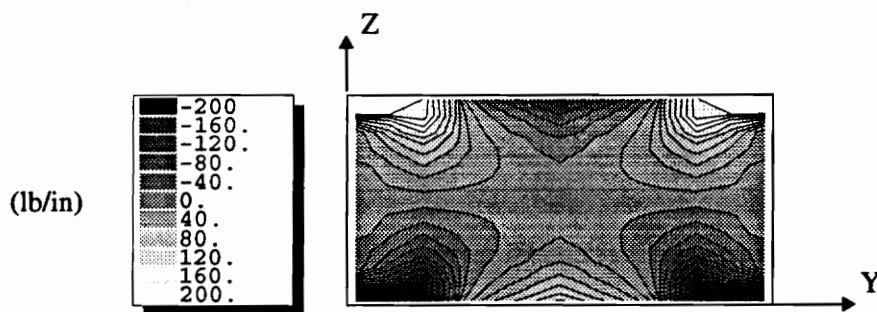


Figure 4.18: Design B9G – Second Rib Ny Load

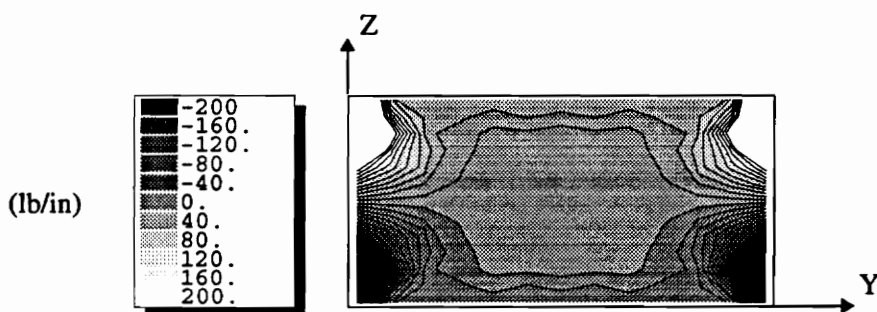


Figure 4.19: Design B9G – Second Rib Nz Load

the rib design in this case is not the induced Ny load, but instead is the Nz load induced by the spars (see Figure 4.19). This fact explains the differences in the local rib buckling modes between design B3G and design B9G.

For designs B3G and B9G, then, the skin design has a large effect on the the rib loads and therefore on the rib design. If the skin is stiff in the transverse direction, significant compressive loads are induced on the lower edge of the rib. If the skin is soft in this direction, these compressive loads are reduced (or they become tensile loads). This explains the negative coupling between the skin and rib design variables in the 2nd and 3rd buckling modes for design B9G. If the skin $\mp 45^\circ$ or 90° design variables are increased, the skin panel gets stiffer in the chordwise direction, the Ny loads induced in the rib panel grow larger, and the rib thickness must be increased.

The spar panel for this design case is composed of 58% 0° plies, 26% $\mp 45^\circ$ plies, and 16% 90° plies. The spar panel is actually thicker (3%) for this case as compared

to design B3G. This thickness increase (biased towards the 0° plies) increases the spar stiffness in the longitudinal direction. This is consistent with the fact that more of the longitudinal load is carried in the spars and near the edges of the skin panel as compared to design B3G.

4.1.3 Design B9GP: Global Approach

A skin design with 96% 0° plies (design B9G) is unrealistic for several reasons. First of all, laminates which contain too many contiguous plies of the same orientation (more than about 4 plies) are susceptible to delamination and matrix cracking. In addition, any panel designed with 96% 0° plies would be exceptionally vulnerable to off-design load cases. For these reasons, design B9G was re-run with ply-percentage constraints imposed on each of the skin, spar, and rib panels. These constraints limited the maximum percentage of the 0° and 90° ply thicknesses to 50% of the total laminate thickness.

The results of this run are presented in Table 4.6. Two buckling constraints were active at the optimal point along with a ply-percentage constraint for both the skin panel and the rib panel. Both active buckling modes are similar to the two modes that were active for design case B3G (see Figures 4.1 and 4.2). The objective function is 10% greater than that for design B9G and 3% less than that for design B3G. Both in the objective function and the response, design B9GP resembles design B3G more than design B9G.

The gradients of the active constraints with respect to the design variables are given in Table 4.7. As with design B3G, there is significant coupling between the skin and spar design variables in mode 1, while mode 2 is dominated by the rib design variable.

The design variables for design B9GP are compared with those for designs B3G and B9G in Figure 4.15. The skin panel for this case is 50% 0° plies (ply-percentage constraint is active), 45% $\mp 45^\circ$ plies, and 5% 90° plies. When the percentage of 0° plies was reduced in comparison with the B9G design to comply with the ply-percentage constraint, most of the difference was made up with $\mp 45^\circ$ plies. This is probably because, unlike the 90° plies, the $\mp 45^\circ$ plies still contribute to the spanwise stiffness of the panel. The total skin thickness is 3% less than that for design B3G and 11% greater than that for design B9G.

The ratio of the skin spanwise stiffness to its chordwise stiffness is greater than

Table 4.6: Results – Design Case B9GP

Design Case: B9GP			
Geometry: 150"x48"x24"			
Rib Spacing: 30.0"			
Loading: Upward Bending			
Active Constraints:			
<i>Ply Percent</i>	Skin/Rib		
<i>Buckling Mode</i>	1	2	
Eigenvalue	1.002	1.006	
Description	$\mp 45^\circ$	90°	0°
Skin ply thk (<i>in</i>)	.119	.0285	.264
Spar ply thk (<i>in</i>)	.0277	.0373	.0652
Rib ply thk (<i>in</i>)	.00726	.006*	.0197
Weight (<i>lb</i>)	1055.3		

* lower bound

Table 4.7: Design B9GP – Active buckling constraint gradients

DV		Mode 1		Mode 2	
1	t_{sk}^{45}	-5.5	(-1.00)	+1.4	(+.023)
2	t_{sk}^{90}	-2.3	(-.416)	-4.6	(-.076)
3	t_{sk}^0	-3.0	(-.548)	-2.2	(-.037)
4	t_{sp}^{45}	-3.0	(-.547)	+0.1	(+.002)
5	t_{sp}^{90}	-1.5	(-.267)	-0.2	(-.003)
6	t_{sp}^0	-1.5	(-.274)	-0.3	(-.006)
7	t_{rb}^{45}	-0.3	(-.059)	-59.3	(-1.00)
8	t_{rb}^{90}	-0.0	(-.005)	+3.5	(+.058)
9	t_{rb}^0	-0.1	(-.021)	-41.3	(-.696)

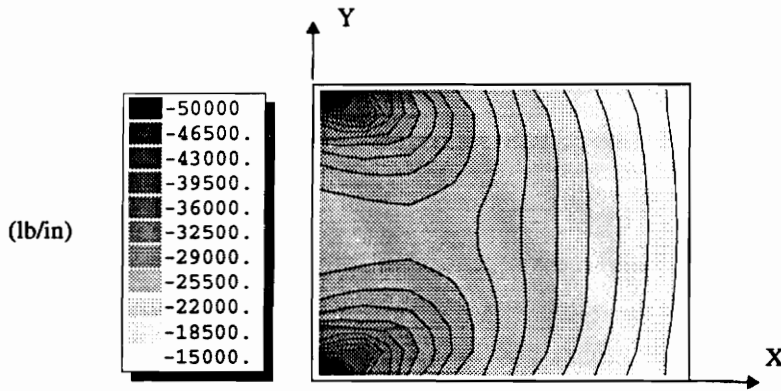


Figure 4.20: Design B9GP – Upper Skin Nx Load

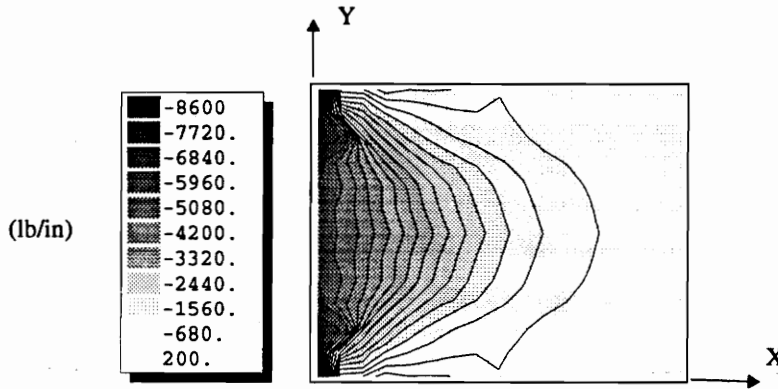


Figure 4.21: Design B9GP – Upper Skin Ny Load

that obtained for design B3G, but is not nearly as large as it was for design B9G. As a result, the skin load distribution is similar to that obtained for design B3G. The spanwise load (N_x) is close to uniform in the chordwise direction except at the root, where the load peaks in the panel corners. At the root, the N_x load at the mid-chord is 24,000 *in-lb* and the load at the edges is 50,000 *in-lb*. In the chordwise direction, the induced load at the root (N_y) peaks at 8,500 *in-lb*, a value between that found for design B3G (13,000 *in-lb*) and that found for design B9G (1400 *in-lb*). This load extends over the first rib bay, but not far beyond that. The skin N_x and N_y loads for this case are illustrated in Figures 4.20 and 4.21.

The rib panel for this case is 36% $\mp 45^\circ$ plies, 15% 90° plies, and 49% 0° plies (ply-percentage constraint). The total thickness is 15% less than that for design B3G

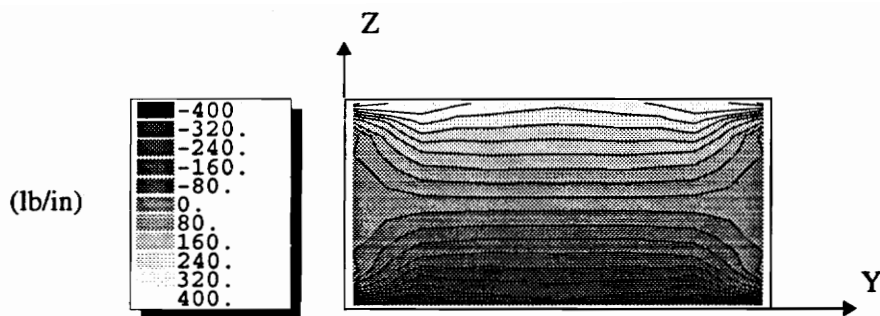


Figure 4.22: Design B9GP – Second Rib Ny Load

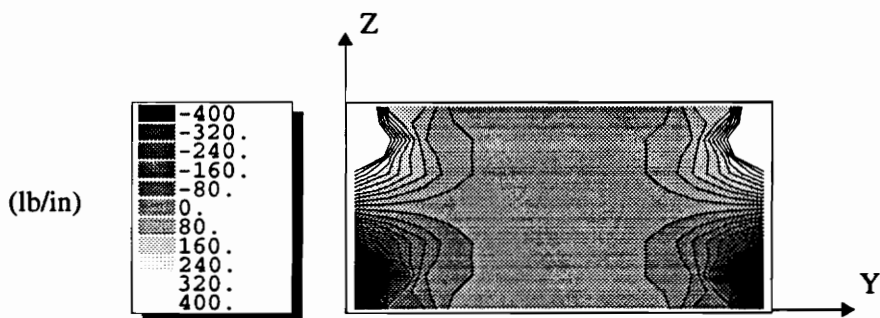


Figure 4.23: Design B9GP – Second Rib Nz Load

and 63% greater than that for design B9G. Unlike design case B9G, where all three rib design variables were at or near their lower bounds, here only the 90° plies are at their lower bound. The N_y and N_z loads induced on the second rib panel (the critical panel) are illustrated in Figures 4.22 and 4.23. These loads are induced by the expansion and contraction of the skin and spar panels as discussed in relation to design B3G. Unlike design B9G, the skin is again stiff enough in the chordwise direction to induce significant rib loads in the N_y direction. As with design B3G, it is these N_y loads which control the rib design.

From the active constraint gradients it can be seen that increasing the 90° plies in the rib panel has an adverse effect on the local rib mode. This can be explained by noting that increasing the 90° plies increases the rib stiffness in the global y -direction. This increased stiffness would have the effect of increasing the N_y stresses (Figure 4.22) which are themselves the cause of this buckling mode. This effect

explains why the 90° plies are at their lower bound. The optimizer instead increases the 0° plies, which have a favorable effect on the rib mode.

In addition to the two active buckling constraints, there is a third constraint that has a small constraint margin ($\lambda = 1.019$). This mode is a local rib buckling mode which has a similar mode shape as those that were active for design B9G: it is a mode wherein the rib buckles locally near the rib-spar interface and is caused by the induced N_z load (Figure 4.23).

The spar panel for case B9GP is 35% $\mp 45^\circ$ plies, 24% 90° plies, and 41% 0° plies. The total spar thickness is 0.1% thicker than that for design B3G and 3% thinner than that for design B9G. The panel has a smaller percentage of 0° plies as compared to design B9G even though no ply-percentage constraints are active for this panel. This reflects the fact that, compared to design B9G, more of the global longitudinal (N_x) load is carried in the center of the skin panel, and less is carried near the skin-spar intersection.

4.1.4 *Summary of Interaction Effects: Designs B3G-B9GP*

In examining the results from designs B3G–B9GP, several related types of “interaction effects” were noted. The first was a simple kind of interaction that occurs in any redundant structure in which there are multiple load paths. If there are two or more panels which are capable of carrying the same load, the load distributes itself between the two panels depending on the relative stiffnesses of the two panels. For example, in the current model, the amount of axial bending load induced in the spar panel is a function of the axial stiffness of the skin panel. Likewise, the amount of axial load carried in the skin panel is affected by the axial stiffness of the spar panel.

In the present structure, other less obvious types of interaction were seen as well. For example, the design of the rib panel was completely determined by the in-plane response of the skin and spar panels. If the skin was stiff in the transverse direction, large N_y loads were induced in the rib panel as a result of the Poisson effect. These were the loads which determined the rib design in this case. If the skin was soft in the transverse direction, the induced N_y loads were much smaller and the rib response and rib design were determined instead by a similar interaction with the spar panel.

These loads induced by the skin and spar panels in the rib panel are not the usually expected rib loads. As already noted, the main function of the rib panel for this load case is to stabilize the skin and spar panels. If a designer was not careful,

the interaction loads that are induced in the rib panel by the skin and spar panels could be easily overlooked. In a real structure, additional larger loads, such as fuel pressure loads, may be applied to the rib panel. In this case, these larger loads will determine the rib design and the skin-spar-rib interaction noted here will be of lesser importance for the rib design. Even in this case, however, these induced loads may still be important for details of the rib design (at the skin-rib interface, for example).

An additional type of rib loading (the rib crushing load) arises when geometrically nonlinear effects are considered. For some designs, this load may be the most important type of loading that the rib panel experiences. A full discussion of these nonlinear effects as they apply to the current structure is presented in Chapter 5.

Another type of interaction effect noted in the present designs can be seen by looking at the critical buckling modes and the active constraint gradients. Each of the designs examined so far has had an active buckling constraint wherein the corresponding buckling mode was characterized by the simultaneous and compatible buckling of the upper skin panel, the inboard spar panels, and the first and second rib panels. An examination of the active constraint gradients revealed significant interaction between the skin and spar design variables in this mode.

The important point here is that, instead of each panel buckling individually in its own mode, there is a single interactive mode wherein each panel buckles compatibly with its neighbors as a single unit. This occurs because each panel is linked to its neighboring panels through its attached edges. The restraints at the edge of any given panel are determined by the stiffness and the deformations of the other panel(s) which shares that edge. Because of this, the design and response of each panel affects the design and response of each panel to which it is attached.

The question that naturally arises at this point is: How does the present global approach to the wing box design (buckling constraints based upon a global eigenvalue analysis of the structure) compare to more conventional approaches to the problem? This question is addressed in the next section.

4.1.5 Designs B3L-B9LP: Local Approach

In this section, designs B3G-B9GP (which were obtained using a buckling constraint based upon an eigenvalue analysis of the entire structure) are compared to results obtained using a simpler, more traditional approach (referred to here as the *local* approach).

In the local approach, the panel buckling constraints are evaluated separately for each subcomponent panel using simplified buckling equations (see the discussion of panel buckling constraints in Chapter 2). In-plane loads for each panel are extracted from the global finite element model. These loads, which are assumed to vary linearly along each panel edge, are then used to evaluate the individual buckling constraints. In obtaining the individual panel loads from the global finite element model, only primary panel loads are considered; smaller localized loads are neglected. In cases where the magnitude of one or more of the primary loads varies nonlinearly from one end of the panel to the other, a linear approximation to this load is used to perform the buckling analysis.

The individual buckling constraints are based on expressions for the buckling of a simply-supported laminated plate [38]. Equations for calculating the buckling loads of a simply supported laminated plate subjected to linearly varying end loads are derived in Appendix A. Buckling loads for an applied N_x load, an applied N_y load, and an applied N_{xy} load are each calculated separately. The overall buckling constraint is then formulated using the following interaction equation [39]:

$$g_l = \left(\frac{N_x}{N_{x_{cr}}}\right) + \left(\frac{N_y}{N_{y_{cr}}}\right) + \left(\frac{N_{xy}}{N_{xy_{cr}}}\right)^2 - 1.0 \leq 0 \quad (4.1)$$

After each change in the design variables during the optimization process, the global model is updated and the panel loads are re-computed. In this way, the internal loads are allowed to redistribute throughout the structure as the design changes.

This local analysis is consistent with the approach taken by several previous researchers (for example, Ref. [16, 18]). The primary difference between this approach and previous approaches involves the modelling of the spar and rib panels. Most previous investigators assumed that the spar and rib panels were capable of carrying shearing loads only. In this study, the spar and rib panels, like the skin panel, carry both in-plane and shearing loads.

The advantages of using the local approach have to do with its simplicity and cost effectiveness. Compared to the local approach (which requires a finite element analysis each time the structure is analyzed), the local approach is considerably more efficient. In the present study, the CPU times for the global approach were from 3-10 times greater than those for the local approach.

Table 4.8: Results – Design Case B3L

Design Case: B3L			
Geometry: 150"x48"x24"			
Rib Spacing: 30.0"			
Loading: Upward Bending			
Active Constraints:			
Buckling Mode*	skin	spar	rib
Description	Ply thickness (in)		
Skin	.142		
Spar	.0469		
Rib	.0145		
Weight (lb)	1149.3		

* local buckling analysis used

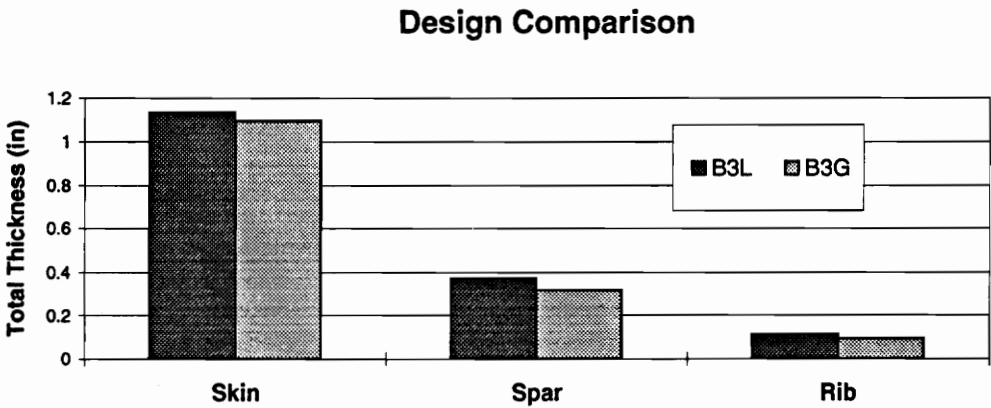


Figure 4.24: Comparison of designs B3G and B3L

Design B3L

The results of design case B3L are given in Table 4.8, and a graphical comparison between designs B3G and B3L is given in Figure 4.24. Comparing the values of the B3L design variables to those obtained using the global approach, it is seen that all three design variables are greater than the corresponding B3G design variables. The skin thickness design variable is 3.3% greater than the skin thickness design variable for design B3G. Likewise, the spar and rib thickness design variables are 18.8% and 22.4% greater than their B3G counterparts. The overall structural weight for design B3L is 5.6% greater than the weight of design B3G.

Three buckling constraints are active at the optimal point. The first constraint is the buckling of the upper-inboard skin panel, the second constraint is the buckling of the inboard spar panels, and the third constraint is the buckling of the second rib panel. The constraint gradients for the three active buckling modes are given in Table 4.9. It is noted that each of the buckling modes is controlled by a single design variable. This is in contrast to design B3G, where the dominant constraint exhibited significant coupling between the skin and spar design variables. This difference may be seen graphically by comparing the representation of the design space for this case (Figure 4.25) with its counterpart for design B3G (Figure 4.3). In the global case, mode 1 is a function of the skin, spar, and (less significantly) the rib design variable. In the local case, the skin mode is not significantly affected by the other two design variables. Note that critical constraints for design B3L are shifted (or translated) in design space relative to those that were critical for design B3G.

How does design B3L perform when analyzed using the global approach? When this analysis is performed, the critical eigenvalue for B3L is 1.12, 12% higher than that obtained for design B3G. This result indicates that, for this case, the local approach yields a more conservative design as compared to the global approach.

The differences between the results for designs B3G and B3L may be partially explained by considering the panel boundary conditions. In the local approach, each panel edge was assumed to be simply supported and no attempt was made to include the effects of the surrounding panels on the critical panel's response. In the global approach, each panel has more accurate boundary conditions because the rotational and translational restraints provided by attached panels are taken into account. This allows the panels to interact and support one another in a more realistic manner.

There are also differences in assumed panel loading between the two design cases.

Design case B3L uses a simplified panel load distribution to evaluate the buckling constraints, while a more complex load distribution actually exists in the global model. In order to give an example of the manner in which the simplified panel loads were obtained from the global model, the loading on the critical skin panel will be examined for design B3L. Figures 4.26–4.27 illustrate the in-plane upper-inboard skin panel loads as obtained from the global finite element model.

In the spanwise (x) direction of the skin panel, there is a large compressive load which is maximum at the chordwise edges. This load was approximated for the purpose of the simplified buckling analysis by a constant load of $-22,470 \text{ lb/in}$ over the entire panel. In the chordwise direction (y), there is a compressive load generated at the root which extends over the length of the panel. This load was approximated for the purposes of the simplified analysis by a load which varied linearly from -5900 lb/in at the root to 0 lb/in at the opposite end of the panel. The shear loads on the panel are small and localized. They were assumed to be zero for the simplified analysis.

In order to test the sensitivity of design B3L to the manner in which these loads were extracted from the global model, several additional optimization runs were made. In each case, different sampling points on the global model were used to obtain the simplified panel loads. The designs obtained in this manner were from 2% to 23% heavier than design B3G. The 2% figure corresponds to the case where the loads used for the simplified buckling analysis were the smallest loads which existed on the corresponding panel in the global model. Likewise, the 23% figure corresponds to the case where the highest loads were used. Both of these extremes are unrealistic; the most accurate figure is somewhere in the middle of this range, with our best estimate being 5.6% (design B3L). Note that the local designs are heavier than the global design regardless of the sampling points chosen.

In addition to the primary loads which were used for the simplified buckling analyses, there are also smaller localized loads on many of the panels. These localized loads are not taken into account in the local approach. If they were, the difference in the weights of the two designs might be greater than shown here.

Designs B9L and B9LP

Turning now to the nine design variable cases, the results for cases B9L and B9LP are presented in Tables 4.10 and 4.12 and comparisons are made to designs B9G

Table 4.9: Design B3L – Active buckling constraint gradients

DV		Skin mode	Spar Mode	Rib Mode
1	t_{sk}	-12.4 (-1.00)	-2.0 (-.036)	-3.9 (-.047)
2	t_{sp}	-0.7 (-.059)	-54.8 (-1.00)	-0.9 (-.010)
3	t_{rb}	+0.0 (+.001)	-0.1 (-.013)	-83.3 (-1.00)

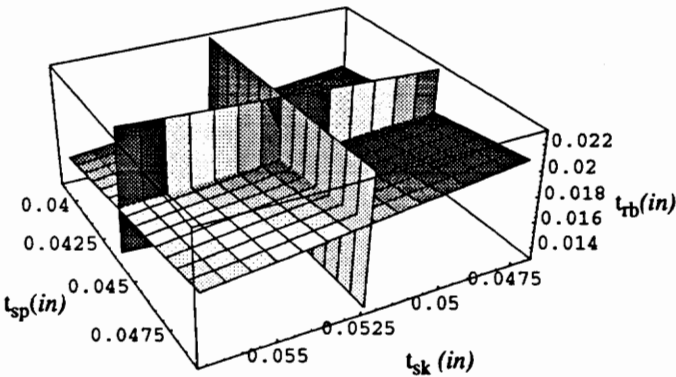


Figure 4.25: Design B3L – Linear Approximation to Design Space

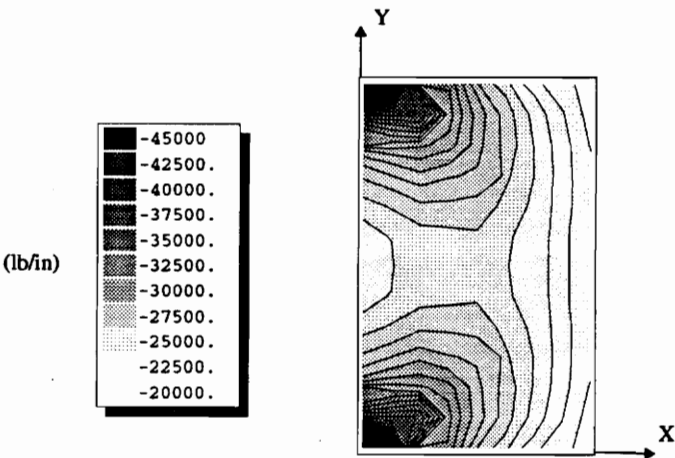


Figure 4.26: Design B3L – Upper Skin Nx Load

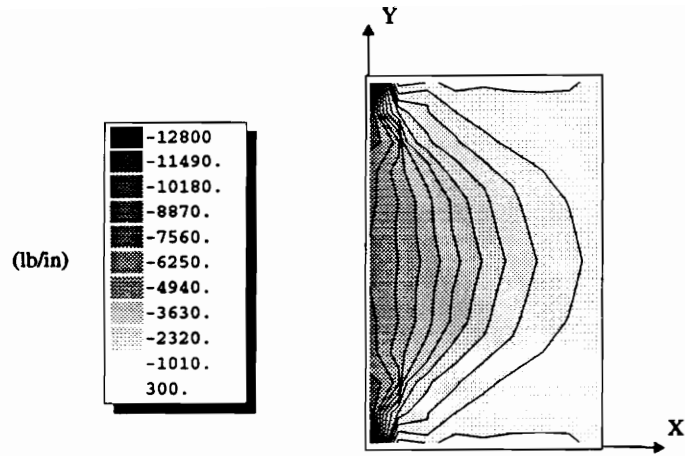


Figure 4.27: Design B3L – Upper Skin Ny Load

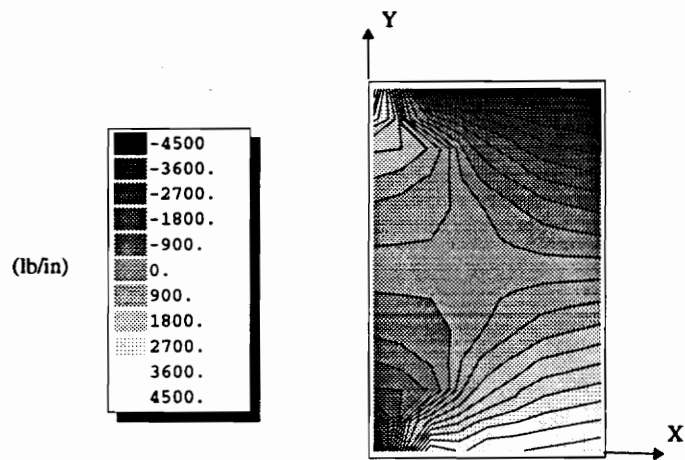


Figure 4.28: Design B3L – Upper Skin Nxy Load

Table 4.10: Results — Design Case B9L

Design Case: B9L			
Geometry: 150"x48"x24"			
Rib Spacing: 30.0"			
Loading: Upward Bending			
Active Constraints:			
<i>Buckling Mode</i> [†]	skin	spar	rib
Description	±45°	90°	0°
Skin ply thk (<i>in</i>)	.00603*	.006*	.494
Spar ply thk (<i>in</i>)	.0677	.00732	.0381
Rib ply thk (<i>in</i>)	.006*	.006*	.00640
Weight (<i>lb</i>)	1031.4		

* lower bound

† simplified buckling analysis used

and B9GP in Figures 4.29 and 4.30. As with design B3L, both designs B9L and B9LP are heavier than their B9G and B9GP counterparts. Design B9L is 7.3% heavier than design B9G (the range was from 3% to 24%) and design B9LP is 5.7% heavier than design B9GP (the range was from 1% to 33%).

As was the case for the skin panel in design B9G, the skin panel in design B9L is comprised of over 96% 0° plies (in both cases, both the ±45° and 90° skin thicknesses are at their lower bounds). The 0° skin thickness for design B9L is 7.4% greater than its B9G counterpart. The B9G and B9L rib panel designs are approximately the same; in both cases all three design variables are at or near their lower bounds. The skin-rib and skin-spar Poisson interaction discussed in relation to design B9G occurs for design B9L as well and appears to drive the rib design.

The B9L spar panel is 10.8% thicker than the B9G spar panel. In addition to this thickness difference, significant differences in the ply distribution exists as well. In design B9G, the spar panel is comprised of 26% ±45° plies, 6% 90° plies, and 58% 0° plies (which will be designated as: [26/6/58]). In design B9L, the percentages are quite different: [75/4/21]. In the global case, the majority of the spar plies were 0°

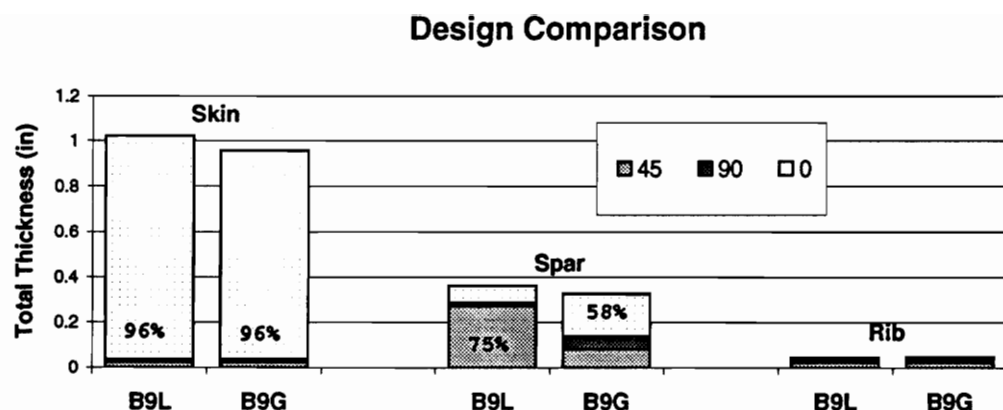


Figure 4.29: Comparison of designs B9G and B9L

plies, while in design B9L, the majority of the spar plies are $\pm 45^\circ$ plies (neither design has many 90° plies). These differences can be important because they indicate that the very nature of a panel design may depend on which approach, global or local, is used to perform the panel buckling analyses.

The active buckling constraint gradients for design B9L are given in Table 4.13. In comparing these constraint gradients with those obtained for design B9G, it is noted that the interaction between the skin, spar, and rib design variables is quite small in comparison. The skin mode is controlled by the skin design variables and the spar mode is controlled by the spar design variables. The only significant coupling that occurs is between the skin and rib design variables in the rib mode (specifically the $\pm 45^\circ$ and 90° plies in the skin affect the rib buckling mode). This may be explained by considering the Poisson interaction as discussed earlier (see section 4.1.1).

When design B9L is analyzed using the global approach, the design is found to be unsafe. The lowest buckling mode occurs at $\lambda = .72$ and is a rib buckling mode. This is a case where the local approach yields a design, which when analyzed using the global approach, is found to fail “prematurely”. It is noted that the B9L spar panel design differed significantly from the corresponding B9G design in this case.

Table 4.11: Results — Design Case B9L-A

Design Case: B9L-A			
Geometry: 150" x 48" x 24"			
Rib Spacing: 30.0"			
Loading: Upward Bending			
Active Constraints:			
<i>Buckling Mode</i> [†]	skin	spar	rib
Description	±45°	90°	0°
Skin ply thk (<i>in</i>)	.006*	.006*	.490
Spar ply thk (<i>in</i>)	.0307	.0311	.101
Rib ply thk (<i>in</i>)	.00615	.006*	.006*
Weight (<i>lb</i>)	1035.0		

* lower bound

† simplified buckling analysis used

The premature rib buckling mode may have been aggravated by interaction with this spar panel.

Besides design B9L, an alternate design (local optimum) was obtained using the local approach. This design has a slightly higher objective function than design B9L and was obtained by starting the optimizer at a different initial design point. This design, designated B9L-A, is presented in Table 4.11. In contrast to design B9L, this design has approximately the same ply distribution in the spar panel as does design B9G. When design B9L-A is analyzed using the global approach, it still fails prematurely in a rib buckling mode, but at a higher load level: $\lambda = .91$.

Taken together, the B9L and B9L-A results indicate that the local approach is potentially dangerous. The local approach may lead to designs that are unnecessarily heavy but not unsafe (B3L), but the danger also exists that the local design (B9L, B9L-A) will be unsafe and may fail prematurely.

Comparing the two designs with ply-percentage constraints (B9GP and B9LP), it is noted that each of the B9LP skin, spar, and rib panels is again thicker than its B9GP counterpart. The skin panel is 3.4% thicker, the spar panel is 19.7% thicker,

Table 4.12: Results — Design Case B9LP

Design Case: B9LP			
Geometry: 150"x48"x24"			
Rib Spacing: 30.0"			
Loading: Upward Bending			
Active Constraints:			
Ply Percent	Skin/Rib		
Buckling Mode [†]	skin	spar	rib
Description	±45°	90°	0°
Skin ply thk (in)	.123	.0278	.275
Spar ply thk (in)	.0338	.0450	.0764
Rib ply thk (in)	.00893	.006*	.0239
Weight (lb)	1115.1		

* lower bound

† local buckling analysis used

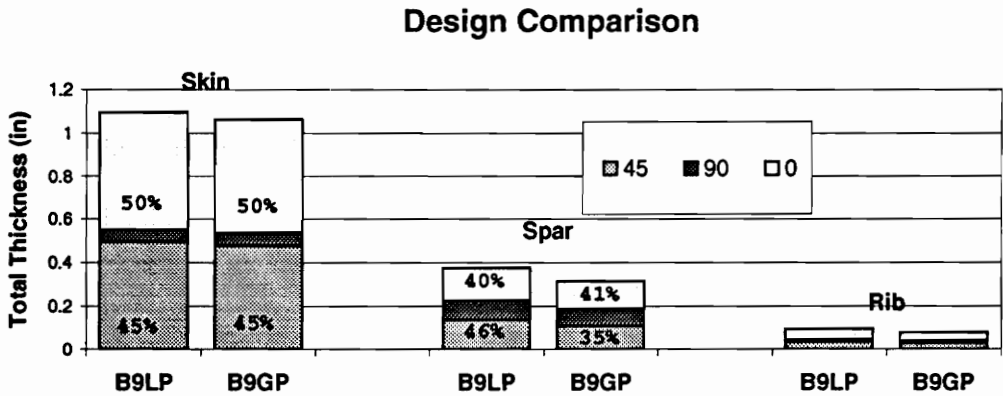


Figure 4.30: Comparison of designs B9GP and B9LP

Table 4.13: Design B9L – Active buckling constraint gradients

DV		Skin mode		Spar mode		Rib mode	
1	t_{sk}^{45}	-5.3	(-1.00)	-1.5	(-.044)	-54.8	(-.420)
2	t_{sk}^{90}	-1.1	(-.218)	-0.2	(-.006)	-17.9	(-.137)
3	t_{sk}^0	-3.5	(-.671)	-0.4	(-.012)	-0.7	(-.006)
4	t_{sp}^{45}	-0.1	(-.021)	-32.9	(-1.00)	+0.4	(+.003)
5	t_{sp}^{90}	-0.1	(-.019)	-16.7	(-.506)	-0.1	(-.001)
6	t_{sp}^0	-0.3	(-.055)	-14.1	(-.428)	+0.3	(+.002)
7	t_{rb}^{45}	-0.0	(-.000)	-0.0	(-.001)	-130.6	(-1.00)
8	t_{rb}^{90}	+0.0	(+.000)	-0.0	(-.001)	-6.2	(-.048)
9	t_{rb}^0	-0.0	(-.000)	-0.0	(-.001)	-58.7	(-.450)

and the rib panel is 18.3% thicker. In the case of the skin panel, the 0° and $\mp 45^\circ$ plies are 3–4% thicker, while the 90° plies are 3% thinner. In the spar panel, the thickness increase occurs nearly uniformly for all three ply types; no significant ply redistribution occurs. This is in contrast to the previous case (designs B9G and B9L), where significant ply redistribution did occur for the spar panel. In the rib panel, no significant ply distribution occurs either; the thickness difference is manifested by a uniform percentage increase in the 0° and $\mp 45^\circ$ plies. The 90° plies are at their lower bounds in both cases.

The active constraint gradients for design B9LP are presented in Table 4.14. The same general trends are found here as were found for designs B3L and B9L, namely that each constraint is controlled primarily by a single design variable. The coupling between skin, spar, and rib design variables in design B9GP is absent in design B9LP. When design B9LP is analyzed using the global approach, the critical eigenvalue is 1.13. Like designs B3L and B9L-A, this design is conservative compared to the global designs.

4.2 Torque

In this section, minimum mass designs are presented for box beams which were subjected to a 9,600,000 *in-lb* torque load. The torque is generated by applying a

Table 4.14: Design B9LP – Active buckling constraint gradients

DV		Mode 1		Mode 2		Mode 3	
1	t_{sk}^{45}	-6.2	(-1.00)	-0.6	(-.019)	+1.8	(+.032)
2	t_{sk}^{90}	-2.7	(-.433)	-0.2	(-.007)	-4.3	(-.076)
3	t_{sk}^0	-3.4	(-.538)	-0.7	(-.022)	-2.4	(-.042)
4	t_{sp}^{45}	-0.2	(-.027)	-31.0	(-1.00)	-0.3	(-.005)
5	t_{sp}^{90}	-0.0	(-.006)	-14.6	(-.472)	-0.0	(-.001)
6	t_{sp}^0	-0.3	(-.052)	-11.8	(-.381)	-0.4	(-.007)
7	t_{rb}^{45}	+0.0	(+.002)	-0.0	(-.001)	-56.7	(-1.00)
8	t_{rb}^{90}	+0.0	(+.003)	-0.0	(-.002)	+10.4	(+.184)
9	t_{rb}^0	+0.0	(+.000)	-0.0	(-.000)	-32.0	(-.565)

200,000 *lb* upward load at the outboard end of the left spar and a 200,000 *lb* downward load at the outboard end of the right spar.

The first two designs (T3G and T9G) were obtained using the global approach. These designs are for the same structure that was used for the bending case: the beam is 150" long, 48" wide, and 24" high with 30" rib spacing. As before, each of the skin, spar, and rib panels were modelled as flat plates using $\mp 45^\circ$, 0° , and 90° ply orientations. Design T3G is described by three design variables, while design B9G is described by nine design variables.

4.2.1 Design T3G: Global Approach

Like design B3G, design T3G is described by the design variables t_{sk} , t_{sp} , and t_{rb} , which describe the ply thicknesses of the skin panel, the spar panel, and the rib panel, respectively. These design variables constraint each panel to be a $(\mp 45/90/0)_s$ quasi-isotropic laminate.

The results of this design case are summarized in Table 4.15. Two buckling constraints were active at the optimal point. The buckling modes corresponding to the these constraints are shown in Figures 4.31 and 4.32. As was the case for many of the bending modes, these buckling modes do not correspond to the buckling of a single isolated panel, but are characterized by the compatible buckling of one or more of

the subcomponent panels comprising the structure. In the first mode, skin, spar, and rib panels buckle, while in the second mode, the skin and rib panels buckle.

The constraint gradients for the two active buckling modes are given in Table 4.16. Each constraint is normalized so that it indicates the percentage change in the constraint with respect to a single ply thickness (.006 in). The numbers given in parenthesis are normalized with respect to the largest derivative for each constraint. Both active constraints are functions of all three design variables. This interaction between the design variables is more pronounced in this (torque) case as compared to the corresponding bending case. This interaction may be seen graphically in Figure 4.33, which shows the linear approximation to the design space near the optimal point.

Looking at this plot, it can be seen that the second active constraint is controlled primarily by the rib design variable, but is also affected to a lesser degree by the skin and spar design variables. Increasing the skin thickness has a positive effect on this constraint (it increases the constraint margin) and increasing the spar thickness has a negative effect on the rib constraint (it decreases the constraint margin).

This particular interaction may be explained by considering the pre-buckling load distribution. In this case, the critical rib panel is loaded primarily by shear loads; it transfers shear from the skin panels to the spar panels. The magnitude of the shear load that is transferred by the critical rib is a function of the relative shear stiffness of the skin and spar panels. If the spar panel thickness is increased, the spar will carry a larger portion of the overall shearing load. This means that more shear must be transferred by the critical rib panel, therefore decreasing the constraint margin. On the other hand, if the skin thickness is increased, the critical rib panel will have to transfer less load and the constraint margin will increase.

As was done with the bending load case, the internal loads in each critical panel will be examined for this twisting load case. The loads induced in the upper skin are shown in Figures 4.34–4.36. Loads are designated according to the global coordinate system (see Chapter 3). Figure 4.34 illustrates the loads in the box beam spanwise direction (N_x), Figure 4.35 illustrates the loads in the box beam chordwise direction (N_y), and Figure 4.36 illustrates the in-plane shear loads (N_{xy}). As before, each of these figures includes that portion of the upper skin extending 60" in the spanwise direction from the inboard edge of the beam (that portion of the skin which constitutes the first two skin panels).

The primary load on the upper skin panels is a shear (N_{xy}) load which ranges

Table 4.15: Results – Design Case T3G

Design Case: T3G			
Geometry: 150"x48"x24"			
Rib Spacing: 30.0"			
Loading: Torque			
Active Constraints:			
Buckling Mode	1	2	
Eigenvalue	.9983	1.007	
Description	Ply thickness (in)		
Skin	.0505		
Spar	.0403		
Rib	.0143		
Weight (lb)	548.7		

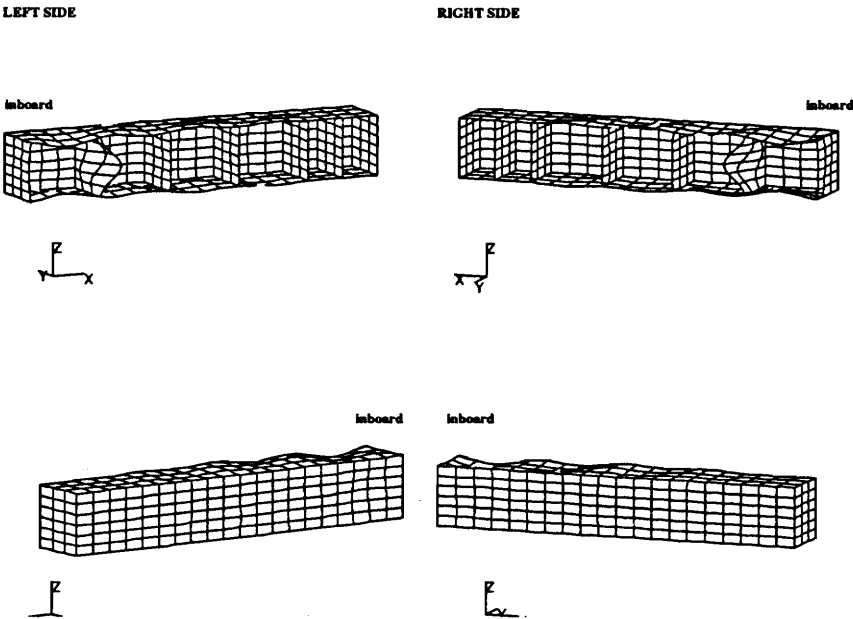


Figure 4.31: Design T3G – Active buckling mode 1 ($\lambda=.9983$)

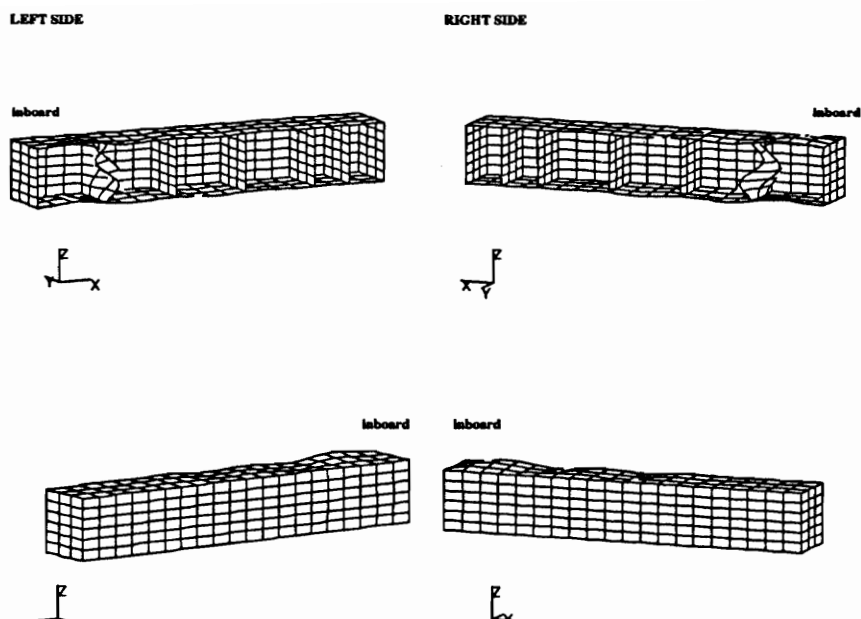


Figure 4.32: Design T3G – Active buckling mode 2 ($\lambda=1.007$)

Table 4.16: Design T3G – Active buckling constraint gradients

DV		Mode 1		Mode 2	
1	t_{sk}	-24.4	(-1.00)	-27.1	(-.456)
2	t_{sp}	-8.6	(-.354)	+10.8	(+.181)
3	t_{rb}	-13.3	(-.543)	-59.5	(-1.00)

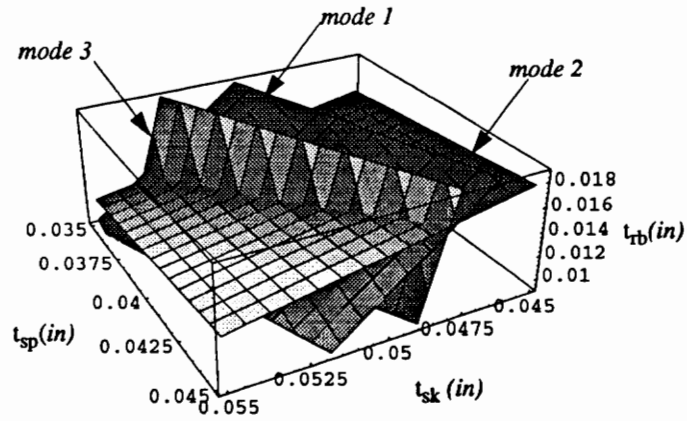


Figure 4.33: Design T3G – Linear Approximation to Design Space

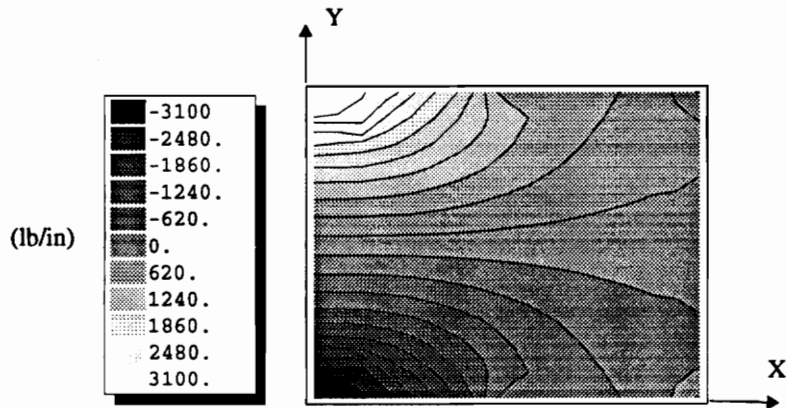


Figure 4.34: Design T3G – Upper Skin Nx Load

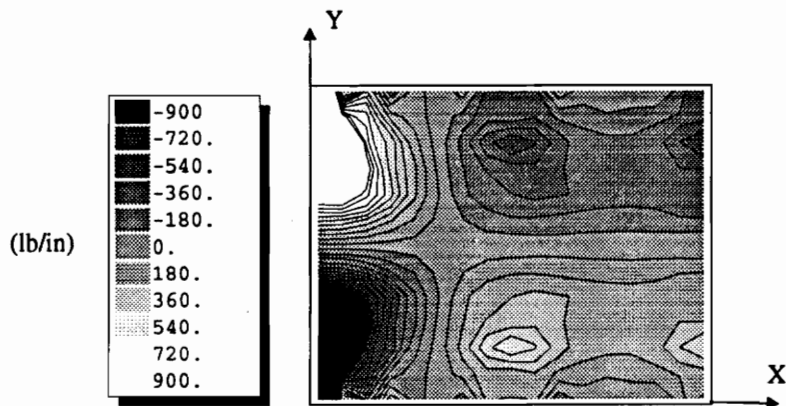


Figure 4.35: Design T3G – Upper Skin Ny Load

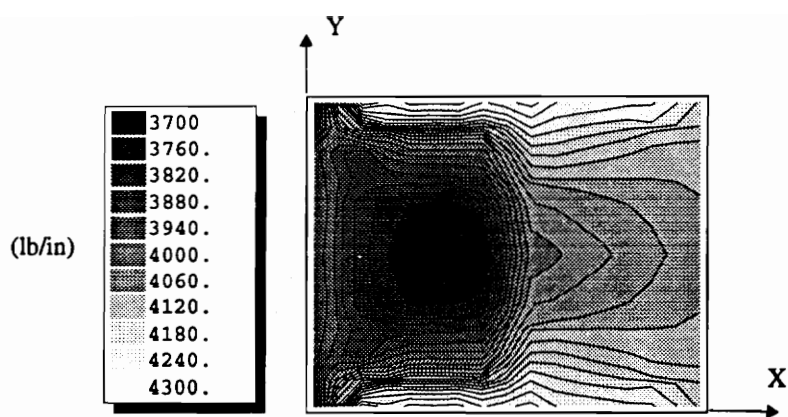


Figure 4.36: Design T3G – Upper Skin Nxy Load

from 3,700 *in-lb* to 4,300 *in-lb* in the innermost panels. This shear load, along with corresponding shear loads in the spar panels, reacts the overall twisting moment applied to the box beam. At the root, the boundary conditions induce additional local loads in the innermost skin panels. These loads resist the beam's tendency to twist out of plane at the root. The local longitudinal loads range from +3,100 *lb/in* at one chordwise edge of the panel to -3,100 *lb/in* at the opposite edge. Likewise, the transverse loads range from -900 *lb/in* to +900 *lb/in*. The loads induced in the lower skin panel are the same, except that the signs of the loads are reversed.

The loads induced in the left spar panel is illustrated in Figures 4.37– 4.39. The spanwise loads (N_x) are shown in Figure 4.37, the vertical loads (N_z) are shown in Figure 4.38, and the shear loads (N_{xz}) are shown in Figure 4.39. In each case, the portion of the spar which is shown extends 60" in the spanwise direction from the inboard end of the box beam.

Like the skin panel, the primary load carried by the spar panel is a 4,200-4,500 *lb/in* shear (N_{xz}) load. At the root, the spar is also subject to an in-plane bending load in the longitudinal direction. This load peaks at $\mp 2,500$ *in-lb* at the upper and lower panel edges, respectively. There are also smaller localized transverse (N_z) loads at the root, varying from +700 *lb/in* to -700 *lb/in*.

The loads in a typical rib panel are illustrated in Figures 4.40–4.42. The loads shown are those induced in the second rib as counted from the inboard end of the box beam. The rib loads in the box beam chordwise direction (N_y) are illustrated in Figure 4.40, the rib loads in the box beam vertical direction (N_z) are illustrated in

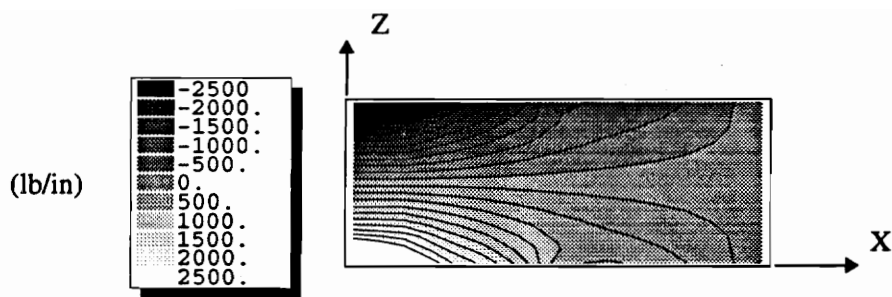


Figure 4.37: Design T3G – Spar Nx Load

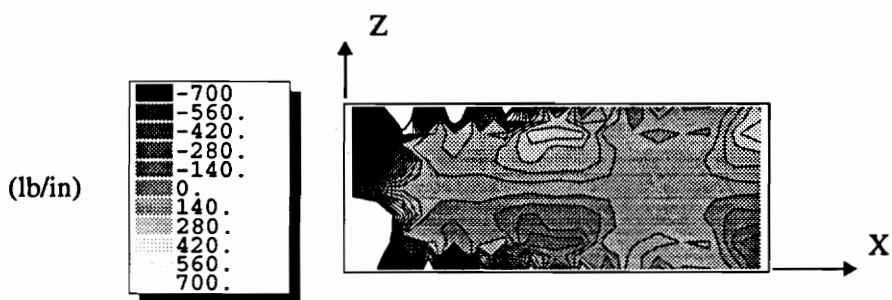


Figure 4.38: Design T3G – Spar Nz Load

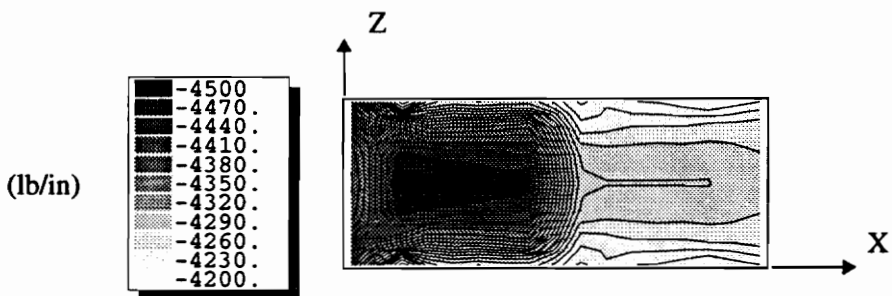


Figure 4.39: Design T3G – Spar Nxz Load

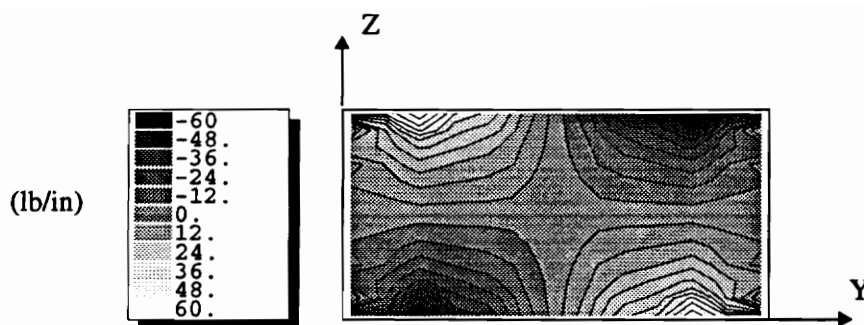


Figure 4.40: Design T3G – Second Rib Ny Load

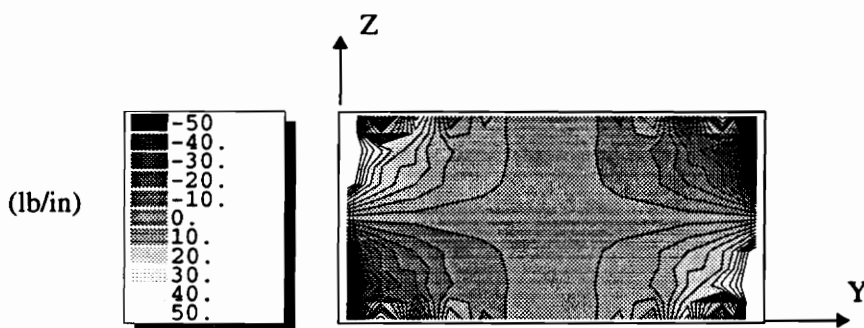


Figure 4.41: Design T3G – Second Rib Nz Load

Figure 4.41, and the rib shear loads (N_{yz}) are illustrated in Figure 4.42.

The primary load carried by the rib panel is a shear (N_{yz}) load which peaks at 200 lb/in at each edge of the panel. Localized N_y and N_z loads of $50\text{-}60 \text{ lb/in}$ also are present at the panel corners.

In summary, then, the primary loads in each of the three panel types for the twisting load case are shearing loads. In the skin and spar panels, these shear loads are approximately equal, with the maximum loads being near $4,200 \text{ lb/in}$. In the rib panels, the maximum shear loads are approximately 200 lb/in . Because of the boundary conditions at the root, localized tensile and compressive loads are present in both the skin and spar panels in addition to the primary shear loads. Small localized loads are also induced in each of the rib panels at the panel corners (at the skin-spar intersection points).

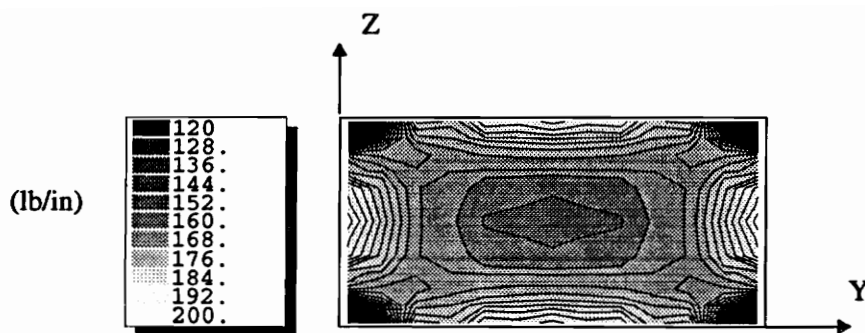


Figure 4.42: Design T3G – Second Rib Nyz Load

4.2.2 Design T9G: Global Approach

Design T9G is for the same structure as was design T3G, but instead of three design variables, nine design variables were used. These design variables are the same as those used for designs B9G and B9GP; instead of constraining each of the panels to a quasi-isotropic configuration, the $\mp 45^\circ$ plies, the 90° plies, and the 0° plies in each panel were allowed to vary independently.

The results for design T9G are presented in Table 4.17. Two buckling constraints were active at the optimal point; the corresponding modes are illustrated in Figures 4.43 and 4.44. Both modes are characterized by skin, spar, and rib buckling along most of the length of the box beam. In comparison to the modes which were active for design T3G, these modes involve the buckling of more of the panels making up the structure. An examination of the active constraint gradients (Table 4.18) reveals there is significant coupling between the skin and spar design variables in both modes. The overall structural weight of design T9G is only 1.6% less than that for design T3G, however. This is in contrast to the bending load case, where the nine design variable design (B9G) was 11.7% lighter than the three design variable design (B3G).

The values of the design variables for designs T3G and T9G are compared in Figure 4.45. Although it is slightly thicker, the skin panel for design T9G is very similar to the quasi-isotropic design obtained for design T3G; it is composed of 53% $\mp 45^\circ$ plies, 22% 90° plies, and 25% 0° plies ([53/22/25]). The spar panel, which is 2% thinner, has fewer $\mp 45^\circ$ plies and more 90° and 0° plies as compared to the quasi-isotropic case (T3G). The rib panel, which is 23% thinner, has fewer 90° plies

Table 4.17: Results – Design Case T9G

Design Case: T9G			
Geometry: 150" x48" x24"			
Rib Spacing: 30.0"			
Loading: Torque			
Active Constraints:			
<i>Buckling Mode</i>	1	2	
Eigenvalue	.9981	1.008	
Description	$\mp 45^\circ$	90°	0°
Skin ply thk (<i>in</i>)	.0543	.0437	.0511
Spar ply thk (<i>in</i>)	.0228	.0594	.0528
Rib ply thk (<i>in</i>)	.0106	.00753	.0155
Weight (<i>lb</i>)	539.8		

and more 0° plies. Note that it was not necessary to impose any ply-percentage constraints on design T9G.

The internal load distribution in each of the component panels is similar to that obtained for design T3G. The only differences which arise are in the magnitudes of the loads; the peak panel loads for design T9G are slightly less than those obtained for design T3G.

4.2.3 Summary of Interaction Effects: Designs T3G and T9G

As was the case for the bending designs, some interaction between the skin and spar panels occurs because of load redistribution. The percentage of the overall torque load carried by the spar panel is affected by the design of the skin panel, and likewise, the percentage of the torque load carried by the skin panel is affected by the design of the spar panel. Because the rib panels transfer load to and from the skin and spar panels, the rib panel loads also depend on the designs of the skin and spar panels.

As with the bending designs, evidence of interaction may also be seen by looking at the active buckling modes and constraint gradients for both design T3G and design T9G. The buckling modes are characterized by the compatible and interactive

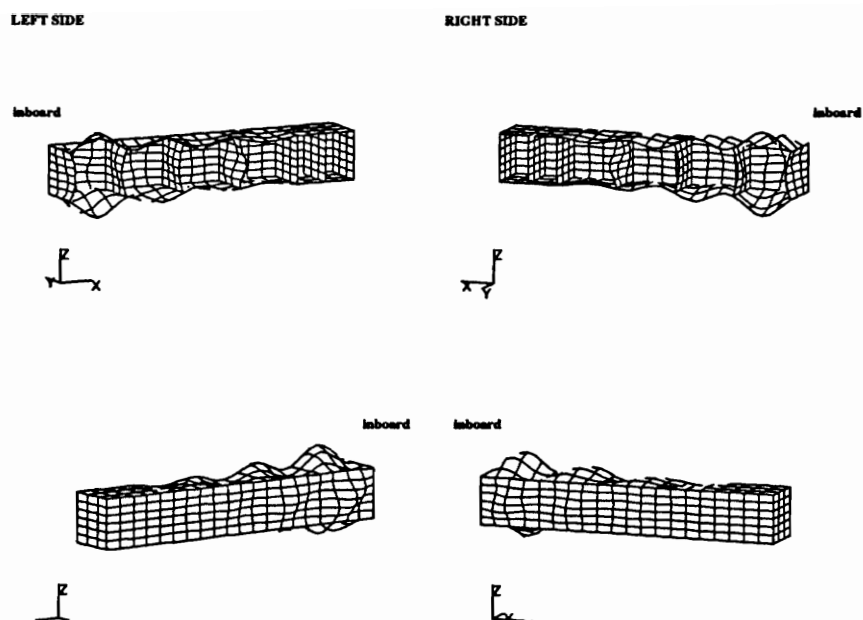


Figure 4.43: Design T9G – Active Buckling Mode 1 ($\lambda = .9981$)

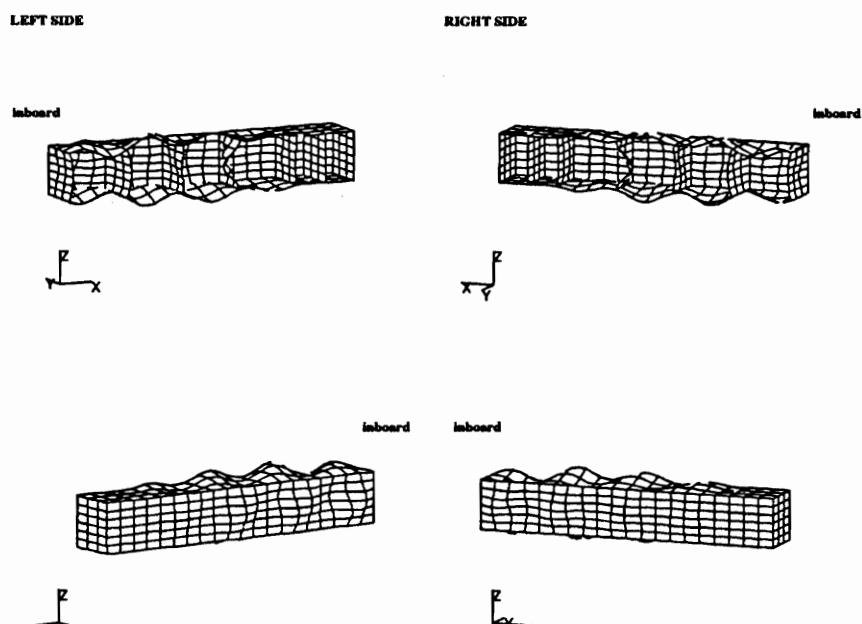


Figure 4.44: Design T9G – Active Buckling Mode 2 ($\lambda = 1.008$)

Table 4.18: Design T9G – Active buckling constraint gradients

DV		Mode 1		Mode 2	
1	t_{sk}^{45}	-10.9	(-1.00)	-10.1	(-.988)
2	t_{sk}^{90}	-5.0	(-.454)	-4.6	(-.447)
3	t_{sk}^0	-5.1	(-.469)	-4.7	(-.461)
4	t_{sp}^{45}	-9.1	(-.835)	-10.3	(-1.00)
5	t_{sp}^{90}	-4.4	(-.400)	-4.9	(-.476)
6	t_{sp}^0	-4.3	(-.390)	-4.8	(-.470)
7	t_{rb}^{45}	-0.4	(-.039)	-0.6	(-.055)
8	t_{rb}^{90}	-0.2	(-.015)	-0.3	(-.027)
9	t_{rb}^0	-0.2	(-.016)	-0.3	(-.028)

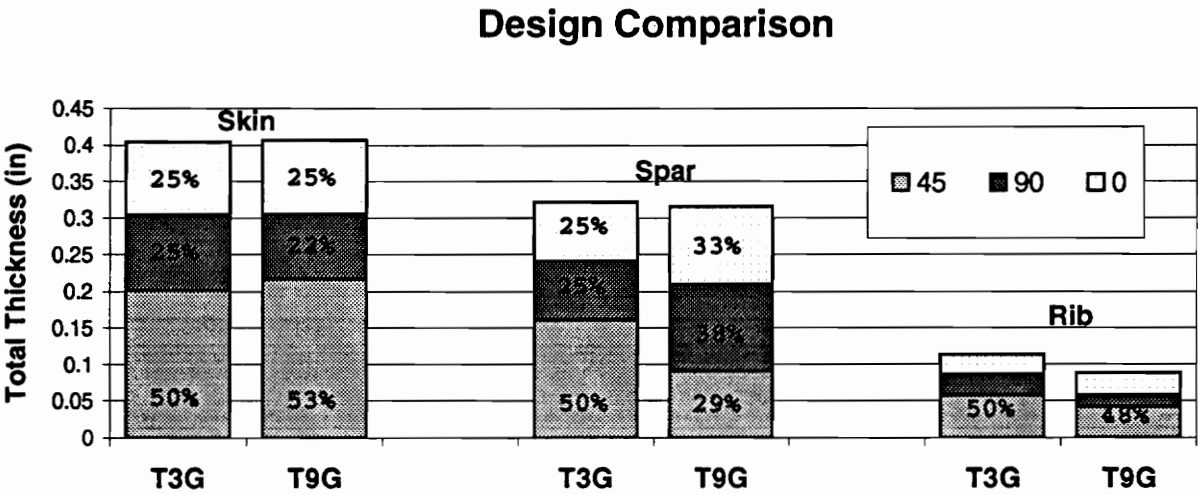


Figure 4.45: Comparison of designs T3G and T9G

buckling of two or more of the sub-component panels, not by the buckling of single, isolated panels. In both designs, the active constraint gradients indicate that there is significant coupling between skin, spar, and/or rib panels.

4.2.4 Designs T3L and T9L: Local Approach

In this section, designs T3G and T9G (which were obtained using a buckling constraint based upon an eigenvalue analysis of the entire structure) are compared to designs T3L and T9L, which were obtained using the local approach. In the local approach, the buckling response of each panel is evaluated separately from the other panels in the structure. This local approach is the same as that described for the bending load case (see Section 4.1.5).

Design T3L

The results of design case T3L are given in Table 4.19, and a graphical comparison between designs T3G and T3L is given in Figure 4.46. Comparing the values of these design variables to those obtained using the global approach, it can be seen that all three design variables are greater than the corresponding T3G design variables. The skin thickness design variable is 3.2% greater than the skin thickness design variable for design T3G. Likewise, the spar and rib thickness design variables are 9.2% and 25.9% greater than their T3G counterparts. The overall structural weight for design T3L is 5.9% greater than the weight of design T3G. These results follow the same trends that were found in the bending load case.

Three buckling constraints are active at the optimal point: the buckling of the upper-inboard skin panel, the buckling of the inboard spar panels, and the buckling of the second rib panel. The constraint gradients for these active buckling modes are given in Table 4.20. In contrast to design T3G, the skin and spar constraints are controlled almost exclusively by their respective design variables and no significant interaction between the design variables occurs. This difference may be clearly seen by comparing the graphical representation of the design space for this case (Figure 4.47) with its counterpart for design T3G (Figure 4.33). The only interaction which occurs is in the rib constraint. This constraint, while dominated by the rib design variable, exhibits a weak interaction with the skin and spar design variables. This interaction occurs as a result of load redistribution as discussed in relation to the second active

Table 4.19: Results – Design Case T3L

Design Case: T3L			
Geometry: 150"x48"x24"			
Rib Spacing: 30.0"			
Loading: Torque			
Active Constraints:			
Buckling Mode*	skin	spar	rib
Description	Ply thickness (<i>in</i>)		
Skin	.0521		
Spar	.0440		
Rib	.0180		
Weight (<i>lb</i>)	581.2		

* local buckling analysis used

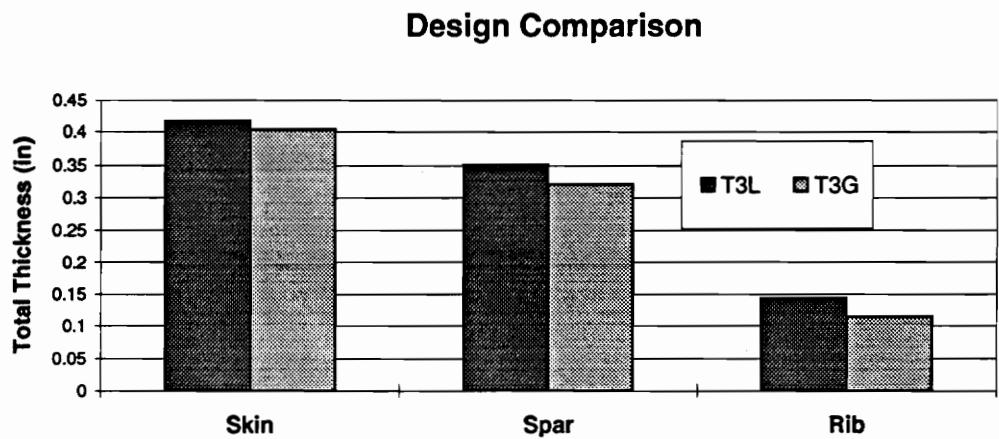


Figure 4.46: Comparison of designs T3G and T3L

Table 4.20: Design T3L – Active buckling constraint gradients

DV		Skin mode		Spar Mode		Rib Mode	
1	t_{sk}	-60.6	(-1.00)	-6.8	(-.096)	-46.1	(-.265)
2	t_{sp}	+0.2	(+.004)	-70.7	(-1.00)	+44.8	(+.258)
3	t_{rb}	-0.9	(-.016)	+1.3	(+.018)	-173.8	(-1.00)

buckling mode for design T3G. Like several of the bending designs, design T3L is more conservative than its global counterpart. When design T3L is analyzed using the global approach, the lowest eigenvalue is 1.13.

In order to determine the sensitivity of these results to the manner in which the individual panel loads were extracted from the global model, several other designs were obtained using the local approach. In each case, different sampling points in the global model were used to obtain the individual panel loads. All of the resulting designs were from 3% to 10% heavier than design T3G. The 3% number represents the case where the smallest loads on the corresponding panel in the global model were used, and 10% represents the case where the largest loads were used.

The actual in-plane load distribution (global model) in the upper skin panel is shown for design T3L in figures 4.48–4.50. In the spanwise (x) direction, the load is compressive at one chordwise edge of the panel and tensile at the opposite edge. This load is generated because the beam is restrained from warping out of plane at the root. This load was approximated for the purpose of the simplified buckling analysis by a symmetric linearly varying load which varied from -1450 *lb/in* to +1450 *lb/in*. In the chordwise direction (y), there are localized tensile and compressive loads at the root. As these loads relatively small and local, they were not included the simplified buckling analysis. The shear load is nearly uniform over the entire panel. The constant value used for the simplified analysis was 3670 *lb/in*.

Design T9L

The results for the nine design variable case (T9L) are presented in Table 4.21 and a comparison is made to design T9G in Figure 4.51. As with design T3L, design T9L is heavier than its global counterpart, T9G, with a difference in this case of 3.4%.

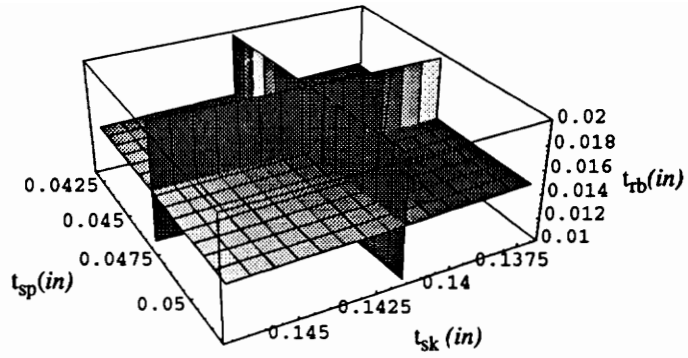


Figure 4.47: Design T3L – Linear Approximation to Design Space

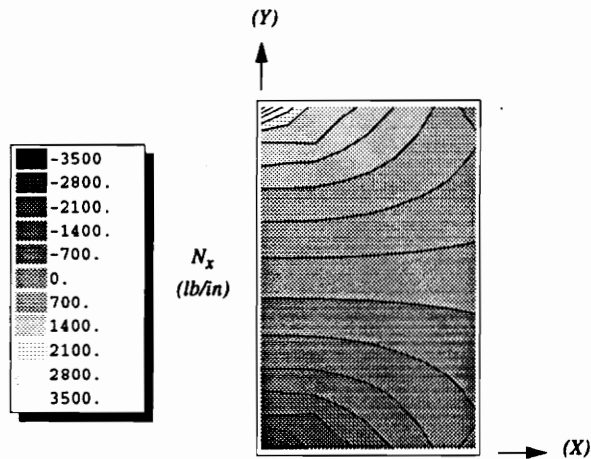


Figure 4.48: Design T3L – Upper Skin Chordwise (N_x) Load

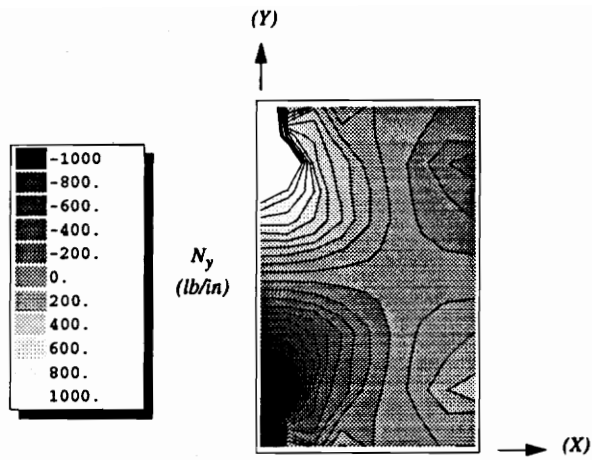


Figure 4.49: Design T3L – Upper Skin Spanwise (N_y) Load

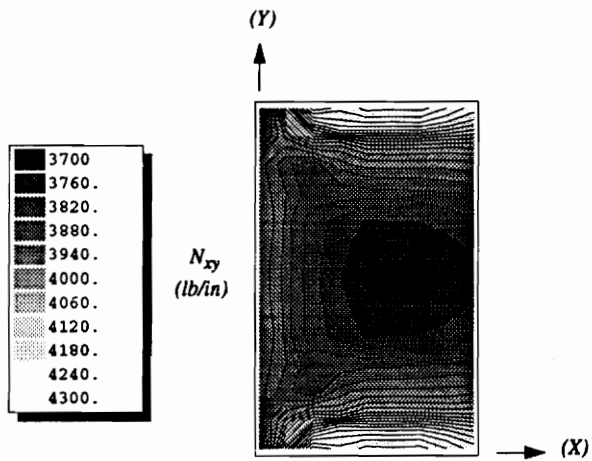


Figure 4.50: Design T3L – Upper Skin Shear (N_{xy}) Load

Table 4.21: Results — Design Case T9L

Design Case: T9L			
Geometry: 150"x48"x24"			
Rib Spacing: 30.0"			
Loading: Torque			
Active Constraints:			
<i>Buckling Mode</i> [†]	skin	spar	rib
Description	$\mp 45^\circ$	90°	0°
Skin ply thk (<i>in</i>)	.0657	.0338	.0397
Spar ply thk (<i>in</i>)	.0247	.0661	.0550
Rib ply thk (<i>in</i>)	.0119	.00862	.0199
Weight (<i>lb</i>)	558.1		

[†] simplified buckling analysis used

In this case, the primary loads on all three panel types are shear loads (there are no large out of plane loads at the root for this design), and the local approach results in designs that are all 3-4% heavier than the global designs.

The skin panel in design T9L is only 0.8% heavier than its T9G counterpart, but the ply distributions are different. Using the global approach (T9G), the skin design was composed of 52% $\mp 45^\circ$ plies, 22% 90° plies, and 26% 0° plies ([52/22/26]). The local design (T9L), with a ply distribution of [64/17/19], has more $\mp 45^\circ$ plies and fewer 90° and 0° plies. This result indicates again (see section 4.1.5) that an optimal design obtained using the local approach may be different from that obtained using the global approach, not just in the overall panel thickness, but in the panel composition as well.

The T9L spar panel is 8.0% thicker than the T9G spar panel, and the T9L rib panel is 18.4% thicker than the T9G rib panel. The two spar panels have approximately the same ply distributions, while the local rib panel has slightly more 0° plies as compared to the global design.

The active buckling constraint gradients for design T9L are given in Table 4.22. In comparing these constraint gradients with those obtained for design T9G, it is noted

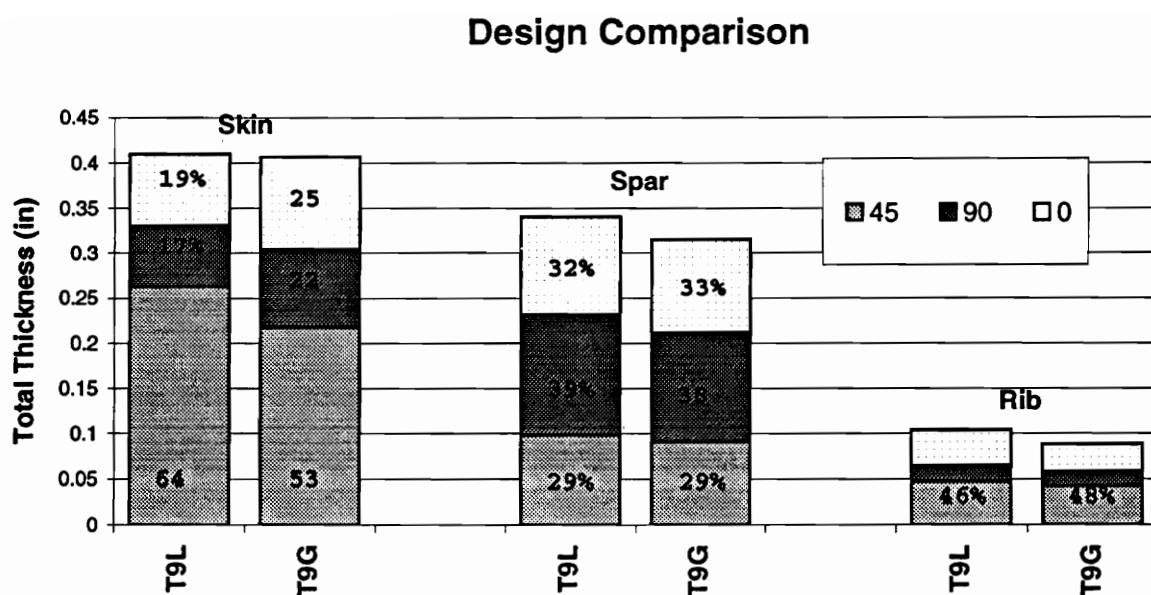


Figure 4.51: Comparison of designs T9G and T9L

that there is no interaction between the skin, spar, and rib design variables in either the skin or spar buckling modes. In the rib mode, there is weak coupling between the $\mp 45^\circ$ plies in the spar panel and the rib design variables. As with the other torque designs, this coupling occurs as a result of load distribution in the structure. When design T9L is analyzed using the global approach, the lowest eigenvalue is 1.08. This result indicates that this design is slightly conservative compared to design T9G.

4.3 Combined Bending and Torque Loads

In this section, designs are presented that were obtained subject to linear combinations of the previous bending and torque load cases. The first two designs, C3G and C9GP, were obtained by applying both the bending and torque load cases simultaneously. Design C3G-1 was obtained by adding half the torque loads to the bending case, and design C3G-2 was obtained by adding half the bending loads to the torque load case.

Table 4.22: Design T9L – Active buckling constraint gradients

DV		Skin mode		Spar mode		Rib mode	
1	t_{sk}^{45}	-35.6	(-1.00)	-1.4	(-.032)	-4.2	(-.035)
2	t_{sk}^{90}	-16.6	(-.465)	-0.1	(-.003)	-1.7	(-.014)
3	t_{sk}^0	-17.0	(-.477)	-0.2	(-.004)	-2.4	(-.020)
4	t_{sp}^{45}	-0.3	(-.009)	-43.0	(-1.00)	+24.1	(+.201)
5	t_{sp}^{90}	-0.0	(-.001)	-20.3	(-.471)	+1.9	(+.016)
6	t_{sp}^0	-0.0	(-.001)	-19.8	(-.460)	+1.7	(+.015)
7	t_{rb}^{45}	+0.1	(+.002)	-0.0	(-.000)	-120.0	(-1.00)
8	t_{rb}^{90}	+0.0	(+.000)	-0.0	(-.000)	-55.5	(-.463)
9	t_{rb}^0	+0.0	(-.000)	-0.0	(-.000)	-66.0	(-.550)

4.3.1 Designs C3G and C9GP: Global Approach

In this section, designs are presented that were obtained by adding the previous bending and torque load cases. The left spar was loaded by a 300,000 *in-lb* upward load at its outboard end, and the right spar was loaded by a 100,000 *in-lb* downward load at its outboard end. Design C3G is described by the usual three design variables, and design C9GP with the usual nine design variables. Design C9GP was obtained subject to ply-percentage constraints imposed on each of the panel types.

Design C3G

The results for design C3G are presented in Table 4.23, and the two active buckling modes are shown in Figures 4.52 and 4.53. The first buckling mode is similar to those modes shown previously for the bending load case and is characterized by the buckling of skin, spar, and rib panels at the inboard end of the structure. The second mode is a local rib mode and resembles modes shown previously for both bending and torque load cases. The constraint gradients (Table 4.24) indicate moderate coupling between the skin and spar design variables in mode 1, and between the spar and rib design variables in mode 2. This may be visualized in Figure 4.54, where the approximation to the design space is plotted. This plot resembles that obtained for the bending load case (design B3G).

Table 4.23: Results – Design Case C3G

Design Case: C3G			
Geometry: 150"x48"x24"			
Rib Spacing: 30.0"			
Loading: Bending/Torque			
Active Constraints:			
<i>Buckling Mode</i>	1	2	
Eigenvalue	.9984	1.008	
Description	Ply thickness (in)		
Skin	.136		
Spar	.0487		
Rib	.0128		
Weight (lb)	1136.0		

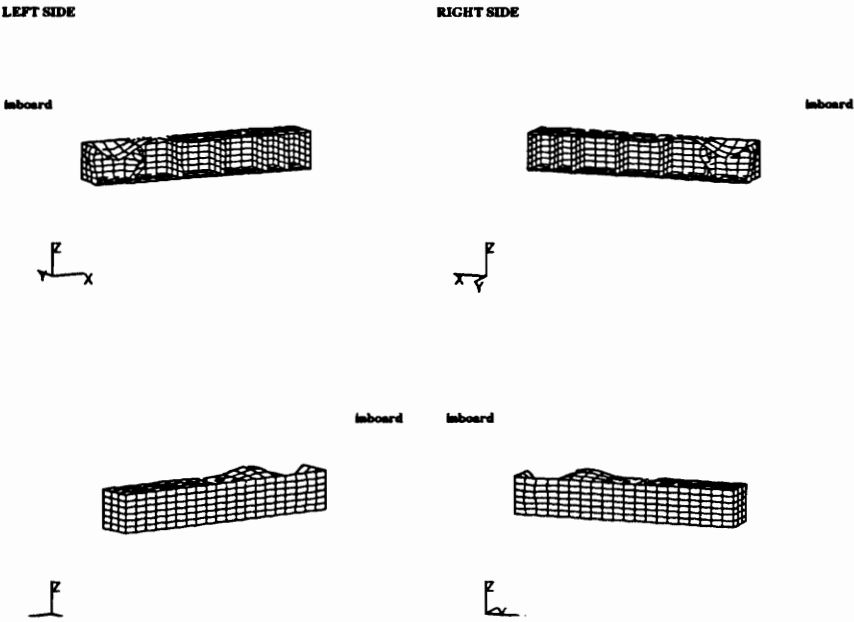


Figure 4.52: Design C3G – Active buckling mode 1 ($\lambda=.9984$)

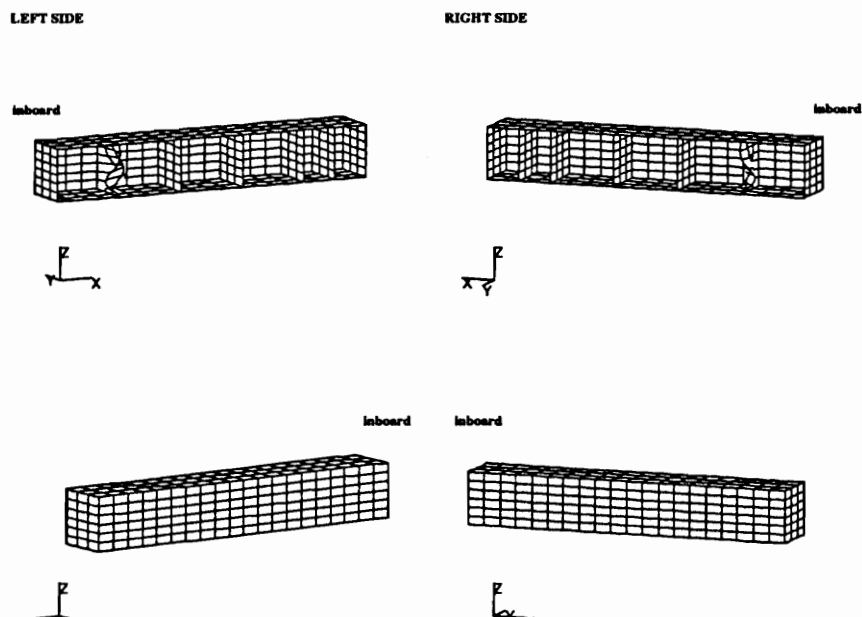


Figure 4.53: Design C3G – Active buckling mode 2 ($\lambda=1.008$)

Table 4.24: Design C3G – Active buckling constraint gradients

DV		Mode 1		Mode 2	
1	t_{sk}	-11.5	(-1.00)	+1.2	(+.012)
2	t_{sp}	-3.2	(-.281)	-14.8	(-.146)
3	t_{rb}	-0.5	(-.044)	-101.1	(-1.00)

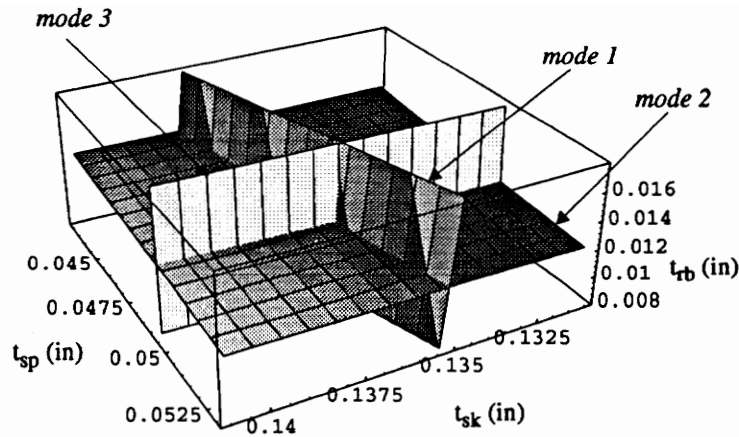


Figure 4.54: Design C3G – Linear Approximation to Design Space

This design is 15.5% heavier than design B3G (bending only) and 129.1% heavier than design T3G (torque only). The values of the design variables for these three designs are compared in Figure 4.55. The spar thickness is approximately 20% greater for the combined loading case as compared to either the torque or bending designs. The skin thickness is approximately the same as that found for the bending design (0.7% less), and much greater (170%) than that found for the torque design. The rib thickness is 8% greater than that found for the bending design and 11% less than that found for the torque design.

The panel internal loads for this design are shown in Figures 4.56–4.67. The upper skin panel loads are shown in Figures 4.56–4.58, the left spar panel loads are shown in Figures 4.59–4.61, the right spar panel loads are shown in Figures 4.62–4.64, and the second rib loads are shown in Figures 4.65–4.67. In all cases, the figures show that portion of the box beam which extends 60" from the root.

The primary loads in the skin panel are a compressive N_x load and a shear load. The axial load, which is biased towards the right side of the box beam, varies from 28,000–48,000 lb/in at the root. The shear load varies from 9000 lb/in at the left edge of the panel down to 20 lb/in at the right edge of the panel. As with the bending load case, there is also an N_y load at the root which has a maximum value near 13,000 lb/in .

Both left and right spar panels are loaded by axial bending loads and shear loads. In the left spar panel, the axial (N_x) loads peak at $\mp 15,000$ lb/in at the top and

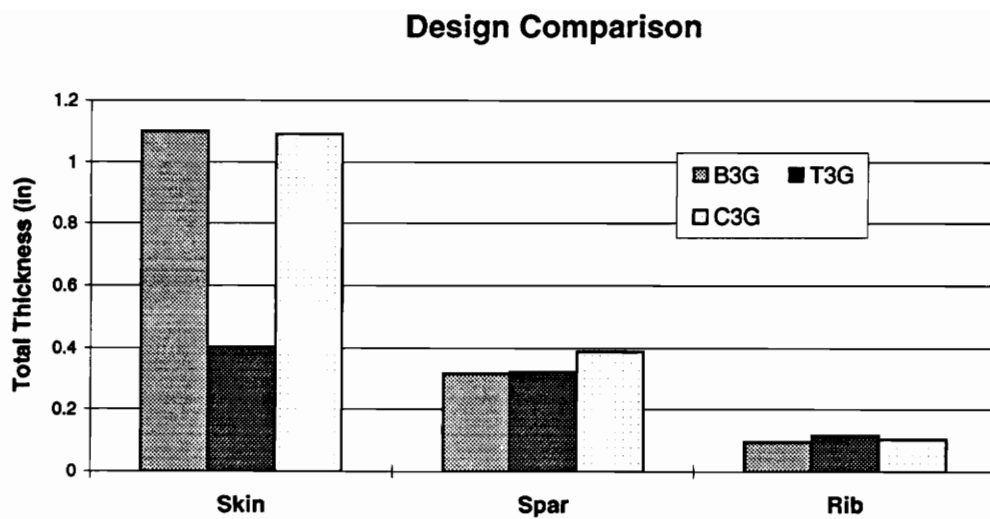


Figure 4.55: Comparison of designs B3G – C3G

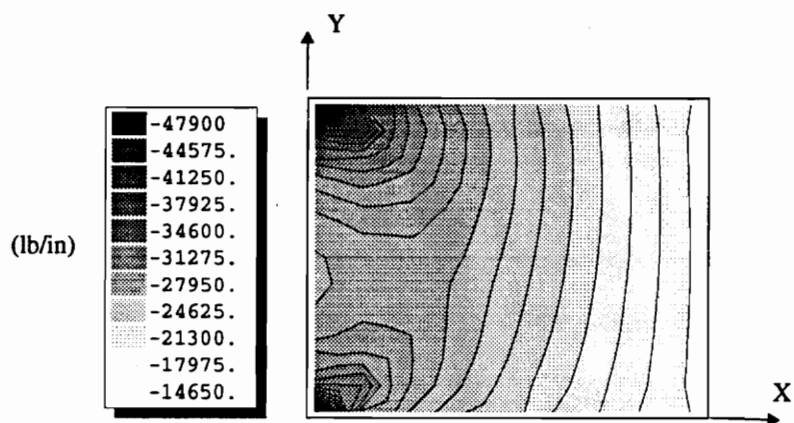


Figure 4.56: Design C3G – Upper Skin Nx Load

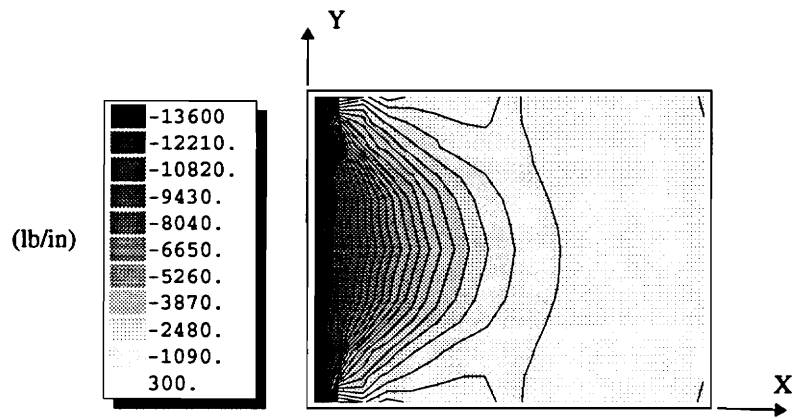


Figure 4.57: Design C3G – Upper Skin Ny Load

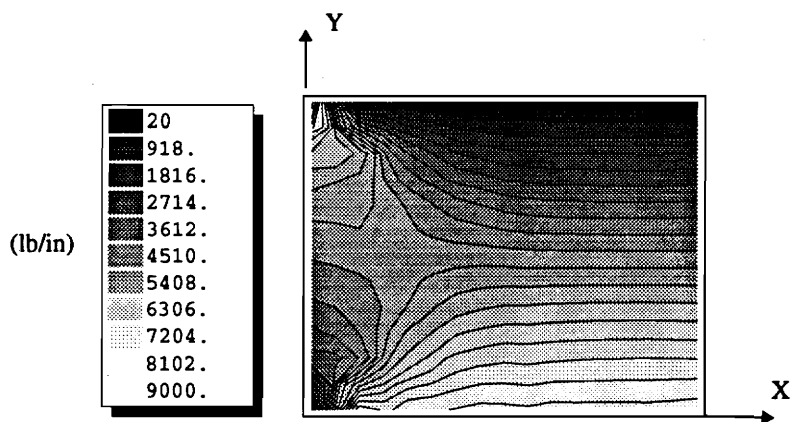


Figure 4.58: Design C3G – Upper Skin Nxy Load

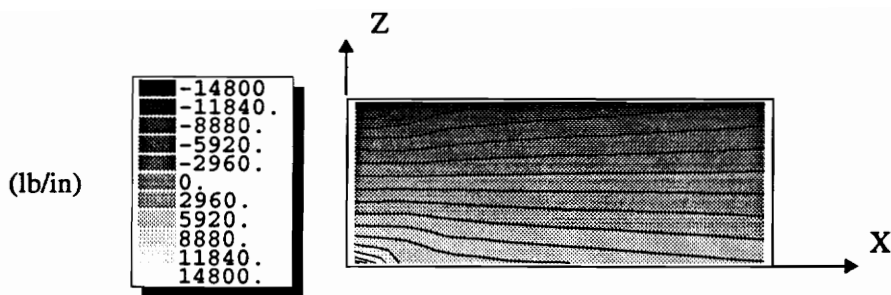


Figure 4.59: Design C3G – Left Spar Nx Load

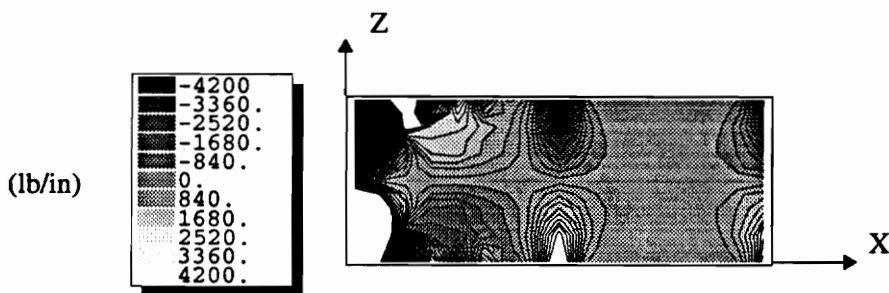


Figure 4.60: Design C3G – Left Spar Nz Load

bottom edges of the panel respectively. The shear load is approximately 8000 lb/in . In the right spar panel, the axial bending loads are slightly higher, at $\pm 17,000 \text{ lb/in}$, while the shear loads are much lower, at approximately 200 lb/in . In both cases, there are smaller local loads induced in the spar panels at the rib-spar interfaces. These loads are caused by the Poisson interaction between the spar and rib panels as discussed in Section 4.1.1.

The second rib panel is loaded in the y -direction by a tensile load on the top edge and a compressive load along the bottom edge. These loads are a result of the Poisson interaction between the skin and rib panels. This same interaction between the spar and rib panels causes vertical loads to be induced in the rib panel at the spar-rib interfaces. As in the torque case, there is also an overall shear load in the panel, which for this particular panel is approximately 45 lb/in .

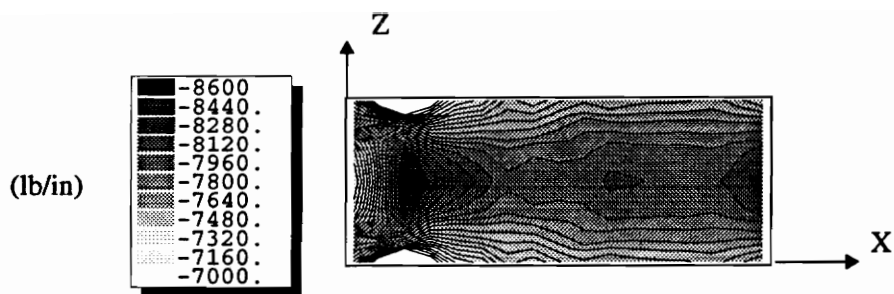


Figure 4.61: Design C3G – Left Spar Nxz Load

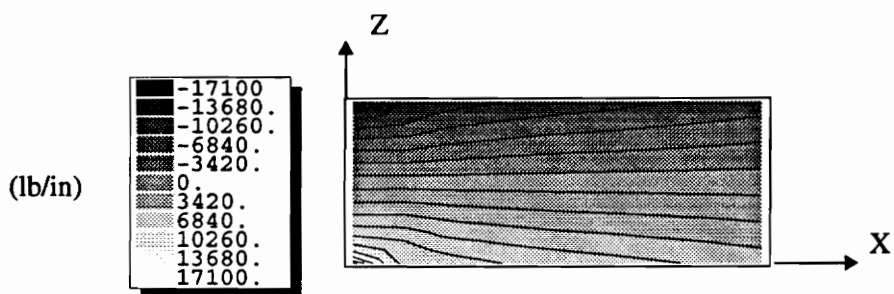


Figure 4.62: Design C3G – Right Spar Nx Load

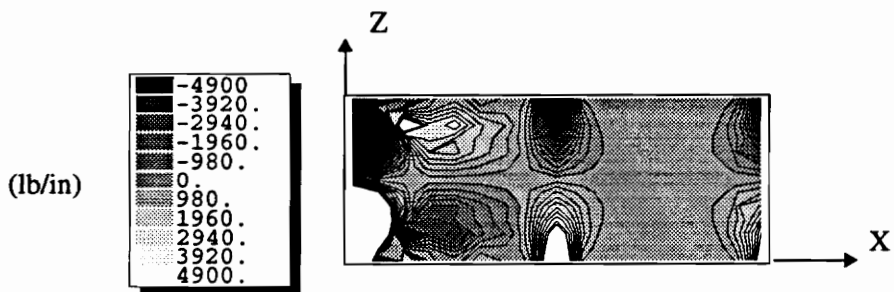


Figure 4.63: Design C3G – Right Spar Nz Load

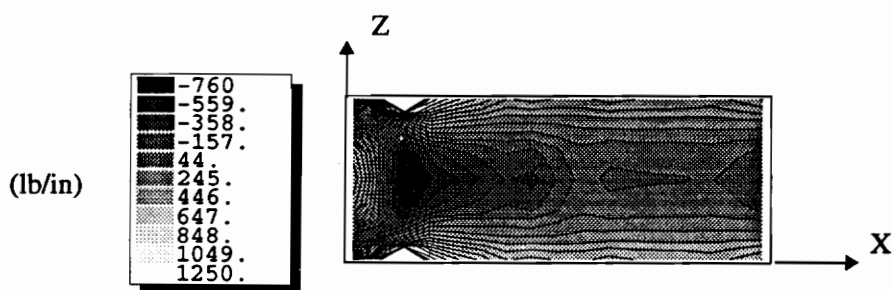


Figure 4.64: Design C3G – Right Spar Nxz Load

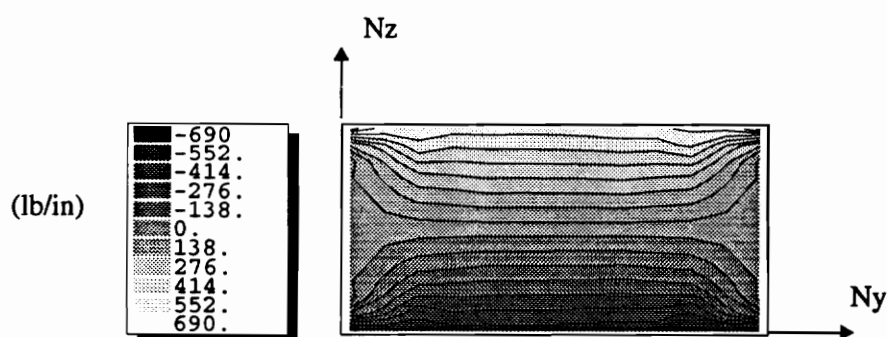


Figure 4.65: Design C3G – Second Rib Ny Load

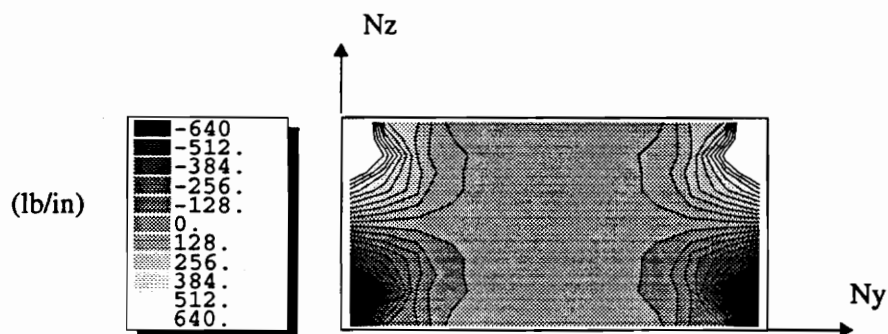


Figure 4.66: Design C3G – Second Rib Nz Load

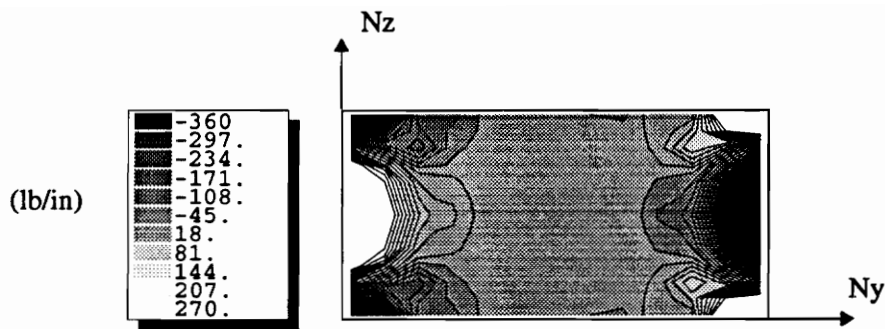


Figure 4.67: Design C3G – Second Rib Nyx Load

Design C9GP

The results for the nine design variable case, C9GP, are presented in Table 4.25. Two buckling constraints were active at the optimum point along with a ply-percentage constraint in the skin panel (Figures 4.68 and 4.69). In the first mode, the skin and rib panels buckle together, and in the second mode, the second rib panel buckles in isolation. The constraint gradients for this case (Table 4.26) indicate significant coupling between skin, spar, and rib design variables for the first mode. In the second mode, there is coupling between the rib design variable and the skin and spar design variables. This may be explained by considering load redistribution effects as explained in Section 4.2.1. Design C9GP is 15.5% lighter than design C3G (three design variables), 0.6% heavier than design B3G (bending only), and 96.7% heavier than design T9G (torque only).

The design variables for designs C3G and C9GP are compared in Figure 4.70. The C9GP skin panel is 2.8% thinner than the C3G skin panel and is composed of 42% $\mp 45^\circ$ plies, 8% 90° plies, and 50% 0° (ply-percentage constraint) plies: [42/8/50]. As with the bending designs, the optimizer has increased the 0° plies as much as possible, while making up most of the difference with the $\mp 45^\circ$ plies. The C9GP spar panel is marginally (0.6%) thicker than its C3G counterpart and has a ply distribution of [37/16/47]. This is similar to the distribution found for the corresponding *bending* design (B9GP): [35/24/41]. The C9GP rib panel is 6.9% thicker than its C3G counterpart and has a ply distribution of [48/13/40]. This distribution is similar to that found for the corresponding *torque* design (T9G): [48/17/35]. The panel loads for this case are very similar to those obtained for design C3G.

Table 4.25: Results – Design Case C9GP

Design Case: C9GP			
Geometry: 150"x48"x24"			
Rib Spacing: 30.0"			
Loading: Bending/Torque			
Active Constraints:			
<i>Ply Percent</i>	Skin		
<i>Buckling Mode</i>	1	2	
Eigenvalue	1.003	1.008	
Description	$\mp 45^\circ$	90°	0°
Skin ply thk (<i>in</i>)	.113	.0411	.263
Spar ply thk (<i>in</i>)	.0363	.0310	.0923
Rib ply thk (<i>in</i>)	.0113	.00604*	.0188
Weight (<i>lb</i>)	1109.1		

* lower bound

4.3.2 Summary of Interaction Effects: Designs C3G and C9GP

The same interaction effects that were discussed in conjunction with the bending and torque cases are active here as well (see Sections 4.1.4 and 4.2.3). In particular, several of the active buckling modes are characterized by the interactive buckling of two or more subcomponent panels. The constraint gradients indicate that there is significant design variable coupling in these modes.

4.3.3 Designs C3L and C9LP: Local Approach

As with the bending and torque loading cases, the designs obtained using the local approach are heavier than those obtained using the global approach. Design C3L is 7.3% heavier than design C3G, and design C9L is 7.1% heavier than design C9G. These designs are presented in Tables 4.44 and 4.28 and comparisons are made to the global designs in Figures 4.71 and 4.72.

All three C3L panel types are thicker than their C3G counterparts. The skin panel is 4% thicker, the spar panel is 15% thicker, and the rib panel is 59% thicker. As for

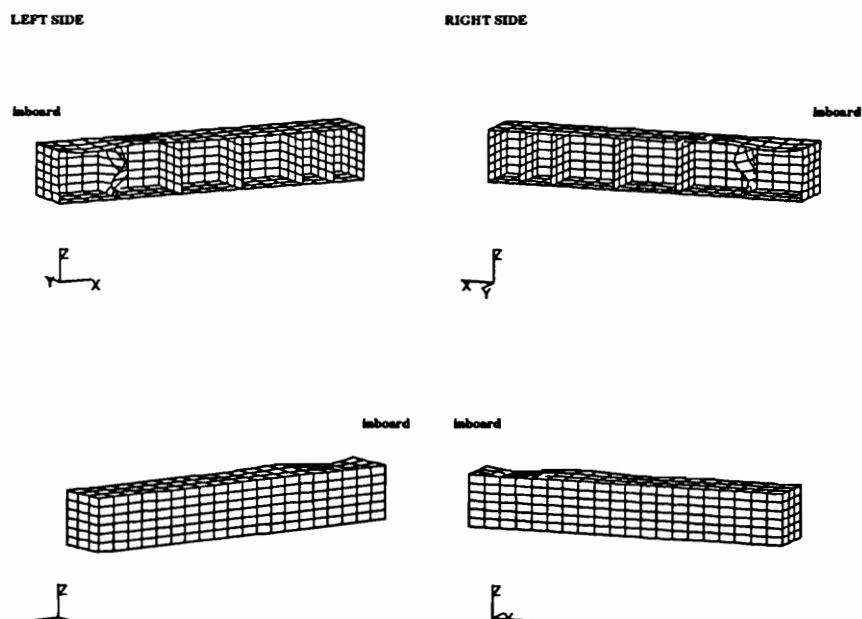


Figure 4.68: Design C9GP – Active Buckling Mode 1 ($\lambda = 1.003$)

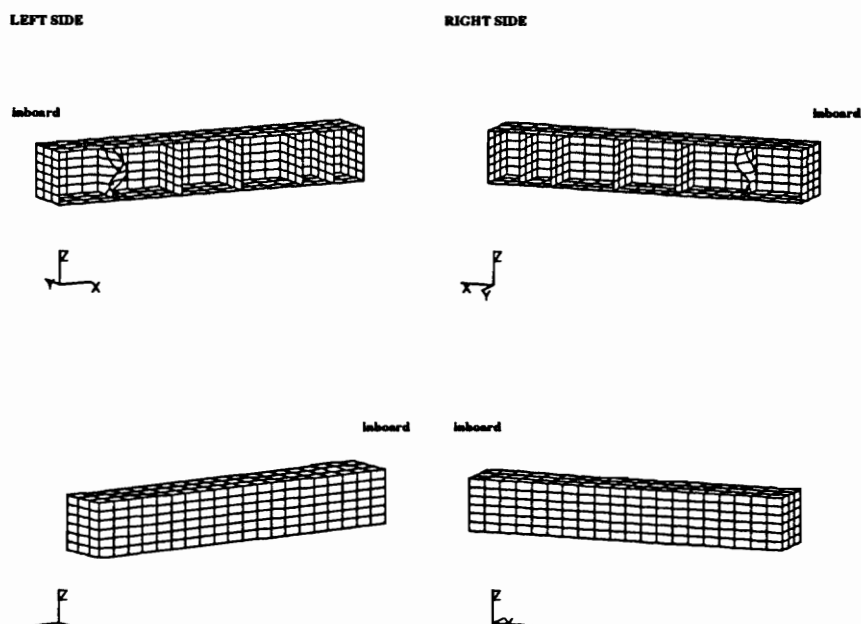


Figure 4.69: Design C9GP – Active Buckling Mode 2 ($\lambda = 1.008$)

Table 4.26: Design C9GP – Active buckling constraint gradients

DV		Mode 1		Mode 2	
1	t_{sk}^{45}	-4.0	(-.578)	-6.1	(+.137)
2	t_{sk}^{90}	-2.2	(-.314)	-1.1	(-.025)
3	t_{sk}^0	-2.7	(-.394)	-0.6	(-.014)
4	t_{sp}^{45}	-5.0	(-.731)	-23.6	(-.533)
5	t_{sp}^{90}	-1.1	(-.158)	-2.5	(-.057)
6	t_{sp}^0	-1.2	(-.176)	-2.6	(-.059)
7	t_{rb}^{45}	-6.9	(-1.00)	-44.3	(-1.00)
8	t_{rb}^{90}	-2.3	(-.330)	-14.5	(-.328)
9	t_{rb}^0	-4.8	(-.693)	-30.8	(-.695)

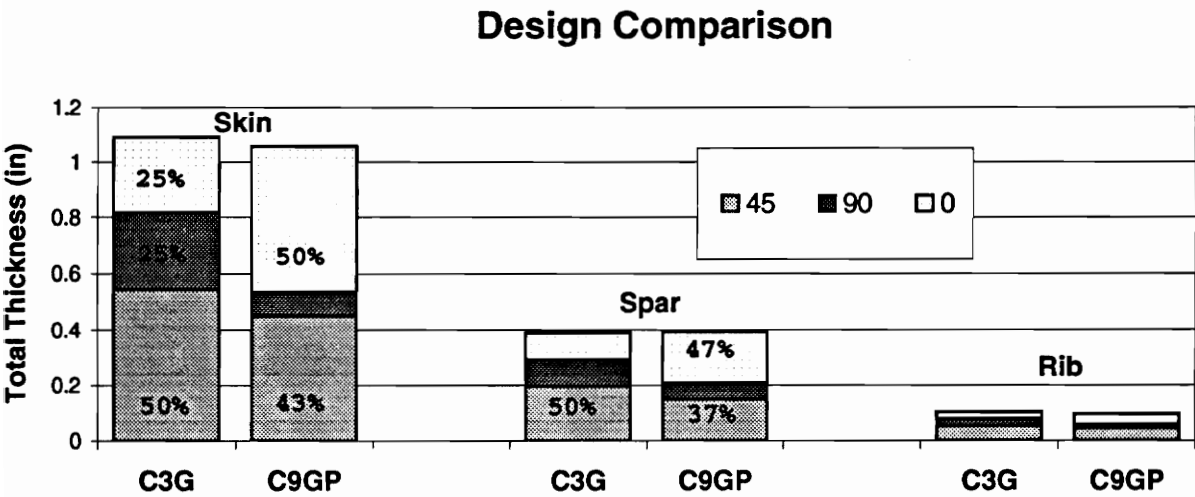


Figure 4.70: Comparison of designs C3G and C9GP

Table 4.27: Results — Design Case C3L

Design Case: C3L			
Geometry: 150"x48"x24"			
Rib Spacing: 30.0"			
Loading: Bending/Torque			
Active Constraints:			
<i>Buckling Mode*</i>	skin	spar	rib
Description	Ply thickness (<i>in</i>)		
Skin	.142		
Spar	.0560		
Rib	.0203		
Weight (<i>lb</i>)	1219.4		

* local buckling analysis used

the nine design variable designs, the C9LP skin panel is 5% thicker, the C9LP spar panel is 15% thicker, and the C9LP rib panel is 28% thicker compared to their C9GP counterparts. The ply distribution in the skin panel in this case is approximately the same for both designs. In the spar panel, the percentage of $\mp 45^\circ$ plies increases in going from the C9GP to C9LP, and in the rib panel, the percentage of 0° plies increases.

From the constraint gradients (Figures 4.29 and 4.30) it may be seen that, in comparison to the global designs C3G and C9GP, the design variable coupling in the interactive mode is weaker. Some coupling occurs in the rib mode because of load redistribution effects (see Section 4.2.1). These results follow the same trends that were obtained for the previous load cases, namely that the local designs are from 5-8% heavier than their global counterparts and exhibit a lesser amount of design variable coupling.

It should be noted that the local panel loads are more complex for this load case as compared to the previous bending and torque load cases. As a result, it is more difficult to properly apply the local approach (some of the panel loads cannot be accurately represented given the simplifications made in the local approach). This

Table 4.28: Results — Design Case C9LP

Design Case: C9LP			
Geometry: 150"x48"x24"			
Rib Spacing: 30.0"			
Loading: Bending/Torque			
Active Constraints:			
<i>Ply Percent</i>	Skin		
<i>Buckling Mode</i> [†]	skin	spar	rib
Description	±45°	90°	0°
Skin ply thk (<i>in</i>)	.125	.0308	.277
Spar ply thk (<i>in</i>)	.0378	.0515	.0985
Rib ply thk (<i>in</i>)	.0125	.006*	.0298
Weight (<i>lb</i>)	1188.3		

* lower bound

[†] local buckling analysis used

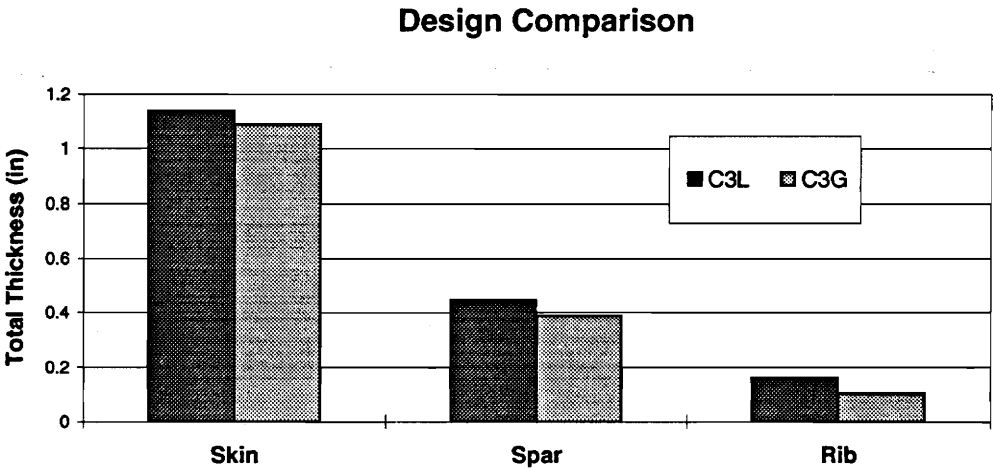


Figure 4.71: Comparison of designs C3G and C3L

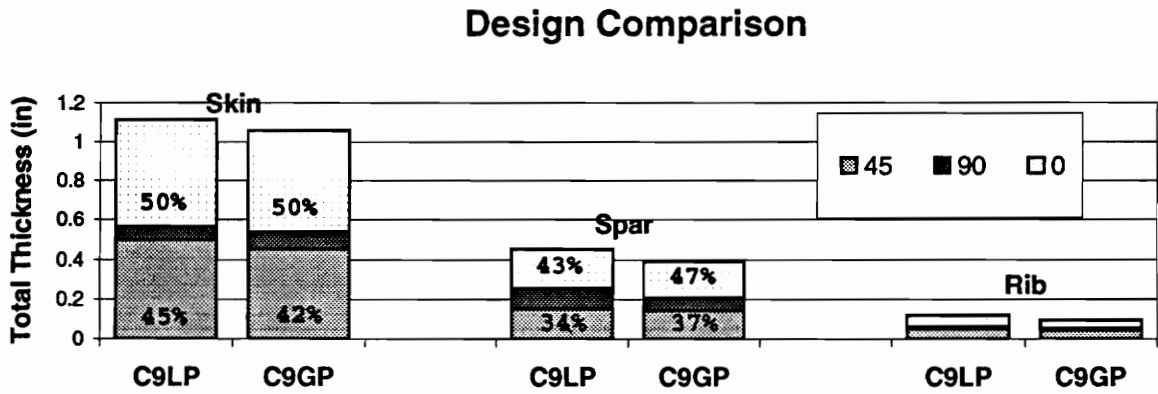


Figure 4.72: Comparison of designs C9GP and C9LP

Table 4.29: Design C3L – Active buckling constraint gradients

DV		Skin mode	Spar Mode	Rib Mode
1	t_{sk}	-12.0 (-1.00)	-2.1 (-.041)	-11.0 (-.116)
2	t_{sp}	-1.7 (0.138)	-50.1 (-1.00)	+17.6 (+.185)
3	t_{rb}	-0.0 (-.000)	-0.2 (-.013)	-95.0 (-1.00)

Table 4.30: Design C9L – Active buckling constraint gradients

DV		Skin mode		Spar mode		Rib mode	
1	t_{sk}^{45}	-5.7	(-1.00)	-1.2	(-.045)	-5.6	(-.104)
2	t_{sk}^{90}	-2.6	(-.455)	-0.2	(-.009)	-6.6	(-.123)
3	t_{sk}^0	-3.2	(-.557)	-0.6	(-.022)	-4.0	(-.075)
4	t_{sp}^{45}	-1.7	(-.292)	-26.2	(-1.00)	+31.0	(+.578)
5	t_{sp}^{90}	-0.2	(-.032)	-13.2	(-.503)	+0.8	(+.014)
6	t_{sp}^0	-0.5	(-.081)	-11.4	(-.435)	+2.3	(+.043)
7	t_{rb}^{45}	+0.0	(+.005)	-0.4	(-.014)	-53.5	(-1.00)
8	t_{rb}^{90}	+0.0	(+.003)	-0.1	(-.003)	+1.3	(+.024)
9	t_{rb}^0	+0.0	(+.000)	-0.0	(-.001)	-36.4	(-.680)

points out a limitation of the local approach, and suggests that the results presented in this section should be treated with caution.

4.3.4 Designs C3G-1 and C3G-2: Global Approach

In this section, two additional designs are presented. Design C3G-1 was obtained subject to a linear combination of half the torque load case and the entire bending load case, while design C3G-2 was obtained subject to half the bending load case and the entire torque load case.

Results for these two cases are presented in Tables 4.31 and 4.32, and their design variables are compared to those for design C3G in Figure 4.73. The C3G-1 skin thickness is approximately the same (+0.5%) as that for design C3G, whereas the C3G-2 skin panel is 21.1% thinner. The spar panels for both designs C3G-1 and C3G-2 are approximately 10% thinner than that for design C3G. The C3G-2 rib panel is 17.0% thinner than its C3G counterpart, and the C3G-1 rib panel is 3.6% thinner.

The results indicate that the skin thickness is primarily determined by the bending loads for the range of loads explored here. The rib thickness is most sensitive to the torque loads, while the spar thickness appears to be equally sensitive to both load cases (both cases induce significant shear loads in the spars).

Table 4.31: Results – Design Case C3G-1

Design Case: C3G-1			
Geometry: 150"x48"x24"			
Rib Spacing: 30.0"			
Loading: Bending/Torque			
Active Constraints:			
<i>Buckling Mode</i>	1	2	
Eigenvalue	1.004	1.005	
Description	Ply thickness (<i>in</i>)		
Skin	.137		
Spar	.0441		
Rib	.0123		
Weight (<i>lb</i>)	1113.7		

Table 4.32: Results – Design Case C3G-2

Design Case: C3G-2			
Geometry: 150"x48"x24"			
Rib Spacing: 30.0"			
Loading: Bending/Torque			
Active Constraints:			
<i>Buckling Mode</i>	1	2	
Eigenvalue	.9985	1.004	
Description	Ply thickness (<i>in</i>)		
Skin	.108		
Spar	.0436		
Rib	.0106		
Weight (<i>lb</i>)	924.4		

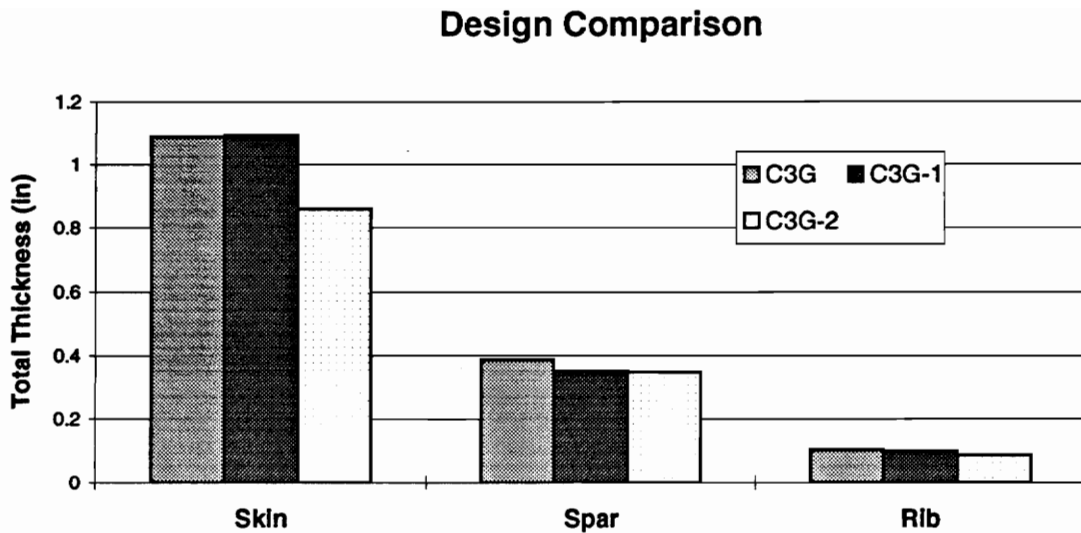


Figure 4.73: Comparison of designs C3G, C3G-1, and C3G-2

4.4 Smeared Stiffener Approach

Up until this point, each of the box beam panels has been modelled as a flat plate. In a “real” structure, such as a wingbox, many of these panels would, of course, be stiffened. Stiffeners would be particularly advantageous on the skin panel for the bending load cases(s), where high spanwise axial and bending stiffness is required. In order to meet this requirement, each of the bending designs presented thus far has had a thick axially stiff skin panel.

In order to assess the effect of a stiffened skin panel on the design and response of the current box-beam, several design runs were made utilizing the *smeared stiffener* approach. This approach, as implemented here, entails the introduction of new design variable types describing the smeared blade stiffener height, spacing, and ply thicknesses. The blade stiffeners described by these new design variables are then mathematically “smeared” in to the base laminate describing the skin panel. The resulting “smeared” panel then behaves *globally* like a stiffened panel. The complete implementation of this approach also requires local buckling constraints to be imposed on the skin panel segments between the smeared stiffeners. This entire procedure is

described in detail in Chapter 2.

In this section, several designs are presented which were obtained using five design variables. The first three design variables are the same as those used in the previous three design variable cases: the first design variable describes the thickness of each skin ply (base laminate), the second design variable describes the thickness of each spar ply, and the third design variable describes the thickness of each rib ply. The fourth design variable describes the thickness of each ply making up the skin stiffeners, and the fifth design variable describes the height of each skin stiffener.

For each of the designs presented here, the stiffener spacing was assumed to be 6.00 in, and the smeared stiffeners were assumed to have a stacking sequence of $(\pm 45/0)_s$, where the 0° plies run along the length of the stiffener. An upper limit of 3.00 in was arbitrarily imposed on the stiffener height design variable.

Design B5GS

The first design, B5GS, is presented in Table 4.33. This design was obtained for the bending load case and is the smeared stiffener analog to design B3G. The first thing to notice is that there is a 47% weight savings over the unstiffened case. The skin laminate was reduced from a total thickness of 1.098 in (unstiffened) to a total thickness of 0.341 in (stiffened). The eight stiffeners in the latter case were each 0.131 in thick and 3.00 in high.

Both the spar and rib laminates increased their thickness in going from the unstiffened to the stiffened case. The spar laminate increased by 29.1% and the rib laminate increased by 53%. These changes are a result of load redistribution in the structure that occurred as the skin panel design changed. It should be remembered that both the skin and spar panels were remained unstiffened in this case; smeared stiffeners were added to the skin panel only. If smeared stiffeners were added to all of the panels (a possible focus of future work), this load redistribution may not occur to the extent that it does here.

Five buckling constraints were active at the optimum point and are shown in Figures 4.74 through 4.78. In addition to these overall buckling constraints, the local buckling constraint on the skin segments between the stiffeners was active as well. Most of the overall buckling modes are characterized by the interactive buckling of one or more subcomponent panels; the one exception is mode 3, which is a local rib buckling mode. As in the unstiffened bending case(s), the constraint gradients

(Figure 4.34) indicate that there is significant coupling between skin and spar design variables in these modes. The stiffener height derivative indicates the percentage change in the constraint value with respect to a variation of 0.10 *in* in the stiffener height.

Design T5GS

The smeared stiffener design for the torque load case, T5GS, is given in Table 4.35. This design is 28% lighter than its unstiffened counterpart, T3G. As with the previous case, most of the weight savings comes from the reduction of the skin panel thickness. The unstiffened panel (T3G) was 0.404 *in* thick, while the stiffened panel is 0.148 *in* thick. The eight stiffeners in this case are each 0.039 *in* thick and 3.00 *in* high. As in the bending case, both the spar and rib panels in the stiffened case are thicker than their T3G counterparts. In this case, the spar panel is 14.4% thicker, and the rib panel is 60.5% thicker.

Five buckling modes were active at the optimal point and are given in Figures 4.79 – 4.83. The local buckling constraint imposed on the skin segments between stiffeners was active as well. The constraint gradients (Table 4.36) indicate that the active buckling modes, with the exception of mode 5, are dominated by the skin design variable, although weaker coupling with the rib design variable occurs. In mode 5, the skin design variables are more strongly coupled to the rib design variables. In all of the active buckling modes, skin panels buckle along the length of the structure. This skin buckling pattern is usually accompanied by the buckling of the inboard skin and spar panels.

Design C5GS

Design C5GS, which was obtained by adding the bending and torque load cases, is presented in Table 4.37. This design is 50% lighter than its unstiffened counterpart, C3G, 10% heavier than design B5GS (bending only) and 60% heavier than design T5GS (torque only). The skin laminate thickness is approximately the same as for the pure bending case (0.339 *in* vs. 0.341 *in*) and the stiffener thickness is slightly greater (0.140 *in* vs. 0.131 *in*). The stiffener height in both cases is 3.00 *in*. The spar panel is 17% thicker than its B5GS counterpart and 30% thicker than its T5GS counterpart. The rib panel is 17% thicker than the B5GS rib, and 8% thinner than

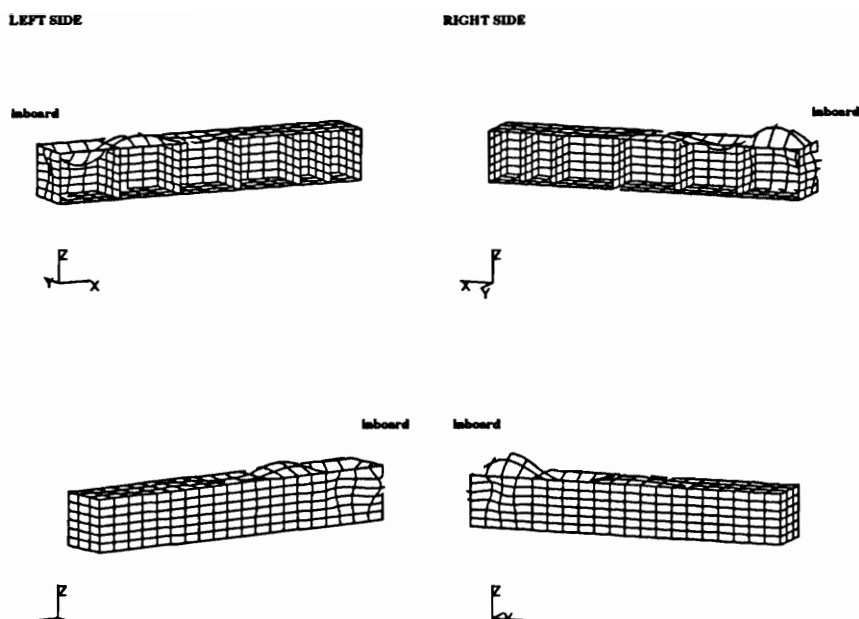


Figure 4.74: Design B5GS – Active Buckling Mode 1 ($\lambda = 1.001$)

the T5GS rib.

The two active buckling modes for design C5GS are shown in Figures 4.84 and 4.85. The first mode is a local rib buckling mode, and the second mode is characterized by the buckling of all three panel types on the right side of the structure. As expected, the constraint gradients (Table 4.38) indicate that the first mode is dominated by the rib design variable and that the second mode is a function of skin, spar, and rib design variables. In addition to the overall buckling constraints, the local skin segment constraint was active as well.

In summary, then, the smeared stiffener approach yields designs which are from 30-50% lighter than their unstiffened counterparts for all three load cases. This approach also leads to designs that are more realistic in terms of the skin panel thicknesses (this is especially true for the bending load case). In all cases, at least one of the active buckling modes exhibits significant interaction between the three different panel types at the optimal design.

Table 4.33: Results — Design Case B5GS

Design Case: B5GS*					
Geometry: 150"x48"x24"					
Rib Spacing: 30.0"					
Loading: Upward Bending					
Active Constraints:					
<i>Inter-Stiffener</i>	skin				
<i>Buckling Mode</i>	1	2	3	4	5
Eigenvalue	1.001	1.005	1.008	1.010	1.010
Description	Ply thickness (<i>in</i>)				
Skin	.0426				
Stiffener	.0219				
Spar	.0510				
Rib	.0181				
Stiffener Ht (<i>in</i>)	3.00				
Weight (<i>lb</i>)	574.7				

* smeared skin stiffeners used

Table 4.34: Design B5GS – Active buckling constraint gradients

DV		Mode 1	Mode 2	Mode 3	Mode 4	Mode 5
1	t_{sk}	-7.1 (-.467)	-9.2 (-.529)	-8.1 (-.126)	-4.5 (-.233)	-9.3 (-.566)
2	t_{stf}	-15.3 (-1.00)	-8.0 (-.489)	-4.4 (-.068)	-19.1 (-1.00)	-9.4 (-.569)
3	t_{sp}	-9.4 (-.616)	-16.4 (-1.00)	-3.6 (-.057)	-6.4 (-.336)	-16.4 (-1.00)
4	t_{rb}	-0.6 (-.039)	-7.4 (-.449)	-64.1 (-1.00)	-0.5 (-.028)	-0.8 (-.049)
5	h_{stf}	-4.2	-1.8	-0.3	-5.6	-2.2

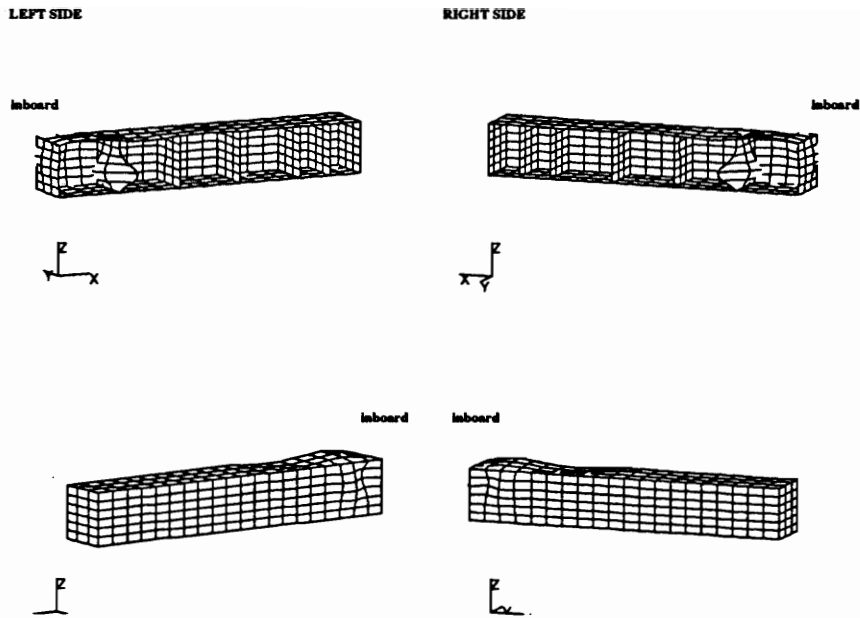


Figure 4.75: Design B5GS – Active Buckling Mode 2 ($\lambda = 1.005$)

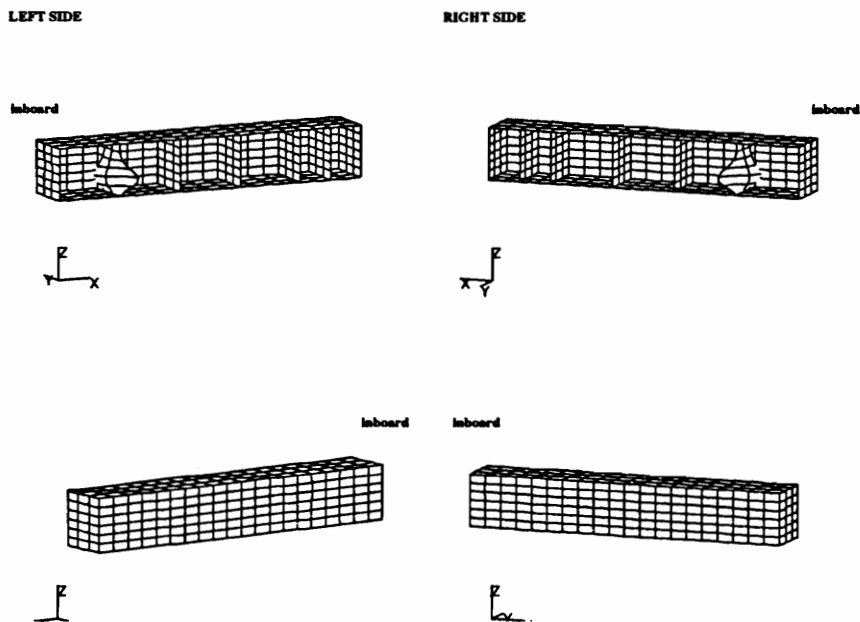


Figure 4.76: Design B5GS – Active Buckling Mode 3 ($\lambda = 1.008$)

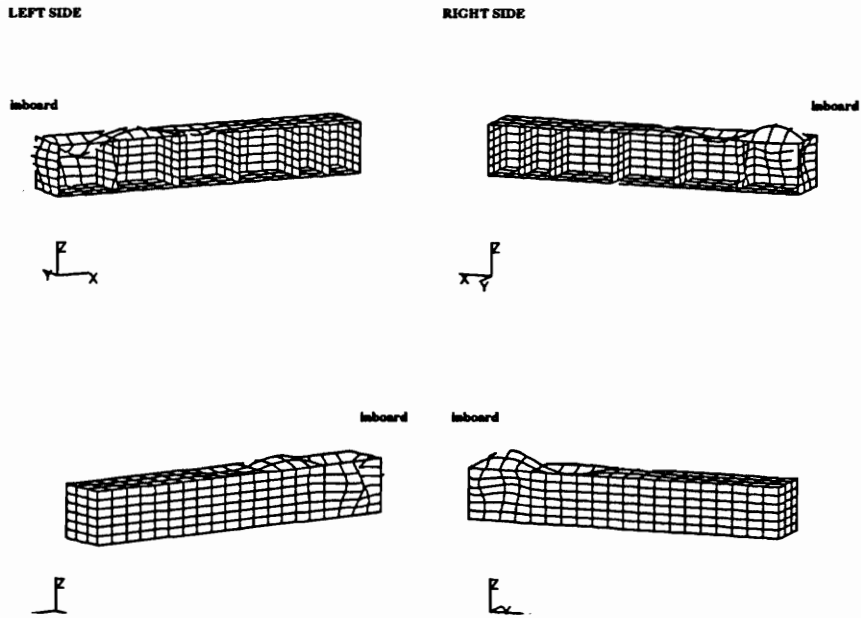


Figure 4.77: Design B5GS – Active Buckling Mode 4 ($\lambda = 1.010$)

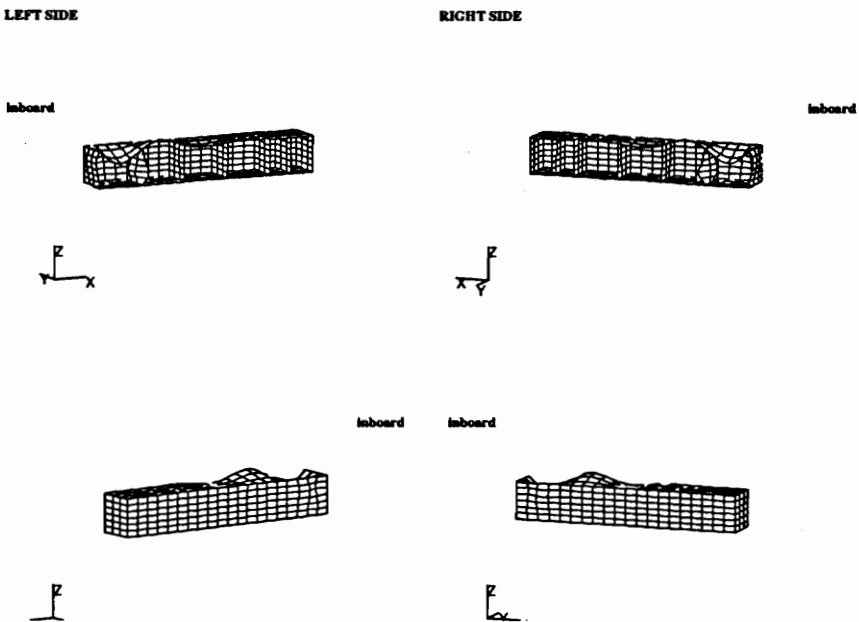


Figure 4.78: Design B5GS – Active Buckling Mode 5 ($\lambda = 1.010$)

Table 4.35: Results — Design Case T5GS

Design Case: T5GS*					
Geometry: 150"x48"x24"					
Rib Spacing: 30.0"					
Loading: Torque					
Active Constraints:					
<i>Inter-Stiffener</i>	skin				
<i>Buckling Mode</i>	1	2	3	4	5
Eigenvalue	1.005	1.006	1.009	1.009	1.012
Description	Ply thickness (<i>in</i>)				
Skin	.0185				
Stiffener	.00646				
Spar	.0461				
Rib	.0229				
Stiffener Ht (<i>in</i>)	3.00				
Weight (<i>lb</i>)	396.1				

* smeared skin stiffeners used

Table 4.36: Design T5GS - Active Buckling constraint gradients

DV		Mode 1	Mode 2	Mode 3	Mode 4	Mode 5
1	t_{sk}	-23.5 (-.417)	-23.9 (-.392)	-24.9 (-.394)	-25.1 (-.385)	-20.1 (-.508)
2	t_{stf}	-56.5 (-1.00)	-61.0 (-1.00)	-63.2 (-1.00)	-65.1 (-1.00)	-11.2 (-.282)
3	t_{sp}	-2.1 (-.038)	-2.7 (-.044)	-0.7 (-.011)	-0.7 (-.011)	-6.7 (-.170)
4	t_{rb}	-6.1 (-.108)	-0.8 (-.013)	-2.4 (-.039)	-0.7 (-.011)	-39.6 (-1.00)
5	h_{stf}	-3.5	-3.8	-3.9	-4.0	-0.7

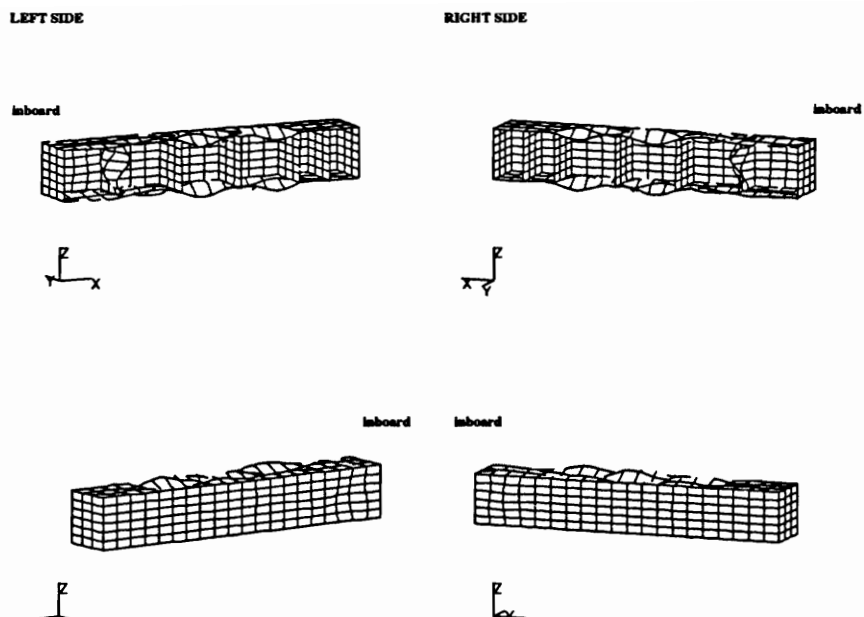


Figure 4.79: Design T5GS – Active Buckling Mode 1 ($\lambda = 1.005$)

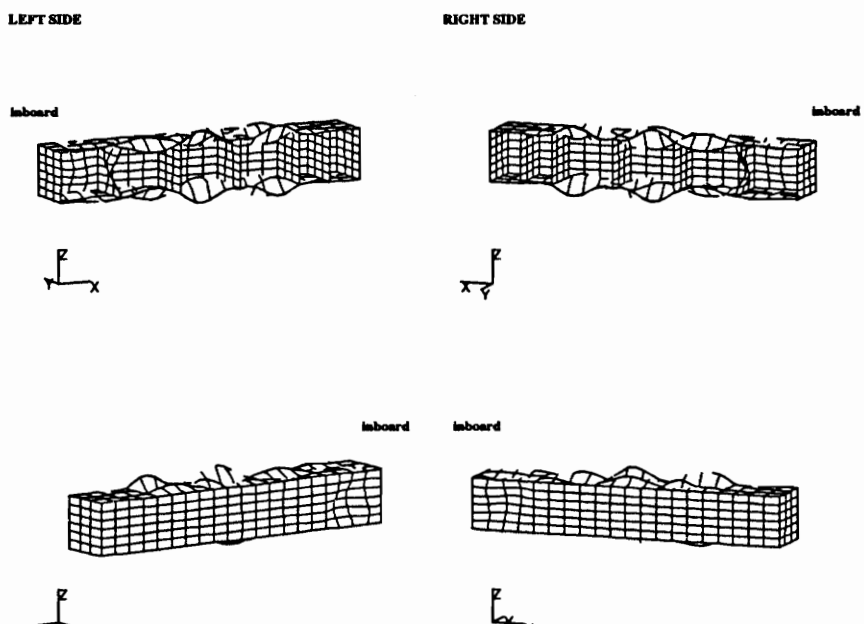


Figure 4.80: Design T5GS – Active Buckling Mode 2 ($\lambda = 1.006$)

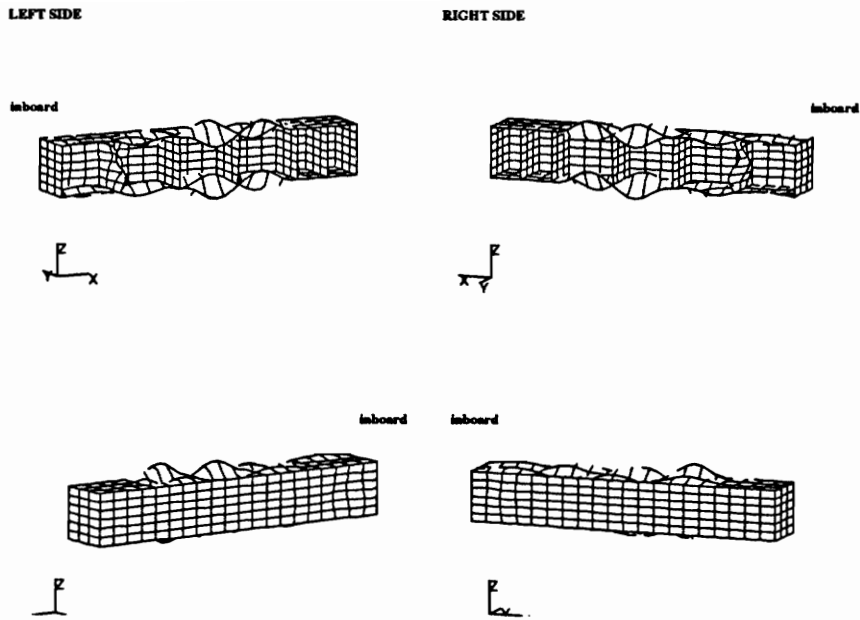


Figure 4.81: Design T5GS – Active Buckling Mode 3 ($\lambda = 1.009$)

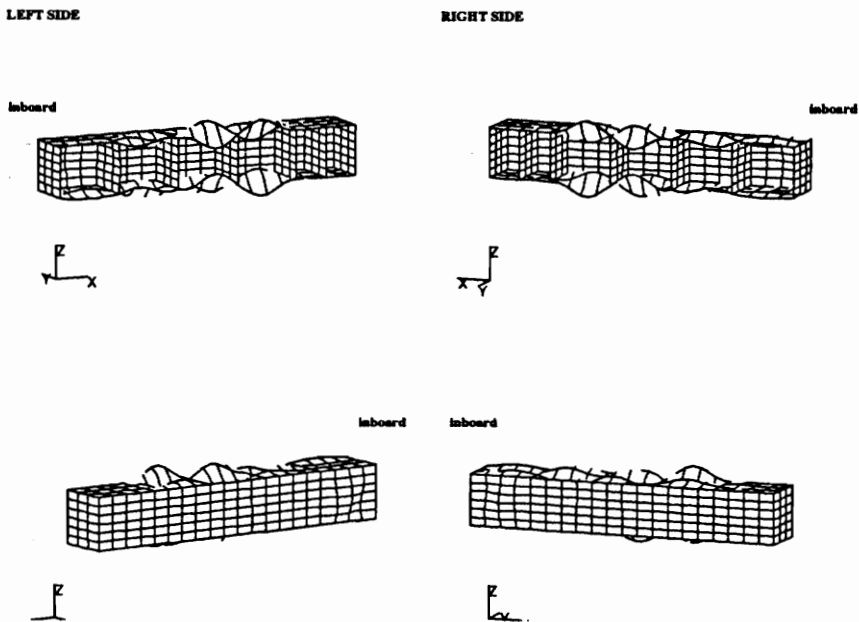


Figure 4.82: Design T5GS – Active Buckling Mode 4 ($\lambda = 1.009$)

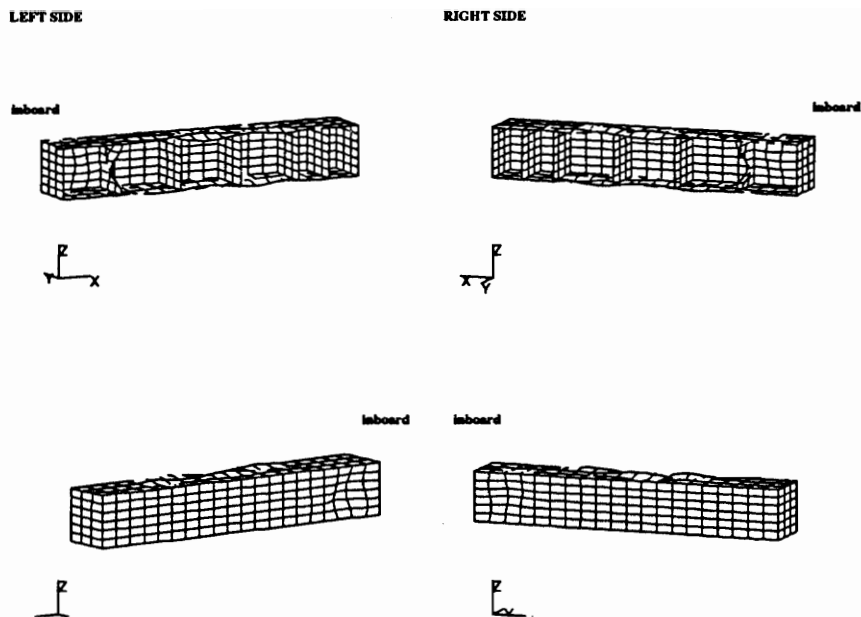


Figure 4.83: Design T5GS – Active Buckling Mode 5 ($\lambda = 1.012$)

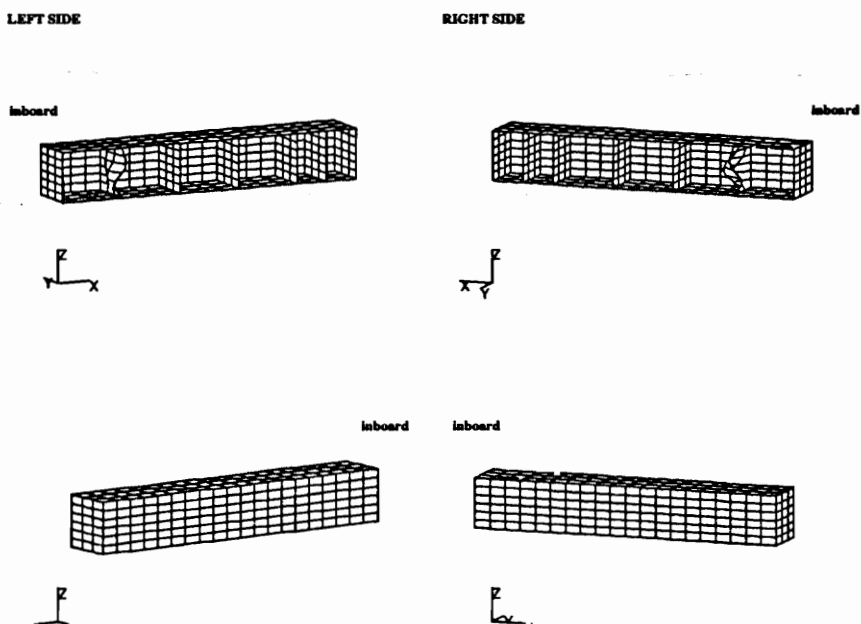


Figure 4.84: Design C5GS – Active Buckling Mode 1 ($\lambda = 1.000$)

Table 4.37: Results — Design Case C5GS

Design Case: C5GS*			
Geometry: 150"x48"x24"			
Rib Spacing: 30.0"			
Loading: Bending/Torque			
Active Constraints:			
<i>Inter-Stiffener</i>	skin		
<i>Buckling Mode</i>	1	2	
Eigenvalue	1.000	1.005	
Description	Ply thickness (<i>in</i>)		
Skin	.0423		
Stiffener	.0233		
Spar	.0597		
Rib	.0212		
Stiffener Ht (<i>in</i>)	3.00		
Weight (<i>lb</i>)	634.4		

* smeared skin stiffeners used

Table 4.38: Design C5GS – Active buckling constraint gradients

DV		Mode 1		Mode 2	
1	t_{sk}	-11.0	(-.175)	-8.0	(-.635)
2	t_{stf}	-2.4	(-.039)	-8.4	(-.664)
3	t_{sp}	+0.2	(+.004)	-12.7	(-1.00)
4	t_{rb}	-62.8	(-1.00)	-5.5	(-.432)
5	h_{stf}	-0.3		-2.3	

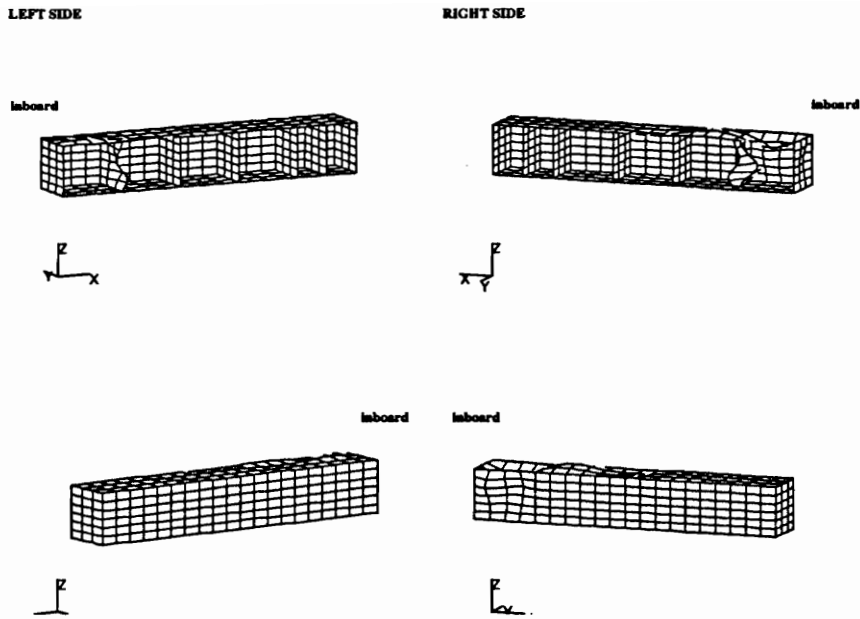


Figure 4.85: Design C5GS – Active Buckling Mode 2 ($\lambda = 1.005$)

4.5 Effect of Rib Spacing

In this section, several designs are presented with rib spacings of 22.5 *in* and 15.0 *in*. These designs are compared to the previously presented designs (30.0 *in* rib spacing) and design trends are deduced.

Bending

First, designs B3G-R1 and B3G-R2 are presented. Both designs were obtained using the usual three design variables and were subject to the bending load case. Design B3G-R1 (22.5 *in* rib spacing) is presented in Table 4.39 and design B3G-R2 (15.0 *in* rib spacing) is presented in Table 4.40. This data is summarized and compared to design B3G (30.0 *in* rib spacing) in Figure 4.86.

The total weight of design B3G was 1088.2 *lb*. When the rib spacing is reduced to 22.5 *in* (B3G-R1), the optimal weight is reduced by 5.9% to 1024.1 *lb*, and when the rib spacing is reduced to 15 *in* (B3G-R2), the optimal weight is reduced by 15.7%. The trend here is clear: the reduced rib spacing leads to a lighter structure in this case. Even though the extra rib panels add more structural weight, these extra ribs

allow offsetting reductions in the skin and spar panel thicknesses. There will, of course, be a limiting value of rib spacing where the weight increase due to the added ribs is not offset by reductions in skin and spar panel thickness, but that point has not been reached here.

The trends can be seen graphically in Figure 4.86. In going from B3G to B3G-R1, there is a 7% reduction in the skin thickness, a 4% reduction in the spar thickness, and a 2% increase in the rib thickness. In going from B3G to B3G-R2, there is a 21% reduction in skin thickness, a 11% reduction in spar thickness, and a 10% increase in rib thickness. As the rib spacing decreases, the skin and spar panels get thinner, while the rib thickness increases.

The same trends can be seen for the nine design variable bending cases: designs B9GP-R1 and B9GP-R2. Designs B9GP-R1 (22.5 *in* rib spacing) and B9GP-R2 (15.0 *in* rib spacing) are described by the same design variables as was design B9GP (30.0 *in* rib spacing). Like design B9GP, they were subject to a ply-percentage constraint. Design B9GP-R1 is presented in Table 4.41, and design B9GP-R2 is presented in Table 4.42. These results are summarized and compared in Figure 4.87.

As the rib spacing decreases, the total weight decreases from 1055.3 *lb* (B9GP) to 981.9 *lb* (B9GP-R1) and 863.3 *lb* (B9GP-R2). This is a reduction of 7.0% and 18.2%, respectively. In the skin panel, there is a reduction in each of the 0°, $\mp 45^\circ$, and 90° plies. In the spar panel, the 0° and 90° plies are reduced, but there is an increase in the $\mp 45^\circ$ plies. In the rib panel, the 0° and $\mp 45^\circ$ plies increase as the rib spacing decreases.

These trends are also the same when the local approach is used instead of the global approach. Designs B3L-R2 and B9LP-R2 are presented in Tables 4.43 and 4.44 (design B3L-R2 is the local analog to design B3G-R2, and design B9LP-R2 is the local analog to design B9GP-R2). The weight for design B3L (30.0" rib spacing) is 1149.3 *lb* and the weight for design B3L-R2 (15.0 *in* rib spacing) is 15% less at 976.1 *lb*. The weight for design B9LP (30.0" rib spacing) is 1115.1 *lb* and the weight for design B9LP-R2 (15.0 *in* rib spacing) is 18% less at 917.3 *lb*. In the nine design variable case, the ply distribution in the panels remains approximately the same as the rib spacing is reduced.

It is noted that designs B3L-R2 and B9LP-R2 (obtained using the local approach) are 6.4% and 5.9% heavier than their global approach counterparts, designs B3G-R2 and B9GP-R2. This trend is similar to that found for the 30.0" rib spacing designs

Table 4.39: Results — Design Case B3G-R1

Design Case: B3G-R1			
Geometry: 150"x48"x24"			
Rib Spacing: 22.5"			
Loading: Upward Bending			
Active Constraints:			
<i>Buckling Mode</i>	1	2	3
Eigenvalue	.9961	1.009	1.011
Description	Ply thickness (<i>in</i>)		
Skin	.127		
Spar	.0378		
Rib	.0121		
Weight (<i>lb</i>)	1024.1		

(B3G,B3L,B9GP,B9LP); there is a 5-6% reduction in the overall structural weight when the global approach is used instead of the local approach.

Torque

The results for the torque case are similar to those found for the bending case. Designs T3G-R1 and T3G-R2, which are three design variable cases, are presented in Tables 4.45 and 4.46. The total weight of design T3G (30.0" spacing) is 548.7 *lb*, that for design T3G-R1 (22.5" spacing) is 8% less at 504.8 *lb*, and that for design T3G-R2 (15.0" spacing) is 18% less at 451.7 *lb*. These trends are shown graphically in Figure 4.88. In going from T3G to T3G-R1, there is a 13% reduction in the skin thickness, a 7% reduction in the spar thickness, and a 3% increase in the rib thickness. In going from T3G to T3G-R2, there is a 30% reduction in skin thickness, a 22% reduction in spar thickness, and a 2% increase in rib thickness.

Designs T9G-R1 and T9G-R2, which are nine design variable cases, are presented in Tables 4.47 and 4.48. These designs are summarized and compared to design T9G in Figure 4.89. As the rib spacing decreases, the total weight decreases from 539.8 *lb* (T9G) to 489.8 *lb* (T9G-R1) and 410.7 *lb* (T9G-R2). This is a reduction of

Table 4.40: Results — Design Case B3G-R2

Design Case: B3G-R2			
Geometry: 150"x48"x24"			
Rib Spacing: 15.0"			
Loading: Upward Bending			
Active Constraints:			
<i>Buckling Mode</i>	1	2	
Eigenvalue	1.000	1.003	
Description	Ply thickness (in)		
Skin	.109		
Spar	.0352		
Rib	.0130		
Weight (lb)	917.3		

Design Comparison

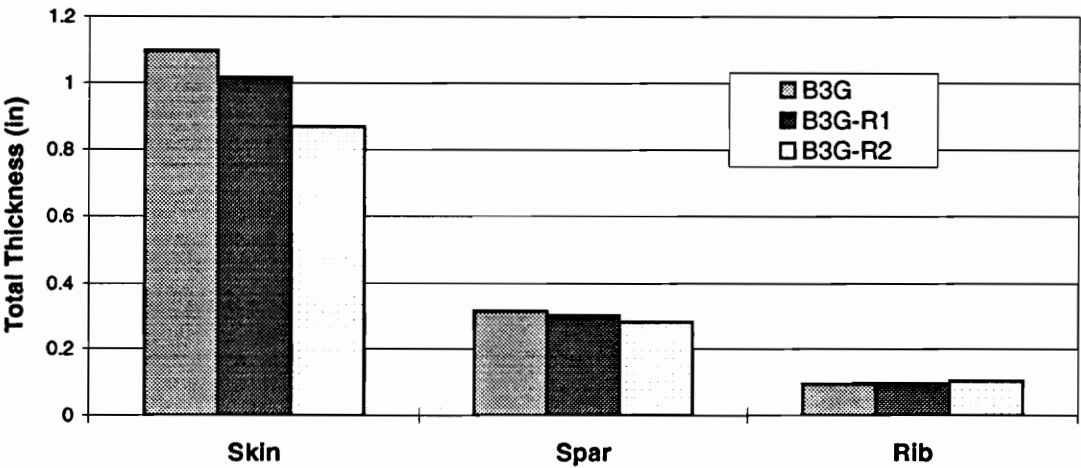


Figure 4.86: Comparison of designs B3G - B3G-R2

Table 4.41: Results — Design Case B9GP-R1

Design Case: B9GP-R1			
Geometry: 150"x48"x24"			
Rib Spacing: 22.5"			
Loading: Upward Bending			
Active Constraints:			
<i>Ply Percent</i>	Skin		
<i>Buckling Mode</i>	Mode 1	Mode 2	
<i>Eigenvalue</i>	1.002	1.003	
Description	$\mp 45^\circ$	90°	0°
Skin ply thk (in)	.112	.0222	.240
Spar ply thk (in)	.0293	.0345	.0582
Rib ply thk (in)	.00789	.00603*	.0207
Weight (lb)	981.9		

* lower bound

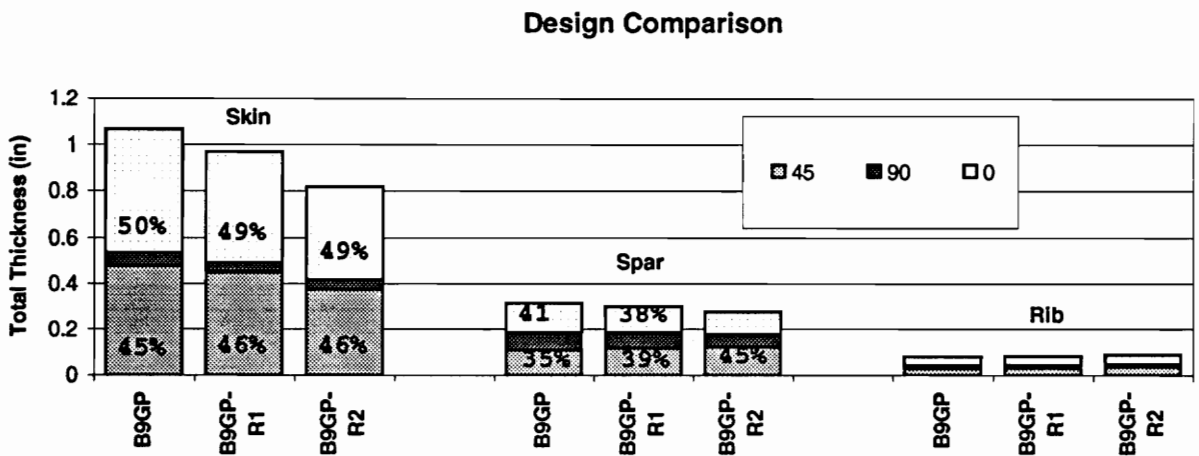


Figure 4.87: Comparison of designs B9GP - B9GP-R2

Table 4.42: Results — Design Case B9GP-R2

Design Case: B9GP-R2			
Geometry: 150"x48"x24"			
Rib Spacing: 15.0"			
Loading: Upward Bending			
Active Constraints:			
<i>Ply Percent</i>	Skin		
<i>Buckling Mode</i>	1	2	3
Eigenvalue	.9974	1.005	1.010
Description	$\mp 45^\circ$	90°	0°
Skin ply thk (<i>in</i>)	.0938	.0195	.200
Spar ply thk (<i>in</i>)	.0310	.0273	.0494
Rib ply thk (<i>in</i>)	.00891	.006*	.0217
Weight (<i>lb</i>)	863.3		

* lower bound

Table 4.43: Results — Design Case B3L-R2

Design Case: B3L-R2			
Geometry: 150"x48"x24"			
Rib Spacing: 15.0"			
Loading: Upward Bending			
Active Constraints:			
<i>Buckling Mode*</i>	skin	spar	rib
Description	Ply thickness (<i>in</i>)		
Skin	.113		
Spar	.0408		
Rib	.0160		
Weight (<i>lb</i>)	976.1		

* local buckling analysis used

Table 4.44: Results — Design Case B9LP-R2

Design Case: B9LP-R2			
Geometry: 150"x48"x24"			
Rib Spacing: 15.0"			
Loading: Upward Bending			
Active Constraints:			
<i>Buckling Mode</i> [†]	skin	spar	rib
Description	±45°	90°	0°
Skin ply thk (<i>in</i>)	.0917	.0288	.212
Spar ply thk (<i>in</i>)	.0396	.0380	.0396
Rib ply thk (<i>in</i>)	.0102	.006*	.0264
Weight (<i>lb</i>)	914.2		

* lower bound

† local buckling analysis used

9% and 34%, respectively. As the rib spacing decreases, the percentages of 0° and ±45° plies in the skin panel increase while the percentage of 90° plies decreases. In the spar panel, the percentage of 90° plies decreases, while the percentage of 0° plies increases. In the rib panel, the percentages of 0° and 90° plies increase while the percentage of ±45° plies decreases.

These trends continue for the local approach as well. Designs T3L-R2 and T9L-R2 are presented in Tables 4.49 and 4.50 (design T3L-R2 is the local version of design T3G-R2, and design T9L-R2 is the local version of design T9G-R2). The weight for design T3L (30.0" rib spacing) is 581.2 *lb* and the weight for design T3L-R2 (15" rib spacing) is 12% less at 508.6 *lb*. The weight for design T9L (30.0" rib spacing) was 558.1 *lb* and the weight for design T9L-R2 (15" rib spacing) is 21% less at 439.2 *lb*. As was the case with earlier designs, the local designs T3L-R2 and T9L-R2 are 5-8% heavier than their global counterparts.

Table 4.45: Results — Design Case T3G-R1

Design Case: T3G-R1			
Geometry: 150"x48"x24"			
Rib Spacing: 22.5"			
Loading: Torque			
Active Constraints:			
<i>Buckling Mode</i>	1	2	
Eigenvalue	1.001	1.002	
Description	Ply thickness (<i>in</i>)		
Skin	.0438		
Spar	.0376		
Rib	.0147		
Weight (<i>lb</i>)	504.8		

Table 4.46: Results — Design Case T3G-R2

Design Case: T3G-R2			
Geometry: 150"x48"x24"			
Rib Spacing: 15.0"			
Loading: Torque			
Active Constraints:			
<i>Buckling Mode</i>	1	2	3
Eigenvalue	.9991	1.005	1.008
Description	Ply thickness (<i>in</i>)		
Skin	.0353		
Spar	.0316		
Rib	.0145		
Weight (<i>lb</i>)	451.7		

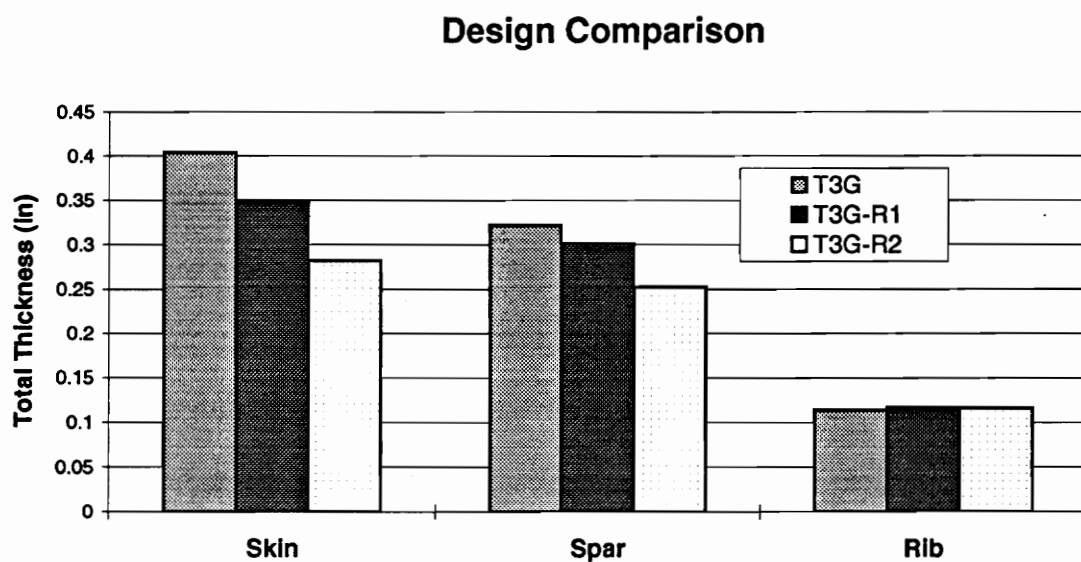


Figure 4.88: Comparison of designs T3G - T3G-R2

Table 4.47: Results — Design Case T9G-R1

Design Case: T9G-R1			
Geometry: 150"x48"x24"			
Rib Spacing: 22.5"			
Loading: Torque			
Active Constraints:			
<i>Buckling Mode</i>	Mode 1	Mode 2	Mode 3
Eigenvalue	1.000	1.006	1.008
Description	$\mp 45^\circ$	90°	0°
Skin ply thk (<i>in</i>)	.0435	.0328	.0556
Spar ply thk (<i>in</i>)	.0166	.0582	.0604
Rib ply thk (<i>in</i>)	.00895	.00646	.0138
Weight (<i>lb</i>)	489.8		

Table 4.48: Results — Design Case T9G-R2

Design Case: T9G-R2					
Geometry: 150"x48"x24"					
Rib Spacing: 15.0"					
Loading: Torque					
Active Constraints:					
<i>Buckling Mode</i>	Mode 1	Mode 2	Mode 3	Mode 4	Mode 5
Eigenvalue	.9964	1.006	1.007	1.012	1.014
Description	±45°	90°	0°		
Skin ply thk (in)	.0411	.00923	.0419		
Spar ply thk (in)	.0171	.0368	.0554		
Rib ply thk (in)	.00651	.00879	.0122		
Weight (lb)	410.7				

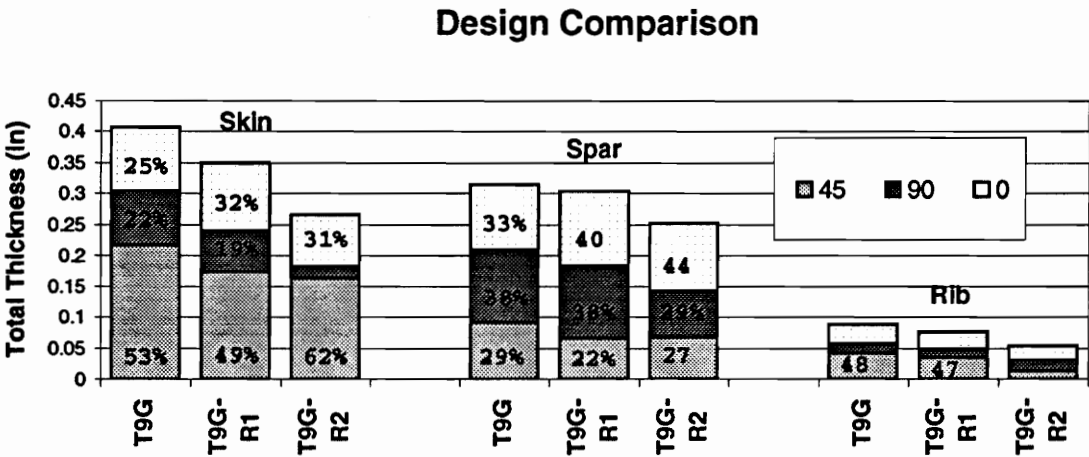


Figure 4.89: Comparison of designs T9G - T9G-R2

Table 4.49: Results — Design Case T3L-R2

Design Case: T3L-R2			
Geometry: 150"x48"x24"			
Rib Spacing: 15.0"			
Loading: Torque			
Active Constraints:			
<i>Buckling Mode*</i>	skin	spar	rib
Description	Ply thickness (<i>in</i>)		
Skin	.0386		
Spar	.0361		
Rib	.0189		
Weight (<i>lb</i>)	508.6		

* local buckling analysis used

Table 4.50: Results — Design Case T9L-R2

Design Case: T9L-R2			
Geometry: 150"x48"x24"			
Rib Spacing: 15.0"			
Loading: Torque			
Active Constraints:			
<i>Buckling Mode</i> [†]	skin	spar	rib
Description	±45°	90°	0°
Skin ply thk (<i>in</i>)	.0430	.00604	.0462
Spar ply thk (<i>in</i>)	.0128	.0452	.0697
Rib ply thk (<i>in</i>)	.00767	.00608*	.0207
Weight (<i>lb</i>)	439.2		

* lower bound

† local buckling analysis used

Smeared Stiffness Designs

When designs incorporating smeared stiffeners on the skin panel are considered, different trends are found. The total weight of design B5GS (bending/30.0 *in* spacing) is 574.7 *lb*. When the spacing is reduced to 22.5 *in* (design B5GS-R1) the weight drops to 567.4 *lb*, and when the spacing is further reduced to 15.0 *in* (design B5GS-R2), the weight increases to 581.7 *lb*. Of these three designs, the design with 22.5 *in* rib spacing (B5GS-R1) is the lightest; design B5GS (30.0 *in* spacing) is 1.3% heavier, and design B5GS-R2 (15.0 *in* spacing) is 2.5% heavier. The designs B5GS-R1 and B5GS-R2 are shown in Tables 4.51 and 4.52, respectively.

The same results are found for designs obtained under torque loading as well. Design T5GS (torque/30.0 *in* spacing) weighs 396.1 *lb*. Design T5GS-R1 (22.5 *in* spacing) weighs 388.4 *lb*, and design T5GS-R2 (15.0 *in* spacing) weighs 394.5 *lb*. Design B5GS is 2.0% heavier and design T5GS-R2 is 1.6% heavier than design T5GS-R1 (22.5 *in* spacing). Designs T5GS-R1 and T5GS-R2 are presented in Tables 4.53 and 4.54, respectively.

As already noted, these trends are different from those obtained for the unstiffened case, and appear to more closely model the results that would be obtained from "real" aircraft structures. Because the stiffened skin panel is more efficient at resisting bending loads as compared to the unstiffened panel, the weight increase that occurs when the rib spacing (the unsupported skin length) is increased is not as large. As the rib spacing increases, the stiffened panel is able to provide the needed bending stiffness in an efficient manner by increasing the stiffener height and stiffener thickness. The only way to add bending stiffness to the unstiffened panel, however, is to increase its total thickness.

It should be noted that additional local optimal designs were obtained for several of the bending cases. These additional designs differed from those presented here in the height and thickness of the smeared stiffeners. For example, several different designs were found for the bending case with 15.0 *in* rib spacing. Here, the active buckling modes were characterized primarily by skin and spar buckling. The important parameter affecting the skin design appeared to be the area of the smeared stiffener, and not its height. As a result, different stiffener combinations were obtained, each of which had approximately the same stiffener area.

Although the constraint gradients were not explicitly shown, all of the designs presented in this section had at least one active buckling mode which was characterized

Table 4.51: Results — Design Case B5GS-R1

Design Case: B5GS-R1*			
Geometry: 150"x48"x24"			
Rib Spacing: 22.5"			
Loading: Upward Bending			
Active Constraints:			
<i>Inter-Stiffener</i>	skin		
<i>Buckling Mode</i>	1	2	3
Eigenvalue	1.004	1.006	1.008
Description	Ply thickness (<i>in</i>)		
Skin	.0425		
Stiffener	.0143		
Spar	.0516		
Rib	.0182		
Stiffener Ht (<i>in</i>)	3.00		
Weight (<i>lb</i>)	567.4		

* smeared skin stiffeners used

by skin, spar, and/or rib design variable coupling.

4.6 Effect of Box Beam Width

In order to determine whether or not the results obtained here can be generalized to structures of different overall dimensions, it would be necessary to greatly expand this design study. In this section, a step is taken in this direction by considering one additional configuration. Here, designs are presented for a box beam which is twice the width of the previous structures. This new structure is 150" long, 96" wide, and 24" high. Because of the large size of this structure, the finite element model used to perform the structural analysis represents only half of the complete box beam; symmetry conditions are enforced along the mid-chord line of the half model. The use of a half-model limits this investigation to the bending load case only (the only load case which is symmetric about the mid-chord line). It also means that buckling modes

Table 4.52: Results — Design Case B5GS-R2

Design Case: B5GS-R2*			
Geometry: 150"x48"x24"			
Rib Spacing: 15.0"			
Loading: Upward Bending			
Active Constraints:			
<i>Inter-Stiffener</i>	skin		
<i>Buckling Mode</i>	1	2	3
Eigenvalue	1.007	1.007	1.008
Description	Ply thickness (<i>in</i>)		
Skin	.0410		
Stiffener	.0101		
Spar	.0529		
Rib	.0186		
Stiffener Ht (<i>in</i>)	3.00		
Weight (<i>lb</i>)	581.7		

* smeared skin stiffeners used

Table 4.53: Results — Design Case T5GS-R1

Design Case: T5GS-R1*							
Geometry: 150"x48"x24"							
Rib Spacing: 22.5"							
Loading: Torque							
Active Constraints:							
<i>Inter-Stiffener</i>	skin						
<i>Buckling Mode</i>	1	2	3	4	5	6	7
Eigenvalue	1.004	1.005	1.013	1.016	1.016	1.018	1.018
Description	Ply thickness (<i>in</i>)						
Skin	.0180						
Stiffener	.006 [†]						
Spar	.0430						
Rib	.0223						
Stiffener Ht (<i>in</i>)	2.27						
Weight (<i>lb</i>)	388.4						

[†] lower bound

* smeared skin stiffeners used

Table 4.54: Results — Design Case T5GS-R2

Design Case: T5GS-R2*			
Geometry: 150"x48"x24"			
Rib Spacing: 15.0"			
Loading: Torque			
Active Constraints:			
<i>Inter-Stiffener</i>	skin		
<i>Buckling Mode</i>	1	2	3
Eigenvalue	.9994	1.004	1.011
Description	Ply thickness (<i>in</i>)		
Skin	.0173		
Stiffener	.006 [†]		
Spar	.0388		
Rib	.0209		
Stiffener Ht (<i>in</i>)	1.54		
Weight (<i>lb</i>)	394.5		

[†] lower bound

* smeared skin stiffeners used

which are not symmetric about the mid-chord line are not considered. Experience with the (complete) model used for the previous design cases indicates that this fact should not significantly affect the final results. Most of the critical non-symmetric modes previously found with the complete model were accompanied by a symmetric counterpart at a nearly identical buckling load.

The first design to be presented (B3GW) was obtained using the usual three design variables and is presented in Table 4.55. The three active buckling modes are shown in Figures 4.90–4.92. The first buckling mode is interactive in the usual sense: it involves the compatible buckling of the two inboard rib panels, the inboard spar panels, and the inboard skin panels. The second mode is a local rib buckling mode; the second rib buckles near the rib-spar interface. In the third mode, this rib panel buckles along with the inboard spar panel at the same location. In all cases, the buckling of the second rib panel appears to be driven by the rib-spar Poisson interaction discussed in conjunction with the bending load case above (section 4.1.1).

A comparison with design B3G is given in Figure 4.93. Each of the skin, spar, and rib thicknesses are smaller than their B3G counterparts. The skin thickness is 4.5% thinner, the spar thickness is 2.2% thinner, and the rib thickness is 30.1% thinner. Although the B3GW ply thicknesses are smaller, the B3GW skin and rib panels are twice as large as they were for design B3G. As a result, design B3GW is 79% heavier than design B3G: 1944.5 *lb* vs. 1088.2 *lb*. The constraint gradients for design B3GW are given in Table 4.56. The design variable coupling is weaker here as compared to design B3G. There is coupling between all three design variables in mode 1, but mode 2 is dominated by the rib design variable, and mode 3 is dominated by the spar design variable.

This same trends are followed for the nine design variable design, B9GPW (Table 4.57). This design is 1820.5 *lb*, 73% heavier than design B9GP. A graphical comparison with design B9GP is given in Figure 4.94. The skin panel is 9% thinner than the corresponding B9GP panel, with fewer 90° plies and more $\mp 45^\circ$ plies. The ply-percentage constraint is active, and the 0° plies make up 50% of the laminate. The spar panel is 1% thinner than its B9GP counterpart and has 50% fewer 90° plies and 47% more $\mp 45^\circ$ plies. The rib panels are 15% thinner, with significant reductions in the 0° and $\mp 45^\circ$ plies.

One buckling mode is active and is shown in Figure 4.95. This mode is the usual interactive mode characterized by the buckling of the skin, spar, and rib panels. The

Table 4.55: Results — Design Case B3GW

Design Case: B3GW			
Geometry: 150"x96"x24"			
Rib Spacing: 30.0"			
Loading: Upward Bending			
Active Constraints:			
<i>Buckling Mode</i>	1	2	3
Eigenvalue	1.001	1.005	1.010
Description	Ply thickness (<i>in</i>)		
Skin	.131		
Spar	.0386		
Rib	.00828		
Weight (<i>lb</i>)	1944.5		

Table 4.56: Design B3GW – Active buckling constraint gradients

DV		Mode 1	Mode 2	Mode 3
1	t_{sk}	-12.5 (-1.00)	-3.3 (-.021)	-0.6 (-.015)
2	t_{sp}	-2.8 (-.226)	-0.0 (-.000)	-44.1 (-1.00)
3	t_{rb}	-1.6 (-.128)	-153.4 (-1.00)	-0.7 (-.015)

constraint gradients for this mode (Table 4.58) indicate weak coupling between the skin, spar, and rib design variables. This coupling is less significant than the coupling that was present in design B9GP.

Results for designs B3LW and B9LPW (local designs) are given in Tables 4.59 and 4.60. Both designs are 6% heavier than their global counterparts. This general trend (local designs that are 5-6% heavier than the corresponding global designs) is the same as was found with most of the previous 48 *in* wide designs. The trend continues in spite of the fact that, as noted, the design variable coupling is somewhat weaker as compared to the previous cases. The constraint gradients for the local designs B3LW and B9LPW are given in Tables 4.61 and 4.62. The gradients for both

RIGHT SIDE

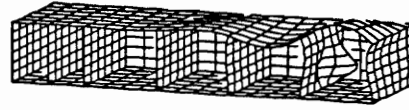


Figure 4.90: Design B3GW – Active buckling mode 1 ($\lambda=1.001$)

RIGHT SIDE

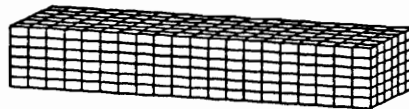
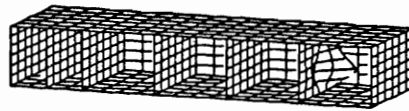


Figure 4.91: Design B3GW – Active buckling mode 2 ($\lambda=1.005$)

RIGHT SIDE

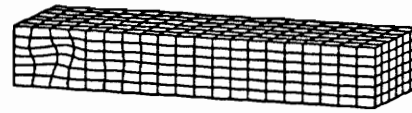
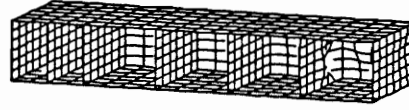


Figure 4.92: Design B3GW – Active buckling mode 3 ($\lambda=1.010$)

Design Comparison

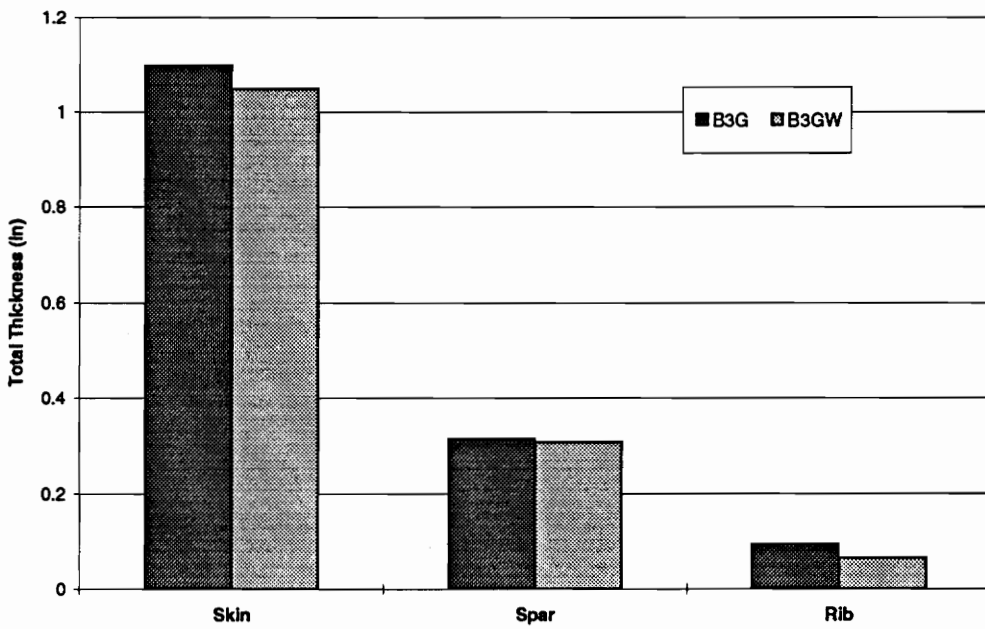


Figure 4.93: Comparison of designs B3G and B3GW

Table 4.57: Results — Design Case B9GPW

Design Case: B9GPW			
Geometry: 150"x96"x24"			
Rib Spacing: 30.0"			
Loading: Upward Bending			
Active Constraints:			
<i>Ply Percent</i>	Skin		
<i>Buckling Mode</i>	1		
<i>Eigenvalue</i>	.9967		
Description	±45°	90°	0°
Skin ply thk (<i>in</i>)	.118	.00825	.239
Spar ply thk (<i>in</i>)	.0408	.0187	.0561
Rib ply thk (<i>in</i>)	.00628	.006*	.0157
Weight (<i>lb</i>)	1820.5		

* lower bound

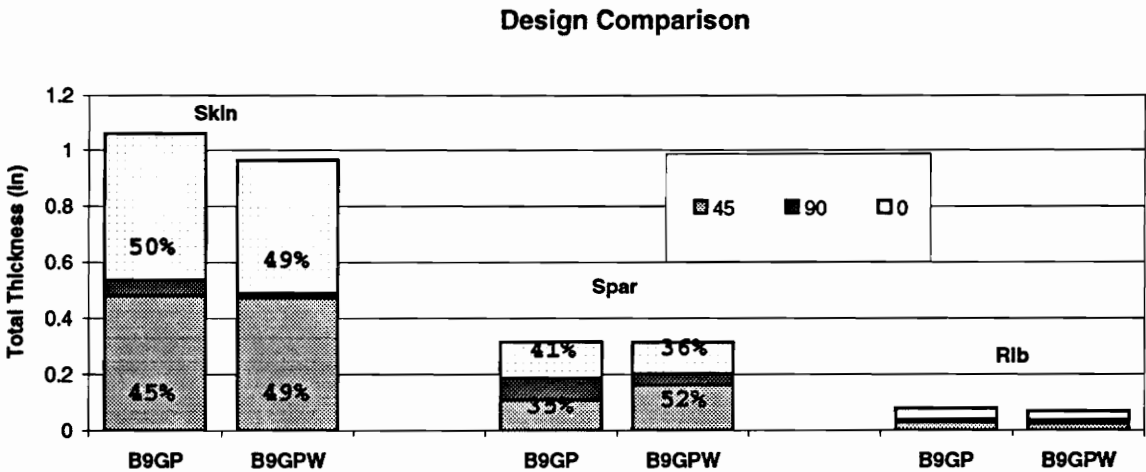


Figure 4.94: Comparison of designs B9GP and B9GPW

RIGHT SIDE

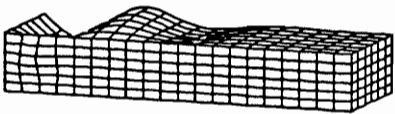
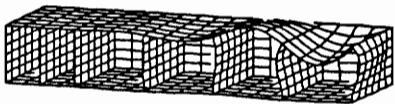


Figure 4.95: Design B9GPW – Active buckling mode 1 ($\lambda=.9976$)

Table 4.58: Design B9GPW – Active buckling constraint gradients

DV		Mode 1	
1	t_{sk}^{45}	-5.7	(-1.00)
2	t_{sk}^{90}	-2.4	(-.430)
3	t_{sk}^0	-4.1	(-.723)
4	t_{sp}^{45}	-1.0	(-.170)
5	t_{sp}^{90}	-0.5	(-.087)
6	t_{sp}^0	-0.6	(-.109)
7	t_{rb}^{45}	-0.7	(-.116)
8	t_{rb}^{90}	-0.1	(-.014)
9	t_{rb}^0	-0.1	(-.021)

Table 4.59: Results – Design Case B3LW

Design Case: B3LW			
Geometry: 150"x96"x24"			
Rib Spacing: 30.0"			
Loading: Upward Bending			
Active Constraints:			
Buckling Mode	skin	spar	rib
Description	Ply thickness (<i>in</i>)		
Skin	.139		
Spar	.0453		
Rib	.00784		
Weight (<i>lb</i>)	2076.9		

* local buckling analysis used

designs show that there is little to no coupling between the skin, spar, and rib design variables in this case.

In summary, it can be stated that the 96 *in* wide designs exhibit the same general trends as did the 48 *in* wide designs. In the global cases, at least one of the critical buckling modes is an “interactive” mode wherein the skin, spar, and rib design variables are coupled (although this coupling seems to be weaker for the 96 *in* wide designs). The designs obtained using the local approach are from 5-8% heavier than the global designs, and do not exhibit significant design variable coupling.

Table 4.60: Results — Design Case B9LPW

Design Case: B9LPW			
Geometry: 150"x96"x24"			
Rib Spacing: 30.0"			
Loading: Upward Bending			
Active Constraints:			
<i>Ply Percent</i>	Skin		
<i>Buckling Mode</i> [†]	skin	spar	rib
Description	±45°	90°	0°
Skin ply thk (<i>in</i>)	.124	.00773	.256
Spar ply thk (<i>in</i>)	.0464	.0207	.0687
Rib ply thk (<i>in</i>)	.006*	.006*	.00903
Weight (<i>lb</i>)	1930.6		

* lower bound

† local buckling analysis used

Table 4.61: Design B3LW – Active buckling constraint gradients

DV		Skin	Spar	Rib
1	t_{sk}	-12.8 (-1.00)	-1.5 (-.024)	-4.1 (-.027)
2	t_{sp}	-0.5 (-.036)	-63.0 (-1.00)	-0.8 (-.005)
3	t_{rb}	+0.0 (-.001)	-0.0 (-.001)	-153.0 (-1.00)

Table 4.62: Design B9LPW – Active buckling constraint gradients

DV		Skin mode		Spar mode		Rib mode	
1	t_{sk}^{45}	-5.8	(-1.00)	-0.6	(-.186)	+3.0	(+.027)
2	t_{sk}^{90}	-2.4	(-.415)	-0.2	(-.006)	-8.4	(-.075)
3	t_{sk}^0	-4.0	(-.693)	-0.5	(-.016)	-3.4	(-.031)
4	t_{sp}^{45}	-0.1	(-.017)	-33.6	(-1.00)	-0.1	(-.001)
5	t_{sp}^{90}	-0.0	(-.008)	-16.5	(-.491)	-0.0	(-.000)
6	t_{sp}^0	-0.2	(-.038)	-14.0	(-.416)	-0.1	(-.001)
7	t_{rb}^{45}	+0.000	(+.000)	-0.0	(-.001)	-111.8	(-1.00)
8	t_{rb}^{90}	+0.0	(+.002)	-0.0	(-.001)	-4.2	(-.037)
9	t_{rb}^0	+0.0	(+.000)	-0.0	(-.001)	-57.6	(-.515)

Chapter 5

NONLINEAR ANALYSIS

It is well known that the design optimization process may lead to structures with a high degree of imperfection sensitivity [43, 44] and that optimized designs based upon ideal structures may fail prematurely when geometric or loading imperfections are introduced. In the same manner, a structure optimized using linear analysis may be sensitive to nonlinear effects that are neglected by the analysis model.

In order to assess the effects of geometric nonlinearities on the response of the structures presented here, several of the designs from Chapter 4 are subjected to a static geometrically nonlinear analysis. The response obtained in this manner is compared to the response previously predicted by the linear buckling analysis, and the implications for the present design study are discussed.

In the first section, those designs obtained subject to the bending load case are examined, and in the following sections, the torque designs and combined bending/torque designs are considered as well.

5.1 Bending Designs

The first design to be considered is design B3G (see Chapter 4). This design is defined by three design variables and was obtained using the global approach. When this design is subjected to a geometrically nonlinear analysis, the structure begins to collapse at less than half the intended design load in a mode different from any of those predicted by the linear analysis. Beginning around 48% of the applied load ($\lambda = .48$), the innermost rib starts to exhibit large out of plane deformations. The maximum out of plane deformation, u_m , is .024 *in* at this load step. As the applied load is increased, these deflections grow rapidly and the rib collapses; at $\lambda = .51$, $u_m = .093$ *in* and is roughly equal to the rib thickness. By the time $\lambda = .89$, $u_m = .39$ *in* and the second rib begins to collapse as well. This sequence is illustrated in Figures 5.1–5.3.

The out of plane displacements of several characteristic points on the structure are plotted as a function of the loading parameter λ in Figure 5.4. The displacement histories of the middle of the upper inboard skin panel, the middle of the left

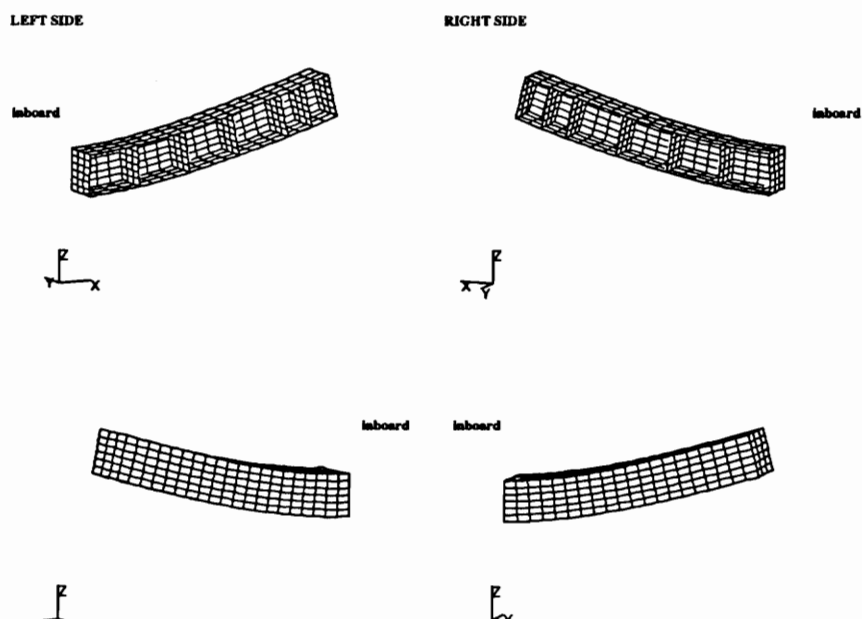


Figure 5.1: Design B3G – Nonlinear Deformed Mesh ($\lambda=.48$ Scale=30X)

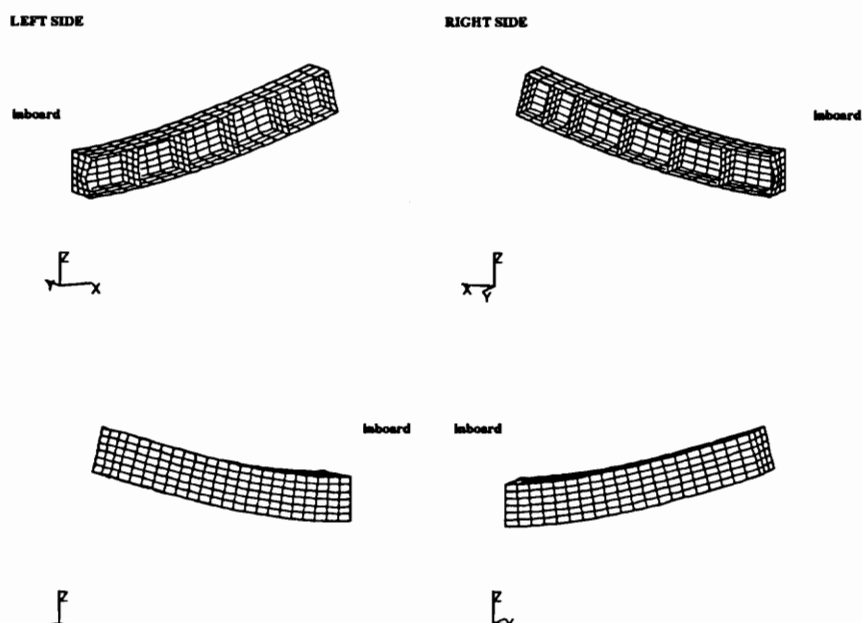


Figure 5.2: Design B3G – Nonlinear Deformed Mesh ($\lambda=.51$ Scale=30X)

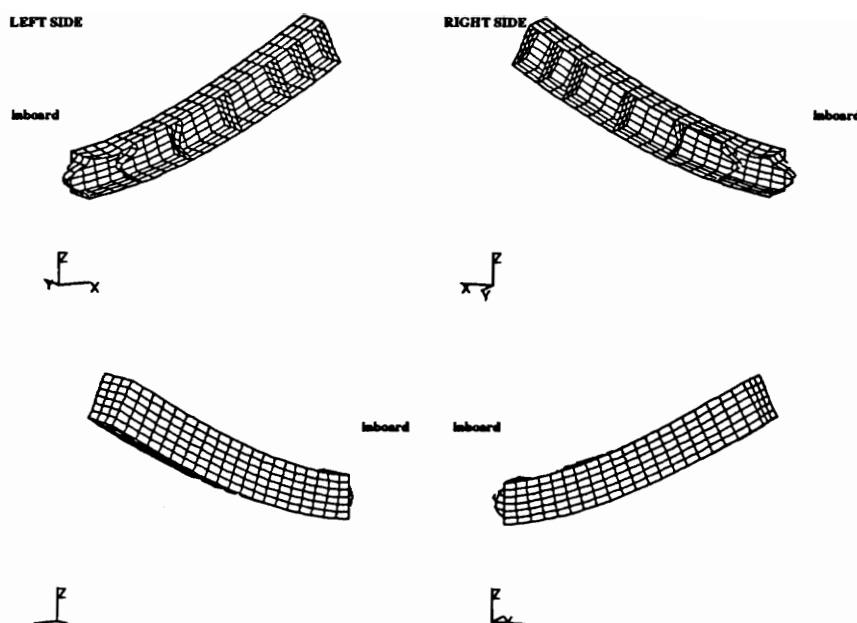


Figure 5.3: Design B3G – Nonlinear Deformed Mesh ($\lambda=.89$ Scale=30X)

inboard spar panel, and the middle of the first rib panel are each plotted. In this and subsequent plots of the bending and combined bending/torque load cases, the displacements of the skin panel are relative to the top edge of the spar panel (this removes that component of the displacement which represents the upward displacement of the box as a whole). All displacements are normalized by the total thickness of their respective panels.

The displacements of all three panels are very small until $\lambda = .48$, at which point the rib panel displacements grow very rapidly with increased load. The skin and spar panel displacements remain small.

The primary causes of the difference between the predicted linear and nonlinear failure modes are the rib crushing loads (or crushing pressure). In a wing type structure, flexural bending of the box beam as a whole induces deformations that tend to push the upper and lower wing box surfaces closer to one another [23] (see Figure 5.5). The rib panels oppose these deformations, and as a result, have compressive loads induced in them. The axial load induced in a given rib panel is roughly proportional to the curvature of the box beam at that point. As this is a nonlinear effect (the crushing loads are a function of the deformed geometry) these loads are not present

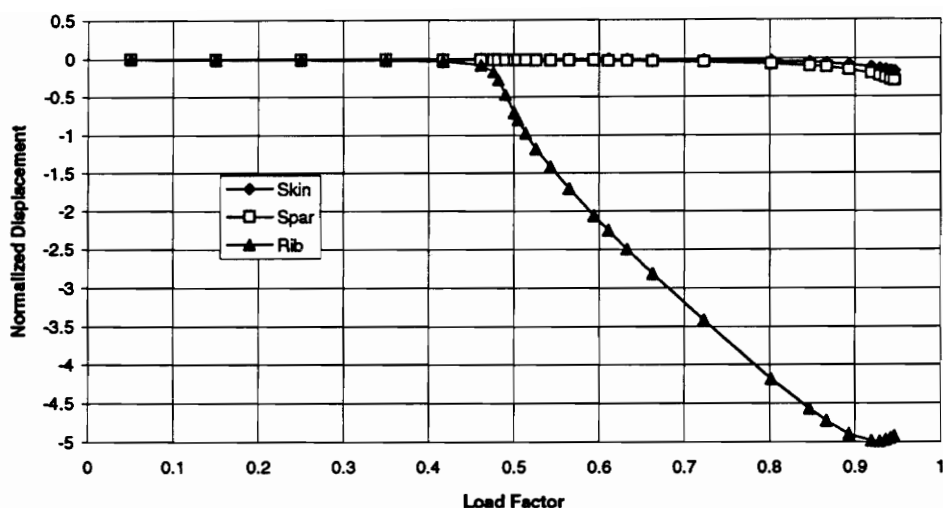


Figure 5.4: Design B3G Nonlinear Deformation History

in a linear analysis.

The manner in which the crushing loads interact with the skin and rib panels to cause premature failure can be understood by examining Figures 5.6–5.8, where the nonlinear skin/rib deformation history is illustrated. First, ($\lambda = .48$), the rib panels deform into an “S” shaped pattern so as to be compatible with the flexural deformation of the box as a whole. At slightly higher values of the loading parameter ($\lambda = .51$) the crushing loads, acting through the eccentricities formed by the deformed rib panel, begin inducing moments in the panel. These moments, while initially not large, act to magnify the panel deformations. As the deformations grow, the induced moments get larger and larger (beam-column effect). These moments quickly grow large enough to initiate a new failure mode; instead of deforming with the skin panel as the linear analysis predicts, the rib begins to deform independently of the skin. Eventually, the rib panel collapses (Figure 5.8). Plots of the axial load and bending moment at the mid-chord of the critical rib are presented in Figures 5.9 and 5.10. The bending moments in the rib are negligible until $\lambda = .48$, at which point they grow rapidly. The crushing loads themselves at this point are 30-40 *lb/in*.

When the nine design variable designs, B9G and B9GP, are subjected to a geo-

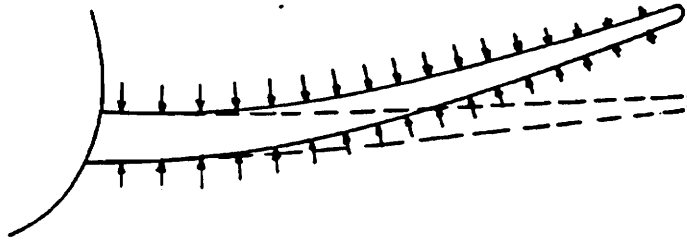


Figure 5.5: Nonlinear Crushing Loads

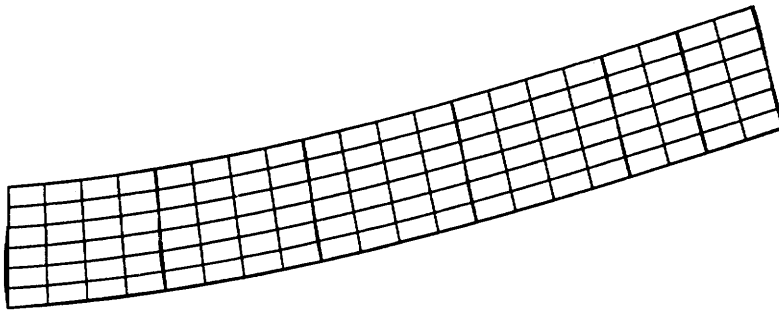


Figure 5.6: Design B3G – Nonlinear Deformed Mesh ($\lambda=.48$ Scale=30X)

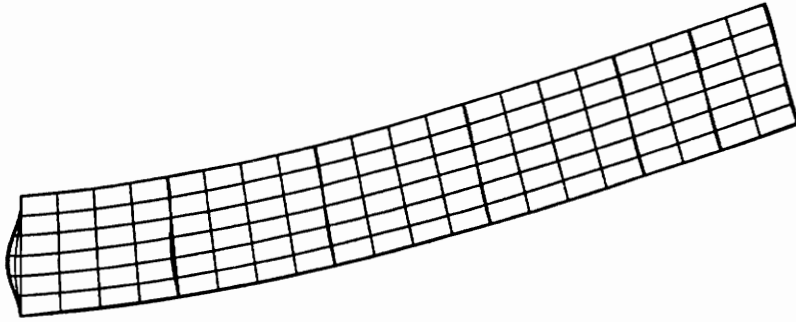


Figure 5.7: Design B3G – Nonlinear Deformed Mesh ($\lambda=.51$ Scale=30X)

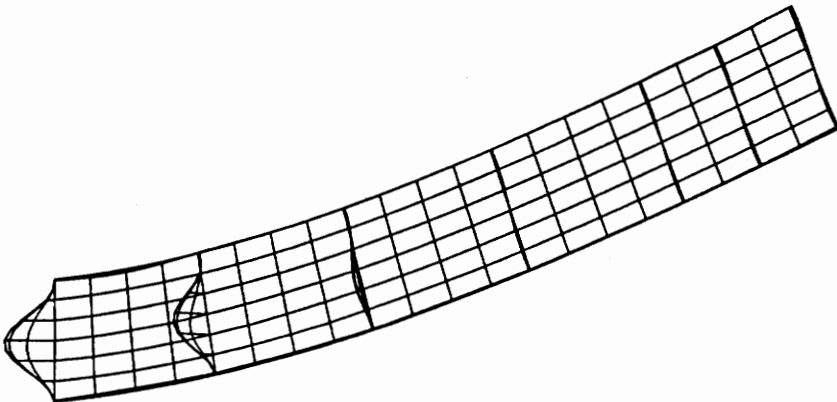


Figure 5.8: Design B3G – Nonlinear Deformed Mesh ($\lambda=.72$ Scale=30X)

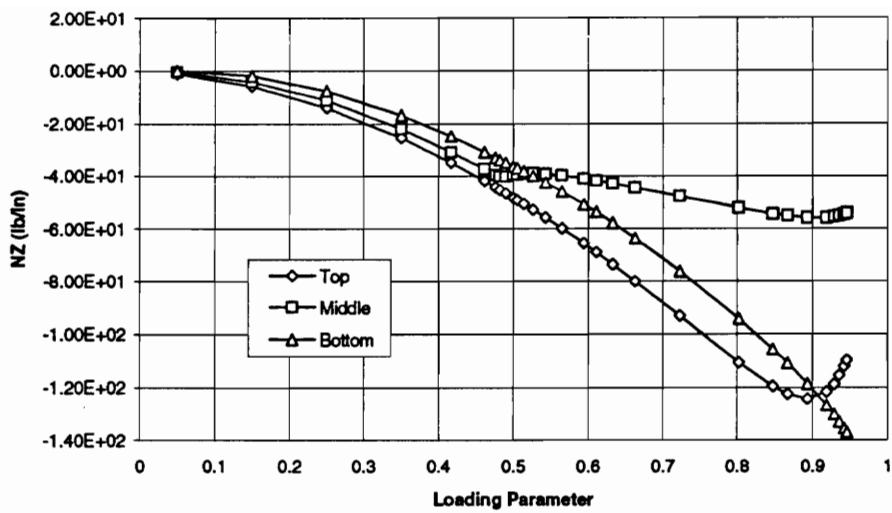


Figure 5.9: Design B3G – Critical Rib Crushing Loads (N_z)

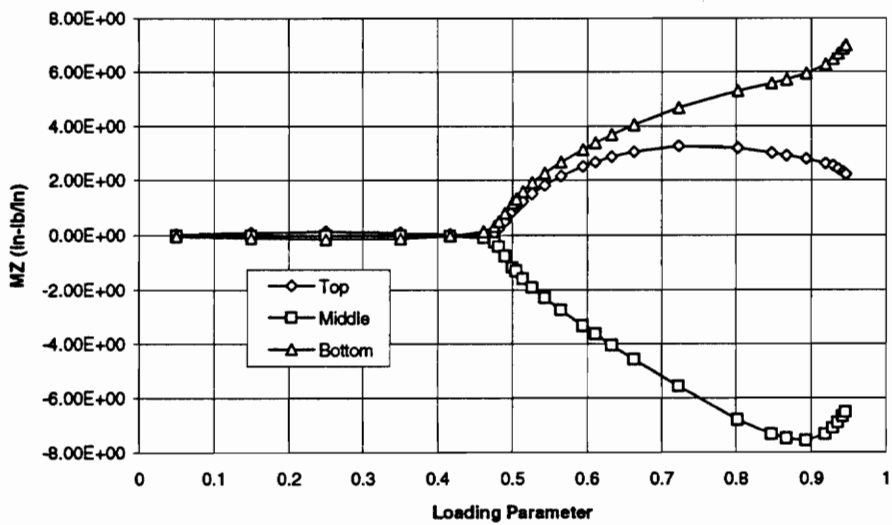


Figure 5.10: Design B3G – Critical Rib Bending Moment (M_z)

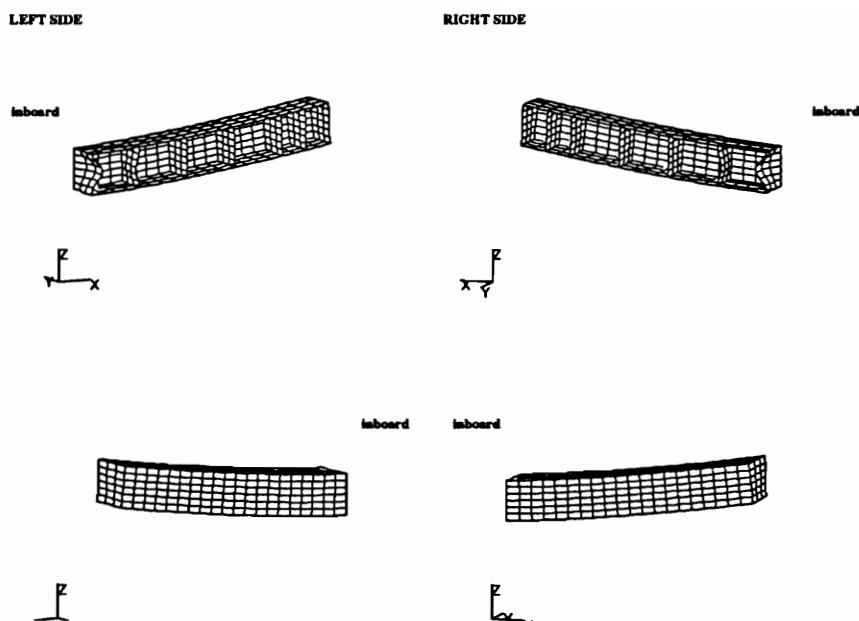


Figure 5.11: Design B9G - Nonlinear Deformed Mesh ($\lambda=.30$ Scale=30X)

metrically nonlinear analysis, they collapse in the same manner at even lower levels of the applied load. The B9G rib begins to collapse at $\lambda = .16$, and the B9GP rib begins to collapse at $\lambda = .40$. The deformed mesh for design B9G at $\lambda = .30$ is shown in Figure 5.11 and the skin, spar, and rib deformation history is plotted in Figure 5.12. The deformed mesh for design B9GP at $\lambda = .45$ is shown in Figure 5.13 and the skin, spar, and rib deformation history is plotted in Figure 5.14. The B9G rib collapses in the opposite direction of the other two designs, but the mechanism is the same.

Design B5GS, which was obtained with smeared stiffeners on the skin panel, behaves in the same manner as these unstiffened designs except that the collapse load is increased; the innermost rib begins its collapse at $\lambda = .72$. The deformed mesh at $\lambda = .83$ is shown in Figure 5.15, and the displacement history of the skin, spar, and rib panels is shown in Figure 5.16.

These results point out the potential dangers of relying solely on linear analysis techniques while at the same time illustrate an important panel interaction mechanism. In this case, the rib panels interact nonlinearly with the skin panels to drive a failure mode which cannot be predicted using linear analysis. For this structure

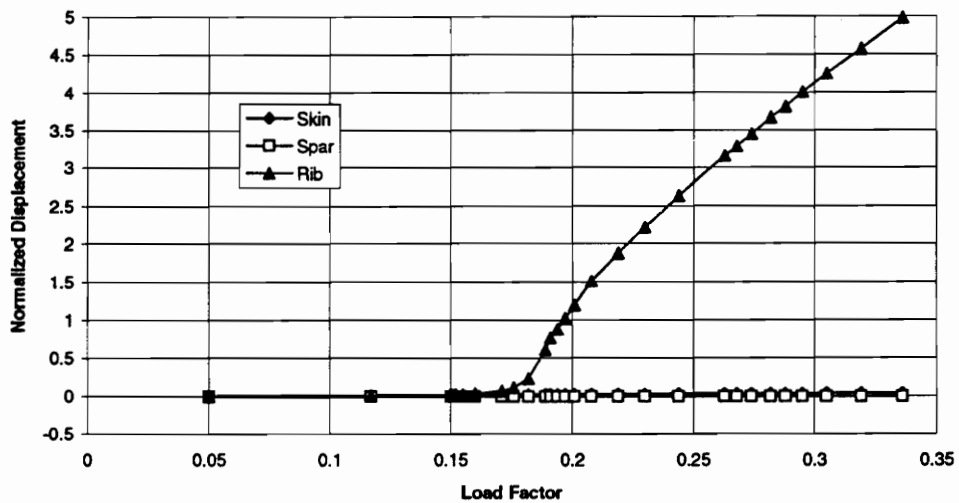


Figure 5.12: Design B9G – Nonlinear Deformation History

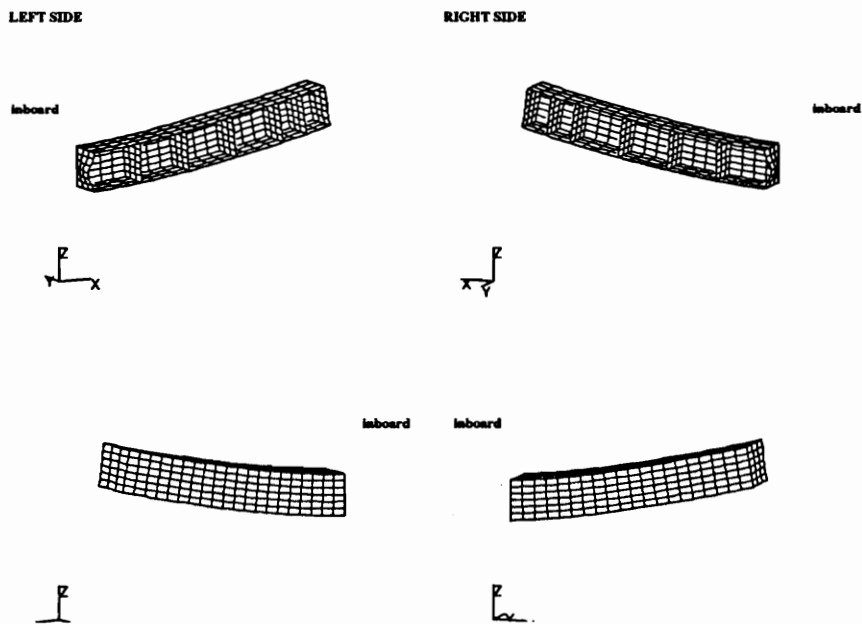


Figure 5.13: Design B9GP – Nonlinear Deformed Mesh ($\lambda = .45$ Scale=30X)

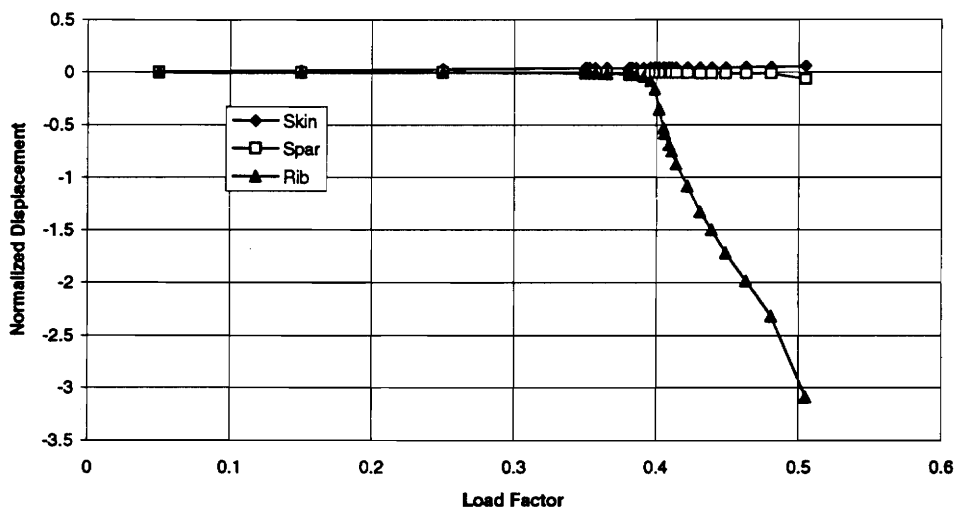


Figure 5.14: Design B9GP – Nonlinear Deformation History

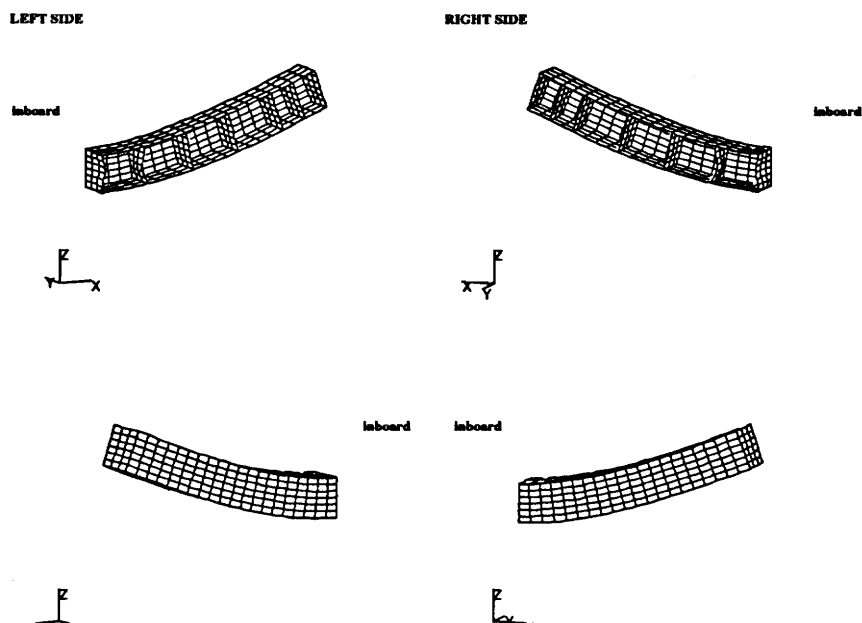


Figure 5.15: Design B9GP – Nonlinear Deformed Mesh ($\lambda = 0.83$ Scale = 30X)

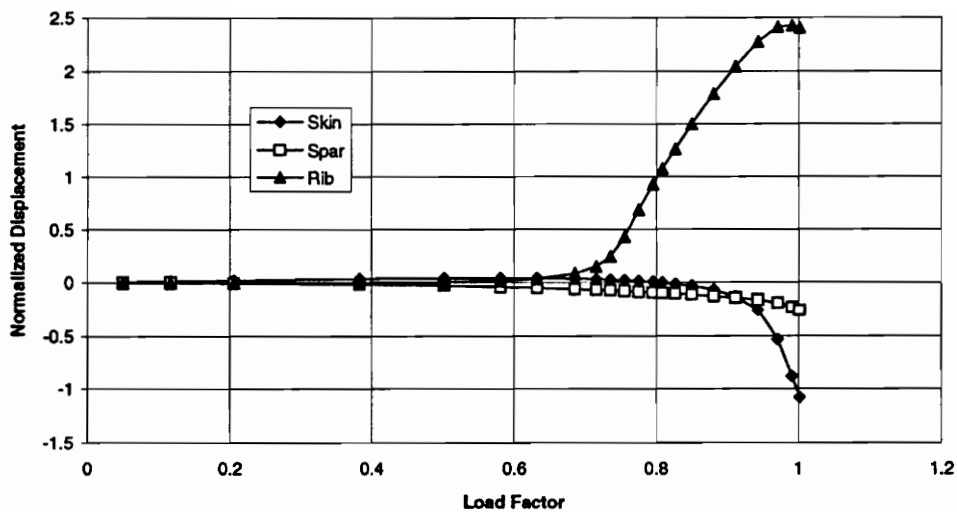


Figure 5.16: Design B5GS – Nonlinear Deformation History

and load case, then, geometrically nonlinear effects must be accounted for during the design optimization process.

These results seem to indicate that the severity of the nonlinearity is dependent on the rib thickness. The B9G rib, which is the thinnest, collapses at a lower load than the other designs. Likewise, the B3G rib, which is the thickest, collapses at the highest load.

Do these results mean that designs B3G–B9GP are completely infeasible and should be discarded? Can any changes can be made to these designs so that the failure load (and mode) predicted by linear analysis agrees with that predicted by the nonlinear analysis?

As it turns out, the parameter which determines whether or not a given design will collapse “prematurely” or not is the rib thickness. When the rib thickness in design B3G is increased by a factor of 1.5 (increased from .0948 *in* to .142 *in*), the new failure mode is the same as that predicted by the linear buckling analysis. Beginning at $\lambda = .72$, the skin, spar, and rib panels begin deforming together in a pattern similar to the interactive mode predicted by the linear analysis. These deformations gradually grow as the applied load increases, growing more rapidly as $\lambda = 1.00$ is

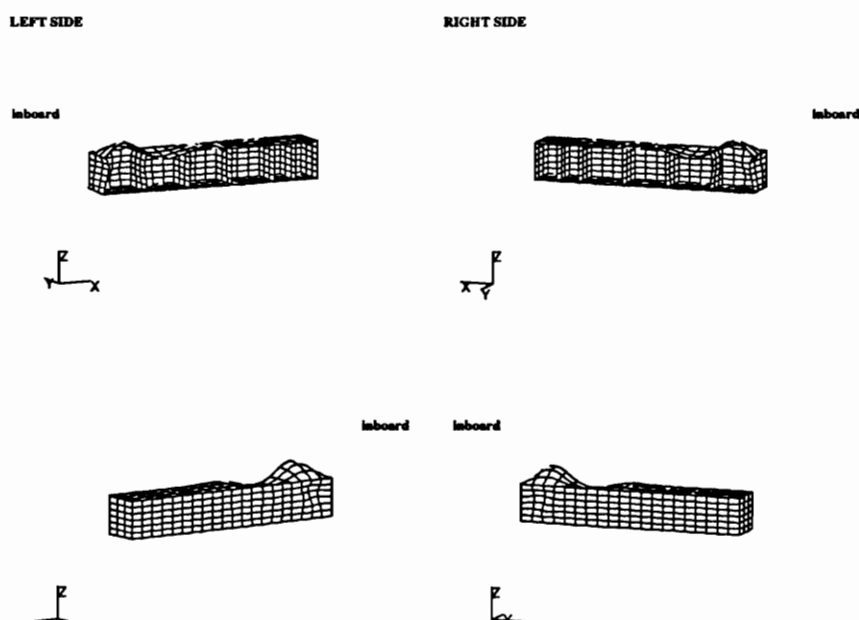


Figure 5.17: Design B3G (increased rib thk) – Critical Buckling Mode ($\lambda = 1.00$)

approached. The predicted linear buckling mode ($\lambda = 1.00$) is shown in Figure 5.17 and the deformed mesh obtained from the nonlinear analysis ($\lambda = 1.01$) is shown in Figure 5.18. The deformations of the skin, spar, and rib panels are plotted as a function of the applied load in Figure 5.19.

As opposed to the linear buckling analysis which assumes that there are no deformations until $\lambda = 1.00$, the structure begins to deform into its final shape at $\lambda = .72$. As soon as loads are applied to the structure, each of the subcomponent panels begins to deform. The skin and spar panels become curved as the box beam bends upward, and the rib panels deform so as to be compatible with the skin and spar panels. These induced deformations play the role of imperfections in each of the panels and cause the structure to behave like an “imperfect” structure.

Increasing the rib thickness, then, allows the “rib collapse” failure mode to be avoided in favor of a failure mode which is the same as, or similar to, that predicted by the linear analysis. This increased rib thickness may not significantly affect the optimal values of the skin and spar design values. An optimization run was made wherein the value of the rib design variable was fixed at 1.5 times its B3G value and the skin and spar design variables were allowed to vary as before. The results of

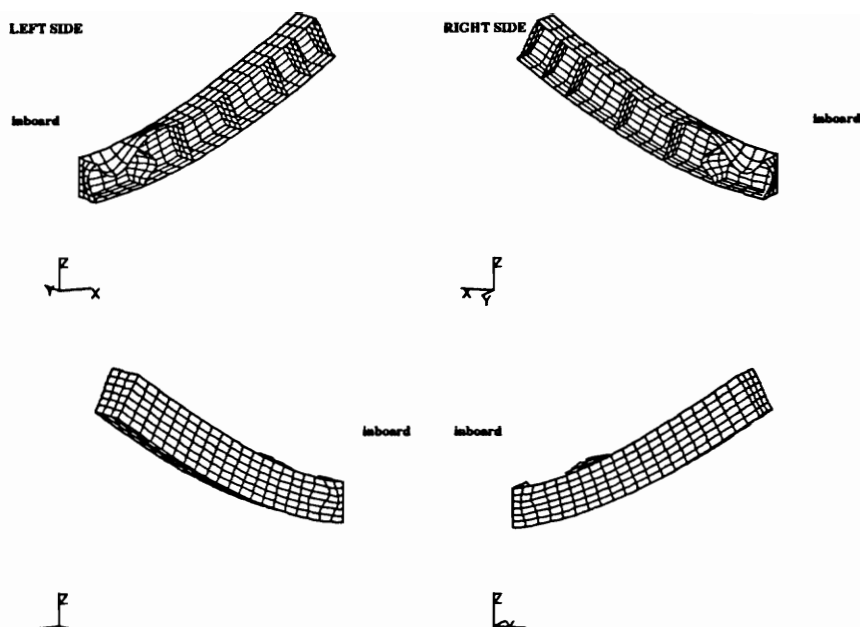


Figure 5.18: Design B3G (increased rib thk) – Nonlinear Deformed Mesh ($\lambda=1.01$ Scale=30X)

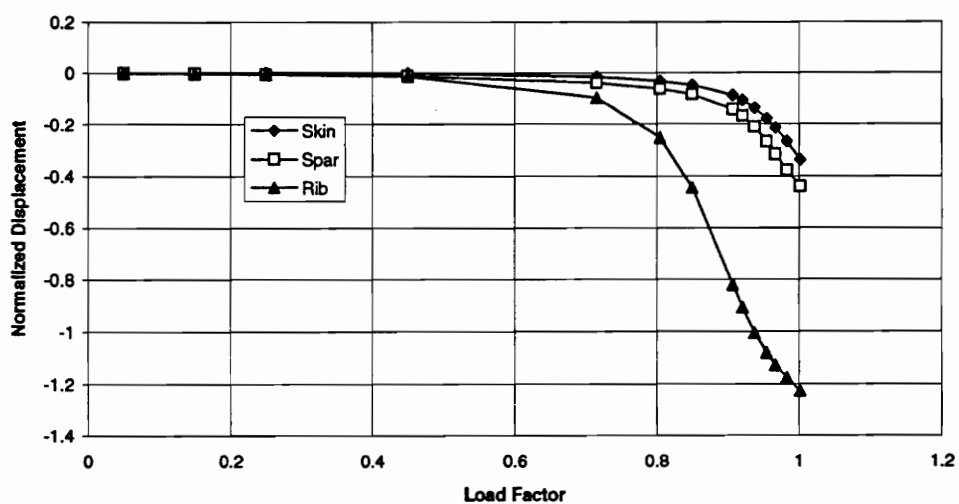


Figure 5.19: Design B3G (increased rib thk) – Nonlinear Deformation History

Table 5.1: Results – Design Case B2G

Design Case: B2G	
Geometry: 150"x48"x24"	
Rib Spacing: 30"	
Loading: Upward Bending	
Active Constraints:	
<i>Buckling Mode</i>	1
Eigenvalue	.9961
Description	Ply thickness (<i>in</i>)
Skin	.137
Spar	.0394
Rib	.0178
Weight (<i>lb</i>)	1101.6

this design run (Design B2G) are given in Table 5.1. The values of the skin and spar design variables are not significantly different from those obtained for design B3G (the maximum difference is 0.2%). This result is obtained because the rib design variable was not strongly coupled to the skin and spar design variables for this bending load case. The total structural weight for this case is 1101.6 *lb*, only 1.2% greater than for design B3G. The increase is small because the rib panels make up a small percentage of the overall structural weight.

These results suggest that the optimal bending designs obtained using the linear analysis may still be used if the rib thickness is increased by some factor. This factor would have to be determined separately in each case (by performing one or more nonlinear analyses), but this procedure would still be more efficient than including nonlinear analysis in the optimization process. To determine the “true” optimal design, of course, nonlinear analysis would have to be included in the design optimization process.

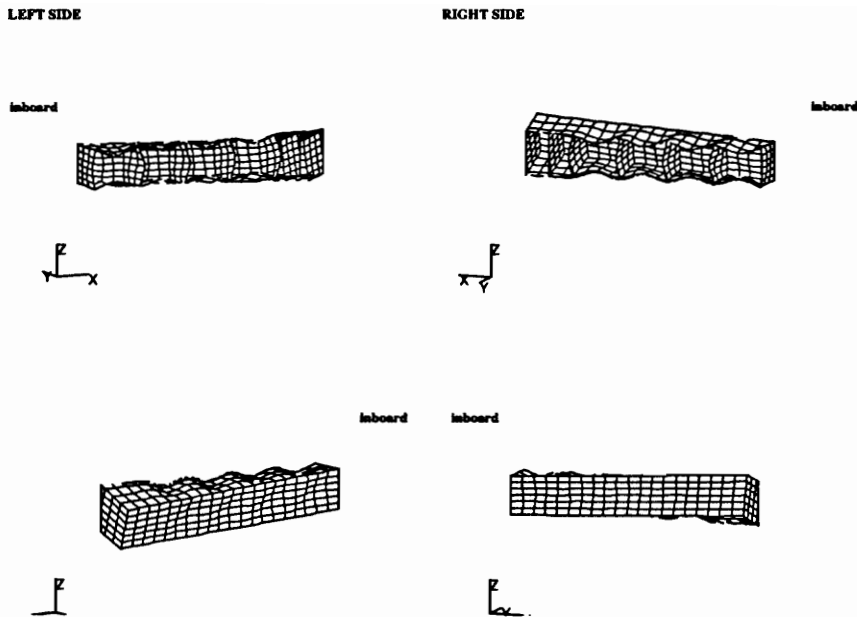


Figure 5.20: Design T3G – Nonlinear Deformed Mesh ($\lambda=1.02$ Scale=10X)

5.2 Torque Designs

When the three design variable torque design, T3G (See Chapter 4), is subjected to a nonlinear analysis, the skin, spar, and rib panels all begin to deform out of plane near $\lambda = .32$. Deformations remain small, however, and do not exceed half the panel thickness until λ nears 0.80. These deformations grow more rapidly as λ approaches 1.00.

The deformed shape at $\lambda = 1.02$ is shown in Figure 5.20, and a plot of the skin, spar, and rib deformation history is given in Figure 5.21. The final deformed shape does not look like either of the active buckling modes predicted by the linear buckling analysis (Chapter 4), but is instead very similar to the *third* buckling mode predicted by the linear analysis. This third mode was not active for design T3G, but was very close to being so: the eigenvalue for this mode was 1.016.

In this case, then, the nonlinear analysis does not predict a new failure mode, but instead predicts a deformation pattern that is similar to that predicted by the third mode obtained from a linear buckling analysis. As with the bending case, deformations are induced in the individual panels as soon as load is applied to the

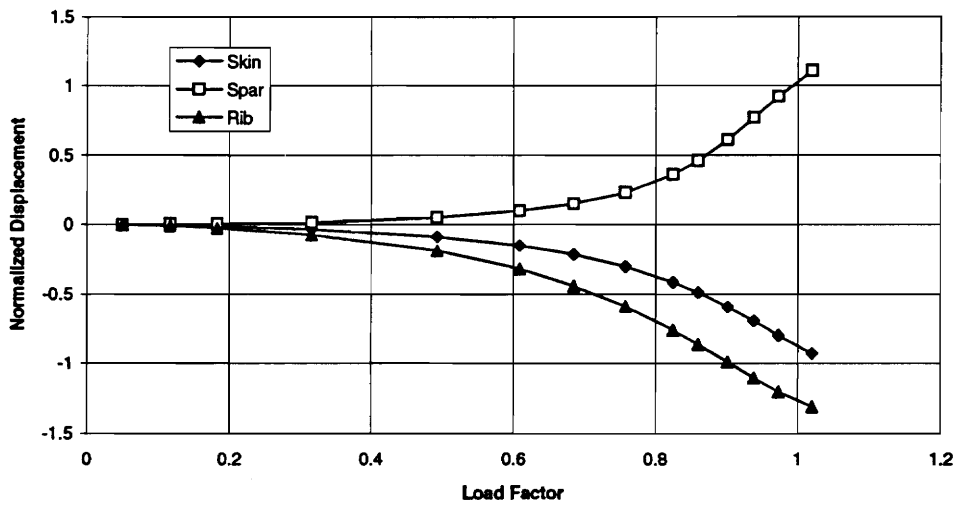


Figure 5.21: Design T3G – Nonlinear Deformation History

structure. As a result, the flat panels behave like imperfect panels, and the final deformation pattern begins to appear at lower load levels.

The nine design variable torque design, T9G, behaves similarly, with the out of plane deformations again beginning again near $\lambda = .32$. The deformed mesh at $\lambda = 1.01$ is shown in Figure 5.22 and the skin, spar, and rib deformation history is illustrated in Figure 5.23.

The torque design with smeared skin stiffeners, TG5S, behaves somewhat differently. Here, out of plane deformations begin near $\lambda = .21$, but in contrast to the unstiffened cases, the normalized spar deformations are larger than the normalized skin and rib deformations. Nevertheless, there does not appear to be any sudden collapse of the structure, and the deformations increase smoothly as the load is increased. The deformed mesh at $\lambda = 1.00$ is illustrated in Figure 5.24 and the deformation history is plotted in Figure 5.25.

5.3 Combined Bending/Torque Designs

Both the three and nine design variable bending/torque designs (C3G and C9GP) behave similarly to the bending designs. In both cases, the innermost rib collapses

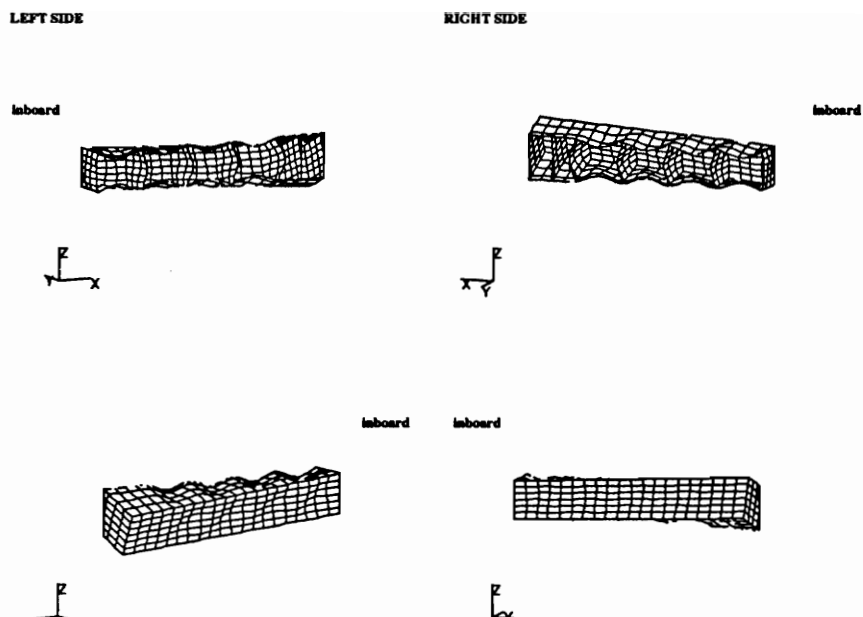


Figure 5.22: Design T9G – Nonlinear Deformed Mesh ($\lambda=1.01$ Scale=10X)

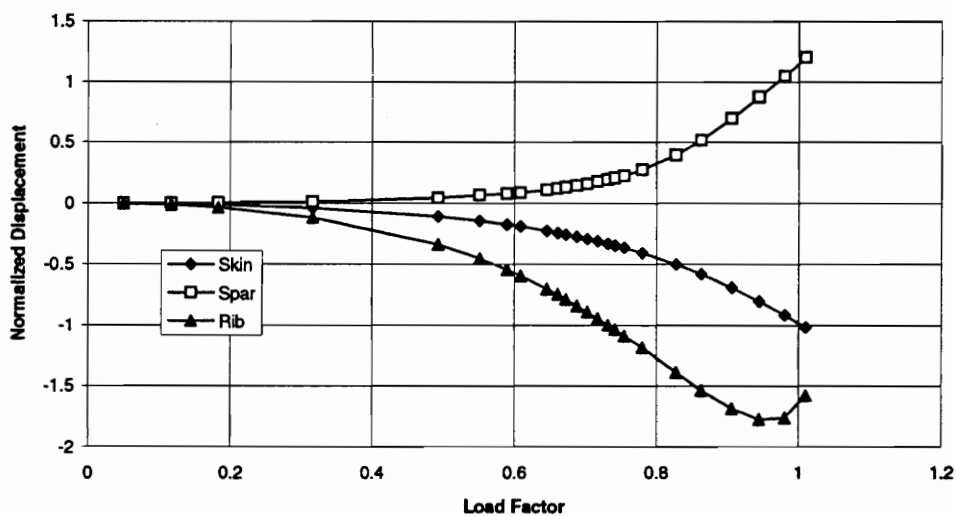


Figure 5.23: Design T9G – Nonlinear Deformation History

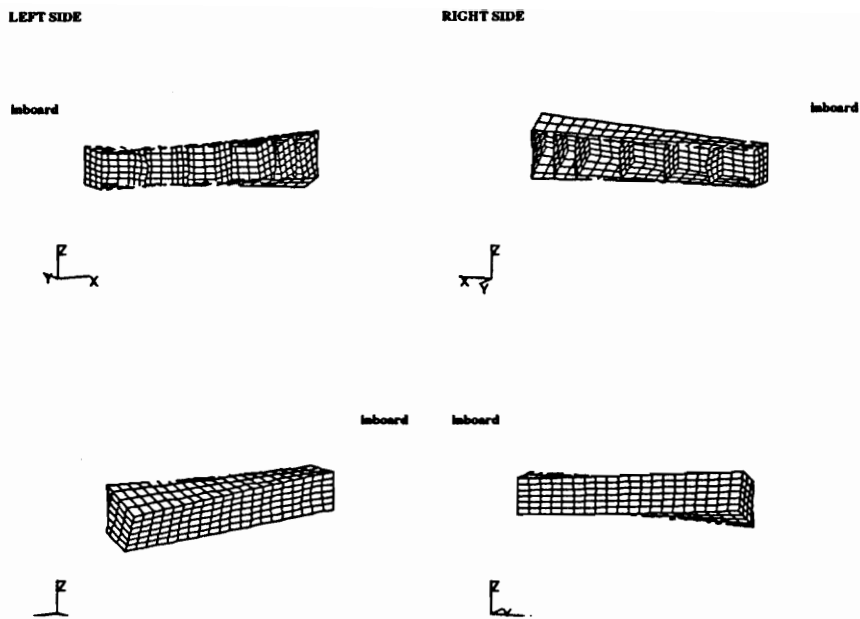


Figure 5.24: Design T9G – Nonlinear Deformed Mesh ($\lambda=1.00$ Scale=10X)

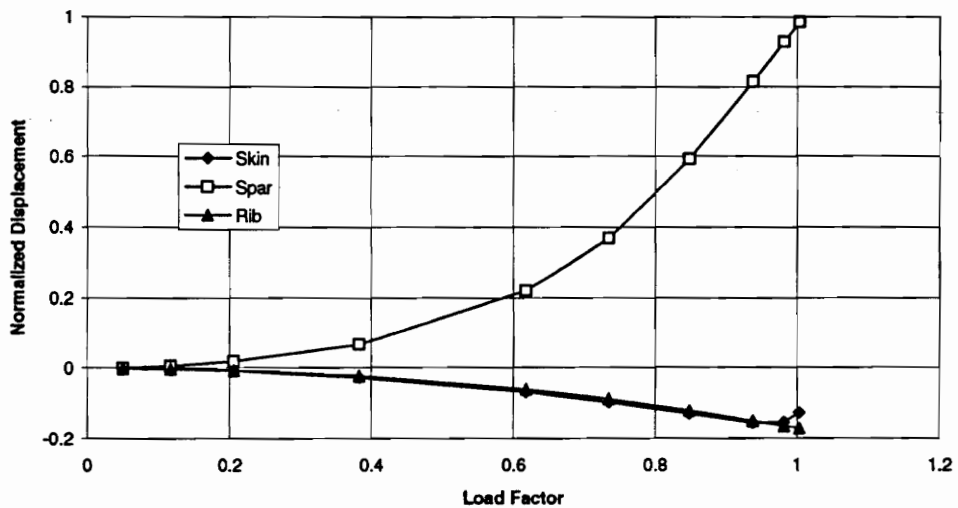


Figure 5.25: Design T5GS – Nonlinear Deformation History

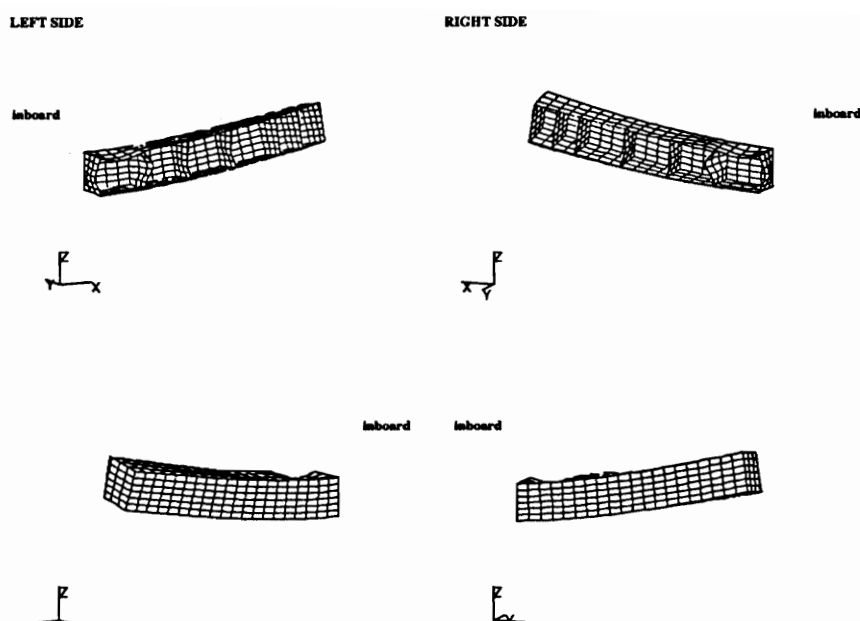


Figure 5.26: Design C3G – Nonlinear Deformed Mesh ($\lambda=0.97$ Scale=10X)

prematurely in a mode not predicted by the linear buckling analysis. The C3G rib begins to collapse at $\lambda = .50$, and the C9GP rib begins to collapse at $\lambda = .58$. The deformed meshes for these two cases are shown in Figures 5.26 and 5.27, and the spar, skin, and rib deformation histories are shown in Figures 5.28 and 5.29. The mechanism causing rib collapse is the same as for the bending designs.

A different result is obtained for the design with smeared skin stiffeners (C5GS), however. In this case, the final deformed shape agrees with that predicted by the linear analysis. The panels begin to deform out of plane immediately upon load deformation, but the deformations do not grow large until λ approaches 1.00. The nonlinear deformed shape is at $\lambda = 1.02$ is illustrated in Figure 5.30 and the skin, spar, and rib deformation history is plotted in Figure 5.31. This behavior can be explained by considering the rib thickness. Design C5GS has a rib thickness that is more than 50% thicker than the C3G and C9GP ribs. As explained in conjunction with the bending designs, this increased rib thickness allows the structure to avoid the rib collapse failure mode that is associated with the other designs.

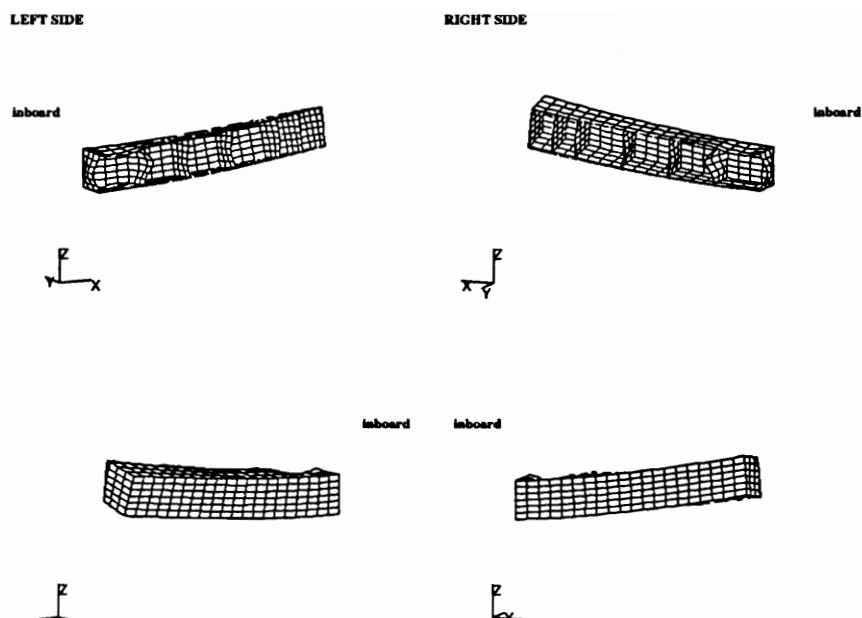


Figure 5.27: Design C9GP – Nonlinear Deformed Mesh ($\lambda=0.97$ Scale=10X)

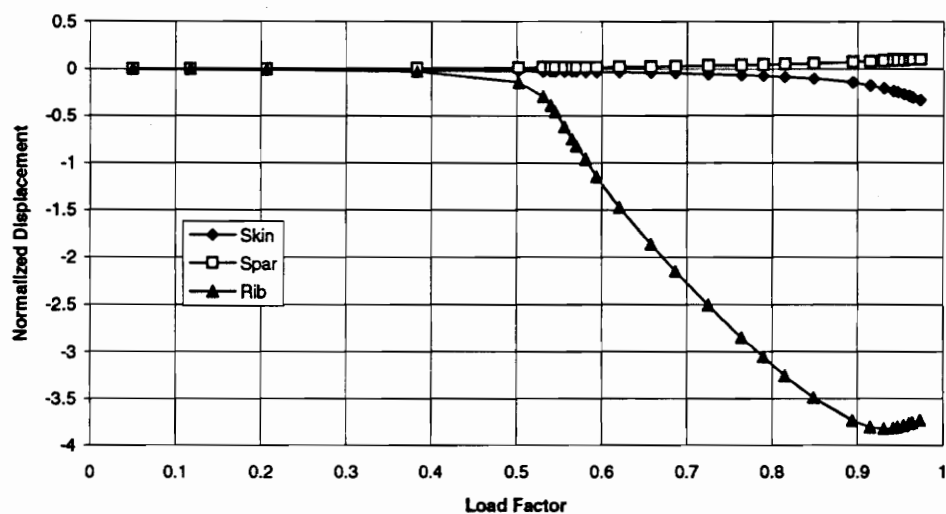


Figure 5.28: Design C3G – Nonlinear Deformation History

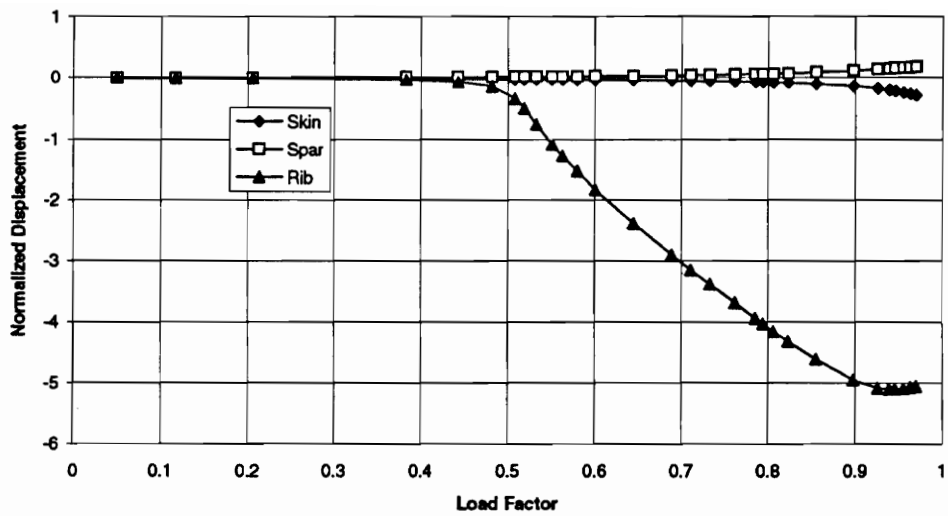


Figure 5.29: Design C9GP – Nonlinear Deformation History

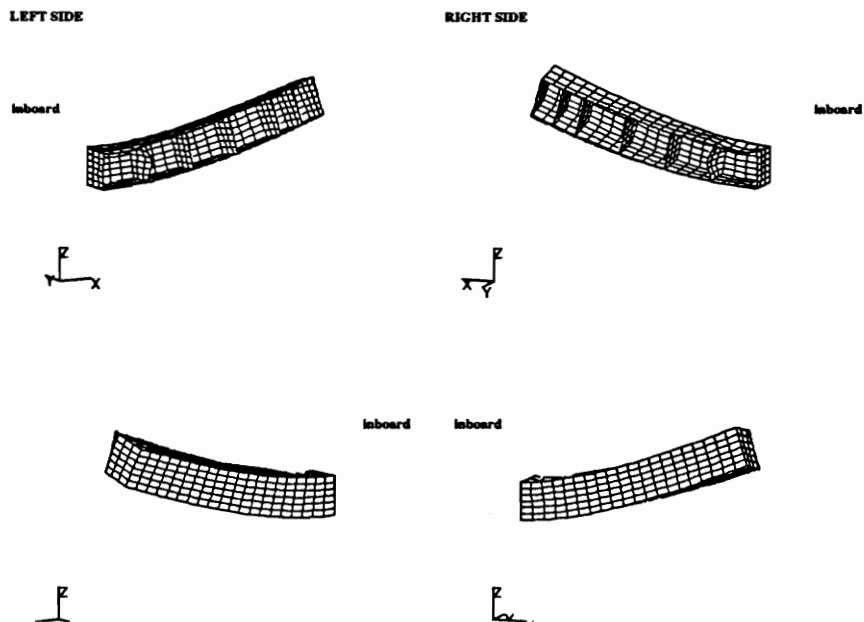


Figure 5.30: Design C5GS – Nonlinear Deformed Mesh ($\lambda=1.02$ Scale=10X)

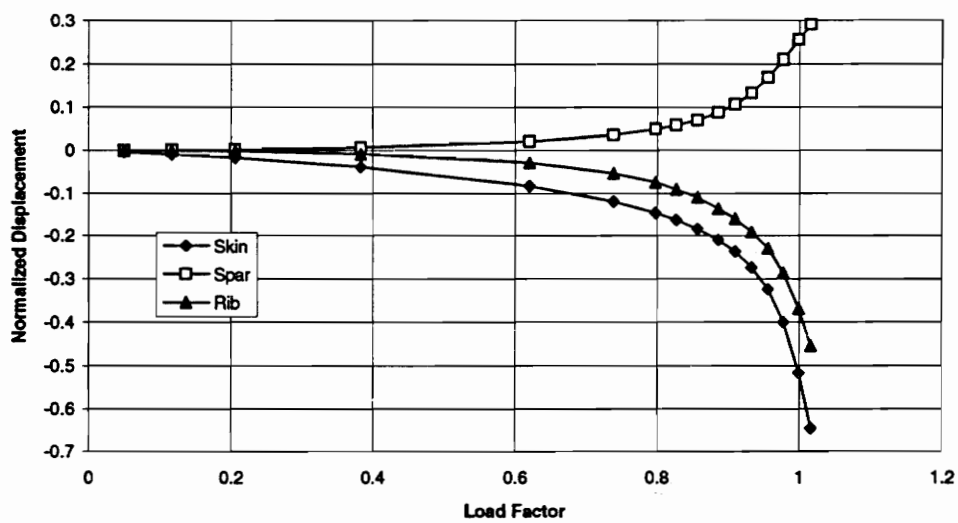


Figure 5.31: Design C5GS – Nonlinear Deformation History

CONCLUSIONS AND RECOMMENDATIONS FOR FUTURE WORK

6.1 Conclusions

All of the designs presented in this study (both local and global) exhibited some form of subcomponent panel interaction (instances where the design and/or response of one panel significantly affected the design and/or response of neighboring or attached panels). Some of this interaction occurred because of simple load redistribution. When the design of one component changed, the global load path changed as well, affecting both the design and response of other components in the structure. This type of interaction is common, and occurs in all redundant structures with multiple load paths. In the bending load case, a second type of interaction occurred. Here, the design of the skin and spar panels affected the critical rib loads and failure modes. This interaction was not a result of load redistribution, but occurred because of loads that the skin and spar panels induced in the rib panel.

Those designs obtained using the global approach (based on a global buckling analysis) exhibited a third and more complex type of interaction which did not occur in those designs obtained using the local approach. Each of the global designs had at least one buckling mode that was characterized by the compatible buckling of one or more of the subcomponent panels in the structure. This “interactive” mode usually involved the buckling of the upper skin panel, the inboard spar panels, and the first or second rib panel. The constraint gradients for this mode indicated that the skin, spar, and rib design variables were coupled (often strongly) in this mode. The coupling in the local designs was either small or non-existent.

The designs obtained using the local approach were from 3-7% heavier compared to their global counterparts. These results were found for several different load cases and for structures with both quasi-isotropic and more general panel designs. When the global panel designs were compared to the local panel designs, no clear trends were found. Most of the local panel designs had the same ply distributions as did their global counterparts with the only difference being the overall panel thickness. Two of the local designs (B9L and T9L) contained panels which had different ply

distributions than their global counterparts. Most of the local designs were more conservative than the global designs. In other words, when the local designs were analyzed using the global approach, they were found to have a higher than necessary buckling load. The local design B9L failed prematurely, however, and this indicates that the local approach potentially yields unsafe designs.

These results indicate that there can be an advantage to using a global analysis instead of a local analysis to design these structures. This is not just because of the usual reasons (concerns with load re-distribution), but because the subcomponent panels have the potential to interact with one another in a complex manner. The resulting global structure can be lighter than its local counterpart, and may have panel designs which differ from those obtained using the local approach. Because of the added expense of the global approach a trade-off may need to be made between the increased accuracy of the global approach and the low cost of the local approach.

Designs obtained with a stiffened skin panel (using smeared stiffeners) were from 30-50% lighter than designs obtained with an unstiffened skin panel. The resulting skin design was more realistic and is similar to designs that are found in "real" aircraft.

When designs with different rib spacings were considered (30.0, 22.5, and 15.0 *in*), different results were obtained for those designs with a stiffened skin panel and those without a stiffened skin panel. The unstiffened designs decreased in weight as the rib spacing decreased as the extra weight of the added rib panels was more than offset by the weight savings obtained in the skin and spar panels. The stiffened designs decreased in weight as the spacing decreased from 30.0 *in* to 22.5 *in*, but increased in weight as the spacing decreased from 22.5 *in* to 15.0 *in*. Here, the weight savings obtained in the skin and spar panels as the rib spacing decreased was much less than in the unstiffened case.

In all the cases examined, the nonlinear behavior of the linearly optimized designs was similar to that of an imperfect structure. In other words, the structure began to deform into its final shape before the design load was reached and there was no distinct buckling or bifurcation point. In the case of the torque load case, the final deformation pattern was the same as or similar to modes predicted by the linear buckling analysis. In most of the cases where bending loads were included, however, the innermost rib began to collapse at low load levels in a mode not predicted by the linear buckling analysis. It was determined that this "rib collapse" failure mode was a function of the rib thickness and that it could be avoided by increasing the rib

thickness beyond the value obtained from the optimization process.

The rib collapse mode illustrates an important nonlinear interaction mechanism and illustrates the potential dangers relying solely on a linear analysis. For the present structure (if it is subjected to bending type loads) nonlinear analysis would need to be used if a “true” optimum were to be found. It is noted that this failure mode is captured by a global approach to the problem, and would not be captured by an approach in which the response of each panel is analyzed separately.

6.2 Recommendations for Future Work

The linear design study could be made more complete by considering additional design variables and design considerations. For example, more realistic designs could be obtained by including design variables to separately describe the upper and lower skin panel designs. In this case, it is likely that the point strain constraints would become active and contribute to the design of the lower skin panel. It would also be beneficial to add additional design variables so that the skin and spar panels could be tapered along the length of the structure so that the different rib panels could have different designs. Additional design runs could be performed which include smeared stiffeners on each of the three panel types, instead of on the skin panel only.

In order to extend the design study in this way, it would probably be necessary to improve the efficiency of the optimization system. One way this may be accomplished is to experiment with different eigensolver routines in order to find an algorithm which is more efficient than that used in the present work.

Additional improvements could be made to the linear design study by considering other load cases and different box-beam geometries. Instead of obtaining separate designs for each load case, it would be beneficial to obtain designs which are subject to two or more load cases at the same time. Designs may be obtained for different values of box-beam length, width, and height, and for a wider range of rib spacing. More complex box-beam designs, such as would be found in a swept wing may also be considered. Different methods of mathematically smearing the stiffeners into the base laminate could be investigated as well.

The results of the geometrically nonlinear analysis of the linearly optimized designs indicate that it may be important to include geometrically nonlinear analysis in the design optimization system for some of these designs. Because this would be

an expensive proposition, it would be worthwhile to consider methods of efficiently including geometrically nonlinear analysis in the design optimization process. This may be accomplished by the development of efficient nonlinear analysis schemes or by linking the nonlinear analysis procedure with the design optimization procedure using a procedure such as that proposed by Haftka [45].

REFERENCES

- [1] Madan, R.C., "Composite Transport Wing Technology Development", NASA CR-178409, February, 1988.
- [2] Sakata, I.F, and Ostrom, R.B., "Study on Utilization of Advanced Composites in Commercial Aircraft Wing Structures – Final Report", NASA CR-145381-2, August, 1978.
- [3] Watts, D.J., "A Study on the Utilization of Advanced Composites in Commercial Aircraft Wing Structure – Final Report", NASA CR-158902-2, July, 1978.
- [4] Griffin, C.F., and Harvill, W.E., "Composite Transport Wing Technology Development – Design Development Tests and Advanced Structural Concepts", NASA CR-4177, 1988.
- [5] Griffin, C.F., and Meade, L.E., "Design, Analysis and Fabrication of the Technology Integration Box Beam", Proceedings of the First NASA Advanced Composites Technology Conference, Seattle, WA, October 29 – November 1, 1990, NASA CP-3104, Part 1, 1991, pp. 157-178.
- [6] Griffin, C.F., "Structural Testing of the Technology Integration Box Beam", Presented at the 9th DoD/NASA/FAA Conference on Fibrous Composites in Structural Design, Lake Tahoe, NV, November 4-7, 1991.
- [7] Davis, D.D., Jr., Farley, G.L., Ambur, D.R., Davis, R.C., Shuart, M.J., Wang, J.T., and Lotts, C.G., "An Analytically Designed Subcomponent Test to Reproduce the Failure of a Composite Wing Box Beam", Presented at the 34th AIAA/ASME/ASCE/AHS/ASC Structures, Structural Dynamics and Materials Conference, La Jolla, CA, April 19-22, 1993.
- [8] Chen, V., Hawley, A., Klotzsche, M., Markus, A., and Palmer, R., "Composites Technology for Transport Primary Structure", Proceedings of the First

NASA Advanced Composites Technology Conference, Seattle, WA, October 29—November 1, 1990, NASA CP-3104, Part 1, 1991.

- [9] Byers, B.A., and Stoecklin, R.L., "Preliminary Design of Graphite Composite Wing Panels for Commercial Transport Aircraft", NASA CR-159150, February, 1980.
- [10] Romeo, G., "Experimental Investigation on Advanced Composite-Stiffened Structures Under Uniaxial Compression and Bending", *AIAA Journal*, Vol. 24, No. 11, November, 1986.
- [11] Adelman, H.M., Haftka, R.T., and Tsach, U., "Application of Fully Stressed Design Procedures to Redundant and Non-Isotropic Structures", NASA TM-81842, July, 1980.
- [12] Stroud, J.S., and Agranoff, N., "Minimum Mass Design of Filamentary Composite Panels Under Combined Loads: Design Procedure Based in Simplified Buckling Equations", NASA TN-D-8257, 1977.
- [13] Swanson, G.D., and Gürdal, Z., "Structural Efficiency Study of Graphite-Epoxy Aircraft Rib Structures", *Journal of Aircraft*, Vol. 27, No. 12, 1990, pp. 1011-1020.
- [14] Stroud, W.J., and Anderson, M.S., "PASCO: Structural Panel Analysis and Sizing Code, Capability and Analytical Foundations", NASA TM-80181, November, 1981.
- [15] Sobieszczanski-Sobieski, J., "An Integrated Computer Procedure for Sizing Composite Airframe Structures", NASA TP-1300, 1979.
- [16] Starnes, J.H., Jr., and Haftka, R.T., "Preliminary Design of Composite Wings for Buckling, Strength, and Displacement Constraints", *Journal of Aircraft*, Vol. 16, 1979, pp. 564-570.
- [17] Haftka, R.T., and Starnes, J.H., Jr., "WIDOWAC (Wing Design Optimization With Aeroelastic Constraints): Program Manual", NASA TM-X-3071, 1974.

- [18] Schmit, L.A., and Mehrinfar, M., "Multilevel Optimum Design of Structures with Fiber-Composite Stiffened-Panel Components", *AIAA Journal*, Vol. 20, No. 1, 1980.
- [19] Watkins, R.I., "Optimal Design of Large Laminated Structures", ICAS Paper No. 88-1.10.2, 1988, pp. 1480-1486.
- [20] Walsh, J., "Application of Mathematical Optimization Procedures to a Structural Model of a Large Finite Element Wing", NASA TM-87597, 1988.
- [21] Antona, E., and Gabrielli, G., "An Experimental Investigation on Wing Box Beams in Bending", ICAS Paper No. 70-83, September, 1970.
- [22] Antona, E., and Romeo, G., "Analytical and Experimental Investigation of Advanced Composite Wing Box Structures in Bending Including Effects of Initial Imperfections and Crushing Pressure", ICAS Paper No. 86-4.2.3, 1986, pp. 255-261.
- [23] Niu, M.C.Y., *Airframe Structural Design-Practical Design Information and Data on Aircraft Structures*, Conmilit Press Ltd., 1990.
- [24] Stewart, C.B. (compiler), "The Computational Structural Mechanics Testbed User's Manual", NASA TM-100644, 1989.
- [25] Knight, N.F. Jr., Gillian, R.E., McCleary, S.L., Lotts, C.G., Poole, E.L., Overman, A.L., and Macy, S.C., "CSM Testbed Development and Large-Scale Applications", NASA TM-4072, 1989.
- [26] Gendron, G., "An Optimization System Based on the Finite Element Code CSM Testbed", Report VPI-E-91-17, Virginia Polytechnic Institute and State University, Blacksburg, Virginia, 1991.
- [27] Gendron, G., "Optimal Design of Geodesically Stiffened Composite Cylindrical Shells", Ph.D. Dissertation, Virginia Polytechnic Institute and State University, September, 1991.

- [28] Stewart, C.B. (compiler), "The Computational Structural Mechanics Testbed Procedures Manual", NASA TM-100646, December, 1991.
- [29] Crisfield, M.A., "A Fast Incremental/Iterative Procedure That Handles Snap-Through", *Computers and Structures*, Vol. 13, 1983, pp. 55-62.
- [30] Stanley, G., and Nour-Omid, S., "The Computational Structural Mechanics Testbed Generic Structural-Element Processor Manual", NASA CR-181728, March, 1990.
- [31] Haftka, R.T., and Gürdal, Z., *Elements of Structural Optimization*, Third revised and expanded edition, Kluwer Academic Publishers, 1992.
- [32] Vanderplaats, G.N., "ADS-A FORTRAN Program for Automated Design Synthesis – Version 1.10", NASA CR-177985, 1985.
- [33] Fleury, C. and Braibant, V., "Structural Optimization; A New Dual Method Using Mixed Variables", LTAS Report SA-115, University of Leige, Leige, Belgium, March, 1984.
- [34] Arora, J.S., *Introduction to Optimum Design*, McGraw-Hill Book Company, 1989.
- [35] Vanderplaats, G.N., "An Efficient Feasible Directions Algorithm for Design Synthesis", *AIAA Journal*, Vol. 22, No. 11, October, 1984, pp. 1633-1640.
- [36] Zoutendijk, M., *Methods of Feasible Directions*, Elsevier Publishing Co., Amsterdam, 1960.
- [37] Vanderplaats, G.N. and Moses, F., "Structural Optimization by Methods of Feasible Directions", *Journal of Computers and Structures*, Vol. 3, July, 1973, pp. 739-755.
- [38] Whitney, J.M., *Structural Analysis of Laminated Anisotropic Plates*, Technomic Publishing Co., Inc., Lancaster, PA, 1987.

- [39] Lekhnitskii, S.G. (S.W. Tsai and T. Cheron, transl.), *Anisotropic Plates*, Gordon and Breach Science Publishers, New York, 1968.
- [40] Stroud, W.J., Greene, W.H., and Anderson, M.S., "Buckling Loads of Stiffened Panels Subjected to Combined Longitudinal Compression and Shear: Results Obtained With PASCO, EAL, and STAGS Computer Programs", NASA TP-2215, 1984.
- [41] Nagendra, S., Haftka, R.T., and Gürdal, Z., "Design of a Blade Stiffened Composite Panel By a Genetic Algorithm", Presented at the 34th AIAA/ASME/ASCE/AHS/ASC Structures, Structural Dynamics and Materials Conference, La Jolla, CA, April 19-22, 1993.
- [42] Stanley, G.M., "The Computational Structural Mechanics Testbed Structural Element Processor ES1: Basic SRI and ANS Shell Elements", NASA CR-4357, 1991.
- [43] Thompson, J.M.T., "Optimization as a Generator of Structural Instability", *International Journal of Mechanical Sciences*, Vol. 14, 1972, pp. 627-629.
- [44] Thompson, J.M.T., and Hunt, G.W., "Dangers of Structural Optimization", *Engineering Optimization*, Vol. 1, No. 2, 1974, pp. 99-110.
- [45] Haftka, R.T., "Integrated Nonlinear Structural Analysis and Design", *AIAA Journal*, Vol. 27, No. 11, November 1989, pp. 1622-1627.

Appendix A

DERIVATION OF THE BUCKLING LOAD OF A SIMPLY SUPPORTED PLATE SUBJECT TO A LINEARLY VARYING EDGE LOAD

The equations used to obtain the buckling load of a simply supported plate subjected to a linearly varying end load are derived here. The development follows the same general procedure that is used in Reference [38] to derive the buckling loads for simply supported plates subject to uniform end loading.

Equations will be derived to obtain the buckling load of a simply supported plate subjected to a load N_x which varies linearly in the y direction. The equations for a N_y load will be similar. In the following development, N_x (positive in tension) will be assumed to vary as follows:

$$N_x(y) = \bar{N}_x(1 - \alpha \frac{y}{b}) \quad (\text{A.1})$$

where α is a constant which may take on any value from 0.0 to 2.0 and \bar{N}_x is a constant representing the maximum value of $N_x(y)$. The plate is assumed to have dimensions a in the x direction and b in the y direction. Assuming the plate to be specially orthotropic ($D_{16} = D_{26} = 0$) the boundary conditions at $x = 0, a$ are

$$w = 0 \quad (\text{A.2})$$

$$M_x = -D_{11} \frac{\partial^2 w}{\partial x^2} - D_{12} \frac{\partial^2 w}{\partial y^2} = 0 \quad (\text{A.3})$$

and the boundary conditions at $y = 0, b$ are

$$w = 0 \quad (\text{A.4})$$

$$M_y = -D_{12} \frac{\partial^2 w}{\partial x^2} - D_{22} \frac{\partial^2 w}{\partial y^2} = 0. \quad (\text{A.5})$$

The expression for the potential energy, V , of N_x due to a deflection, w , is:

$$V = \frac{1}{2} \int_0^a \int_0^b N_x \left(\frac{\partial w}{\partial x} \right)^2 dx dy \quad (\text{A.6})$$

where it is assumed that the midplane strain, ϵ_x^0 , has the form

$$\epsilon_x^0 = \frac{1}{2} \left(\frac{\partial w}{\partial x} \right)^2. \quad (\text{A.7})$$

For the pure bending case, the strain energy of the plate, U , takes on the form:

$$U = \frac{1}{2} \int_0^a \int_0^b \left[D_{11} \left(\frac{\partial^2 w}{\partial x^2} \right)^2 + 2D_{12} \frac{\partial^2 w}{\partial x^2} \frac{\partial^2 w}{\partial y^2} + D_{22} \left(\frac{\partial^2 w}{\partial y^2} \right)^2 + 4D_{66} \left(\frac{\partial^2 w}{\partial x \partial y} \right)^2 \right] dx dy + C \quad (\text{A.8})$$

where C is an arbitrary constant. From Hamilton's principle, the governing equations and boundary conditions may be obtained:

$$\int_{t_0}^{t_1} (\partial U + \partial V) dt = 0 \quad (\text{A.9})$$

where $t_0 \leq t \leq t_1$ is an arbitrary time interval. The first variation of the potential energy is:

$$\delta V = \int_0^a \int_0^b \bar{N}_x \left(1 - \alpha \frac{y}{b} \right) \frac{\partial w}{\partial x} \frac{\partial}{\partial x} (\delta w) dx dy \quad (\text{A.10})$$

Integrating by parts and using Green's Theorem, we have

$$\delta V = \int_{S_x} \bar{N}_x \left(1 - \alpha \frac{y}{b} \right) \frac{\partial w}{\partial x} \delta w dy - \int_0^a \int_0^b \bar{N}_x \left(1 - \alpha \frac{y}{b} \right) \frac{\partial^2 w}{\partial x^2} \delta w dx dy \quad (\text{A.11})$$

where S_x is defined along the edges where x is constant.

In a similar manner, the first variation of the strain energy may be written as:

$$\begin{aligned} \delta U &= - \int_0^a \int_0^b \left(\frac{\partial^2 M_x}{\partial x^2} + 2 \frac{\partial^2 M_{xy}}{\partial x \partial y} + \frac{\partial^2 M_y}{\partial y^2} \right) \delta w dx dy \\ &+ \int_{S_x} \left[-M_x \frac{\partial}{\partial x} \delta w + \left(\frac{\partial M_x}{\partial x} + 2 \frac{\partial M_{xy}}{\partial y} \right) \delta w \right] dy \\ &+ \int_{S_y} \left[-M_y \frac{\partial}{\partial y} \delta w + \left(\frac{\partial M_y}{\partial y} + 2 \frac{\partial M_{xy}}{\partial x} \right) \delta w \right] dx - 2M_{xy} \delta w \end{aligned} \quad (\text{A.12})$$

where M_x and M_y are as defined above, and

$$M_{xy} = -2D_{66} \frac{\partial^2 w}{\partial x \partial y}. \quad (\text{A.13})$$

Inserting δV and δU in equation A.9, the following equation is obtained:

$$\begin{aligned} & \int_0^a \int_0^b [D_{11} \frac{\partial^4 w}{\partial x^4} + 2D_{12} \frac{\partial^4 w}{\partial x^2 \partial y^2} + D_{22} \frac{\partial^4 w}{\partial y^4} \\ & + 4D_{66} \frac{\partial^4 w}{\partial x^2 \partial y^2} - \bar{N}_x (1 - \alpha \frac{y}{b}) \frac{\partial^2 w}{\partial x^2}] \delta w \, dx \, dy \\ & + \int_{S_x} (D_{11} \frac{\partial^2 w}{\partial x^2} + D_{12} \frac{\partial^2 w}{\partial y^2}) \frac{\partial}{\partial x} (\delta w) \, dy \\ & - \int_{S_x} (D_{11} \frac{\partial^3 w}{\partial x^3} + D_{12} \frac{\partial^3 w}{\partial x \partial y^2} + 4D_{66} \frac{\partial^3 w}{\partial x \partial y^2} - \bar{N}_x (1 - \alpha \frac{y}{b}) \frac{\partial w}{\partial x}) (\delta w) \, dy \\ & + \int_{S_y} (D_{12} \frac{\partial^2 w}{\partial x^2} + D_{22} \frac{\partial^2 w}{\partial y^2}) \frac{\partial}{\partial y} (\delta w) \, dx \\ & - \int_{S_y} (D_{22} \frac{\partial^3 w}{\partial y^3} + D_{12} \frac{\partial^3 w}{\partial x^2 \partial y} + 4D_{66} \frac{\partial^3 w}{\partial x^2 \partial y}) (\delta w) \, dx \\ & + 4 \frac{\partial^2 w}{\partial x \partial y} \delta w = 0. \end{aligned} \quad (\text{A.14})$$

A solution is assumed of the form:

$$w = \sum_{m=1}^M \sum_{n=1}^N A_{mn} \sin \frac{m\pi x}{a} \sin \frac{n\pi y}{b}. \quad (\text{A.15})$$

This solution satisfies all of the boundary conditions. As a result, when the solution is substituted in equation A, it simplifies as follows:

$$\begin{aligned} & \sum_{i=1}^M \sum_{j=1}^N \sum_{m=1}^M \sum_{n=1}^N \int_0^a \int_0^b [\frac{m^4 \pi^4}{a^4} D_{11} + 2 \frac{m^2 \pi^2}{a^2} \frac{n^2 \pi^2}{b^2} (D_{12} + 2D_{66}) + \frac{n^4 \pi^4}{b^4} D_{22} \\ & + \frac{m^2 \pi^2}{a^2} \bar{N}_x (1 - \alpha \frac{y}{b})] A_{mn} \sin \frac{m\pi x}{a} \sin \frac{n\pi y}{b} \sin \frac{i\pi x}{a} \sin \frac{j\pi y}{b} \, dx \, dy \delta A_{ij} \end{aligned} \quad (\text{A.16})$$

Performing the integration, the following equation is obtained:

$$\begin{aligned} & \sum_{m=1}^M \sum_{n=1}^N \frac{ab}{4} \left[\frac{m^4 \pi^4}{a^4} D_{11} + 2 \frac{m^2 \pi^2}{a^2} \frac{n^2 \pi^2}{b^2} (D_{12} + 2D_{66}) + \frac{n^4 \pi^4}{b^4} D_{22} - \frac{m^2 \pi^2}{a^2} \bar{N}_x \right] A_{mn} \\ & + \sum_{j=1}^N [\bar{N}_x \frac{m^2 \pi^2 \alpha}{2ab} \int_0^b y \sin \frac{j\pi y}{b} \sin \frac{n\pi y}{b} dy] A_{mn} = 0 \end{aligned} \quad (\text{A.17})$$

For the purposes of this derivation, the last term in this equation will be designated ϕ :

$$\phi(n, j) = \int_0^b y \sin \frac{j\pi y}{b} \sin \frac{n\pi y}{b} dy. \quad (\text{A.18})$$

The value of this integral depends on whether $n = j$ or $n \neq j$. If $n = j$, the integral is:

$$\phi(n, j) = \int_0^b y \sin^2 \frac{n\pi y}{b} dy = \frac{b^2}{4}. \quad (\text{A.19})$$

If $n \neq j$, the integral is:

$$\phi(n, j) = \frac{1}{2} \left[\frac{b^2}{(j-n)^2 \pi^2} ((-1)^{j-n} - 1) \right] - \frac{1}{2} \left[\frac{b^2}{(j+n)^2 \pi^2} ((-1)^{j+n} - 1) \right]. \quad (\text{A.20})$$

The final set of algebraic equations which are used to obtain the buckling load are as follows:

$$\begin{aligned} & \sum_{m=1}^M \sum_{n=1}^N \frac{ab}{4} \left[\frac{m^4 \pi^4}{a^4} D_{11} + 2 \frac{m^2 \pi^2}{a^2} \frac{n^2 \pi^2}{b^2} (D_{12} + 2D_{66}) + \frac{n^4 \pi^4}{b^4} D_{22} \right. \\ & \left. - \frac{m^2 \pi^2}{a^2} \bar{N}_x \right] A_{mn} + \sum_{j=1}^N \bar{N}_x \frac{m^2 \pi^2 \alpha}{2ab} \phi(n, j) A_{mn} = 0. \end{aligned} \quad (\text{A.21})$$

To obtain other than the trivial solution ($A_{mn} = 0$), the determinate of the coefficient matrix must be zero. The smallest value of \bar{N}_x for which this condition is met will be the critical buckling load.

In order to illustrate how the buckling load is affected by α , results are presented in Figure A.1 for a $(\pm 45)_s$ simply-supported plate with total thickness, h , of .024 in. The value of \bar{N}_x at buckling is plotted on the y axis, and α is plotted on the x axis. When $\alpha = 0.0$ (constant load) the critical buckling load is 487.2 lb. This is the same

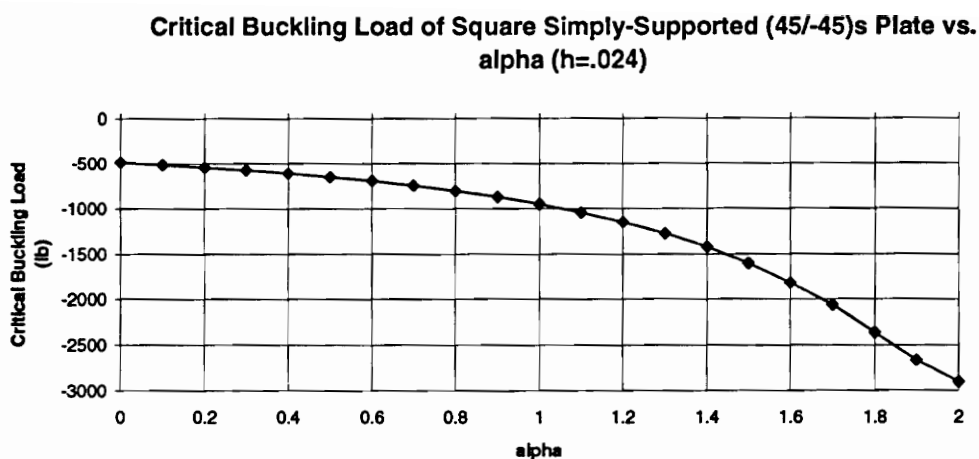


Figure A.1: Variation of the Critical Buckling Load with α

buckling load that is obtained from the standard buckling equations. When $\alpha = 1.0$ (the applied load varies from \bar{N}_x to zero) the buckling load has increased to 947.6 *lb*, and at $\alpha = 2.0$, (the applied load varies from $+\bar{N}_x$ to $-\bar{N}_x$) the buckling load is 2903.4 *lb*.

VITA

The author was born on July 24, 1966 in Hartford City, Indiana. After graduating from Pennsbury High School in Fairless Hills, Pennsylvania in 1984, he entered the engineering program at Virginia Tech. As part of his undergraduate career, he participated in the Co-operative Education Program, working on and off in a stress and dynamics engineering group at Martin Marietta Aero and Naval Systems in Baltimore, Maryland. After graduating summa cum laude with a B.S. in Aerospace Engineering in 1989, he worked as a stress analyst for General Dynamics Fort Worth Division in Fort Worth, Texas. He began his graduate studies in the Engineering Science and Mechanics Department at Virginia Tech in 1991.

